

Kent Academic Repository

Full text document (pdf)

Citation for published version

Yang, Qingling (2020) Design and Synthesis of Dual Polarized Millimetre Wave Array Antennas for Advanced Wireless Communications. Doctor of Philosophy (PhD) thesis, University of Kent,.

DOI

Link to record in KAR

<https://kar.kent.ac.uk/85615/>

Document Version

UNSPECIFIED

Copyright & reuse

Content in the Kent Academic Repository is made available for research purposes. Unless otherwise stated all content is protected by copyright and in the absence of an open licence (eg Creative Commons), permissions for further reuse of content should be sought from the publisher, author or other copyright holder.

Versions of research

The version in the Kent Academic Repository may differ from the final published version.

Users are advised to check <http://kar.kent.ac.uk> for the status of the paper. **Users should always cite the published version of record.**

Enquiries

For any further enquiries regarding the licence status of this document, please contact:

researchsupport@kent.ac.uk

If you believe this document infringes copyright then please contact the KAR admin team with the take-down information provided at <http://kar.kent.ac.uk/contact.html>

Design and Synthesis of Dual Polarized Millimetre Wave Array Antennas for Advanced Wireless Communications

Qingling Yang

A thesis submitted to University of Kent for the degree of
Doctor of Philosophy
in Electronic Engineering

January 2021

I would like to dedicate this thesis to my wife and son ...

Declaration

I hereby declare that except where specific reference is made to the work of others, the contents of this thesis are original and have not been submitted in whole or in part for consideration for any other degree or qualification in this, or any other university. This thesis is my own work and contains nothing which is the outcome of work done in collaboration with others, except where specifically indicated in the text.

Qingling Yang
January 2021

Acknowledgements

The author would like to acknowledge the many people that made this work possible, especially my advisors, Prof. Steven Gao and Dr. Paul Young, for their valuable insights and inspirational guidance. I would also like to thank China Research Institute of Radiowave Propagation (CRIRP) for its financial support. I would also like to express my gratitude to Dr. Qi Luo and Dr. Lehu Wen for their tremendous help and invaluable suggestions. I am also grateful to the following people for their help during my PhD program: Dr. Xiaofei Ren, Prof. Jian Wu, Mr. Di Kong, Mr. Wei Liu of CRIRP, Dr. Chunxu Mao of University of Surrey, Dr. Hang Xu of Huawei Technologies, Dr. Benito Sanz Izquierdo of University of Kent, Prof. Yongling Ban of UESTC, Prof. Wei Hu of Xidian University and Prof. Xuexia Yang of Shanghai University. I would also like to thank the staff at the School of Engineering and Digital Arts, University of Kent for their professional supports and suggestions, especially Mrs. Yan Zhang, Mr. Antonio Mendoza, Mrs. Qi Zheng, Mr. Edwin Lui, Ms. Joanna Gentry and Mrs. Frankie Power of the technical team, and Ms. Judith Spinks, Mrs. Jane Huxley and Mr. Israel Etonam Mensah of the finance team. I am also thankful to the school manager Ms. Mita Mondal and the school postgraduate administrator Ms. Claire Carter for their coordination.

Abstract

The millimetre-wave (mmWave) antenna arrays in traditional designs are usually very complicated, bulky and expensive. They suffer compromised radiation efficiency because of high insertion loss caused by the intricate feed networks. In addition, the cross polarization level is degraded, especially for the multibeam antenna arrays. To reduce the complexity and improve the electric characteristics, it is significant to develop mmWave antenna arrays with multi-functionality such as dual polarization, cross polarization suppression, beam switching and power splitting/combining, etc.

In this thesis, four designs of sub-mmWave and mmWave dual polarized antenna arrays with low complexity, compact size and good electrical performance are proposed. Firstly, a dual slant polarized cavity-backed slot-coupled patch antenna arrays with modified feed networks is developed. This antenna array features high XPD, simple structure and low profile. Then, a dual polarized 2D multibeam shorted-patch antenna array with high XPD when beams scan to the maximum pointing angles is developed. Differential feed technique is used to design the multibeam antenna array for the first time. The third design is a dual polarized frequency-scanning cross slot antenna array realized on a single laminate. To enable high port isolation and excitation from orthogonal directions, a SIW crossover is proposed. This antenna array shows advantages in terms of low complexity, high XPD, high aperture efficiency and wide beam scanning range. A dual polarized slot-coupled patch antenna array differentially fed by an orthomode transducer is developed in the last design. The feed networks are taken into consideration of designing the subarray antenna. The via-loaded crossover is used to enable structure simplification and triple resonance is excited to improve operation bandwidth. This antenna array features low complexity, high XPD, high radiation efficiency, high gain and high integration.

In this thesis, the design methods and synthesis procedures are detailed in order to deliver a comprehensive guide of designing the dual polarized antenna arrays. The design concept and outcomes of these antenna arrays are evaluated in the high frequency full-wave solver. All of the antenna arrays are prototyped and measured for validating the simulations. The measurements are in good agreement with the simulations, evidencing that the proposed antenna arrays have advantages in terms of high XPD, high aperture efficiency, high port isolation, low complexity and low profile. The design concepts depicted in this thesis and the developed antenna arrays could find potential applications in mobile communication systems and satellite communication systems.

Table of contents

List of figures	ix
List of tables	xvi
Nomenclature	xvii
1 Introduction	1
1.1 Motivation	1
1.2 Aim and objectives	4
1.3 Main contributions	5
1.4 Outline of the thesis	6
2 Overview of Dual Polarized Millimetre-Wave Antenna Arrays	8
2.1 Background	8
2.2 Methodology for analysis of dual polarized antennas	10
2.3 State of the art in dual polarized mmWave antenna arrays	12
2.3.1 Dual slant polarized antenna arrays	12
2.3.2 Dual polarized 2D multibeam antenna arrays	14
2.3.3 Dual polarized frequency-scanning antenna arrays	16
2.3.4 Dual polarized antenna arrays with high gain and high integration	17
2.4 Feed techniques	19
2.5 Summary	22
3 Dual Slant Polarized Cavity-Backed Slot-Coupled Patch Antenna Array	23
3.1 Cavity-backed slot-coupled patch antenna	23
3.1.1 Configuration of antenna element	24
3.1.2 Synthesis procedure	25
3.1.3 Bandwidth improvement	28
3.2 Antenna array design	33
3.2.1 Configuration of antenna array with dual slant polarization	34
3.2.2 Equal power divider with grounded patch	35
3.2.3 Series feed network	36

3.2.4	Experiment and results	39
3.2.5	Comparison and discussion	44
3.3	Summary	45
4	Differentially Fed Dual Polarized 2D SIW Multibeam Antenna Array	46
4.1	Architecture of differentially fed dual polarized 2D multibeam antenna array	46
4.2	Differentially fed dual polarized antenna	47
4.2.1	Antenna configuration	49
4.2.2	Working principles	51
4.2.3	Antenna optimization	54
4.3	2D Multibeam antenna array	57
4.3.1	Configuration	58
4.3.2	Butler Matrix design	60
4.3.3	Differential power divider	64
4.3.4	Interlayer transmission	66
4.4	Experiment and results	67
4.4.1	Return loss and port isolation	67
4.4.2	Radiation patterns	69
4.4.3	XPD and gain	71
4.4.4	Discussion and comparison	72
4.5	Summary	74
5	Frequency-Scanning Dual Polarized Cross Slot Antenna Array	76
5.1	Architecture of antenna array	76
5.2	Configuration of antenna array	77
5.3	Dual-polarized cross slot antenna and antenna array design	79
5.3.1	Configuration of antenna element	80
5.3.2	Design procedure	83
5.3.3	Performance of antenna element	87
5.3.4	Subarray antenna	88
5.3.5	Ten-way power divider	90
5.3.6	SIW-to-GCPW transition	91
5.4	Experiment and results	94
5.4.1	Return loss and port isolation	94
5.4.2	Radiation patterns	95
5.4.3	Gain and radiation efficiency	96
5.4.4	Comparison and discussion	98
5.5	Summary	98

6	Dual Polarized SIW Antenna Array With Orthomode Transducer	100
6.1	Architecture of the antenna array	100
6.2	Dual polarized 2×2 -element subarray antenna	102
6.2.1	Configuration	102
6.2.2	Simulated results	104
6.2.3	Via-loaded crossover	105
6.2.4	Triple resonance	107
6.2.5	2×8 antenna array with four subarrays	110
6.3	Differentially fed planar antenna array with dual polarization	112
6.3.1	Configuration of antenna array	112
6.3.2	Planar orthomode transducer	115
6.3.3	Four-way power divider	117
6.3.4	180° SIW elbow	118
6.4	Fabrication and experimental results	120
6.4.1	Fabricated prototype	121
6.4.2	Reflection and port coupling coefficient	122
6.4.3	Radiation patterns and gain	122
6.4.4	Comparison and discussion	125
6.5	Summary	126
7	Conclusion and Future Work	127
7.1	Conclusion	127
7.2	Future work	130
	References	131
	List of Publications	151

List of figures

2.1	Network representation of (a) antenna with single polarization, and (b) antenna with dual polarization.	10
2.2	Ludwig's definitions of co-polarization and cross polarization. (a) Definition I. (b) Definition II. (c) Definition III.	11
2.3	Architecture of different dual slant polarized antenna arrays. (a) Separated aperture. (b) Interleaved aperture. (c) Shared aperture.	13
2.4	Dual polarized patch antenna with different feed structures. (a) Simple feed. (b) Differential feed [192].	19
2.5	Dual polarized patch antenna fed by microstrip lines designed on different laminate layers [205].	20
2.6	Dual polarized patch antenna fed by SIWs designed on different laminate layers [207].	21
2.7	Turnstile junction orthomode transducer [216].	22
3.1	Configuration of the cavity-backed slot-coupled patch antenna with $\pm 45^\circ$ dual slant polarization. (a) Exploded view. (b) Radiating patch. (c) Cross slot on the ground. (d) SIW cavity.	24
3.2	Configuration of (a) corner-fed cross slot antenna, (b) edge-fed cross slot antenna.	25
3.3	Simulated <i>S</i> -parameters of the corner-fed and edge-fed slot antennas.	26
3.4	Field distribution in the SIW cavity of (a) corner-fed slot antenna, and (b) edge-fed slot antenna.	27
3.5	Simulated normalized radiation patterns of (a) corner-fed slot antenna, and (b) edge-fed slot antenna.	28
3.6	Simulated <i>S</i> -parameters of the proposed dual slant polarized antenna.	29
3.7	Simulated normalized radiation patterns of the proposed dual slant polarized antenna.	29
3.8	Simulated gain and XPD of the proposed dual slant polarized antenna.	30
3.9	Simulated normalized radiation patterns of the proposed dual slant polarized antenna.	30

3.10	Simulated $ S_{11} $ of the proposed antenna with different truncated corner size (r_c).	31
3.11	Simulated $ S_{11} $ of the proposed antenna with different gaps between patches (w_g).	31
3.12	Configuration of the dual slant polarized antenna array. (a) Exploded view. (b) Top view. (c) Bottom view.	33
3.13	Layout of the designed equal power divider.	34
3.14	Circuit representation of the designed power divider.	35
3.15	Simulated S -parameters of the power divider with or without the shorted patch.	35
3.16	Layout of the designed series feed network.	36
3.17	Equivalent circuit of the designed series feed network.	37
3.18	Simulated reflection coefficient at port #1 of the designed series feed network.	37
3.19	Simulated transmission coefficients from port #1 to #9 in the designed series feed network.	38
3.20	Fabricated prototype of the designed dual slant polarized antenna array. (a) Top view. (b) Bottom view.	40
3.21	Measured and simulated return loss and port isolation of the designed dual slant polarized antenna array.	40
3.22	Simulated return loss of (a) the series feed network at port #1 when all the output ports are shorted to the ground, (b) the series feed network at port #1 when all the output ports are loaded with the input impedance of the antenna element.	41
3.23	Gain and efficiency of the designed dual slant polarized antenna array.	41
3.24	Normalized radiation patterns in the planes of (a) $\varphi = 45^\circ$ at 27.2 GHz, (b) $\varphi = -45^\circ$ at 27.2 GHz, (c) $\varphi = 45^\circ$ at 28 GHz, (d) $\varphi = -45^\circ$ at 28 GHz, (e) $\varphi = 45^\circ$ at 28.8 GHz and (f) $\varphi = 45^\circ$ at 28.8 GHz.	42
3.25	Simulated normalized far field radiation patterns in the planes of (a) $\varphi = 45^\circ$, and (b) $\varphi = -45^\circ$ at 28 GHz with different board-to-board misalignment Δd	43
4.1	Architecture of the proposed differentially fed dual polarized 2D multi-beam antenna array.	47
4.2	Configuration of the proposed differentially fed dual polarized antenna. (a) Exploded view. (b) Layout of the shorted patch. (c) Layout of GND-1.	48
4.3	(a) Electric field distribution, and (b) Equivalent magnetic current when differential port d1 is excited. (c) Electric field distribution, and (d) Equivalent magnetic current when differential port d2 is excited.	50

4.4	Evolution process of the proposed differentially fed dual polarized patch antenna. (a) Reference antenna Ant-1. (b) Reference antenna Ant-2. (c) Proposed antenna.	52
4.5	Simulated S -parameters of the antennas in the design process.	53
4.6	Simulated S -parameters and gain of the proposed differentially fed dual polarized patch antenna.	54
4.7	Simulated normalized far field radiation patterns of the proposed differentially fed dual polarized patch at 28 GHz when differential port #d1 is excited.	54
4.8	Simulated normalized far field radiation patterns of the proposed differentially fed dual polarized patch at 28 GHz when differential port #d2 is excited.	55
4.9	Simulated S -parameters of the proposed differentially fed dual polarized patch antenna with or without the grounding vias.	56
4.10	Simulated S_{dd11} of the proposed differentially fed dual polarized patch antenna by varying the length of the feed strip.	57
4.11	Configuration of the proposed differentially fed dual polarized 2D multi-beam array antenna.	58
4.12	Layout of the 2×2 antenna array and the differential power dividers.	59
4.13	Layout of the designed Butler Matrix and the $-3\text{dB}/90^\circ$ hybrid coupler.	60
4.14	Simulated S -parameters and phase response of the designed SIW hybrid coupler.	61
4.15	Simulated S -parameters of the designed SIW Butler Matrix.	62
4.16	Simulated phase response of the designed SIW Butler Matrix.	62
4.17	Layout of the differential power dividers.	63
4.18	Simulated $ S_{11} $ of the designed differential power divider with different slant slot angles.	63
4.19	Simulated S -parameters and phase difference between port #2 and #3 of the designed differentia power divider when port #1 is excited.	64
4.20	Layout of (a) interconnection and (b) reference SIW.	65
4.21	Simulated S -parameters of the SIW interconnection and phase difference between the SIW interconnection and the reference SIW.	65
4.22	Top view and bottom view of the fabricated prototype of the designed differential fed dual polarized 2D multibeam antenna array.	66
4.23	Measured and simulated return loss of the designed differentially fed dual polarized 2D multibeam antenna array at the feed port #1 and #5.	67
4.24	Simulated isolation between port #1 and #8 of the designed 2D multibeam antenna array.	68

4.25	Measured isolation between port #1 and #8 of the designed 2D multibeam antenna array.	68
4.26	Measured and simulated normalized far field radiation patterns of the proposed differentially fed dual polarized 2D multibeam array antenna with VP when port #1 is excited. (a)26.8 GHz at quasi E-plane. (b) 28 GHz at quasi E-plane. (c) 29.2 GHz at quasi E-plane. (d)26.8 GHz at quasi H-plane. (e)28 GHz at quasi H-plane. (f) 29.2 GHz at quasi H-plane. . . .	70
4.27	Measured and simulated normalized far field radiation patterns of the proposed differentially fed dual polarized 2D multibeam array antenna with HP when port #5 is excited. (a)26.8 GHz at quasi E-plane. (b) 28 GHz at quasi E-plane. (c) 29.2 GHz at quasi E-plane. (d)26.8 GHz at quasi H-plane. (e)28 GHz at quasi H-plane. (f) 29.2 GHz at quasi H-plane. . . .	72
4.28	Measured and simulated XPD of the designed 2D multibeam antenna array at the feed port #1 and #5.	73
4.29	Measured and simulated realized gain, and simulated directivity of the designed 2D multibeam antenna array at the feed port #1 and #5.	73
5.1	Concept diagram of the dual polarized antenna array designed on a single laminate.	77
5.2	Illustration of the radiation principle of a serially fed linear antenna array.	78
5.3	Illustration of the radiation principle of a serially fed linear antenna array.	79
5.4	Field distribution of (a) conventional square SIW cavity and (b) cross slot antenna designed by using the conventional square SIW cavity.	80
5.5	Configuration of the proposed dual polarized cavity-backed cross slot antenna element.	81
5.6	Evolution process toward the developed dual polarized cavity-backed cross slot antenna element. (a) Two perpendicular SIWs. (b) Proposed SIW cavity supporting TE_{120} and TE_{210} modes. (c) Proposed dual polarized cross slot antenna.	82
5.7	Simulated coupling coefficients between port #1 and #3 in different structures shown in Fig. 5.6.	83
5.8	Magnetic field inside the cylindrical cavities of the designed dual-polarized subarray antenna.	84
5.9	Simulated reflection coefficients at port #1 of the proposed dual polarized antenna with different position l_m of the metallized vias.	84
5.10	Simulated reflection coefficients at port #1 of the proposed dual polarized antenna with different size d of the metallized vias.	85
5.11	Simulated port coupling coefficients of the proposed dual polarized antenna with different position l_m of the metallized vias.	86

5.12	Simulated port coupling coefficients of the proposed dual polarized antenna with different size d of the metallized vias.	86
5.13	Radiation efficiency of the designed dual polarized cavity-backed cross slot antenna with different slot width w_s	87
5.14	Simulated S -parameters and radiation efficiency of the designed dual polarized antenna.	88
5.15	Simulated normalized radiation patterns of the designed dual polarized antenna.	88
5.16	Subarray composed of two linear antenna arrays. (a) Configuration. (b) Field distribution with port #1 and #2 excited simultaneously.	89
5.17	Diagram of half a power divider.	89
5.18	Layout of the designed ten-way power divider.	90
5.19	Simulated coupling factors at output ports #1 to #5 of the ten way power divider.	91
5.20	Simulated phase differences between the adjacent output ports of the designed ten-way power divider.	91
5.21	Layout of the designed SIW-to-GCPW transition.	92
5.22	Simulated S -parameters of the designed SIW-to-GCPW transition.	93
5.23	Fabricated prototype of the designed dual polarized cross slot antenna array.	93
5.24	Measured and simulated reflection coefficients of the designed dual polarized cross slot antenna array.	94
5.25	Measured and simulated port coupling coefficients of the designed dual polarized cross slot antenna array.	95
5.26	Normalized co-polarization radiation patterns at different frequencies. (a) Measured. (b) Simulated.	96
5.27	Measured and simulated cross-polarization radiation patterns of the designed antenna array at different frequencies when port #1 is excited.	97
5.28	Gain, directivity and radiation efficiency of the designed dual polarized cross slot antenna array.	97
6.1	Architecture of the proposed differentially fed dual polarized antenna array.	101
6.2	Architecture of the proposed differentially fed dual polarized antenna array.	102
6.3	Configuration of the designed dual polarized 2×2 -element subarray antenna.	103
6.4	Simulated S -parameters and realized gain of the designed dual polarized 2×2 -element subarray antenna.	104
6.5	Simulated normalized far field radiation patterns of the designed dual polarized 2×2 -element subarray antenna.	105
6.6	Simulated electric field pattern inside the via-loaded crossover structure.	106
6.7	Simulated port isolation of the designed crossover without the grounding vias and with different position of ground vias.	106

6.8	Magnetic field inside the cylindrical cavities of the designed dual-polarized subarray antenna.	108
6.9	Simulated reflection coefficient $ S_{11} $ of the designed subarray antenna without the cylindrical cavity and with different size of the cylindrical cavity.	108
6.10	Simulated reflection coefficient $ S_{11} $ of the designed subarray antenna without the cylindrical cavity and with different size of the cylindrical cavity.	109
6.11	Simulated electric field of (a) inside the crossover structures and (b) over the patch radiators of the four subarray antennas.	110
6.12	Simulated magnitude and phase of the electric fields \vec{E}_y at the centre of the cross slots.	111
6.13	Configuration of the proposed differentially fed dual polarized planar antenna array.	113
6.14	Detailed structures of the designed differentially fed dual polarized antenna array on different layers. (a) Antenna array aperture. (b) TE ₄₁₀ and TE ₁₄₀ SIW cavities. (c) Via-loaded crossover structures. (d) Power dividers and orthomode transducer.	114
6.15	Stackup diagram of the designed differentially fed dual polarized antenna array.	115
6.16	Configuration of the designed planar orthomode transducer. (a) Exploded view. (b) Top layer. (c) Bottom layer.	116
6.17	Simulated S-parameters and phase differences between the output ports of the designed orthomode transducer.	117
6.18	Layout of the designed SIW four-way power divider.	118
6.19	Simulated reflection coefficient at feed port #1 and transmission coefficients from port #1 to ports #2–#5 of the designed four-way power divider.	118
6.20	Configuration of the designed SIW elbow. (b) Bottom layer. (b) Transverse slots on the ground plane. (c) Top layer.	119
6.21	Simulated reflection coefficient $ S_{11} $ and transmission coefficient $ S_{21} $ of the designed SIW 180° elbow.	120
6.22	Simulated electric field pattern inside the cascaded structure including the orthomode transducer, the four-way power dividers and the 180° SIW elbows.	120
6.23	Fabricated prototype of the designed differentially fed dual polarized antenna array. (a) Top and bottom view. (b) Different copper layers of the antenna array.	121
6.24	Measured and simulated reflection coefficients $ S_{11} $ and $ S_{22} $, and the port coupling coefficient $ S_{21} $	122

6.25	Normalized far-field radiation patterns at the frequencies 19.4 GHz, 20 GHz and 20.6 GHz when port #1 or port #2 is excited.	123
6.26	Measured and simulated gain, directivity and radiation efficiency of the designed differential fed dual polarized antenna array.	124

List of tables

3.1	Dimensions of the dual slant polarized antenna: mm	25
3.2	Impedances in each junction of the series feed network	37
3.3	Comparison between this work and other mmWave slant polarized antennas	44
4.1	Dimensions of the differential fed dual polarized patch antenna: mm . . .	49
4.2	Theoretical phase response of the designed Butler Matrix	60
4.3	Dimensions of the components used in the design of the multibeam antenna array	61
4.4	Comparison between this multibeam array antenna and the reported works	74
5.1	Dimensions of the designed dual polarized cavity-backed cross slot an- tenna: mm	81
5.2	Dimensions of the designed ten-way power divider: mm	90
5.3	Dimensions of the designed SIW-to-GCPW transition: mm	92
5.4	Comparison between this work and other frequency-scanning array antennas	98
6.1	Dimensions of the designed 2×2 -element subarray antenna: mm	104
6.2	Dimensions of the components used in designing the feed network: mm .	117
6.3	Comparison between this antenna and the reported dual-polarized antenna arrays	125
7.1	Summary of the developed dual polarized antenna arrays in this thesis . .	129

Nomenclature

Roman Symbols

A	physical size of an antenna
B	operation bandwidth
C	channel capacity
D	antenna directivity
f	frequency of electromagnetic wave
G	antenna realized gain
$N(f)$	noise power spectrum
$S(f)$	signal power spectrum

Greek Symbols

$\eta_{ap.}$	aperture efficiency
$\eta_{rad.}$	radiation efficiency
λ	wavelength of electromagnetic wave

Acronyms / Abbreviations

2D	Two Dimensional
3D	Three Dimensional
ADAS	Advanced Driver Assistance System
AiP	Antenna in Package
AoC	Antenna on Chip
BW	Bandwidth

CA	Carrier Aggregation
CNC	Computer Numerical Control
dB	Decibel
dBi	Decibel Isotropic
FBR	Front-to-Back Ratio
GCPW	Grounded Co-Planar Waveguide
GHz	Gigahertz
HFSS	High Frequency Structure Simulator
HP	Horizontal Polarization
IEEE	Institute of Electrical and Electronics Engineers
ITU	International Telecommunication Union
LHCP	Left Hand Circular Polarization
LTCC	Low Temperature Co-Fired Ceramic
MHz	Megahertz
MIMO	Multiple-Input and Multiple-Output
mm	Millimetre
mmWave	Millimetre-Wave
OFDM	Orthogonal Frequency-Division Multiplexing
OMT	Orthomode Transducer
PCB	Printed Circuit Board
RF	Radio Frequency
RHCP	Right Hand Circular Polarization
SAR	Synthetic Aperture Radar
SIW	Substrate Integrated Waveguide
ME	Magneto-electric
SLL	Side Lobe Level

SOTM	Satellite Communication on the Move
TE	Transverse Electric
THz	Terahertz
TM	Transverse Magnetic
VNA	Vector Network Analyzer
VP	Vertical Polarization
WLAN	Wireless Local Area Network
WMAN	Wireless Metropolitan Area Network
WPAN	Wireless Personal Area Network
XPD	Cross Polarization Discrimination

Chapter 1

Introduction

1.1 Motivation

In the past decade, wireless communications have experienced a rapid growth due to the advent of applications such as internet-of-things, satellite communications on the move (SOTM), virtual reality, autonomous vehicles, live streaming, positioning, intelligent transportation, and smart manufacturing, etc. These applications require the wireless networks able to provide high channel capacity, multi-functionality and high reliability. According to the Shannon–Hartley theorem [1, 2], the channel capacity is described as

$$C = \int_0^B \log_2 \left[1 + \frac{S(f)}{N(f)} \right] \quad (1.1)$$

where B is the operation bandwidth, f is the frequency of carrier waves, $S(f)$ is the signal power spectrum and $N(f)$ is the noise power spectrum. The Shannon–Hartley theorem states the maximum data rate (bits/second) can be obtained over a wireless channel of a given operation bandwidth in the presence of Gaussian noise. From (1.1), it is obvious that the data rate of a single channel can be improved by increasing either the operation bandwidth B or the signal-to-noise ratio $S(f)/N(f)$.

Currently, most of the wireless communication systems for civil use are working below 6 GHz since the electromagnetic waves at these frequencies are able to travel over a longer distance and permeate solid obstacles like buildings better than the waves at the high frequency spectrum. However, because the frequency spectrum under 6 GHz is highly congested, it has become increasingly clear and critical to unlock the spectrum at millimetre-wave (mmWave) frequencies so as to meet the needs of high speed wireless communications. Since then, mmWave communications have received lots of attention from scientific communities and industry sectors. According to the International Telecommunication Union (ITU) designation, the mmWave frequencies are defined as the spectrum band of the electromagnetic waves from 30–300 GHz [3]. In the past few years, a wide variety of telecommunication standards have been specified in the mmWave frequency range. For

example, IEEE 802.16 specifies a frequency range of 10–66 GHz for wireless metropolitan area network (WMAN) applications [5]. IEEE 802.11ad and IEEE 802.15.3c standards specify the carrier frequencies 45–66 GHz for wireless personal area networks (WPANs) [6]. IEEE 802.11ad specifies the 60 GHz frequency band for the next generation of wireless local area network (WLAN). The mmWave frequencies are also playing an important role in the fifth generation (5G) mobile networks [7]. The frequency bands such as 26 GHz, 28 GHz, 38 GHz and 60 GHz have been opened up and auctioned for 5G use in countries like USA, China, South Korea, Japan, UK and other European countries, etc. As a key enabler for intelligent transportation, 24 GHz and 77 GHz radars have been used in advanced driver assistance systems (ADASs) to reduce road accidents and the associated casualties [8]. As can be seen from these standards, the specified frequencies near the bottom of the defined mmWave frequency band, namely the sub-millimetre-waves (sub-mmWaves) from 20 to 30 GHz, have also been allocated to the 5G mobile networks and many other applications [4]. They also have found their applications in cancer cell detection, electronic countermeasures and remote sensing due to the high resolution.

As one of key components, the antenna, which couples the electrical connection to electromagnetic waves, is indispensable in any wireless communication system. The antenna operating with dual polarization can significantly increase the channel capacity and system reliability for wireless communications. According to (1.1), the channel capacity could be doubled for wireless systems equipped with dual polarized antennas. In addition, the dual polarized wireless systems also show advantages in smaller size, lower cost, and lighter weight.

In spite of many benefits offered and broad application prospects envisaged in mmWave frequencies, there are a bunch of technical challenges and open problems that must be fully considered and addressed in advance of putting this technology into major deployment. The major challenges for dual polarized mmWave antenna array design are mainly reflected in the following aspects:

At first, the mmWave waves experience higher path loss from the atmosphere compared with the waves at low frequency bands. Thus, to ensure adequate link budget between the transmitter and the receiver, it is essential that the antenna is capable of delivering high gain beams to specified directions. This requires that a set of multiple antennas should operate together as an antenna array. The gain of an antenna array is determined by antenna element gain, aperture size of the antenna array and transmission loss caused by the feed networks. It is predicted that the gain increases 3 dB by doubling the number of antenna elements without considering the loss from the feed networks [218]. In fact, it is impossible to avoid the loss from feed networks even though laminates with low loss tangent can be applied in design. For example, the attenuation due to dielectric loss in a

microstrip line is given as [219]

$$\alpha_d = \frac{k_0 \epsilon_r (\epsilon_r - 1) \tan \delta}{2\sqrt{\epsilon_e} (\epsilon_r - 1)} \text{ Np/m} \quad (1.2)$$

which indicates that the higher frequency waves will experience more significant attenuation. With the increase in the the number of antenna elements, the path length of the feed networks is increased accordingly, which will result in higher loss for the antenna system. Thus, it is very likely for a mmWave antenna array that the realized gain will be reduced even though it has larger number of antenna elements [168, 220, 221]. In mmWave frequencies, it is critically important to choose the feed networks properly prior to the antenna array design. Most commonly used in low frequencies, the transmission lines such as microstrip lines and co-planar waveguides suffer significant loss in mmWave frequencies. Thus, the antenna array fed by these transmission lines has low radiation efficiency, especially when the antenna array has a large number of elements. The mmWave antennas have very small physical size, which calls for high integration between the antennas and the RF front end modules in order to reduce the loss caused by the transmission lines. In addition, with the increase of directivity, the beamwidth of a single radiation beam from the antenna array will be narrowed. Thus, the antenna array working at mmWave frequencies must be equipped with multibeam or beam-switching networks to increase the signal coverage area in some applications.

Secondly, a wide range of antenna structures are considered not suitable for mmWave applications under the prerequisites such as compact size, low profile, low cost, high gain and ease of integration. These antenna structures include horn antennas, log-periodic antennas, wire dipoles/monopoles, and parabolic reflectors, etc. Besides, it is not practical to design a mmWave antenna array just by scaling down the dimensions of antenna arrays working at microwave or RF frequencies. The travelling wave antennas have wide operation bandwidth, such as long wire antennas, Yagi-Uda antennas, helical antennas and spiral antennas, etc. However, one of the most disadvantages of these antenna types is that they usually have very large electric size. In these antennas, unstable radiation beams are widely observed and the beam pointing angles do not keep constant at different operation frequencies. Due to the small size of antenna elements, it gives the designer much less freedom to design the antenna array and include the feed networks in such a small footprint. Besides, the broadband impedance matching techniques and the methods of extracting dual polarized waves in low frequency bands can not be used in mmWave bands.

Thirdly, the feed methods used in microwave and RF frequencies cannot be applied in the mmWave antenna array design. For example, coaxial lines are widely adopted as the feed structure in the low frequency bands due to its simplicity and ultra wideband characteristic. However, it brings many problems such as uncontrollable consistency, low integration, high profile and high cost in mmWave applications. To avoid grating lobes in

visible space, the separation between the adjacent antenna elements should be designed in the range of $0.4\lambda_0 - 0.7\lambda_0$. Thus, the feed networks should have low complexity and compact size in order to interleave them in between the antenna elements. In dual polarized mmWave antenna arrays, the design difficulty will be escalated as two sets of feed network must be included in such a constraint space. Besides, fabrication uncertainties and material instability also pose a major threat to the performance of mmWave antenna arrays. Because of this, most of the mmWave antennas are implemented by using low temperature co-fired ceramics (LTCCs) and printed circuit boards (PCBs) with high accuracy and convenience of integration. It often requires the designer to keep a tight contact with the antenna contractors and update the design based on their feedback.

At mmWave frequencies, there are some other factors that also needs to be taken into account when designing the dual polarized antenna arrays. For example, due to the compact size of the antenna elements, it is very difficult to arrange the antenna elements and the feed networks into a small footprint. In addition, the dual polarized antenna needs two independent feed networks, which may cause feed network congestion. In addition, to improve the signal-to-noise ratio and anti-interference capability of the wireless systems, the dual polarized antenna should also work with high cross polarization discrimination (XPD) and high isolation between the feed ports.

1.2 Aim and objectives

The aim of this thesis is to investigate and develop novel designs of dual polarized mmWave and sub-mmWave antenna arrays for 5G and satellite communications. The dual polarized antenna array is a key enabler for these systems in order to increase the channel capacity and reliability, etc. The structure complexity, loss, XPD, profile and size are particularly important as they have a major impact on the efficiency, stability, cost, and integration with the frontends. This thesis is set to address these crucial aspects in sub-mmWave and mmWave dual polarized antenna arrays. The objectives of this thesis are:

1. Review and compare sub-mmWave and mmWave dual polarized antenna array architectures, identify a workable dual polarized antenna array structure and the required key enabling technologies;
2. Review the methodology of designing dual polarized antenna arrays in sub-mmWave and mmWave frequency bands;
3. Develop and demonstrate a dual slant polarized antenna array for 5G mmWave base stations;
4. Develop a 2D multibeam antenna array for mmWave 5G indoor communications.

5. Investigate and develop low complexity feed networks and dual polarized antenna arrays for 5G and satellite communications.

1.3 Main contributions

In this thesis, the methods of realizing dual polarized antenna arrays are investigated. By applying these proposed techniques, four highly integrated dual polarized antenna arrays with high XPD and low complexity are designed for different application scenarios. The novelty and major contributions of this thesis are listed as follows:

1. Dual slant polarized array antenna with high XPD and low profile
 - Using a corner-fed SIW cavity supporting diagonal TE_{120} and TE_{210} modes in the antenna element design to realize high XPD and high port isolation;
 - Designing the corner-truncated patches connected by a thin cross strip to realize dual resonance with good impedance matching;
 - Modified feed networks with a grounded patch inserted in each bend to suppress the side effect caused by discontinuity.
2. Dual polarized differentially fed 2D multibeam array antenna with high XPD and simple configuration
 - New scheme of 2D multibeam antenna array to enable differential feed;
 - Using a differentially fed shorted patch as the antenna element to simplify the configuration and improve the XPD when beams scan off the boresight;
 - Employing the power dividers with slanted slots as the differential network to feed each antenna element;
 - Using two Butler Matrices perpendicularly placed with each other in two different laminate layers to realized 2D beam switching.
3. Dual polarized frequency-controlled array antenna realized on a single laminate
 - New architecture to enable the dual polarized antenna array designed on a single laminate;
 - Crossover structure with four metallized vias placed around the cross junction to achieve high port isolation;
 - Subarray antenna designed to exemplify the performance of the dual polarized antenna element;
 - Corporate ten-way power divider to feed the dual polarized antenna array uniformly.

4. Dual polarized array antenna differentially fed by an orthomode transducer with low complexity and high XPD
 - New architecture of dual polarized differentially fed antenna array to enable high port isolation and high XPD;
 - Via-loaded crossover structure to achieve high port isolation of the 2×2 -element subarray antenna;
 - Triple resonance excited in the antenna element to improve the operation bandwidth;
 - Planar orthomode transducer to achieve differential excitation for the dual polarized antenna array.

1.4 Outline of the thesis

In this thesis, four sub-mmWave and mmWave dual polarized antenna arrays are proposed concerning the suppression of cross polarization levels, simplification of feed networks, impedance bandwidth improvement, and gain enhancement. The antennas proposed in this thesis are realized by using SIWs and microstrips so as to achieve low profile, light weight, small size and low cost. The thesis is organized as follows.

Chapter 1 briefly introduces the motivation for leading the research and main contributions of this thesis. In addition, the achievements and publications during my postgraduate research are also summarized in this chapter.

Chapter 2 gives the background and significance of sub-mmWave and mmWave dual-polarized antenna arrays. Then, the methodology for analysis of dual polarized antennas are discussed. Finally, the state of the art in dual polarized sub-mmWave and mmWave antenna arrays are comprehensively reviewed.

Chapter 3 presents the design of the mmWave dual slant polarized cavity-backed slot-coupled patch antenna array. The working mechanism are synthesised thoroughly. The role of the corner-fed SIW cavity supporting diagonal TE_{120} and TE_{120} is discussed. Then, impedance bandwidth improvement caused by the cross strip connecting the corner-truncated patches is given. The design method, optimization and validation of the feed networks are discussed in detail. The measured results and tolerance analysis are presented at last.

Chapter 4 gives the design method for realizing differentially fed dual polarized 2D multibeam antenna array. The design and working principle of the cavity-backed shorted patch are discussed at first. Then, the overall configuration followed by the component designs is presented. The fabrication prototype and the measured results are discussed in the last section.

Chapter 5 gives the design method for realizing dual polarized frequency-scanning antenna array on a single laminate. The role of the designed crossover structure is discussed in detail. Then, parameter studies are carried out to have a better understanding of the working principle of the designed dual polarized antenna element. A subarray antenna is designed to exemplify the antenna element performance in the antenna array. The fabrication and measured results of this antenna array are presented at last.

Chapter 6 presents the design of the dual polarized antenna array differentially fed by an orthomode transducer with low complexity and high XPD. The architecture of realizing such an antenna array is given at first. Then, the role and working principle of the via-loaded crossover structure are discussed. Triple resonance introduced in the antenna element to improve the bandwidth is synthesised thoroughly. The overall configuration and three key components are then presented and discussed in detail. In the last section, the measured results and comparison with other reported works are given.

Chapter 7 gives a conclusion remark of this thesis. A brief summary of the features and technical contributions of the proposed dual polarized antenna arrays is then presented. The discussion of future work is given at last.

Chapter 2

Overview of Dual Polarized Millimetre-Wave Antenna Arrays

2.1 Background

Wireless communications are expected to deliver faster and better broadband in applications such as transport, medical care, warehousing and storage, construction, manufacturing, broadcasting, agriculture and environment, etc. Advanced antenna technologies, such as massive and full dimensional MIMO (multiple-input and multiple-output), mmWave technology, and carrier aggregation (CA) are considered as key approaches of enabling these applications. Thus, in order to tailor to the needs, antennas should be designed as actively driven dense antenna arrays with high integration, low cost, small size, multi-functionality such as dual polarization, beam switching, duplexing, filtering and reconfigurability, etc.

As one of key techniques widely used in modern wireless networks, dual polarized antennas can offer two orthogonal channels over the same carrier frequency. There are many practical applications of dual polarized antennas, including but not limited to the following aspects. 1) Frequency reuse. It was theoretically proved that a dual polarized antenna system introduces no interference and allows the two orthogonal data streams to be duplexed and de-duplexed independently without distortion [9–12]. This concept can be traced back to the cross polarization definition proposed by Arthur C. Ludwig in 1973 [13]. In addition, the channel capacity in a dual polarized wireless system is nearly doubled compared with that of a single polarized wireless system. 2) Integrated transceivers. Integration between the transmitter and the receiver is enabled to realize self-duplexing in a dual polarized antenna system because the orthogonal components usually share the same radiation aperture. It has been demonstrated in [14–17] that the antennas operate with self-duplexing for satellite communications. The integrated transceiver also finds its use in short range communications and radar systems for full duplexing [18–22]. 3) Polarization diversity. A wide variety of problems are raised particularly when wireless systems operate in urban environment, such as multipath effect, high interference, significant obstacle,

and severe shadowing, etc [23, 24]. However, these effects are significantly mitigated by introducing polarization diversity as it enables the wireless system to be immune from polarization mismatching and show strong resistance to the arbitrary placement of transmitting or receiving antennas [25–28]. 4) Polarization agility [29–32]. For example, the dual linearly polarized antenna can operate with either vertical polarization (VP) or horizontal polarization (HP) by utilizing passive or active switches. Meanwhile, it can also work as a dual circularly polarized antenna by imposing 90° and -90° phase variation between the excitation ports [33, 34]. 5) Sensitivity improvement. It is very commonly seen in the applications of synthetic aperture radars (SARs) and satellite communications. For example, a wideband dual-polarized patch antenna where the isolation between two orthogonal channels is higher than 25 dB was proposed in [35]. In [36, 37], different dual polarized patch antennas working at multiple bands were proposed for SAR applications. Dual circularly polarized antenna arrays and reflectarrays have been employed in the small satellites launched by ESA and NASA to achieve high system sensitivity [38, 39].

Even though dual polarized antennas have gained much popularity among the industry sectors and academic communities since they offer a broad range of benefits for modern wireless networks, their applications in mmWave frequency bands still have a long way to go as many problems related to this topic remain unsolved. Currently, most of research activities on dual polarized mmWave antenna arrays are concentrated on traditional patch [40–43] and slot antennas [44–47]. However, these antenna arrays usually have low XPD and unstable radiation patterns. Another important issue to be concerned with is that high complexity is extensively found in dual polarized antenna arrays. This is because each polarization excitation requires an independent feed network. To avoid congestion, the feed networks for exciting different polarizations are usually designed in different laminate layers. This arrangement will ramp up the integration difficulty and also introduce significant loss caused by the feed networks, thus deteriorating the overall performance of the antenna system, especially when antenna arrays operate at mmWave frequency bands. To overcome these problems, a hybrid design concept that enables the feed networks to be fully incorporated in the design of the dual polarized antenna array has been developed in the past few years [48]. Compared with traditional designs of dual polarized antenna arrays, the hybrid design shows the following advantages:

- reduced complexity
- higher XPD
- higher integration
- smaller size
- lower loss and higher efficiency
- lower cost

In mmWave applications, the fabrication tolerance also plays an important role in antenna performance due to its small size. The fabrication technologies applicable for mmWave antennas are PCB, LTCC [49], antenna on chip (AoC)/antenna in package (AiP)

[50], computer numerical control (CNC) [51] and 3D printing [52], etc. In the frequency band 20–110 GHz, the PCB and LTCC processing technology are two of most important approaches in prototyping mmWave antennas because they enable the antennas to have low profile, low cost, small size and high integration with RF front ends. Patch antennas fed with microstrip lines are very commonly seen in the antenna arrays working below the K band frequencies due to the ease of fabrication and their conformability. However, they suffer significant surface waves and high loss at mmWave frequency bands. Compared with patch antennas fed with microstrip lines, the slotted waveguides can be considered as a more favourable candidate for mmWave applications thanks to their low dielectric loss and neglectable wave leakage. The downsides of traditional rectangular waveguides are bulky, high profile, high difficulty in fabrication and integration. Obviously, these negative factors make the waveguide-based antennas not suitable for large scale applications. To overcome these side effects, the waveguide-based antenna reported in [53] was implemented by using diffusion bonding technology. However, the fabrication of these antennas are overpriced and low efficiency, and it cannot be easily applied to antennas with multiple laminate layers as well. In the past two decades, a versatile structure known as the substrate integrated waveguide (SIW) or laminated waveguide has become a research hotspot as it inherits the advantages of traditional waveguides and can be easily integrated with other planar circuits by using the same fabrication technology. The fundamental principles and transmission characteristics of the SIW structure can be found in massive publications [54–57]. A wide variety of antennas, filters, couplers, power splitters, oscillators and mixers are designed by using SIWs.

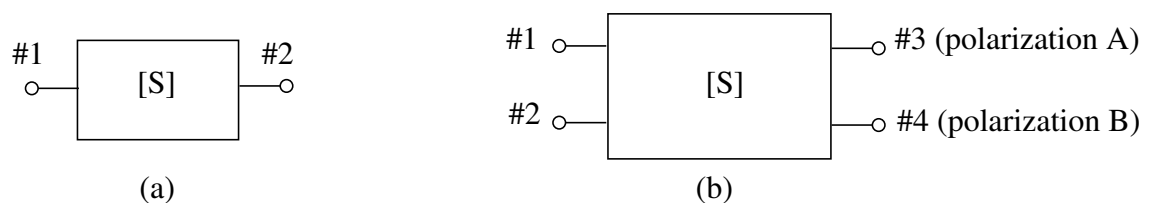


Fig. 2.1 Network representation of (a) antenna with single polarization, and (b) antenna with dual polarization.

2.2 Methodology for analysis of dual polarized antennas

In the design of microwave components and antennas, it is usually very useful to carry out network analysis so as to characterize their performance. The network representation of an antenna with single polarization is shown in Fig. 2.1(a) where port #1 is the interface between the antenna and the receiver or transmitter, and port #2 represents free space. Thus, S_{11} is the reflection coefficient of the antenna. The dual polarized antenna can be considered as a four-port network, as shown in Fig. 2.1(b). In this network, ports #1 and

#2 are the feed ports for exciting polarization A and B, respectively. S_{11} and S_{22} are the reflection coefficients. S_{21} and S_{12} represent the coupling coefficients between port #1 and #2. For a dual linearly polarized antenna, S_{41} and S_{32} can be used to characterize the cross polarization levels, and they represent axial ratio (AR) for a dual circularly polarized antenna. In general, low cross polarization levels, high return loss and high port isolation should be achieved in a dual polarized antenna.

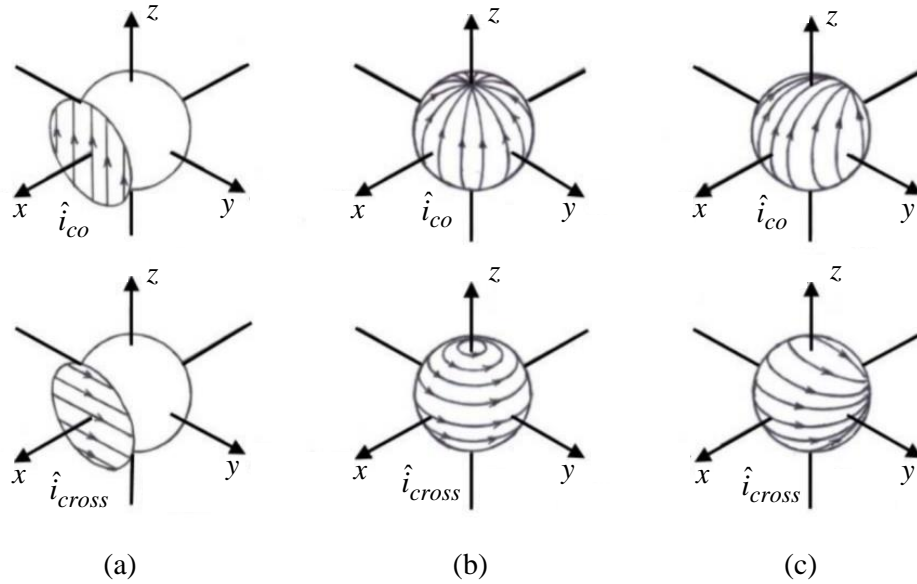


Fig. 2.2 Ludwig's definitions of co-polarization and cross polarization. (a) Definition I. (b) Definition II. (c) Definition III.

As mentioned, the cross polarization level of a dual polarized antenna can be obtained by resorting to the network analysis. In general, the cross polarization is defined as the polarization that is orthogonal to the co-polarization or reference polarization. This definition can only be applied to define the circular polarization, and obviously it is not correct to characterize the linear and elliptical polarization. In view of this, A. C. Ludwig proposed three definitions on the cross polarization and co-polarization which are illustrated in Fig. 2.2 [13]. Eqs. (2.1)–(2.3) present these definitions with formulas.

Definition I: The unit vector directions of cross-polarization and co-polarization agree with the unit vectors of the Cartesian coordinate. The vector of electric fields is projected to the \hat{i}_x and \hat{i}_y vectors located in the aperture plane.

$$\hat{i}_{co}^{(1)} = \hat{i}_y = \sin \theta \sin \phi \hat{i}_r + \cos \theta \sin \phi \hat{i}_\theta + \cos \phi \hat{i}_\phi, \quad (2.1a)$$

$$\hat{i}_{cross}^{(1)} = \hat{i}_x = \sin \theta \cos \phi \hat{i}_r + \cos \theta \cos \phi \hat{i}_\theta - \sin \phi \hat{i}_\phi, \quad (2.1b)$$

Definition II: The vectors \hat{i}_θ and \hat{i}_ϕ are used to denote the unit vector directions of cross polarization and co-polarization, respectively. The cross polarized and co-polarized

field vectors coincide with the unit vectors \hat{i}_θ and \hat{i}_ϕ in the antenna with perfect linear polarization.

$$\hat{i}_{co}^{(2)} = \hat{i}_\theta = \frac{1}{\sqrt{1 - \sin^2 \theta \sin^2 \phi}} \left[-\sin^2 \theta \sin \phi \cos \phi \hat{i}_x + (1 - \sin^2 \theta \sin^2 \phi) \hat{i}_y - \sin \theta \cos \theta \sin \phi \hat{i}_z \right], \quad (2.2a)$$

$$\hat{i}_{cross}^{(2)} = -\hat{i}_\phi = \frac{\cos \theta \hat{i}_x - \sin \theta \cos \phi \hat{i}_z}{\sqrt{1 - \sin^2 \theta \sin^2 \phi}}, \quad (2.2b)$$

Definition III: In this definition, the unit vectors of the cross polarization and co-polarization is obtained by rotating the unit vectors \hat{i}_θ and \hat{i}_ϕ with respect to the radial direction by the angle ϕ .

$$\hat{i}_{co}^{(3)} = \cos \theta \sin \phi \hat{i}_\theta + \cos \phi \hat{i}_\phi = - (1 - \cos \theta) \sin \phi \cos \phi \hat{i}_x + [1 - \sin^2 \phi ((1 - \cos \theta))] \hat{i}_y - \sin \theta \sin \phi, \quad (2.3a)$$

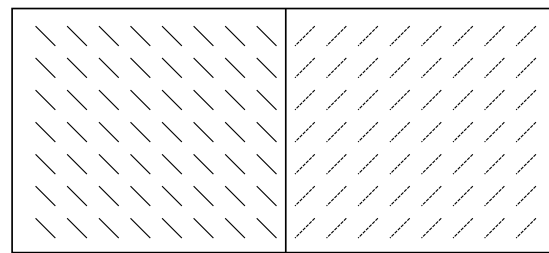
$$\hat{i}_{cross}^{(3)} = \cos \phi \hat{i}_\theta - \sin \phi \hat{i}_\phi = [1 - \cos^2 \phi (1 - \cos \theta)] \hat{i}_x - (1 - \cos \theta) \sin \phi \cos \phi \hat{i}_y - \sin \theta \cos \phi \hat{i}_z. \quad (2.3b)$$

It is obvious that the first definition cannot represent the far field radiation patterns of an antenna because the far field vectors coincide with the tangential directions of the spherical coordinate system. However, this definition can be used to confirm the polarization state of a source and near fields. In the second and third definitions, the unit vectors of cross polarization and co-polarization are parallel with the tangential directions of the spherical coordinate system. Thus, they can be used to well represent the far field radiation patterns of the antennas.

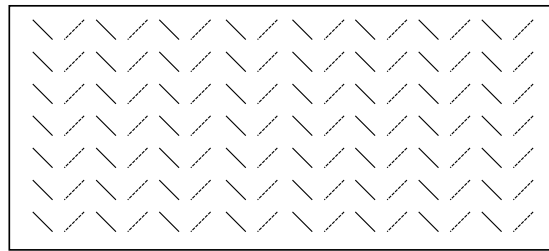
2.3 State of the art in dual polarized mmWave antenna arrays

2.3.1 Dual slant polarized antenna arrays

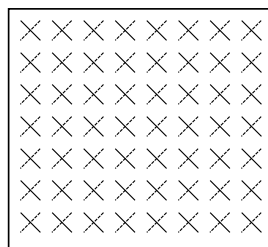
It has been theoretically and experimentally proved that $\pm 45^\circ$ dual slant polarized antennas show advantages over HP/VP antennas [58]. For $\pm 45^\circ$ dual slant polarized antenna systems, the mean signal strength received by the two orthogonally polarized antennas is almost identical. However, the received signal levels in HP/VP antenna systems show remarkable disparity. Thus, $\pm 45^\circ$ dual slant polarized antennas can deliver better results in many application scenarios.



(a)



(b)



(c)

Fig. 2.3 Architecture of different dual slant polarized antenna arrays. (a) Separated aperture. (b) Interleaved aperture. (c) Shared aperture.

In the past twenty years, major scientific attention has been focused on $\pm 45^\circ$ dual slant polarized antennas working at microwave and RF applications, such as 2G/3G/4G/5G (sub-6 GHz) base stations [59–66]. With recognisability such as large bandwidth, high directivity and compactness size of antennas, the mmWave technology has attracted wide interest from the industry sectors and scientific communities, as it is a key enabler to meet the capacity requirement of delivering high data rate for future wireless communications. Most reported works related to slant polarized antennas for mmWave applications are only able to operate with a single polarization [67–74]. Even though the $\pm 45^\circ$ dual slant polarized mmWave antenna array shows great potential in future wireless communications, it has not yet been fully explored as a limited number of works have been reported on this topic. From these reported works, the $\pm 45^\circ$ dual slant polarized mmWave antenna arrays can be divided into three categories: separated aperture [40, 75] [see Fig. 2.3(a)], interleaved aperture [76, 77] [see Fig. 2.3(b)] and shared aperture [78] [see Fig. 2.3(c)]. The first two types of antenna arrays play a dominant role in the research of $\pm 45^\circ$ dual

slant polarized mmWave antenna arrays. For dual polarized antenna arrays with separated and interleaved aperture, the orthogonally polarized waves are received and transmitted by different antenna elements, whereas in the dual polarized with shared aperture the orthogonally polarized waves are received and transmitted by a same antenna element. Apparently, the first two types of dual slant polarized antenna arrays have simple configuration and they can be easily implemented at mmWave frequencies. However, the drawbacks of these antenna arrays are also significant, such as large size, low aperture efficiency and increased cross polarization level. In addition, to avoid grating lobes, the antenna elements in these antenna arrays must have very small size, resulting in very narrow bandwidth. In some applications, dual slant polarized antenna array with interleaved aperture can be designed to work in dual frequency band, where the antenna elements working at the high frequency are located in between the low band antenna elements [47, 79–81].

Dual slant polarized antenna arrays with shared aperture can realize polarization diversity in a true sense. In general, dual polarized antenna arrays with shared aperture are composed of shared aperture dual polarized antenna elements and two sets of feed networks. The feed networks extract orthogonally polarized waves from the shared aperture dual polarized antenna elements when they work with the receiving mode. In the transmitting mode, the feed networks deliver guided waves to the dual slant polarized antenna elements for exciting orthogonally polarized radiation fields. In most of shared aperture dual slant polarized antenna array designs, the geometric shape of antenna elements is usually symmetric, such as square, circle, ring and hexagon, etc. In [78], a 60 GHz shared aperture $\pm 45^\circ$ dual slant polarized antenna was designed by using LTCC to realize high gain, but this antenna is very bulky (aperture size $\approx 2.4\lambda_0 \times 2.4\lambda_0$), making it not suitable for antenna array design in consideration of grating lobes. For sub-6 GHz applications, a large percentage of $\pm 45^\circ$ dual slant polarized antennas are evolved from the basic cross dipole thanks to its broad bandwidth, low cross polarization level and wide scanning angle [59–66]. However, these antennas cannot be scaled up and directly applied to mmWave antenna design because of high profile ($\approx \lambda/4$) and difficulty in designing the feed structures at mmWave frequencies. All of these aforementioned antennas cannot fulfil the requirements of dual slant polarization, low cross polarization level, compact size, simple structure and low profile simultaneously.

2.3.2 Dual polarized 2D multibeam antenna arrays

To broaden beam coverage and increase spatial diversity, the antenna systems capable of beam scanning are widely required in modern wireless communications. Currently, beam scanning for antenna arrays can be roughly divided into two categories: mechanical scanning and electrical scanning. Mechanical scanning antenna arrays have been served as an important role of direction finding in radar systems for years [82–86]. The term *mechanical scanning* refers to changing of the beam pointing angle by mechanical rotation

or varying the physical position of the antenna aperture by electric motors. Mechanical scanning antennas have relatively low cost and high beam pointing accuracy. In addition, the gain and SLL of mechanical scanning antennas keep constant at different beam scanning angles. However, mechanical scanning antennas also have many disadvantages, such as limited speed of scanning, large size, mechanical vibrations and mechanical failure brought by fatigue and wearing of moving parts, making them unsuitable for many application scenarios such as fast tracking and indoor communications, etc. In contrast, electrical scanning antenna arrays have gained more and more popularity in the past decade thanks to the fast beam switching capability and small size [87–90]. They bring many benefits for the wireless systems expected to realize flexible detecting and tracking, fast interception, and high data rate transmission. Different from the mechanical scanning systems, the electrical scanning system can also achieve hopping beams and enable time-division multiplexing to increase the channel capacity. Thus, electrical scanning antenna systems have become central in modern radar and wireless communications such as 5G/6G base stations, SOTM and ADAS, etc.

So far, electrical scanning has been realized in phased antenna arrays and multibeam antenna arrays. For the phased antenna array, it has high adaptivity and high anti-interference capability, thus it enables multi-object targeting and multifunction operation [91–95]. However, the versatility achieved in phased antenna arrays is at the expense of high cost (expensive T/R modules), high complexity and high power consumption [95]. In contrast, electrical scanning achieved by using passive multibeam networks has much lower cost, wider operation bandwidth, and higher design flexibility. Multibeam antenna arrays have been widely deployed in civil and commercial uses. Generally speaking, passive multibeam networks are categorized with three groups: circuit-based multibeam networks [96–107], quasi-optical lenses [108–124] and reflectors [125–131]. For the first group, it includes Butler Matrices [96–102], Blass Matrices [103, 104], Nolen Matrices [105–107], etc. They are usually designed by using passive components such as phase shifters, hybrid couplers, crossovers and magic-Ts, etc. For the second group, the most representative designs are Rotman Lenses [108–111], R-KR Lenses [112, 113], geodesic lens [114–116], Luneburg Lens [117–120], dielectric lens [121–124]. Compared with quasi-optical lens and reflector antennas, scanning antenna arrays designed by using circuit-based multibeam networks have lower cost and much smaller size. Thus, they are more preferable in the wireless system that requires miniaturization and high integration.

In many applications, scenarios such as pico or femto base stations in 5G mmWave communications, the multibeam array antenna should operate with dual polarization and be equipped with 2D beam scanning capability in order to improve spatial diversity and further increase the channel capacity. 2D beam scanning is also required in automotive radars and inter-satellite links. In addition, to enhance the SNR and minimize the channel interference, the 2D multibeam antenna array with dual polarization should have high

XPD and good isolations between channel ports for different polarizations. The passive multibeam networks for 2D beam scanning antenna arrays are designed by employing the cross-connected Butler Matrices [100–102] or Rotman Lenses [110, 111] in many cases. However, the drawbacks of these designs are low integration, high insertion loss, and bulky size. In general, the slot and patch antennas, ME dipoles are most commonly used to design a mmWave multibeam antenna array due to their simple configuration and high integration [132–137]. However, it is found from the reported works that these dual polarized antenna elements are not applied in 2D multibeam antenna arrays because they cannot be integrated with the feed networks. Therefore, most of the 2D multibeam array antennas can only operate with a single polarization. In addition, when the beam is steered off the boresight, the cross polarization level for a 2D multibeam array antenna is usually not lower than -15 dB. In some cases, the cross polarization level is even worse, which is around -10 dB when beam scans off the boresight [137]. This is because, for example, if the radiated waves from an antenna element are only HP at the boresight the antenna element will generate VP components when the beam scans away from the boresight, causing the antenna array an increased cross polarization level. Thus, how to design a 2D multibeam antenna array with high XPD, low complexity and high integration is still an open problem that remains unsolved.

2.3.3 Dual polarized frequency-scanning antenna arrays

As one of travelling wave antennas, the frequency-scanning antenna has been a research hotspot and its application has been extended to microwaves and mmWaves since it made a debut in 1940 by W. W. Hansen [138]. Compared with the standing wave antennas, the frequency-scanning antennas show advantages in terms of wide operation bandwidth, flexible beam scanning ability and good directional radiation performance [139–142]. Thus, they are very commonly used in air-borne conformal imaging radars and target location applications [143]. In addition, they are also deployed in enclosed buildings or tunnels to enhance the signal coverage area for mobile users and devices [144].

In general, the frequency-scanning antennas can be realized with structures like rectangular waveguides, circular waveguides and ridged waveguides which enable the antennas with high mechanical rigidity, high power capacity and low loss [145–147]. However, this kind of antennas are very bulky, heavy and expensive. In addition, it is quite challenging to integrate them with the RF front ends. Thus, they cannot be applied in applications that require small size, low profile and high integration. To satisfy these requirements, the planar frequency-scanning antennas designed by using microstrip lines, co-planar waveguides, slot lines have become more and more popular in recently years due to their low profile, light weight, ease of integration and high performance [148–156]. However, surface waves, which would significantly degrade the radiation patterns and radiation efficiency, would be excited in the frequency-scanning antennas designed by using these

structures. Besides that, these antennas have high loss and low efficiency in sub-mmWave and mmWave frequencies. To overcome these problems, SIWs have emerged which inherit the advantages of both the rectangular waveguides and the planar structures such as microstrip lines [157]. Thus, the frequency-scanning antennas designed by using SIWs have low loss, low profile, and light weight. In addition, high integration between the frequency-scanning antennas and the RF front end can be achieved. Due to the enclosed structure, the SIW frequency-scanning antennas can also prevent surface waves from propagation.

The frequency-scanning performance can be affected by many factors, such as antenna configuration, filled dielectric material, operation frequency and guided wave modes. The traditional designs related to frequency-scanning antennas do not function well in terms of beam scanning performance. For example, the uniform frequency-scanning antenna arrays are only able to direct beams into the first quadrant [142]. The uniform frequency-scanning antenna arrays with periodic perturbation are able to achieve backward radiation, but unfortunately they cannot realize broadside radiation [158–162]. The frequency-scanning antenna array reported in [163, 164] suffer low aperture efficiency and low XPD, although they can operate with dual polarization and be realized on a single substrate. This is because the orthogonal polarized antenna elements in these designs are interleaved in different rows. The antenna array in [165] has very limited frequency-scanning range which is less than 18° . The linear antenna arrays reported in [166, 167] have relatively wide frequency-scanning range. However, they are only able to operate with a single polarization and cannot be applied to planar antenna arrays. In addition, they must be implemented with multiple laminates. All the reported works cannot fulfil the requirements of dual polarization, wide frequency scanning range, high XPD, high aperture efficiency, simple configuration and high integration, simultaneously.

2.3.4 Dual polarized antenna arrays with high gain and high integration

As well-known, with the increase of operation frequency, dielectric loss, metallic loss and path loss will be escalated consequently. The antennas working at sub-mmWave and mmWave frequency bands face challenges on high loss, high cost, low radiation efficiency, and severe wave leakage from feed networks. In sub-mmWave and mmWave frequencies, the complexity and loss from feed networks will be escalated considerably with the increase of antenna elements [168–170]. Thus, it is very likely that the antenna gain keeps unchanged or even decreases with the increase of the number of antenna elements.

In some applications such as mobile devices or space borne communication systems, the antenna array must be highly integrated with the feed networks in order to achieve

low loss, small size, light weight, and low cost. Most traditional designs are unable to seamlessly integrate with the feed networks because of constraint space in mmWave frequencies [171–175]. In addition, the traditional designs related to mmWave dual polarized antenna arrays having a large number antenna elements are usually complicated in configuration. This is because to excite dual polarization the antenna array should be equipped with two feed networks that can work independently. To avoid congestion of the two feed networks, currently there are two different solutions reported in literature. In the first solution [43, 117, 176–180], the feed networks are designed to interleave between the antenna elements of the dual polarized antenna array. For this solution, the antenna array can be integrated with the feed networks and realized by using a single laminate. However, it is obvious that the antenna arrays designed from this solution have large size or low aperture efficiency. This kind of antenna arrays also suffer severe cross polarization radiation due to strong coupling occurring between the linear antenna arrays. Besides, another drawback brought by this solution is that grating lobes may appear in visible space.

In the second solution, the antenna array aperture together with the feed networks for exciting orthogonal polarization states are implemented on different laminate layers [181–184]. The dual polarized antenna array with metallic rectangular waveguides realized from this solution have gained much popularity due to low loss, high power handling capacity and good self-consistent electrical shielding performance [45, 48, 177, 185]. In the reported works, rectangular waveguides acting as the feed networks have two different forms: full corporate and series-corporate. Antenna arrays excited by full corporate rectangular waveguides can operate in a wide bandwidth, while antenna arrays having series-corporate hybrid feed networks have less complexity and smaller size. However, the disadvantages of antenna arrays realized with rectangular waveguides are large size, high profile, high prototyping cost, and high difficulty in integrating with the RF front ends. In the past two decades, considerable attention has been attracted to SIWs since they combines the advantages of the rectangular waveguide and planar structures like microstrip lines and striplines [186–189]. Thus, antenna arrays realized with SIWs can be completely integrated with planar RF circuits by using the PCB processing technology. Much like the dual polarized antenna arrays realized with rectangular waveguides, traditional SIW dual polarized antenna arrays are implemented with their feed networks for exciting different polarization in different laminate layers. As a consequence, these dual polarized antenna arrays have very high complexity and significant loss at sub-mmWave and mmWave frequency bands. In addition, high complexity could result in impedance mismatching, high realization difficulty, high cost and high fabrication error. The dual polarized antenna array realized by using parallel-plate waveguides is considered as another effective approach of lowering the design complexity [190, 191]. However, these antenna arrays suffer low XPD and have very narrow operation bandwidth. In view of these facts, how to design

a mmWave antenna array with high gain, high integration, low loss, low cost and high efficiency is currently a research hotspot.

2.4 Feed techniques

In mmWave frequencies, limited by the space and fabrication tolerance, it is quite challenging to design a shared aperture dual polarized antenna array fully integrated with the feed networks. According to the reported designs, the feed techniques applicable for mmWave shared aperture dual polarized antenna arrays can be divided into three categories: 1) orthogonal feeds designed on the same layer [192–204], 2) orthogonal feeds designed on different layers [205–210], and 3) orthomode transducer [211–215].

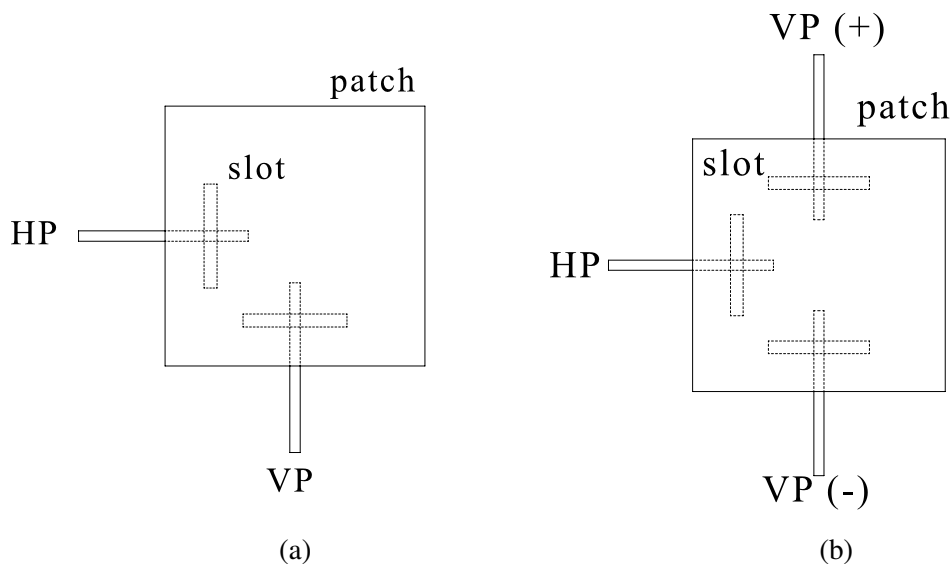


Fig. 2.4 Dual polarized patch antenna with different feed structures. (a) Simple feed. (b) Differential feed [192].

To realize dual polarization, orthogonal feeds designed on the same layer are frequently used in patch antennas fed with microstrip lines because of their compactness. Two classic patch antenna designs with orthogonal feeds designed on the same layer are illustrated in Fig. 2.4 [192–196]. In Fig. 2.4(a), the microstrip lines are placed beneath two neighbouring edges of the patch antenna. Two slots are etched on the ground plane, which enable the standing waves on the microstrip lines to excite the patch for dual polarization. This shared aperture dual polarized patch antenna has very simple configuration, but it suffers low port isolation due to strong orthogonal coupling. The bandwidth of this antenna is quite narrow because the slots are positioned near the edges of the patch to avoid congestion. Thus, to increase the bandwidth, one helpful solution is by adopting the stacked patches where each patch is expected to create a independent resonance frequency. When these resonances are close enough, the operation bandwidth can be expanded as a result. An evolved feed scheme that uses differential feed for one of the polarizations is shown in Fig. 2.4(b). Two

parallel slots are etched on the ground plane beneath the patch antenna for the vertical polarization. Since the two slots are fed by the microstrip lines from opposite direction, they are out of phase with each other in structure. Thus, to compensate the 180° phase for the vertical orientation, it is natural that a balun should be used to connect the two vertical feed lines. This differential feed scheme brings many beneficial results regarding to the antenna performance, such as significantly improved XPD and isolation between the two feed ports. However, the antenna based on this feed scheme has large physical size and it is difficult to extend it into the design of planar antenna arrays. To reduce back radiation or improve front-to-back ratio (FBR) caused by the coupling slots in the feed schemes shown in Fig. 2.4, the metallic probes can be used to replace these slots [197–200]. Alternatively, the patch antenna directly fed by the microstrip lines in the same layer is also widely used in dual polarized mmWave antenna designs [201, 202]. However, this approach suffers two significant disadvantages: very narrow bandwidth and spurious radiation from the microstrip lines.

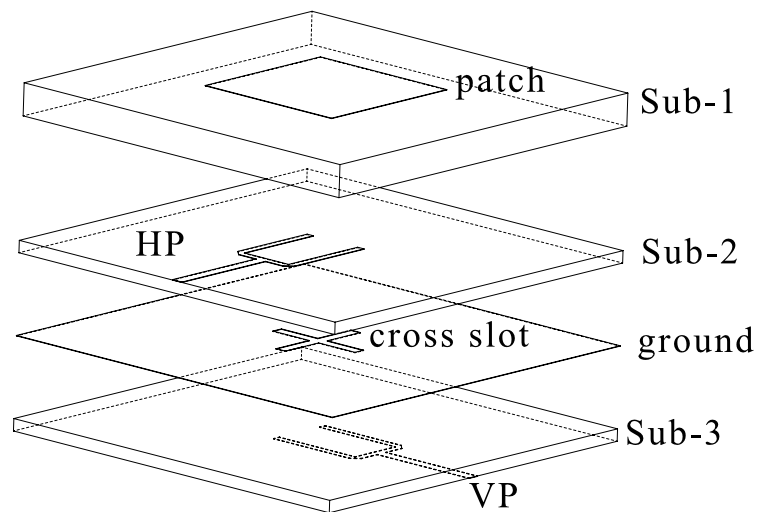


Fig. 2.5 Dual polarized patch antenna fed by microstrip lines designed on different laminate layers [205].

As to the orthogonal feeds designed on different layers, it can be found in many shared aperture dual polarized antenna designs using microstrips, SIWs and waveguides. In these designs, to reduce the coupling between the feed ports, the feed structures are separated in different layers and they are orthogonal to each other in geometry. As shown in Fig. 2.5, the square patch antenna is driven by the two orthogonal feed lines through a cross slot etched in the ground plane [205, 206]. The feed lines actually is a 50 to $100\ \Omega$ T-shaped power divider, which is used to enhance the operation bandwidth and suppress the differential mode radiation. To achieve symmetrical radiation patterns, the feed lines, cross slot and square patch are placed symmetrically. In this structure, because the feed lines for VP is more distant from the square patch, a slight difference will be observed between the

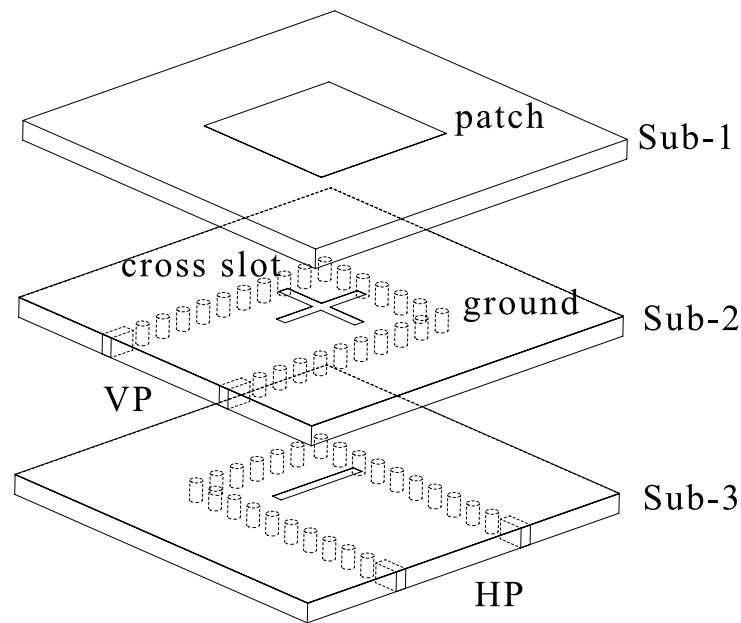


Fig. 2.6 Dual polarized patch antenna fed by SIWs designed on different laminate layers [207].

responses from the two feeds. Fig. 2.6 shows orthogonal feeds designed on different layers by using SIWs or waveguide [177, 186, 187, 207–210]. Similarly, the square patch antenna placed on the top is fed by a cross slot etched in the ground plane. The feed structures are constructed by a shorted-end SIW. The shorted-end section is about $\lambda/4$ away from the slots. In this structure, the slot for coupling the signals in the SIW of Sub-3 is located right along the centre line of the SIW of Sub-2. Therefore, high isolation between the two feed ports for HP and VP can be obtained. The antenna with orthogonal feeds designed on different layers can achieve wide bandwidth and high port isolation, but it should be implemented by using multiple laminates and thus has very high complexity.

The orthomode transducer, also known as the polarisation duplexer, is often used to combine or to split two orthogonally polarized waves received by or transmitted from a differentially fed dual polarized antenna [216, 217]. In addition, it can be also found in horn antenna design where it isolates orthogonally polarized waves or to transmit signals from different feed ports [211–215]. Fig. 2.7 shows the typical structure of a turnstile junction orthomode transducer. It has a square or circular feed port and four rectangular waveguide ports which are followed by the feed ports of an antenna. Due to its highly symmetrical structure, the orthomode transducer exhibits high isolation, and the antenna fed by an orthomode transducer has low cross polarization levels. Any potential asymmetries of the orthomode transducer resulted from fabrication uncertainties should be managed so as to maintain high isolation between the orthogonal ports. The orthomode transducer designed by using waveguide has high power handling capacity, but it has high profile and large size, thus it cannot fully integrated with the planar front end circuits.

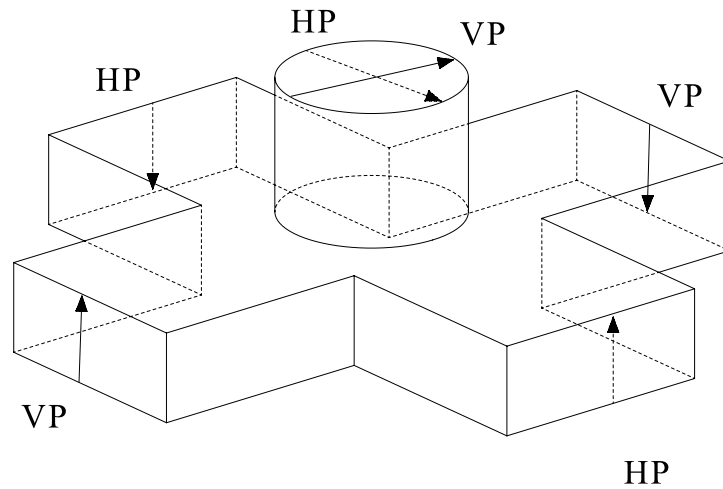


Fig. 2.7 Turnstile junction orthomode transducer [216].

2.5 Summary

In this chapter, the background and design methodology of dual polarized mmWave antenna arrays are introduced at first. Then, the state of the art in dual polarized mmWave antenna arrays is presented. At last, the feed techniques that have been used in designing dual polarized mmWave antenna arrays are detailed.

Chapter 3

Dual Slant Polarized Cavity-Backed Slot-Coupled Patch Antenna Array

In some application scenarios such as base stations, the antenna with dual slant $\pm 45^\circ$ polarization is highly required. The microstrip antenna, due to its low profile, light weight and ease of fabrication, has been widely used in wireless communication systems. In this chapter, a mmWave $\pm 45^\circ$ dual slant polarized cavity-backed slot-coupled patch antenna array with low cross polarization level, low profile and simple structure is presented. To exemplify the performance of the proposed antenna element, a 2×8 antenna array using the designed antenna element is prototyped and tested. The experiment shows that the designed antenna array has good performance in terms of operation bandwidth, port isolation, realized gain, cross polarization level, and aperture efficiency.

3.1 Cavity-backed slot-coupled patch antenna

In this section, a new design is explored to improve the XPD and the operation bandwidth of the patch antenna. In conventional mmWave slot-coupled patch antenna designs, the patch antenna is driven by a microstrip line through a slot etched on the ground plane, which results in low XPD and high back radiation [193]. In this design, an SIW cavity supporting diagonal TE_{120} and TE_{210} modes are employed to feed the patch antenna through a cross slot etched over the cavity. Due to the orthogonality between the TE_{120} and TE_{210} modes, high XPD is achieved in the proposed antenna. To demonstrate the characteristics of the cavity supporting the diagonal TE_{120} and TE_{210} modes, two reference cavity-backed slot antennas are also investigated in this section. In addition, this section will also discuss how the thin strip connecting the patches affects the resonance characteristics of the antenna.

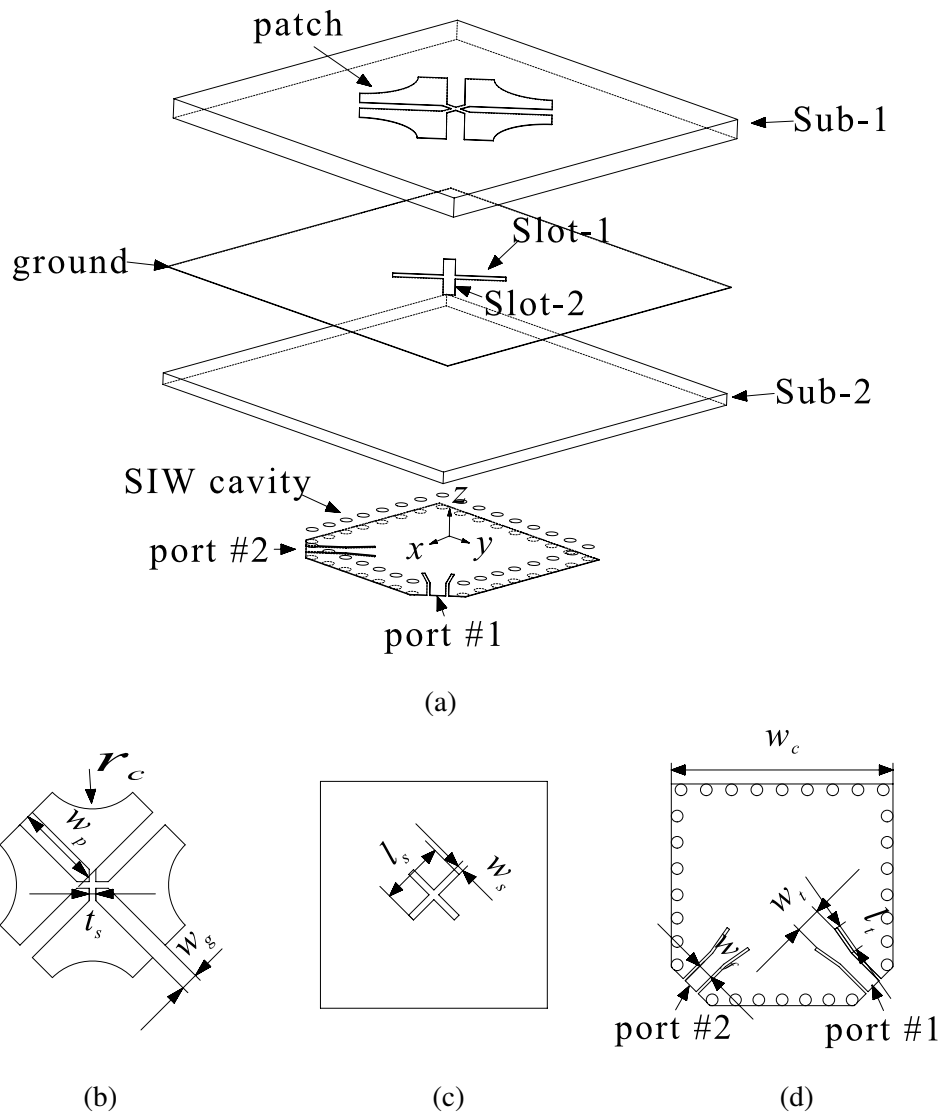


Fig. 3.1 Configuration of the cavity-backed slot-coupled patch antenna with $\pm 45^\circ$ dual slant polarization. (a) Exploded view. (b) Radiating patch. (c) Cross slot on the ground. (d) SIW cavity.

3.1.1 Configuration of antenna element

Fig. 3.1 shows configuration of the proposed cavity-backed slot-coupled patch antenna. The antenna is designed with two stacked laminates. The radiating patch is printed on the top layer of laminate Sub-1, whereas the feed lines are printed on the bottom layer of laminate Sub-2. In fact, the radiating patch consists of four corner-truncated patches connected by a thin cross strip at the centre. The metallized vias of the SIW cavity are plated in laminate Sub-2, and the SIW cavity is excited at two neighbouring corners for dual slant polarization. The radiating patch, SIW cavity and feed lines share the common ground plane which is sandwiched between the two laminates. In the ground plane, a cross slot (Slot-1 and Slot-2) is etched to enable the electromagnetic waves inside the SIW cavity

to excite the radiating patch above. Slot-1 with a tilted angle of $\varphi = -45^\circ$ couples the input signal from port #1 to excite the radiating patch for -45° slant polarization, while Slot-2 with a tilted angle of $\varphi = 45^\circ$ is used to excite the radiating patch for 45° slant polarization. The dimensions of the parameters used in designing the proposed antenna are shown in Table 3.1. The cavity-backed configuration used in this design could not only improve the radiating efficiency, but also reduce back radiation from the coupling slot. Rogers RO4003C laminates with a relative dielectric constant $\epsilon_r = 3.55$ and loss tangent $\tan \delta$ of 0.0027 are adopted in the design. The thickness of laminate Sub-1 is set to 0.508 mm in consideration of the bandwidth enhancement and surface wave suppression. To avoid using wide microstrips, the thickness of Sub-2 should be relatively thin, which is selected to 0.305 mm in this design. The design and optimization are carried out by using ANSYS Electronics Desktop HFSS 19.

Table 3.1 Dimensions of the dual slant polarized antenna: mm

r_c	w_p	t_s	w_g	l_s	w_s	w_c	w_f	w_t	l_t
1.46	2.19	0.17	0.45	2.84	0.30	5.40	0.60	1.22	1.10

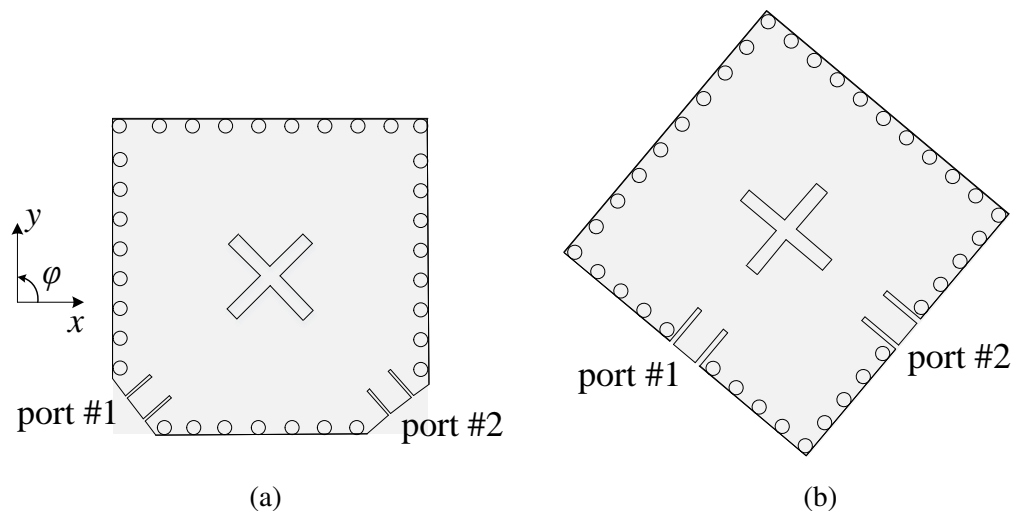


Fig. 3.2 Configuration of (a) corner-fed cross slot antenna, (b) edge-fed cross slot antenna.

3.1.2 Synthesis procedure

The proposed antenna is evolved from a cavity-backed slot antenna shown in Fig. 3.2(a). It has a cross slot etched over an SIW cavity. To achieve dual slant $\pm 45^\circ$ polarization, the cross slot is 45° tilted away from the y -axis direction, and the SIW cavity is excited at two neighbouring corners. To have a better understanding of the corner-fed SIW cavity used in the antenna design, another reference antenna, namely the edge-fed cavity-backed slot

antenna, is also studied. As illustrated in Fig. 3.2(b), the cross slot is in parallel with the edges of the SIW cavity, and the SIW cavity is excited at the middle of two neighbouring edges. To achieve dual slant $\pm 45^\circ$ polarization, the overall structure is rotated 45° around the z -axis [222].

In the two reference antennas, the SIW cavity supporting TE_{120} and TE_{210} modes is used to excite the cross slot cut out from the top copper layer of the cavity. From [223], the resonance frequency of a designated TE_{mnp} mode in a square SIW cavity can be obtained by

$$f_{mnp} = \frac{c}{2\pi\sqrt{\epsilon_{r,eff}}} \sqrt{\left(\frac{m\pi}{W_{eff}}\right)^2 + \left(\frac{n\pi}{W_{eff}}\right)^2 + \left(\frac{p\pi}{h}\right)^2} \quad (3.1)$$

where $\epsilon_{r,eff}$ is the effective permittivity of the filled laminate in the cavity. W_{eff} and h are the effective width and height of the SIW cavity, respectively. An SIW cavity has the same resonance characteristics as a square metallic cavity filled with the same dielectric material. It is empirically true that a square SIW cavity can be deemed as a square metallic cavity by using the following equivalence

$$W_{eff} = W - 1.08\frac{d^2}{s} + 0.1\frac{d^2}{W} \quad (3.2)$$

In (3.2), W is the physical width of the square metallic cavity filled with the same laminate. d and s are the via diameter and separation between the adjacent neighbouring metallized vias, respectively. One can obtain the initial SIW cavity size by solving (3.1) and (3.2).

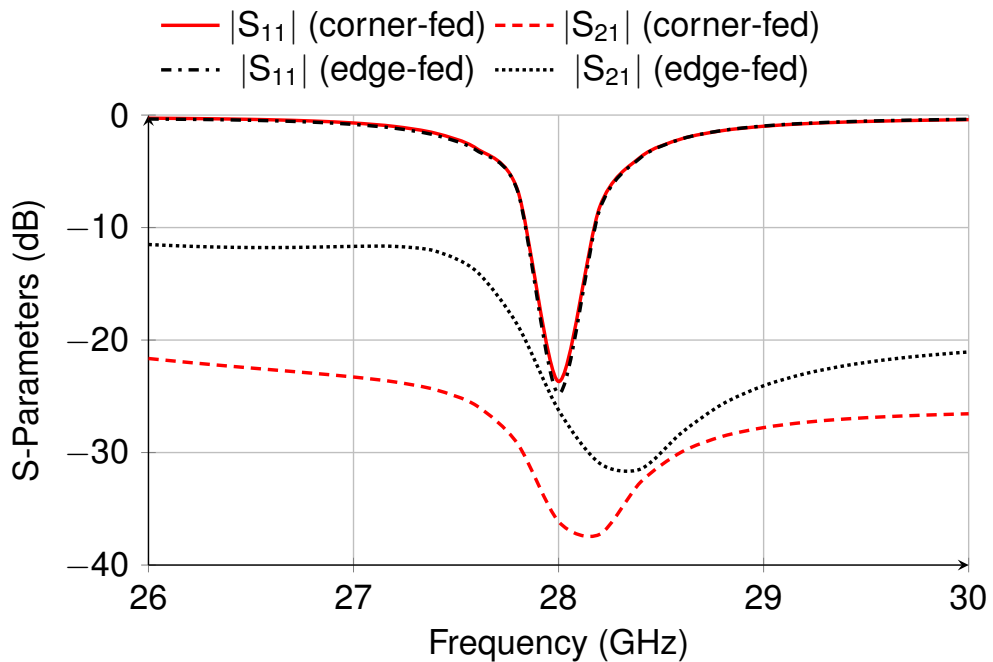


Fig. 3.3 Simulated S -parameters of the corner-fed and edge-fed slot antennas.

A simulation is carried out to help us understand the differences between the two reference antennas in performance. The simulated reflection coefficient $|S_{11}|$ and port coupling coefficient $|S_{21}|$ of the two reference antennas are illustrated in Fig. 3.3. It is seen that their reflection coefficient curves are completely overlapped, but the coupling coefficient between port #1 and #2 in the corner-fed cavity backed slot antenna is much lower than that of the edge-fed cavity-slot antenna, though the major difference between the two reference antennas is exhibited by their feed position. The coupling coefficient of the edge-fed cavity-backed antenna is only 26 dB at the centre frequency 28 GHz. However, the coupling coefficient at 28 GHz reaches to lower than -36 dB in the corner-fed cavity-backed slot antenna. Because only the TE_{120} mode or TE_{210} mode is excited in the SIW cavity and slot antennas have high quality factor, the impedance bandwidth of the two reference antennas for the reflection coefficient less than -10 dB is quite limited, which ranges from 27.8 GHz to 28.2 GHz.

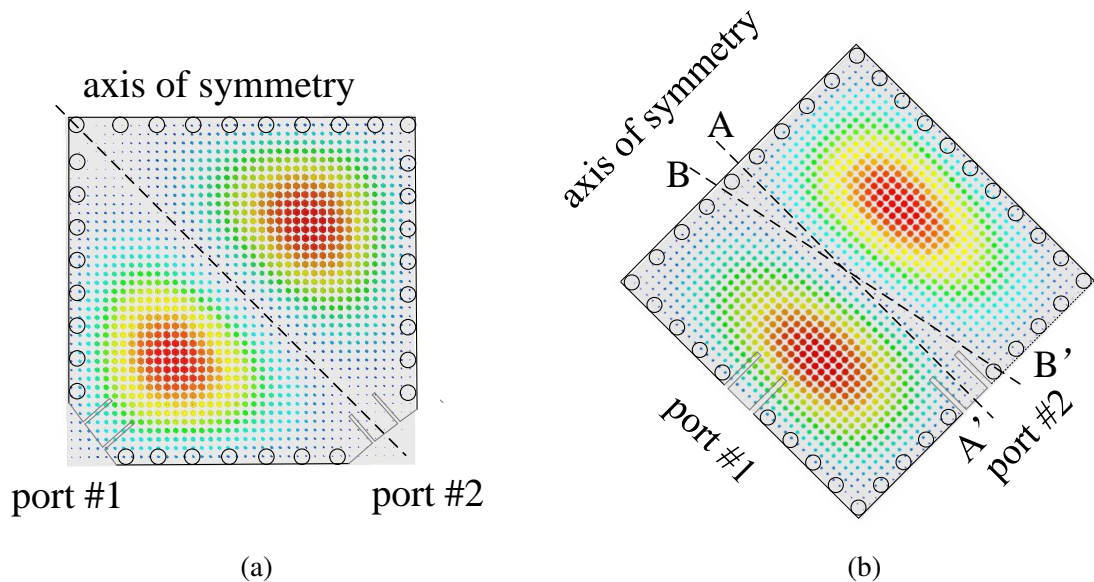


Fig. 3.4 Field distribution in the SIW cavity of (a) corner-fed slot antenna, and (b) edge-fed slot antenna.

To investigate the reason why the port isolation in the corner-fed cavity-backed slot antenna is better than that of the edge-fed one, Fig. 3.4 presents the electric field distribution inside the cavity of the two antennas. It can be seen from Fig. 3.4(a) that the corner-fed cavity is inhabited odd symmetric TE_{120} mode field pattern with respect to the backward diagonal line when port #1 is under excitation. In this case, the backward diagonal line is exactly the boundary, which is located between the electric fields with opposite phase. By contrast, as can be observed in Fig. 3.4(b), the electric field inside the edge-fed SIW cavity is odd symmetric with respect to the reference line BB' . Its electric field pattern does not coincide with the ideal TE_{120} mode field, whose field distribution is odd symmetric with respect to the axis of symmetry AA' .

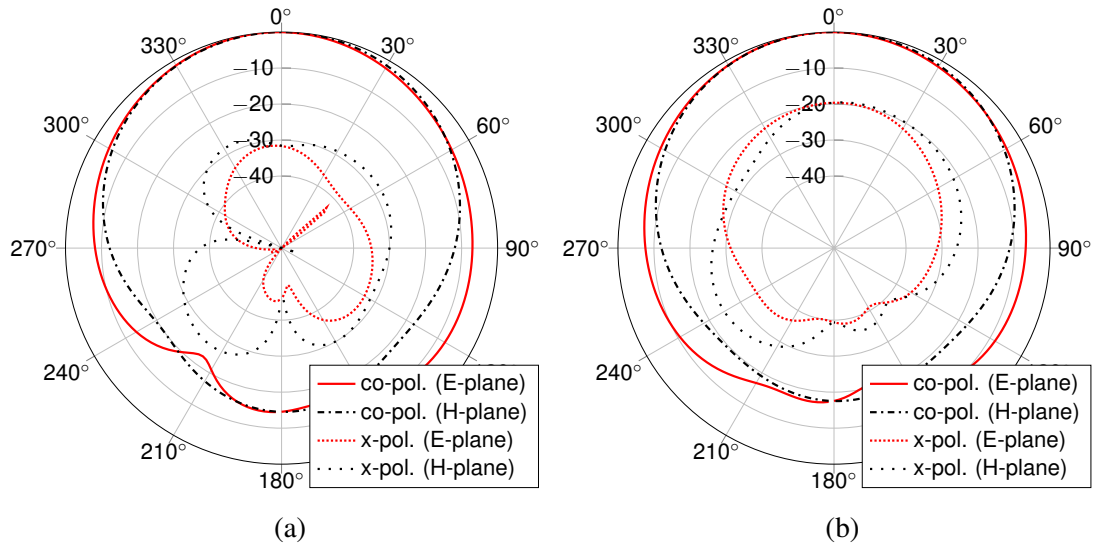


Fig. 3.5 Simulated normalized radiation patterns of (a) corner-fed slot antenna, and (b) edge-fed slot antenna.

In the edge-fed cavity, the rotation of TE_{120} mode field from AA' to BB' is mainly because of perturbation introduced by the feed ports. However, this perturbation caused by the feed ports is insignificant in the corner-fed cavity, as the effective size of the edge-fed cavity for supporting the diagonal TE_{120} mode is larger than the size of the edge-fed cavity. It is also evidenced in [224] that perturbation for the modes inside an enclosed cavity can be easily induced when the cavity is designed to have a very low profile. In consequence, the port isolation in the edge-fed cavity is lower than that of the corner-fed cavity. The far field radiation patterns of the corner-fed and edge-fed cavity backed antenna are illustrated in Fig. 3.5. The E-plane and H-plane presented in this figure are denoted as the plane of $\varphi = 45^\circ$ and $\varphi = -45^\circ$, respectively. The co-polarization patterns of the two reference cavity-backed slot antennas in E- and H-plane are almost identical to each other. This is because they share the same slot aperture. However, it is worth noting that the cross polarization patterns from the two antennas are considerably different. The XPD of the corner-fed cavity-backed slot antenna is much lower than that of the edge-fed cavity slot antenna. The XPD in the corner-fed antenna is higher than 32 dB. In contrast, the XPD in the edge-fed antenna is only 19 dB. Linked to the electric field inside the corner-fed and edge-fed cavity shown in Fig. 3.4, the disparity of XPD in the two antennas is mainly originated from the rotation of TE_{120} mode field in the edge-fed cavity. Due to the TE_{120} mode field rotating by a certain angle with respect to the reference line AA' , the cross polarization electric fields radiated from the cross slot is significantly increased.

3.1.3 Bandwidth improvement

As can be learnt from the last section, the corner-fed cavity-backed slot antenna shows advantages over the edge-fed one, since the corner-fed cavity-backed slot antenna has

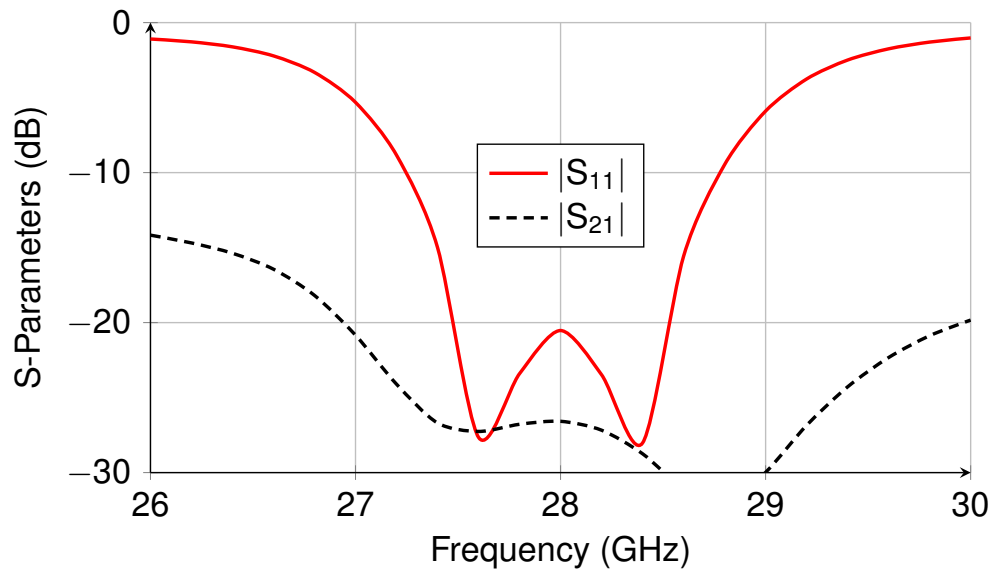


Fig. 3.6 Simulated S -parameters of the proposed dual slant polarized antenna.

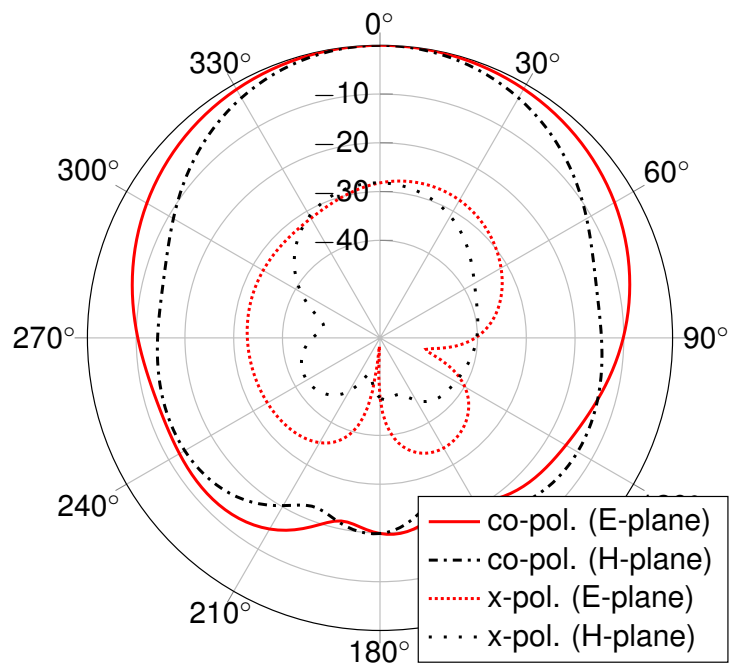


Fig. 3.7 Simulated normalized radiation patterns of the proposed dual slant polarized antenna.

higher XPD (32 dB) and higher port isolation (36 dB). However, the most significant disadvantage of this antenna is that the operation bandwidth is quite limited, which is only 400 MHz, 27.8–28.2 GHz. Because high data rate must be conveyed between transmitters and receivers, such as for on-line streaming and multi-user MIMO 5G/6G applications, the antennas have relatively wide bandwidth are more attractive in wireless communications due to they can provide more channels with high data capacities.

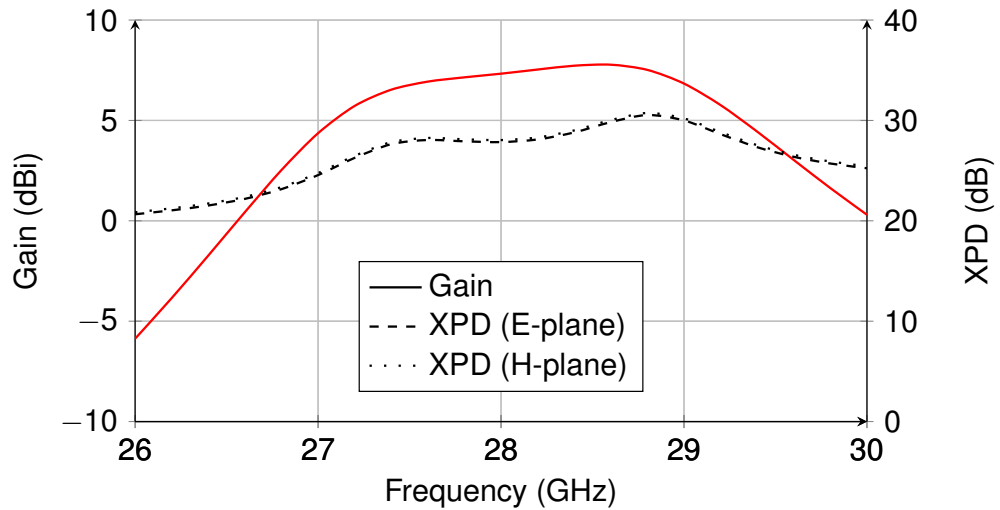


Fig. 3.8 Simulated gain and XPD of the proposed dual slant polarized antenna.

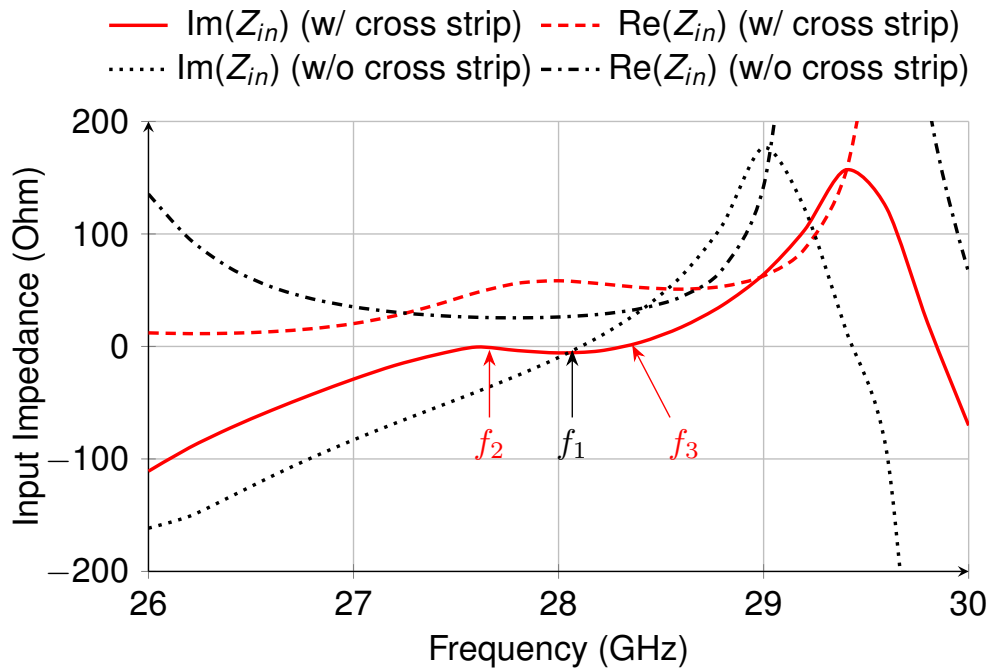


Fig. 3.9 Simulated normalized radiation patterns of the proposed dual slant polarized antenna.

Thus, in order to enhance the operation bandwidth of the antenna, four parasitic patches with corner truncation are introduced. They are placed over the Sub-1 and they are connected by a thin cross strip as shown in Fig. 3.1(a). Figs. 3.6-3.8 present the simulated performance of the designed cavity-backed slot-coupled patch antenna. As can be seen from Fig. 3.6, the proposed antenna resonates at 27.6 GHz and 28.4 GHz. The impedance bandwidth of this antenna for $|S_{11}|$ and $|S_{22}|$ less than -10 dB ranges from 27.2 GHz to 28.8 GHz. Compared with the bandwidth of the antenna without the truncated patches, the operation bandwidth of the proposed antenna is increased from 400 MHz to 1.6 GHz.

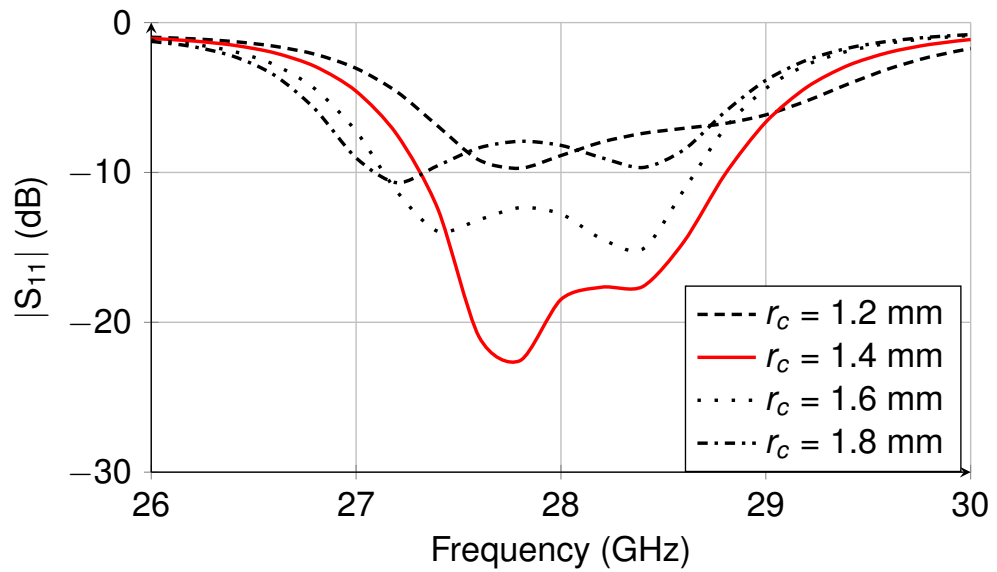


Fig. 3.10 Simulated $|S_{11}|$ of the proposed antenna with different truncated corner size (r_c).

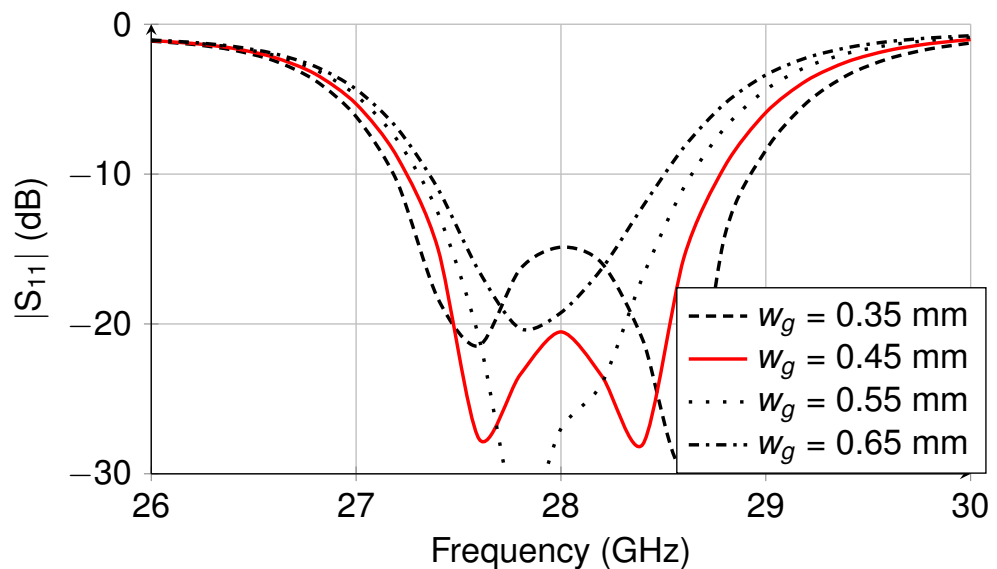


Fig. 3.11 Simulated $|S_{11}|$ of the proposed antenna with different gaps between patches (w_g).

From Fig. 3.6, it is observed that the isolation between port #1 and #2 maintains higher than 26.5 dB over the impedance bandwidth 27.6 GHz and 28.4 GHz. When looking back to the corner-fed cavity backed slot antenna without the truncated patches, it can be concluded that the port isolation in the proposed antenna is slightly decreased. This is mainly because the presence of the corner-truncated patches introduces perturbation to the field distribution of the TE_{120} and TE_{210} mode inside the SIW cavity. Fig. 3.7 shows the co-polarization and cross polarization patterns of the proposed antenna in the E- and H-plane. Symmetric co-polarization patterns are observed in both the E-plane and H-plane. At the boresight, the XPD of the proposed antenna is 28 dB. To have a better understanding

of the XPD performance, Fig. 3.8 gives the simulated XPD varied with frequencies. It is seen that the XPD is higher than 26.3 dB in both the E- and H-plane over the impedance bandwidth of the proposed antenna. The simulated realized gain is also included in Fig. 3.8. The realized gain is in the range of 6.2-7.2 dBi over the bandwidth 27.2-28.8 GHz.

The thin cross strip connecting the corner-truncated patches helps improve the impedance matching of the proposed antenna. To verify the positive effect brought by this thin cross strip, a comparison between the proposed antenna and its counterpart with no cross strip is carried out. Fig. 3.9 presents the simulated input impedance characteristics of the two antennas. $\text{Im}(Z_{in})$ and $\text{Re}(Z_{in})$ represent the imaginary and real part of the input impedance, respectively. The configuration of the reference antenna that has no cross strip is similar to the design reported in [225] where the slot-coupled patches can produce dual resonance at the lower frequency band. However, it is seen that the reference antenna resonates exclusively at $f_1 = 28.1$ GHz. The parasitic patches placed on the top surface of Sub-1 introduce no additional resonances. The single resonance in the reference antenna at $f_1 = 28.1$ GHz is originated from the cross slot cut out from the ground plane. The leading cause of this single resonance in the reference antenna is that the separate patches placed over the cross slot significantly increase the capacitance of the antenna which works at mmWave frequencies. Due to so much capacitance introduced, this side effect could not be merely alleviated by varying the patch size or the gap between the patches. In the proposed antenna, the cross strip that connects the four individual patches can be regarded as an inductor to counteract the capacitance introduced by the patches. This has been evidenced by the input impedance of the proposed antenna, as shown in Fig. 3.9. By introducing the cross strip, it is seen that $\text{Im}(Z_{in})$ at the frequencies lower than f_1 levels up from negative to zero. Then, a new resonance appears at $f_2 = 27.6$ GHz. In addition, the resonance resulted from the cross slot moves from $f_1 = 28.1$ GHz to $f_3 = 28.4$ GHz. Within the bandwidth between the two resonances, $\text{Im}(Z_{in})$ of the proposed antenna is nearly flatted to zero, while $\text{Re}(Z_{in})$ is maintained in the range 47–54 Ω . This demonstrates that good impedance matching is obtained in the proposed antenna.

It has been discussed thoroughly that the cross strip used to connect the separate patches aids in creating dual resonance of the proposed antenna. As a matter of fact, the size of truncated corner (r_c) and the gap between the patches (w_g) also play an important part in determining the resonance characteristics of the proposed antenna. Thus, it would be beneficial to investigate how the parameters r_c and w_g affect the antenna performance. Fig. 3.10 presents the simulated reflection coefficients $|S_{11}|$ with different truncated corner size r_c . It is observed that the first resonance frequency f_2 moves toward the lower frequency band, and the second resonance resulted from the cross slot stays stable. This demonstrates that the truncated corner of the patches only makes great difference on the first resonance. Fig. 3.11 shows the reflection coefficients $|S_{11}|$ with different truncated corner size w_g . It can be seen that the two resonances of the proposed antenna move

toward to the centre frequency and the two resonance frequencies are overlapped when $w_g = 0.65$ mm. This indicates that the gap between the patches has an effect on the two resonance frequencies. Thus, proper selection of w_g helps realize good impedance matching over a relatively wide bandwidth.

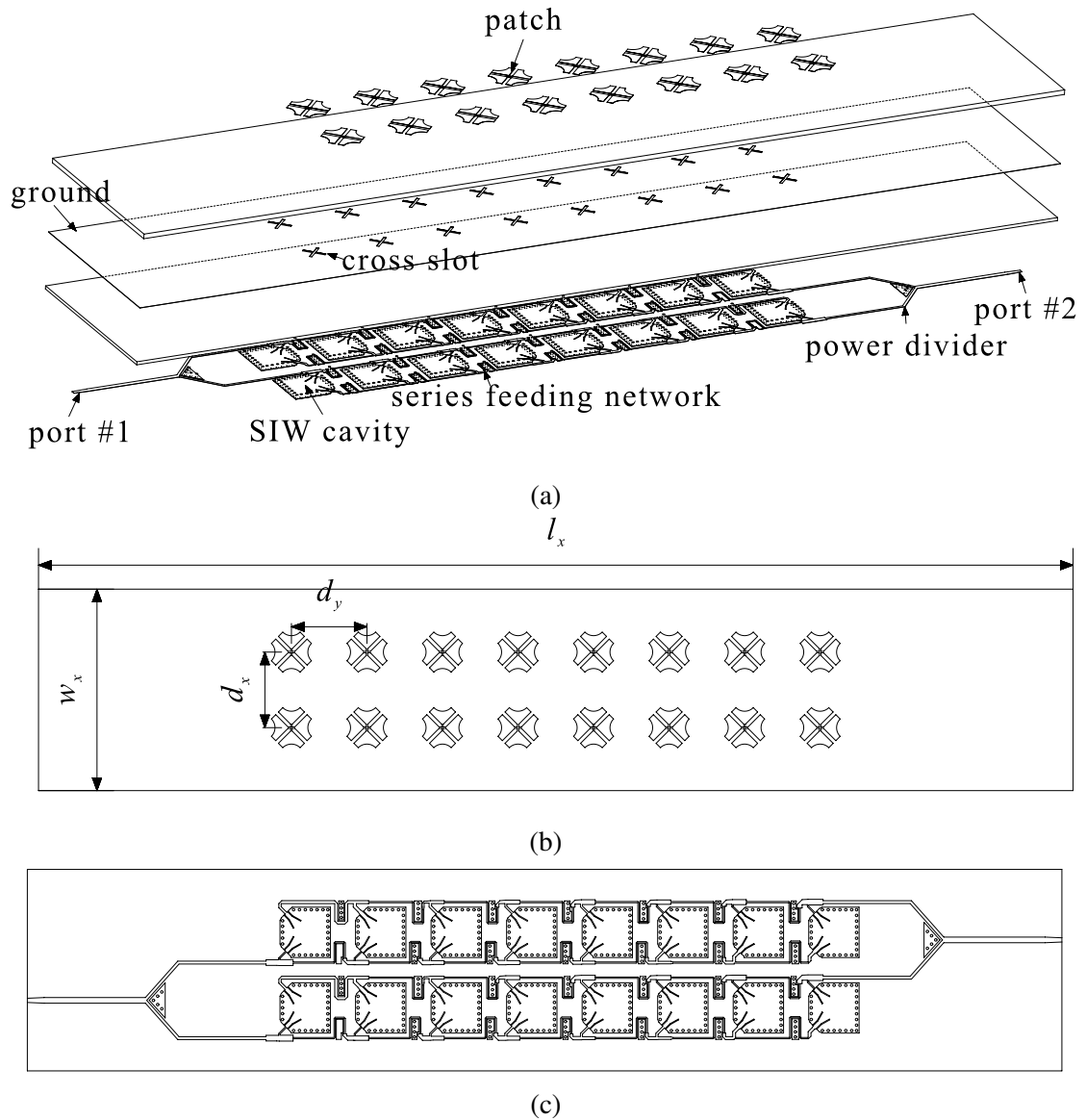


Fig. 3.12 Configuration of the dual slant polarized antenna array. (a) Exploded view. (b) Top view. (c) Bottom view.

3.2 Antenna array design

In this section, a dual slant polarized 2×8 antenna array is developed by using the designed cavity-backed slot-coupled patch antenna. To uniformly excite the antenna elements, a

series feed network and an equal power divider are also synthesised in this section. The centre operation frequency and the insertion loss of the microstrip lines are significantly affected by the severe parasitic effect resulted from the discontinuity of microstrip lines at mmWave frequencies. Thus, to combat this effect, special attention has been paid to the design of the series feed network and the power divider. Then, the designed antenna array is prototyped and tested. The side effect caused by the board-to-board misalignment when manually assembling the antenna will also be discussed.

3.2.1 Configuration of antenna array with dual slant polarization

Based on the designed cavity-backed slot-coupled antenna, a 2×8 dual slant polarized antenna array is designed to verify the overall performance of the proposed antenna element. Fig. 3.12(a) shows the exploded view of the designed antenna array. It consists of 2×8 antenna elements, four series feed networks and two corporate power dividers. Port #1 is the feed port for exciting -45° polarization, and port #2 is the feed port for exciting $+45^\circ$ slant polarization. Each feed port is connected to an equal power divider designed with a grounded patch placed between the two output branches. The microstrip series feed network with a grounded patch inserted in each bend is used to connect and drive the antenna elements. The benefits of the grounded patch used to design the power divider and the series feed network will be detailed in the following section. The antenna elements are uniformly excited with the same phase by tuning the characteristic impedance and electric length of the microstrip lines used in designing the series feed network. As shown in Fig. 3.12(b), the spacings between the adjacent antenna elements in the x - and y -axis direction are $d_x = d_y = 9$ mm ($0.84\lambda_0$). The overall dimension of the designed antenna array is $l_x \times w_x = 123$ mm \times 24 mm.

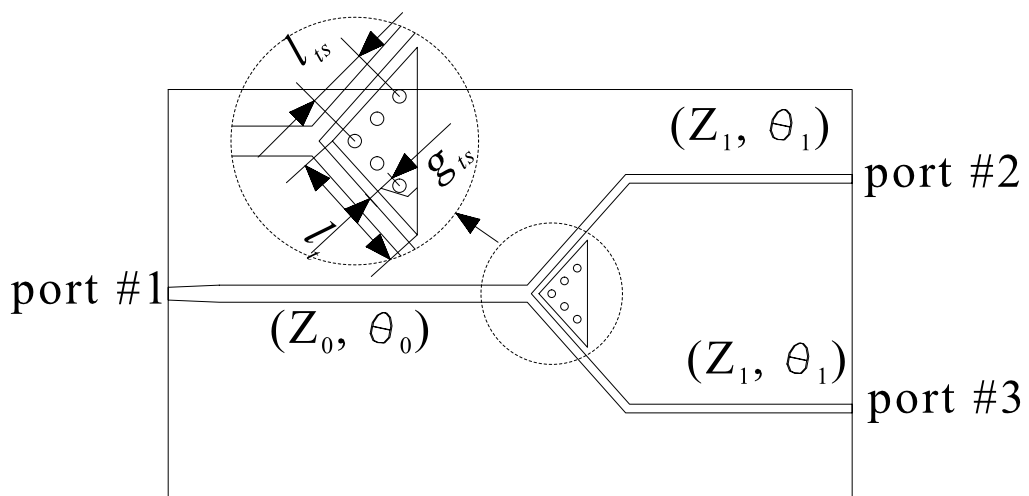


Fig. 3.13 Layout of the designed equal power divider.

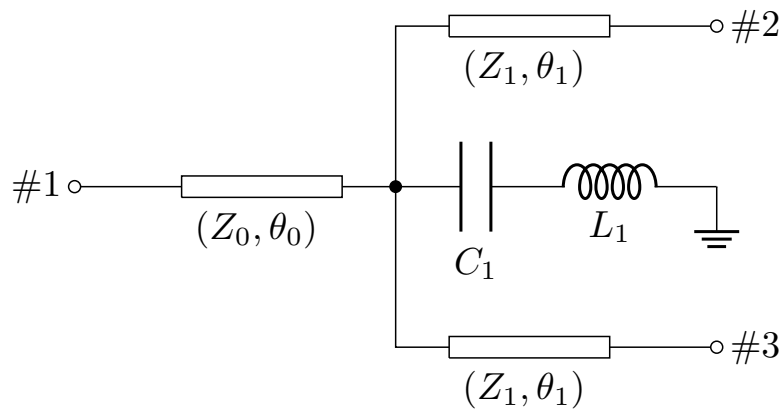
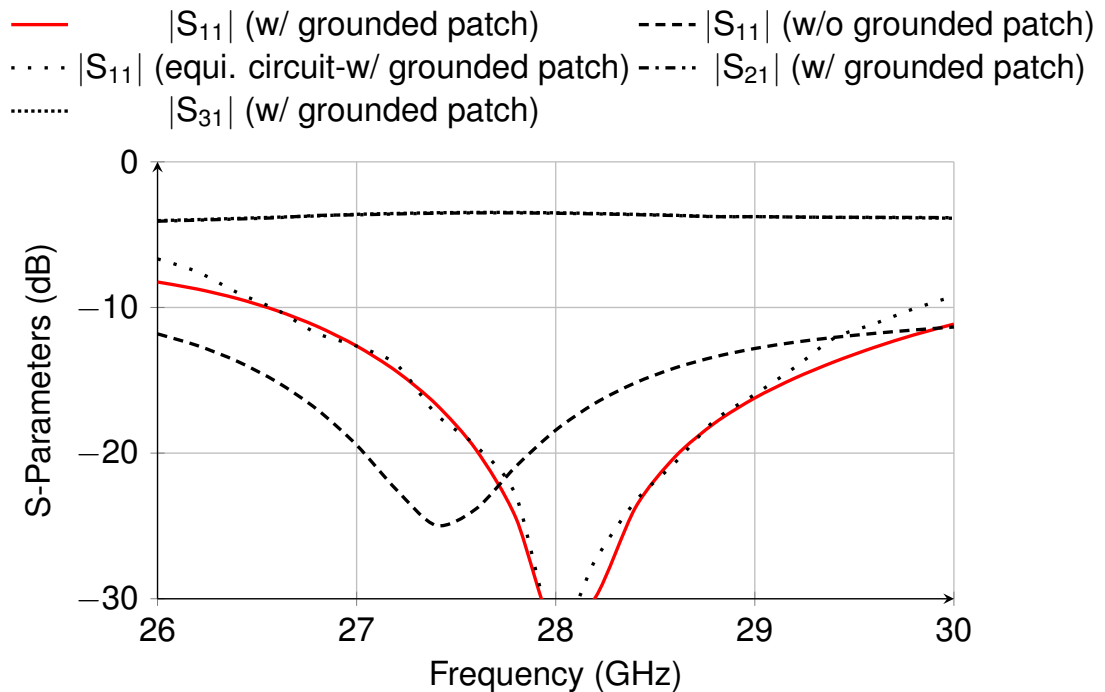


Fig. 3.14 Circuit representation of the designed power divider.


 Fig. 3.15 Simulated S -parameters of the power divider with or without the shorted patch.

3.2.2 Equal power divider with grounded patch

As discussed in the last section, the power divider connected to the feed ports is used to equally split the input power and deliver it to the antenna elements through the series feed networks. The layout of the designed equal power divider is presented in Fig. 3.13. To realize good impedance matching, it is calculated from the transmission line theory [219] that the characteristic impedances of the microstrip lines connected to the feed port #1 and the output ports #2 and #3 are $Z_0 = 50\Omega$ and $Z_1 = 71\Omega$, respectively. In addition, as an impedance transformer, the transmission line connected to port #2 and #3 should have an electric length of $\lambda/4$. However, as a matter of fact, the centre operation frequency of return loss at the feed port #1 will move toward the lower frequency band if the power

divider is designed by using these theoretical values. The frequency shifting is mainly caused by strong parasitic effect originated from structure discontinuity of the power divider at mmWave frequencies. The parasitic effect cannot be alleviated by tuning the impedance or the electric length of the microstrip lines.

In this design, this problem is addressed by placing a grounded patch between the two output branches of the power divider. As can be seen from Fig. 3.13, the V-shaped metallized vias connect the triangular patch to the ground plane. The equivalent circuit representation of the proposed equal power divider is developed and illustrated in Fig. 3.14 to help us understand the physical insight of the inserted grounded patch. As seen from this figure, the grounded patch can be considered as a series L-C circuit shunt to the output branches having characteristic impedance of Z_1 and electric length of θ_1 . The coupling between the output branches and the grounded patch is modelled as the capacitance C_1 , and the grounding vias are taken as the inductance L_1 . Therefore, the centre frequency of return loss at port #1 can be manipulated by tuning the design parameters l_{ts} , g_{ts} and l_t because they play a significant role in deciding L_1 and C_1 . The numerical values of the inductor L_1 and the capacitor C_1 can be obtained by performing the curve fitting by using the EM simulation. Fig. 3.15 presents the simulated S -parameters of the proposed power divider, the equivalent circuit and the power divider designed without the grounded patch. The centre frequency of return loss at port #1 of the power divider without the grounded patch is located at 27.4 GHz. By placing the grounded patch between the output branches, the centre frequency of return loss at port #1 shifts to 28 GHz. The simulated results of the proposed power divider and its circuit representation agree well with each other. The transmission coefficients from port #1 to ports #2 and #3 of the proposed power divider, $|S_{21}|$ and $|S_{31}|$, is in the range from -3.4 dB to -3.5 dB over the operation bandwidth of the designed cavity-backed slot-coupled antenna.

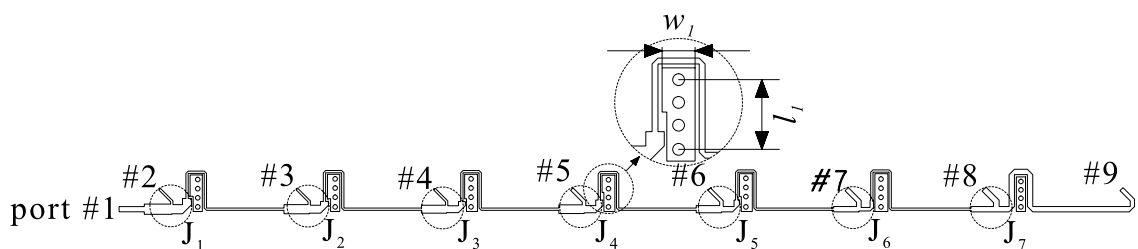


Fig. 3.16 Layout of the designed series feed network.

3.2.3 Series feed network

In this 2×8 antenna array, the microstrip series feed network is used to connect and uniformly feed the designed cavity-backed slot-coupled antennas. As can be seen from Fig. 3.12, the series feed network is realized on the bottom layer of Sub-2. The detailed layout of this series feed network is illustrated in Fig. 3.16. It is mainly composed of

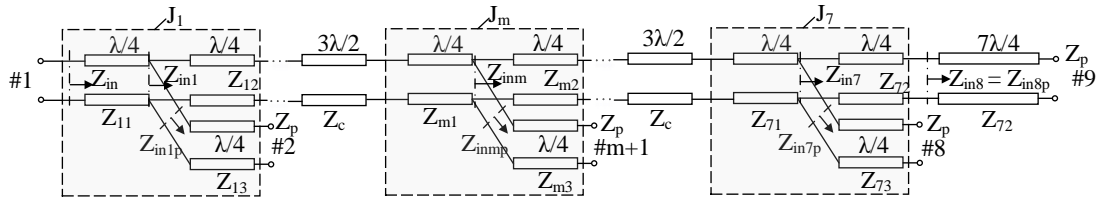


Fig. 3.17 Equivalent circuit of the designed series feed network.

Table 3.2 Impedances in each junction of the series feed network

Junction	Z_{m1} (Ω)	Z_{m2} (Ω)	Z_{m3} (Ω)
J_1	50	53	100
J_2	53	58	100
J_3	58	63	100
J_4	55	61	87
J_5	61	71	87
J_6	71	86.6	87
J_7	71	71	71

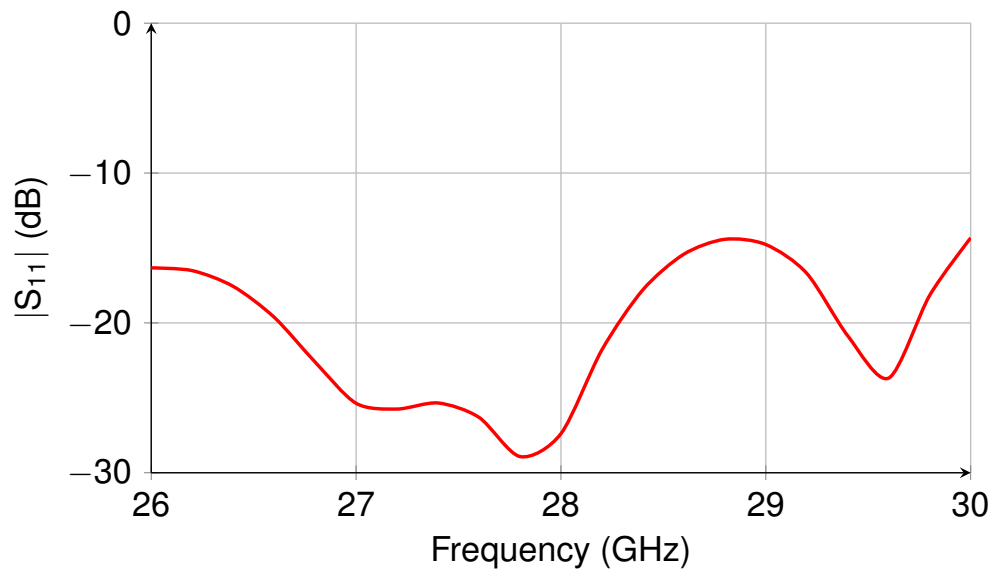


Fig. 3.18 Simulated reflection coefficient at port #1 of the designed series feed network.

seven microstrip junctions and each junction includes three quarter-wavelength impedance transformers. Port #1 is the excitation port, and ports #2 to #9 are the output ports which connect to the feed ports of the designed cavity-backed slot-coupled antenna with input impedance of Z_p . The circuit representation of this series feed network is given in Fig. 3.17, in which Z_{m1}, Z_{m2}, Z_{m3} ($m = 1, 2, \dots, 7$) are the branch impedances of the m^{th} junction. In addition, Z_{inm} ($m = 1, 2, \dots, 8$) and Z_{inmp} ($m = 1, 2, \dots, 7$) are the input impedances observed from different points. The characteristic impedances of these microstrip lines are derived from the transmission line theory [219], which can be written as

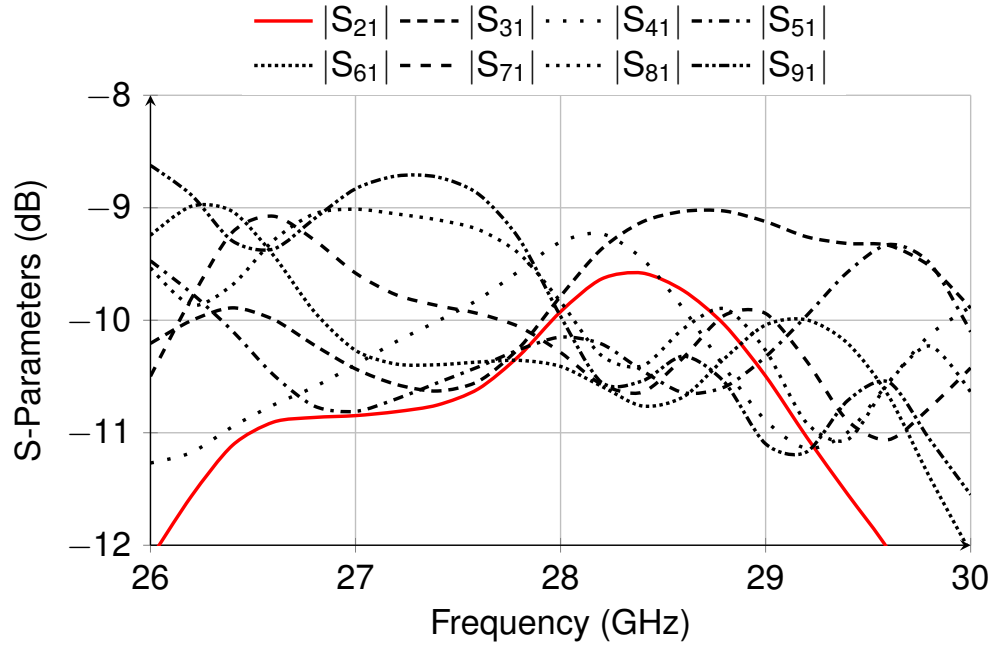


Fig. 3.19 Simulated transmission coefficients from port #1 to #9 in the designed series feed network.

$$Z_{in7} = \frac{Z_{in8p} \cdot Z_{in7p}}{Z_{in8p} + Z_{in7p}} = \frac{(Z_{73}^2/Z_p) \cdot (Z_{72}^2/Z_p)}{(Z_{73}^2/Z_p) + (Z_{72}^2/Z_p)} \quad (3.3)$$

$$Z_{71} = \sqrt{Z_{in7} Z_c} \quad (3.4)$$

$$Z_{inm} = \frac{(Z_{m2}/4Z_p^2) \cdot Z_{inmp}}{(Z_{m2}/4Z_p^2) + Z_{inmp}} = \frac{(Z_{m2}/4Z_p^2) \cdot (Z_{m3}^2/Z_p)}{(Z_{m2}/4Z_p^2) + (Z_{m3}^2/Z_p)} \quad (3.5)$$

$$Z_{m1} = \sqrt{Z_{inm} Z_c}, \dots, Z_{11} = \sqrt{Z_{in1} Z_{in}} \quad (3.6)$$

In the above calculations, the input impedance of the antenna element is assumed to be $Z_p = 50\Omega$, and the characteristic impedance of the microstrip line having the electric length of $3\lambda/2$ is chosen as $Z_c = 100\Omega$. In order to make sure that the microstrip lines have proper width (not too narrow or too wide), the characteristic impedances of the microstrip lines are expected in the range of 50-100 Ω . The characteristic impedances of the microstrip junctions J_1 to J_7 can be obtained by working out (3.3)-(3.6). The calculated impedances of these microstrip junctions are tabulated in Table 3.2.

Because of structure discontinuity, severe parasitic effect are also introduced at the microstrip bends. This would result in the centre frequency of return loss at the feed port #1 shifting to the lower frequency band. To overcome this side effect, a grounded patch with the size of $l_1 = 1.8$ mm and $w_1 = 0.8$ mm is placed in each bend of the microstrip lines, which is much of the same to the designed equal power divider. Fig. 3.18 illustrates the simulated return loss of the designed microstrip series feed network at the feed port #1. It is seen that the return loss at port #1 is higher than 14 dB over the frequency bandwidth 26–30GHz. The simulated transmission coefficients from the feed port #1 to ports #2–#9 are in the range from –10.5 dB to –9.3 dB at 28 GHz, and the magnitude variation is ± 1.1 dB over the operation bandwidth of the designed antenna 27.2–28.8 GHz. In view of the fact that there are eight output ports in the proposed microstrip series feed network, this magnitude variation is acceptable in practical applications.

3.2.4 Experiment and results

Based on the designed cavity-backed slot-coupled antenna, the equal power divider, and the microstrip series feed network, the 2×8 antenna array is prototyped and measured to exemplify its performance. The fabricated prototype of the designed antenna array is given in Fig. 3.20. The shoring vias located outside the antenna array aperture are used to make sure that the ground planes of the two laminates are completely connected. In order to align the two laminate boards, two locating holes are placed beside the feed ports. The measurement of *S*-parameters of the antenna array is conducted by using the network analyser Anritsu 37397C, and the radiation patterns are measured in the far-field anechoic chamber.

Fig. 3.21 shows the measured and simulated return loss and the isolation between the feed ports #1 and #2. The measured results are in reasonable agreement with the simulated ones. The simulated overlapped bandwidth for return loss at ports #1 and #2 higher than 10 dB is from 26.3 GHz to 28.8 GHz. In addition, the measured isolation between the feed ports #1 and #2 is higher than 23 dB at 28 GHz and it is more than 20 dB over the frequency band of interest, 27.2–28.8 GHz. Good impedance matching outside the antenna operation bandwidth is mainly caused by 1) the propagating loss from the series feed network, and 2) incomplete mismatching of the antenna outside the bandwidth.

To analysis the loss from the series feed network, all the output ports of the series feed network are terminated as short circuit and only port #1 is left as the feed port. Even though the signal transmission and reflection inside the feed network is very intricate, the simulation based on this model can quantitatively analysis the loss from the series feed network in a certain degree. As shown in Fig. 3.22(a), the average return loss at port #1 is about 6 dB when the frequency is lower than 27.2 GHz, and it is about 8 dB when the frequency is higher than 28.8 GHz. However, it is a very ideal case where the antenna is assumed to be totally mismatched outside the bandwidth. As shown in Fig. 3.6, the return

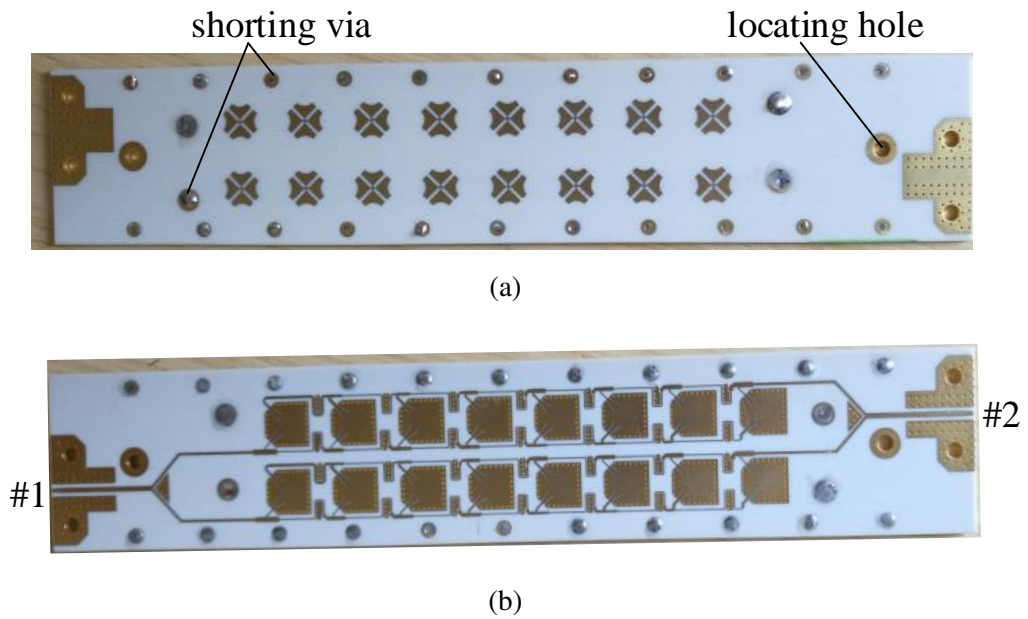


Fig. 3.20 Fabricated prototype of the designed dual slant polarized antenna array. (a) Top view. (b) Bottom view.

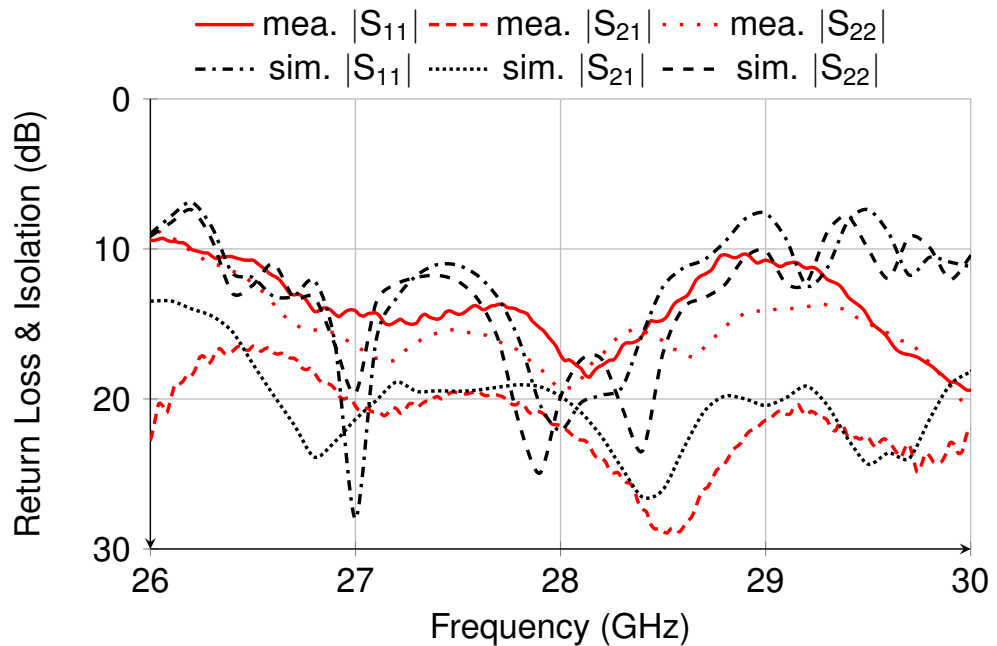


Fig. 3.21 Measured and simulated return loss and port isolation of the designed dual slant polarized antenna array.

loss outside the operation bandwidth of the antenna element is in the range from 1.5 dB to 10 dB, which indicates that a certain percentage of input signals outside the bandwidth is absorbed by the antenna. In view of this fact, the other simulation is based on the model that all the output ports of the series feed network is loaded with the input impedance of the antenna element which is shown in Fig. 3.9. This simulation includes the effects of

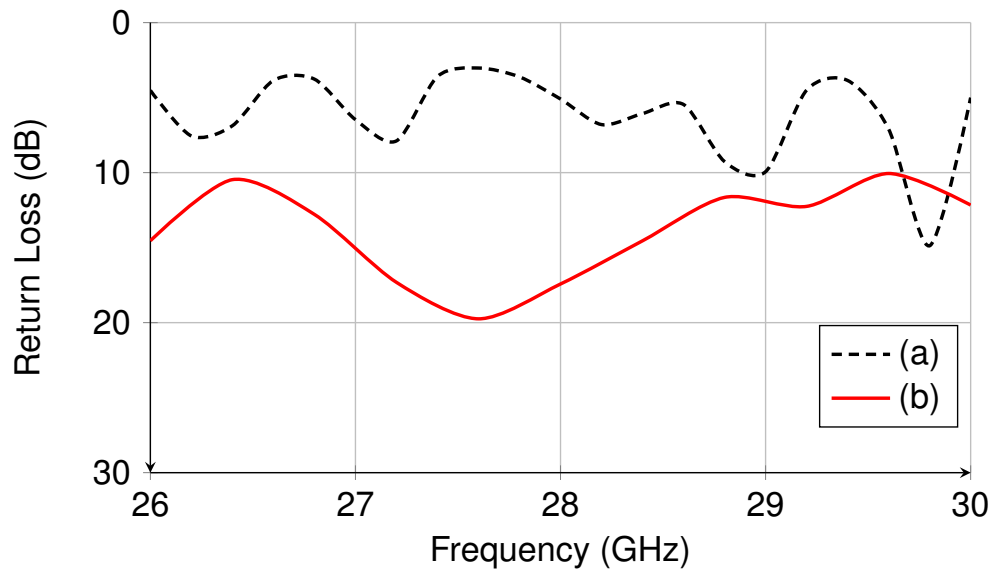


Fig. 3.22 Simulated return loss of (a) the series feed network at port #1 when all the output ports are shorted to the ground, (b) the series feed network at port #1 when all the output ports are loaded with the input impedance of the antenna element.

the propagating loss from the feed network and incomplete mismatching of the antenna outside the bandwidth. As shown from Fig. 3.22(b), the return loss increases to higher than 10 dB from 26 GHz to 30 GHz. Thus, it can be concluded that good impedance matching is observed outside the bandwidth because of the aforementioned two reasons.

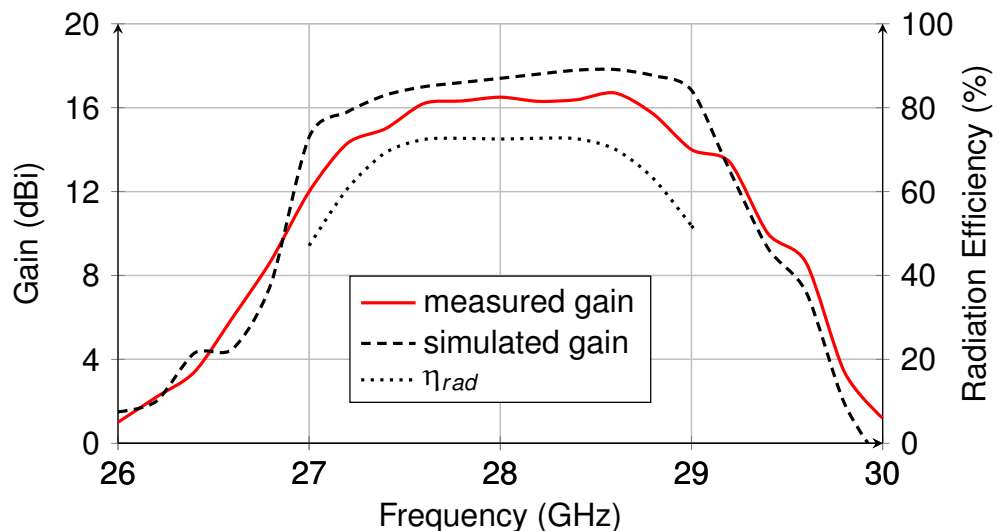


Fig. 3.23 Gain and efficiency of the designed dual slant polarized antenna array.

Fig. 3.23 presents the measured and simulated realized gain with the feed port #1 excited. The maximum gain measures up to 16.7 dBi, and the bandwidth of the gain 2 dB less than the maximum gain is in the range of 27.2-28.9 GHz, which is almost the same to the impedance bandwidth of the antenna element. The measured gain is about 0.9 dB less

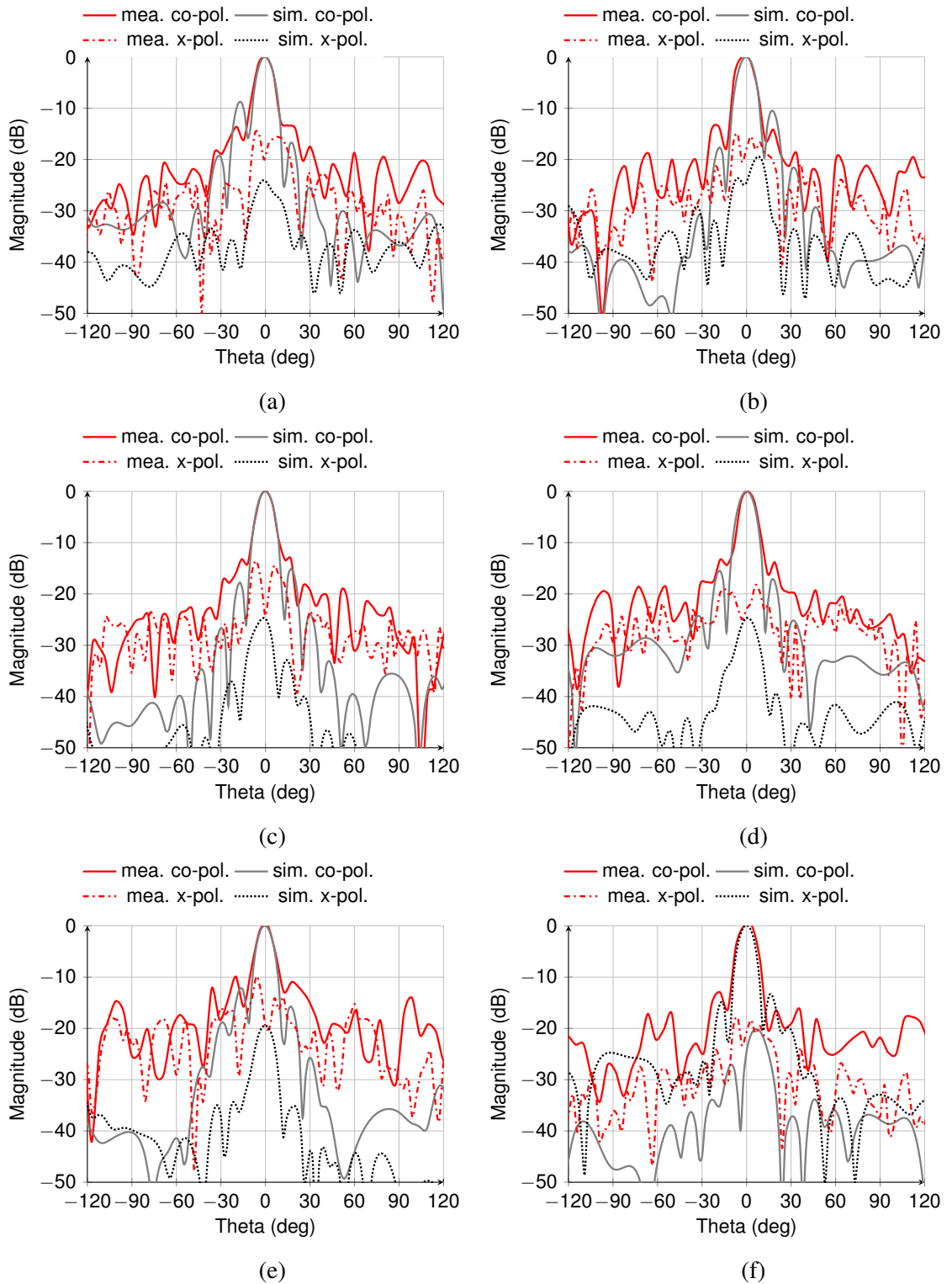


Fig. 3.24 Normalized radiation patterns in the planes of (a) $\varphi = 45^\circ$ at 27.2 GHz, (b) $\varphi = -45^\circ$ at 27.2 GHz, (c) $\varphi = 45^\circ$ at 28 GHz, (d) $\varphi = -45^\circ$ at 28 GHz, (e) $\varphi = 45^\circ$ at 28.8 GHz and (f) $\varphi = 45^\circ$ at 28.8 GHz.

than the simulated gain. This is mainly because the loss originated from the connectors are not calibrated in the measurement. The radiation efficiency is obtained from the simulated

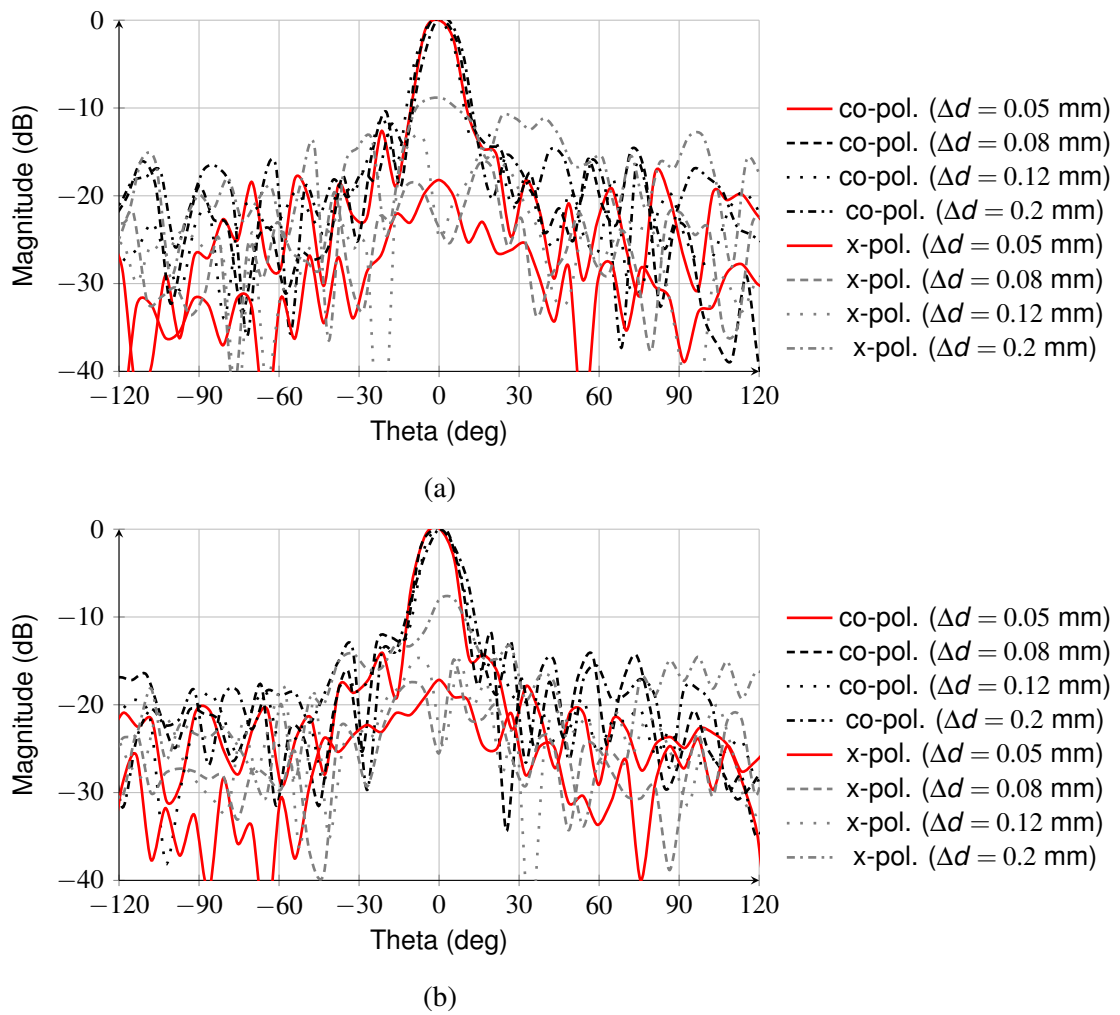


Fig. 3.25 Simulated normalized far field radiation patterns in the planes of (a) $\varphi = 45^\circ$, and (b) $\varphi = -45^\circ$ at 28 GHz with different board-to-board misalignment Δd .

directivity and the simulated gain. The radiation efficiency peaks at 75% and drops to 60% at the edge frequencies, 27.2 GHz and 28.9 GHz.

The radiation pattern measurements are carried out in the far-field anechoic chamber. The measured and simulated normalized far-field radiation patterns at 27.2 GHz, 28 GHz and 28.8 GHz are given in Fig. 3.24. As predicted, the radiation patterns of co-polarization in the plane of $\varphi = 45^\circ$ look the same as the co-polarization radiation patterns in the plane of $\varphi = -45^\circ$ at different frequencies. The SLLs of these measured radiation patterns of co-polarization are lower than -14 dB at the centre frequency 28 GHz. The measured cross-polarization radiation patterns are different from the simulated ones. At the boresight, the measured and simulated XPDs are 25 dB at the centre frequency. The measured cross polarization radiation patterns have a null at the boresight, while off the boresight the cross polarization level is increased. In this fabricated antenna array, the alignment between the two laminates is completed manually. The board-to-board misalignment could significantly spoil the overall performance of the antenna array. In order to characterize this positioning

Table 3.3 Comparison between this work and other mmWave slant polarized antennas

Ref.	B	Pol.	XPB	$\eta_{ap.}$	h	$N_x \times N_y$	Peak Gain
[40]	9.3%	dual	16dB	20%	$0.067\lambda_0$	1×8	15.2dBi
[71]	5.7%	single	n.a.	51%	$0.207\lambda_0$	1×8	13.5dBi
[73]	6.6%	single	18dB	44%	$5.1\lambda_0$	4×4	17.2dBi
[76]	2.3%	dual	10dB	22%	$0.017\lambda_0$	6×7	22.1dBi
[78]	15.3%	dual	n.a.	22%	$0.226\lambda_0$	1×1	12.3dBi
This work	6.0%	dual	25dB	39%	$0.076\lambda_0$	2×8	16.7dBi

error, the dislocation between the bottom and top laminate layer along the y -axis direction [please refer to Fig. 3.12(a)] is specified as Δd . For example, perfect alignment between the two laminate boards is achieved when $\Delta d = 0$ mm. The simulated radiation patterns of the antenna array with different board-to-board misalignment Δd are presented in Fig. 3.25. As can be seen from the two sub-figures, the co-polarization radiation patterns do not change significantly with different Δd . However, the XPBs in the diagonal planes $\varphi = 45^\circ$ and $\varphi = -45^\circ$ are deteriorated with the increase of Δd . It should be pointed out that a null appears at the boresight of the cross polarization patterns when the misalignment Δd is between 0.08 mm and 0.15 mm. These cross polarization radiation patterns are very similar to the measured ones. For this reason, it can be deduced that the disagreement between the measured and simulated cross polarization patterns is resulted from the misalignment between the two laminate layers.

3.2.5 Comparison and discussion

Table 3.3 compares the proposed antenna array and the reported mmWave slant polarized antenna arrays. In this table, the aperture efficiency of an antenna array is obtained from the formula [226]

$$\eta_{ap.} = \frac{G_{peak}\lambda_0^2}{4\pi A_{ap}} \quad (3.7)$$

where G_{peak} is the maximum realized gain, and A_{ap} is the effective area of the antenna array. As can be seen from Table 3.3, although the slant polarized antenna array reported in [71] and [73] are advantageous in terms of high aperture efficiency, they are only capable of working with a single slant polarization and have relatively high profile. The antenna arrays reported in [40] and [76] has low XPB less than 16 dB, low aperture efficiency not more than 22% and large size, because the orthogonally polarized antenna elements are interleaved or separated in different rows. In [78], the reported antenna has high gain and can work with dual polarization. However, this antenna has low aperture efficiency and it cannot be applied to the antenna array design, as this antenna has very large size. In

contrast, the proposed antenna array can operate with $\pm 45^\circ$ dual slant polarization while having high aperture efficiency (39%), high XPD (25 dB), and low profile ($0.076\lambda_0$). The proposed antenna array also has cost competitiveness since low cost laminates Rogers RO4003C with small size and small thickness are used in this design.

3.3 Summary

In this chapter, a $\pm 45^\circ$ dual slant polarized antenna array working at 28 GHz was developed for mmWave base station applications. The corner-fed cavity-backed slot-coupled patch antenna was proposed as the antenna element. To illustrate the benefits brought by the corner-fed cavity, a edge-fed cavity-backed slot antenna is introduced to work as the reference antenna. It is seen that the corner-fed SIW cavity-backed slot antenna has higher XPD and improved port isolation. The designed antenna element can operate with an improved bandwidth by placing four corner-truncated patches connected by a cross strip. The antenna was fully synthesised in terms of the beneficial effect caused by the cross strip and corner truncation. Then, an antenna array with 2×8 antenna elements was designed. To feed the antenna elements, an equal power divider and a microstrip series feed network was developed. In order to suppress the side effect caused by structure discontinuity, the grounded patch was introduced in designing the power divider and the series feed network. At last, the antenna array was prototyped, tested and analysed. The obtained results show that the proposed antenna array has advantages in terms of high XPD, good aperture efficiency, compact size, low profile and simple structure when compare it with the reported works. The developed mmWave dual slant polarized antenna array would be an attractive candidate for base station or indoor and outdoor applications.

Chapter 4

Differentially Fed Dual Polarized 2D SIW Multibeam Antenna Array

As one of MIMO techniques, the multibeam antenna array is widely used in modern wireless communication systems to increase the channel capacity and signal coverage area. However, the design of dual polarized 2D multibeam antenna arrays faces challenges such as high complexity and high cross polarization level. In this chapter, a new design of the dual-polarized 2D multibeam antenna array using differential-fed antenna elements is presented. The differential feeds for HP is realized in the same laminate with the antenna aperture, which makes the designed multibeam array antenna together with multibeam networks able to be realized with only two PCB laminates. The developed multibeam array antenna exhibits stable radiation patterns, low cross polarization level and good beam switching capability, simple structure and low cost. The proposed dual-polarized 2D multibeam antenna array is an attractive candidate for mmWave wireless communications.

4.1 Architecture of differentially fed dual polarized 2D multibeam antenna array

As discussed in the first section of this chapter, the most prevailing problems in dual polarized 2D multibeam antenna arrays are high cross polarization level and complicated geometry. To address these problems, a new architecture of dual polarized 2D multibeam antenna array using the differential feed technique is proposed, as shown in Fig. 4.1. As well-known and seen from extensive reported works, the differential feed technique used in antenna designs helps improve XPD and increase port isolation because it suppresses common mode radiation and noise [227–229]. In this proposed architecture, the antenna array consists of 2×2 antenna elements and the dual polarized antenna elements are placed with a 90° sequential rotation. The antenna elements are followed by the differential power dividers, and then they are connected to the multibeam networks. The solid and

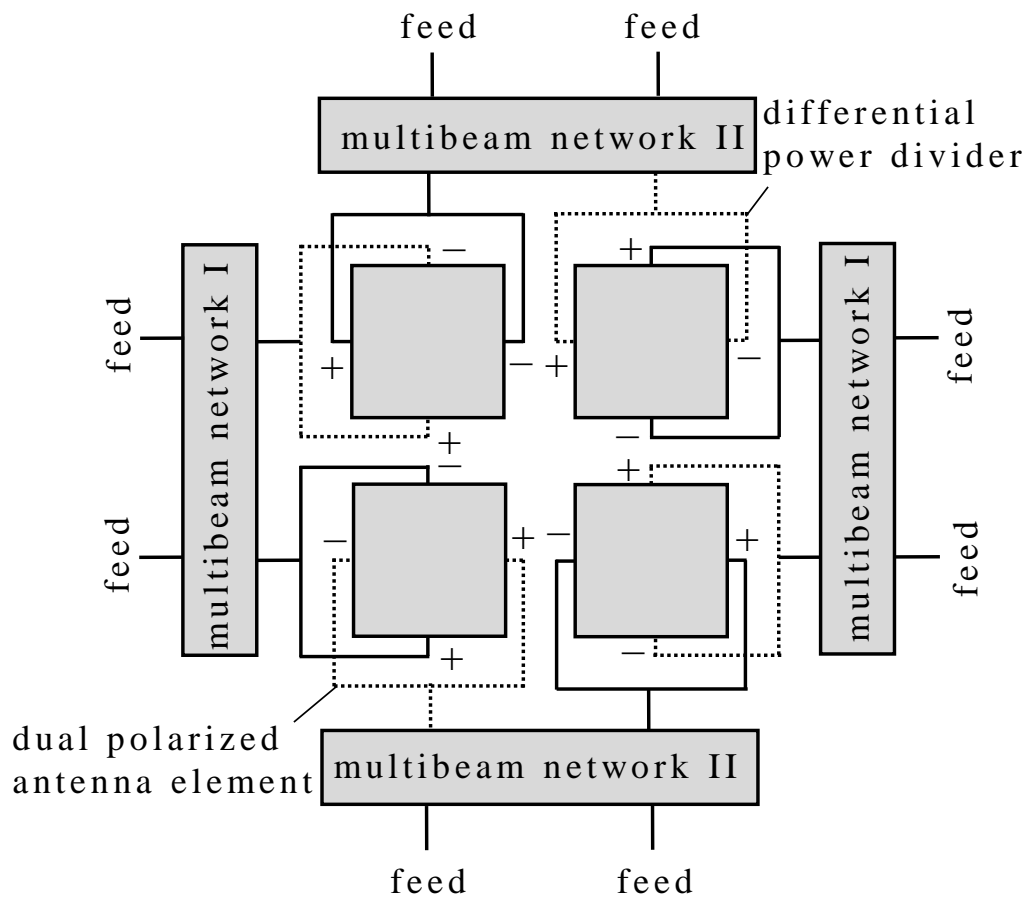


Fig. 4.1 Architecture of the proposed differentially fed dual polarized 2D multibeam antenna array.

dashed lines in this figure represent that the corresponding structures are implemented in different laminate layers to avoid congestion. Due to the antenna array working with dual polarization, two sets of the multibeam network (namely multibeam network I and II) are required to achieved 2D multibeam radiation. The multibeam networks can be realized by using the circuit-based multibeam networks, such as Butler Matrices, Blass Matrices or Nolen Matrices, etc.

4.2 Differentially fed dual polarized antenna

In this section, a new design of mmWave differentially fed dual polarized antenna applicable for multibeam antenna arrays is developed to improve the XPD, increase port isolation and achieve wide -3 dB beamwidth. In most conventional mmWave dual polarized antenna designs, the radiator is separated with the feed structures by a shared ground plane and they are designed in different laminate layers. This indicates that all the differential feed structures are situated in the same layers, which will result in congestion of feed network and introduce high complexity in multibeam antenna array design [137]. In this design,

the feed structures of the antenna elements for exciting HP and VP radiation are separated and designed in different laminate layers, which not only can avoid congestion of feed networks but also greatly reduce the complexity of the overall structure of the multibeam antenna array.

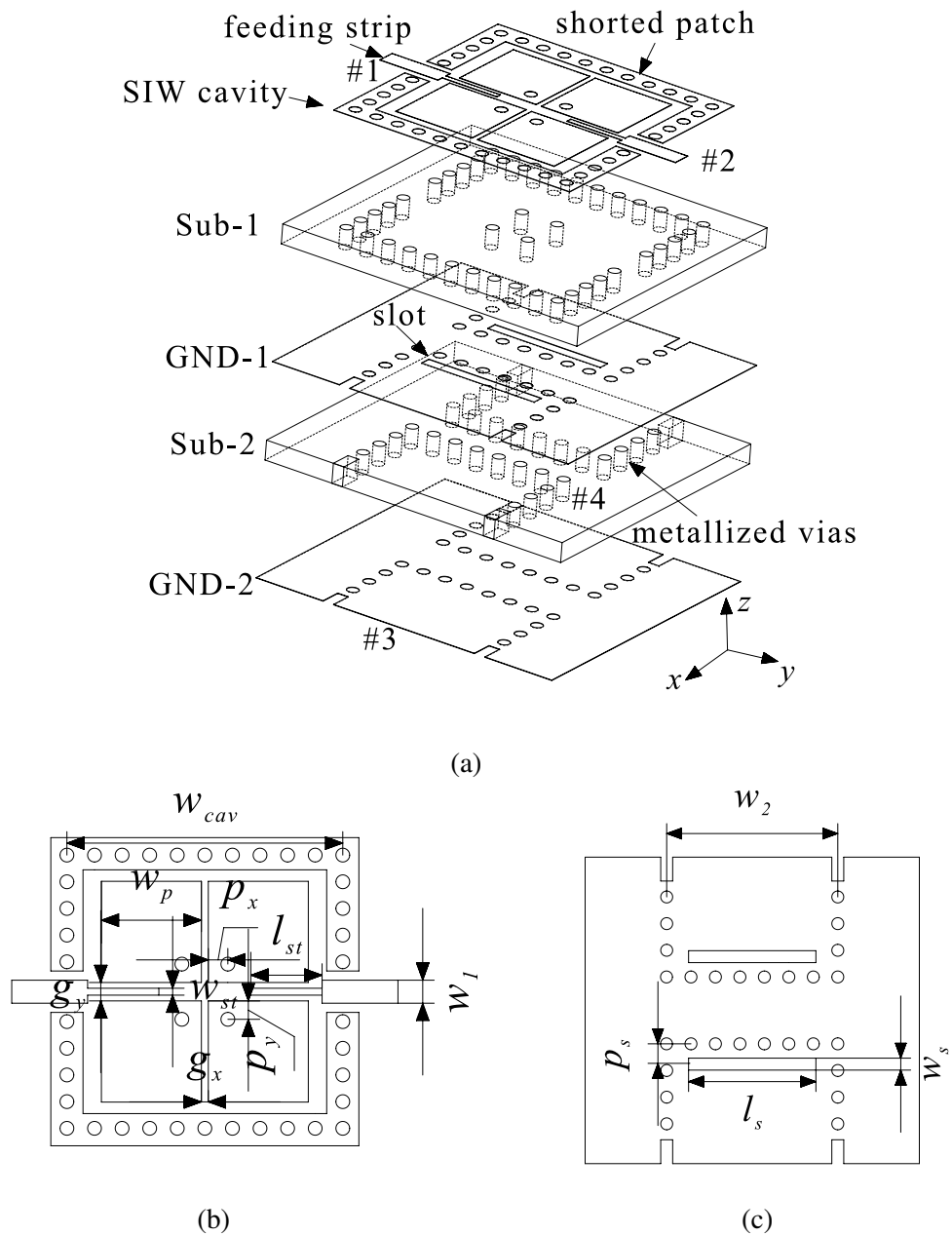


Fig. 4.2 Configuration of the proposed differentially fed dual polarized antenna. (a) Exploded view. (b) Layout of the shorted patch. (c) Layout of GND-1.

Table 4.1 Dimensions of the differential fed dual polarized patch antenna: mm

w_{cav}	l_p	w_p	g_x	g_y	p_x	p_y
6.40	2.20	2.20	0.15	0.40	0.43	0.40
l_{st}	w_{st}	w_1	w_2	l_s	w_s	p_s
1.55	0.15	0.50	4.30	3.20	0.30	0.50

4.2.1 Antenna configuration

The configuration of the proposed differentially fed dual polarized antenna is illustrated in Fig. 4.2, which is implemented in two substrates. The top substrate (Sub-1) includes the antenna aperture and a pair of differential feeds for HP. In the bottom substrate (Sub-2), it includes a pair of differential feeds for VP. The two orthogonal polarizations share the same radiation aperture. The SIW cavity in Sub-1 and the feed structures for VP in Sub-2 are realized by a series of plated vias with a diameter of $d = 0.3$ mm. The SIW cavity designed in Sub-1 is used to prevent potential surface waves from propagating when beams scan off the boresight. The via spacing is set to $p = 0.6$ mm for the purpose of minimizing wave leakage between adjacent vias and ensure the cavity is physically realizable [230]. Four patches with a dimension of $w_p \times l_p$ are printed inside the SIW cavity. In addition, four inductive posts with a diameter of 0.3 mm and an offset position of (p_x, p_y) are designed to connect the four patches to the ground plane. Due to constraint space, it is critically challenging to apply traditional differentially fed dual polarized antennas into the design of an multibeam antenna array. In this presented design, the problem is elaborately addressed by designing the differential feed ports for HP with two stepped microstrip lines, where a narrow strip is inserted from the opening of the SIW cavity. The feed strips are small enough to be fit into the gap between two patches. While for VP, the differential feed ports are realized with SIWs in Sub-2. The width of the SIW feeds is set to $w_2 = 4.3$ mm for avoiding higher modes within the operation frequency of interest. As shown in Fig. 4.2(c), two transverse slots with the length of l_s and the width of w_s are etched on the top copper layer of Sub-2. They are used to couple the input energy from ports #3 and #4 to excite the shorted patches for VP. In this design, Sub-1 and Sub-2 are the low cost Rogers 4003C laminate with a thickness of 0.508 mm, relative permittivity of 3.55, loss tangent of $\tan \delta = 0.0027$, and an electro-deposited copper foil of 0.5 oz (17 μm). The detailed design parameters of the differentially fed dual polarized antenna are illustrated in Table 4.1. All the simulations in this work are performed by using the high frequency full wave electromagnetic solver, ANSYS Electronics Desktop HFSS.

To facilitate the analysis of the proposed differentially fed dual polarized antenna, the feed pair of port #1 and #2 is designated as the differential feed port d1 for HP, while the feed pair of port #3 and #4 is designated as the differential feed port d2 for VP. Thus, according to the mixed-mode theory [231], the reflection coefficient and port coupling

coefficient of a differential feed antenna can be written as

$$S_{dd11} = \frac{1}{2}(S_{11} + S_{22} - S_{12} - S_{21}) \quad (4.1)$$

$$S_{dd22} = \frac{1}{2}(S_{33} + S_{44} - S_{34} - S_{43}) \quad (4.2)$$

$$S_{dd21} = \frac{1}{2}(S_{31} + S_{42} - S_{32} - S_{41}) \quad (4.3)$$

where $S_{ij}(i, j = 1, 2, 3, 4)$ can be extracted from the simulated S -parameters. By applying (4.1) – (4.3), one can obtain the differential S -parameters to evaluate the impedance performance of the designed differentially fed dual polarized antenna.

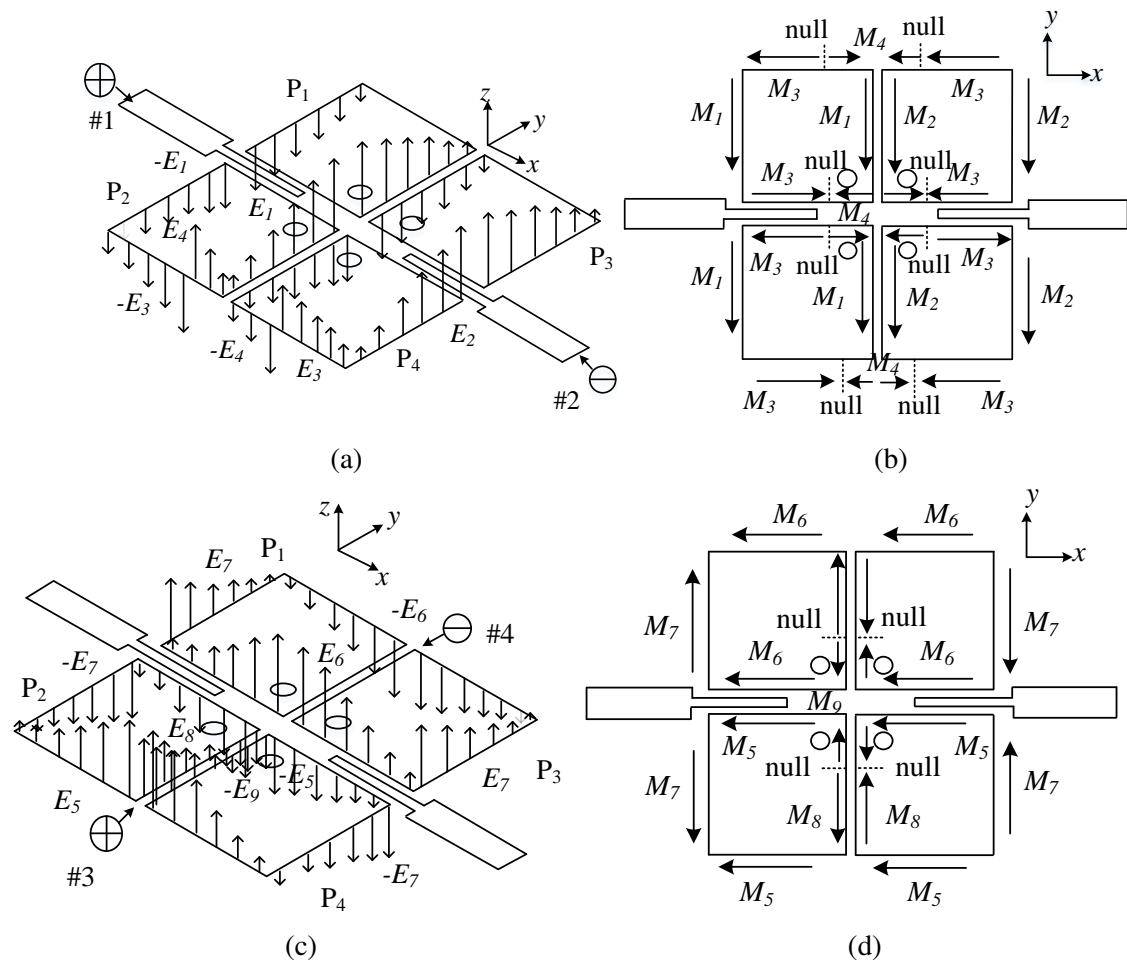


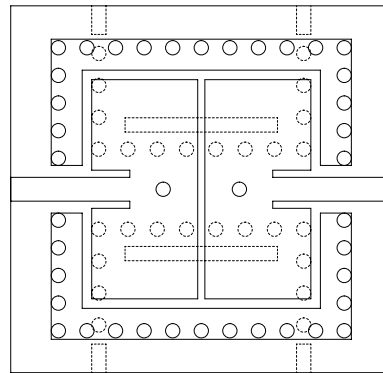
Fig. 4.3 (a) Electric field distribution, and (b) Equivalent magnetic current when differential port d1 is excited. (c) Electric field distribution, and (d) Equivalent magnetic current when differential port d2 is excited.

4.2.2 Working principles

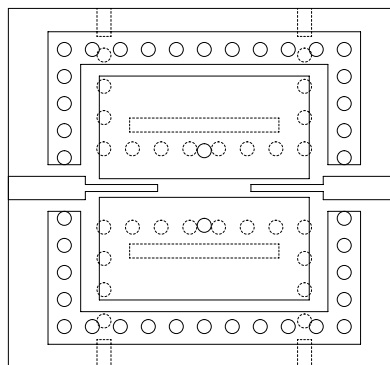
The structure of the proposed antenna is somewhat similar to ME dipoles, but their operation principle is quite different. As reported in [136] and [137], a ME dipole with single polarization is usually composed of an electric dipole and a vertical patch antenna acting as a magnetic dipole. Essentially, to enable the magnetic dipole, the height of the vertical patches should be approximately 0.25λ , where λ is the wavelength in the laminate. In order to simultaneously excite the electric dipole and magnetic dipole, a coupling slot etched in the ground plane of the antenna or Γ -shaped probes placed between the vertical patches are widely used in ME dipole designs. In the proposed design, the thickness of Sub-1 is only 0.508 mm ($\approx 0.09\lambda$), which is far less than the resonating length of a magnetic dipole. The inductive posts loaded to the patches help improve the impedance matching of the antenna, rather than act as a magnetic dipole. In this design, the inductive posts are not excited due to the thin laminate and the feed methods which are different from those in ME dipoles. Thus, the proposed antenna is considered as a patch antenna. Although ME dipoles exhibit advantages such as wide bandwidth and symmetric patterns, low XPDs (10 dB) are observed when beams scan to the maximal pointing angles, and differential feed is difficult to be applied in ME dipoles multibeam array antennas working at mmWave bands due to high complexity and constrained space.

For simplicity and without loss of generality, the most intuitive way of synthesising patch antennas is based on the theory of the cavity model method [232]. From this theory, a patch antenna can be considered as a cavity which consists of a dielectric filled cavity placed on a perfect ground plane. The dielectric filled cavity is covered with a perfect patch. According to the Huygens' principle, the equivalent electric currents J_s and magnetic currents M_s along the side walls of the dielectric filled cavity contribute to the radiation of the patch antenna. Among these current sources, the electric currents can be neglected since they are very weak. The electric distribution and equivalent magnetic currents of the proposed differentially-fed dual-polarized antenna are illustrated in Fig. 4.3. To facilitate the analysis, the proposed antenna is considered as an array with 2×2 grounded patch elements, namely P_1 , P_2 , P_3 and P_4 . The grounded patch array radiates HP waves when the differential port d1 is excited. As can be seen from Fig. 4.3(a), the electric fields radiated from each patch element, which are in the yo z -plane, are almost the same to each other. Besides, the radiated electric field patterns from the patches P_1 and P_2 (or P_3 and P_4) are similar to those of a traditional patch resonating at the TM_{010} mode. In view of this, the antenna can be taken as two patch antennas with the resonating length w_p and the width $(2l_p + g_y)$. Fig. 4.3(b) shows the magnetic currents M_1 and M_2 at the edges along the y -axis. These currents have the same direction implying that constructive radiation fields can be derived in the E-plane (xoz -plane, $\varphi = 0^\circ$). The inductive posts used to short the patches to the ground plane aid the improvement of the impedance matching. As can be seen from Fig. 4.3(b), the presence of these posts also moves the currents nulls between

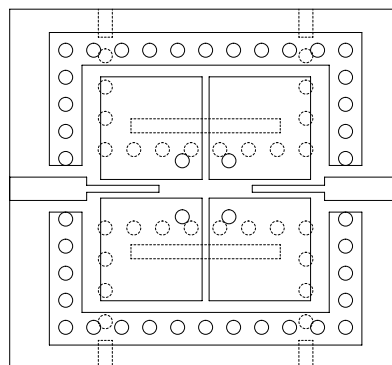
M_3 and M_4 off the edge centre. Fortunately, The XPD in the E-plane resulted from these magnetic currents along the x -axis direction would be very small due to the anti-symmetry of these currents. Similar radiation patterns can be obtained in the H-plane (yoz -plane, $\varphi = 90^\circ$). As a result, for the proposed antenna with the differential port d1 excited, the edges along the y -axis make for the far field radiation, while the edges having the same direction with the x -axis make for non-radiation.



(a)



(b)



(c)

Fig. 4.4 Evolution process of the proposed differentially fed dual polarized patch antenna. (a) Reference antenna Ant-1. (b) Reference antenna Ant-2. (c) Proposed antenna.

When the differential port d2 of this antenna is excited for VP radiation, the patch antenna is fed by capacitive couplings from the two transverse slots below the grounded patches, as shown in Fig. 4.2. Because the TE_{10} is the dominant mode of the feed SIWs in Sub-2, the electric fields close to the shorted end wall of the feed SIWs show vertical polarization. The grounded patches situated over the transverse slots are then excited as a result. In this case with the differential port d2 excited, the radiating edges are those having the same direction with the x -axis. As can be seen from Fig. 4.3(c), the electric fields from these radiating edges are same as the radiation electric fields of a traditional patch antenna. In this case, the proposed antenna can be viewed as two patch antennas with the resonating length l_p and the width $(2w_p + g_x)$. The magnetic currents when the antenna works with VP are shown in Fig. 4.3(d). Constructive radiation can be derived in the E-plane (yo z -plane, $\varphi = 90^\circ$) because the currents M_5 and M_6 share the same direction. It should be noted that the magnetic currents M_7 – M_9 from these edges along the y -axis direction slightly differ from those depicted in Fig. 4.3(b). As can be seen from Fig. 4.3(d), the magnetic currents along the external edges have nulls, while the magnetic currents M_8 and M_9 which are at the internal edges along the y -axis direction have a null off the edge centre. Even so, the XPD resulted from these y -axis directed magnetic currents is neglectable since these currents are also anti-symmetric along the y -axis. Due to the differential feed technique used, the induced current on the feed strips connected to the differential port d1 is extremely small with differential port d2 excited, which indicates high isolation between the differential port d1 and d2 can be obtained in the proposed antenna.

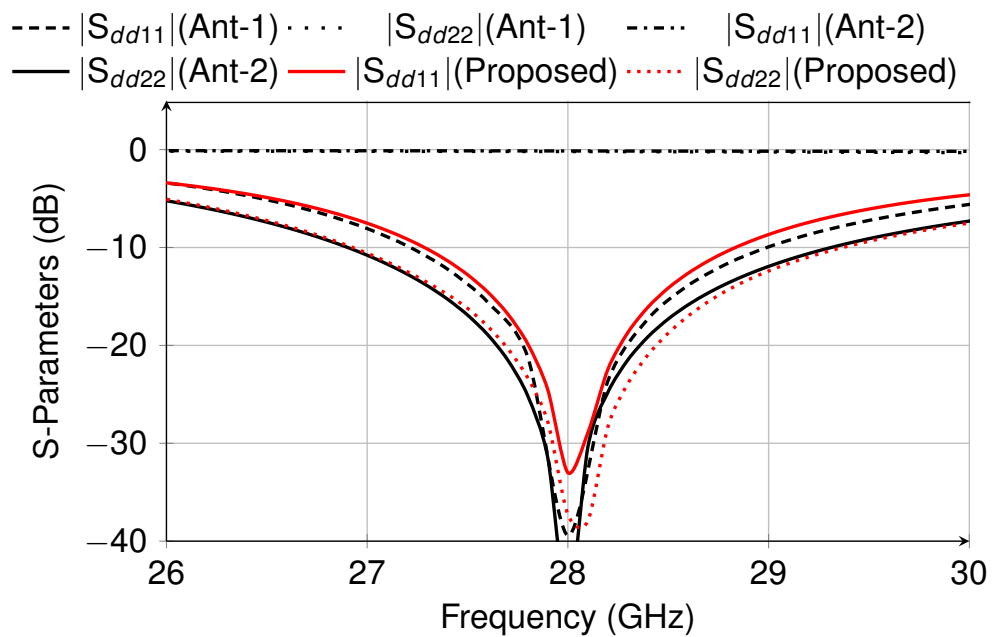


Fig. 4.5 Simulated S-parameters of the antennas in the design process.

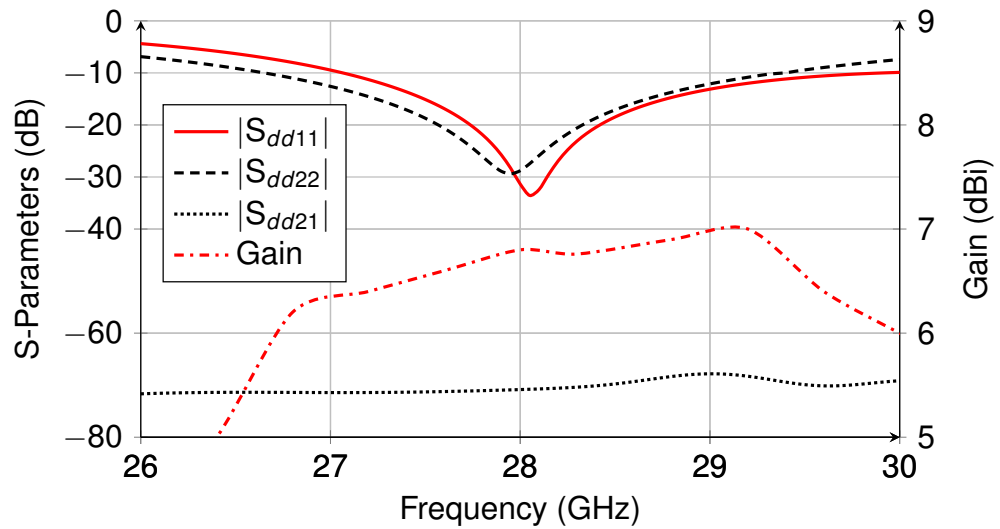


Fig. 4.6 Simulated S -parameters and gain of the proposed differentially fed dual polarized patch antenna.

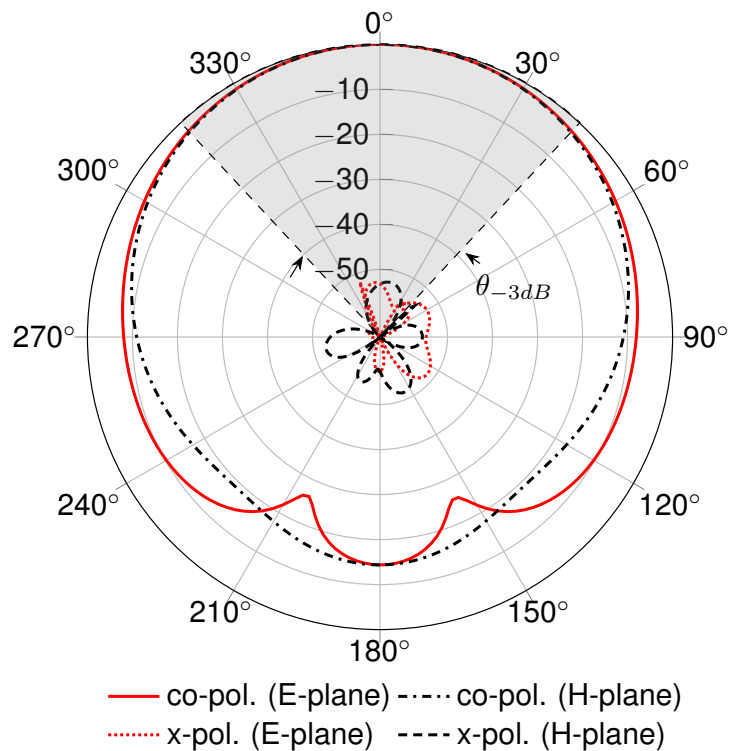


Fig. 4.7 Simulated normalized far field radiation patterns of the proposed differentially fed dual polarized patch at 28 GHz when differential port #d1 is excited.

4.2.3 Antenna optimization

To have a better understanding of the proposed antenna, two other reference antennas, Ant-1 and Ant-2, are also investigated. As illustrated in Fig. 4.4(a), the reference antenna Ant-1 is implemented with two rectangular patch antennas printed inside the square SIW cavity. Two inset microstrip lines are designed to feed the antenna for HP, and two SIWs

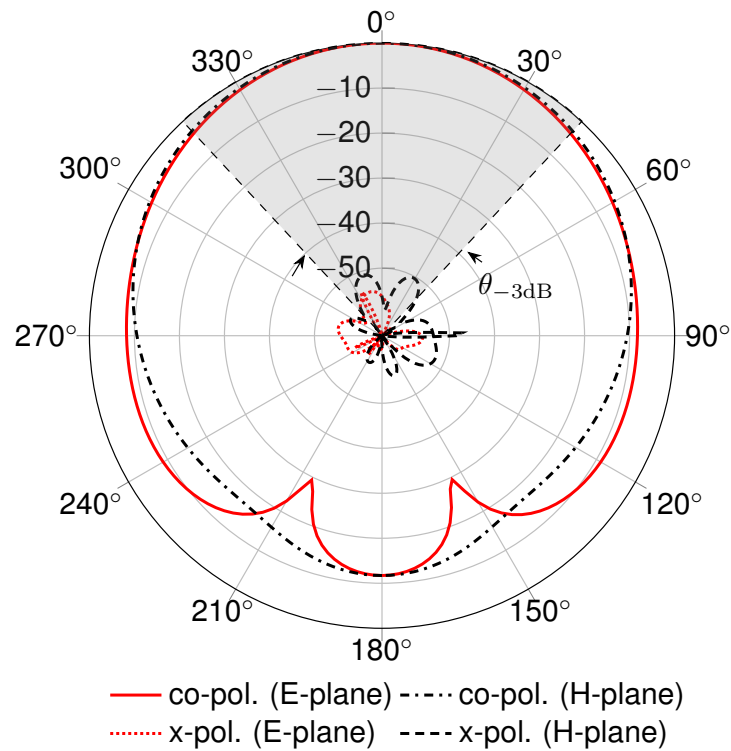


Fig. 4.8 Simulated normalized far field radiation patterns of the proposed differentially fed dual polarized patch at 28 GHz when differential port #d2 is excited.

with two transverse slots etched over the ground plane are used to feed the antenna for VP. To achieve good impedance matching, two grounded posts are inserted beside the gap between the two patches. The length of the rectangular patch l_p affects the resonance frequency, and the patch width w_p decides the input impedance when the antenna operates with HP. From the simulation, it is found that the patch length should be around 0.9λ in order to realize good impedance matching. On the contrary, this will result in non-resonance when the patch antenna operates with VP. The simulated results are shown in Fig. 4.5. The input signals at the differential port d2 are almost totally reflected. Thus, in order to comprehend the resonance features of the proposed patch antenna when operating with VP, the reference antenna Ant-2 is studied. In this antenna, two patches are printed inside the SIW cavity, and they are separated by a narrow gap. The feed strips for exciting HP are small enough to be inserted in the narrow gap between the two patches. The antenna can be regarded as a slot coupled patch antenna when it works with VP. The simulation depicted in Fig. 4.5 demonstrates that the reference antenna Ant-2 has realized good impedance matching at the differential port d2. However, total reflection is observed at the differential port d1, which is quite similar to the reference antenna Ant-1 with differential port d2 excited. In view of the simulated results from the two reference antennas, the proposed antenna is realized by splitting a patch into four elements, which brings good impedance matching at both the differential ports d1 and d2. The proposed antenna can be considered as a combination of the reference antenna Ant-1 and Ant-2. The optimized

dimension of the patch element is $2.6 \text{ mm} \times 2.6 \text{ mm}$, which corresponds to $0.39\lambda \times 0.39\lambda$. As can be seen from Fig. 4.5, splitting the patch into four elements does not affect the performance of this differentially fed antenna. Hence, the proposed patch antenna can be considered as an inset fed patch antenna when it works with HP, and a slot coupled patch antenna when it works with VP.

The simulated performance of the proposed differentially fed dual polarized patch antenna can be found in Figs. 4.6–4.8. Fig. 4.6 presents the simulated S -parameters and realized gain of the proposed antenna. As can be seen from this figure, the proposed antenna has an overlapped impedance bandwidth from 26.8 GHz to 29.2 GHz for $|S_{dd11}|$ and $|S_{dd22}|$ less than -10 dB . The proposed antenna shows high port isolation, which is higher than 68 dB over the operation bandwidth. In addition, the proposed antenna also exhibits stable gain, which ranges from 6.2 dBi to 7 dBi over the bandwidth. Fig. 4.7 and Fig. 4.8 show the simulated far field radiation patterns of the proposed antenna in the E- and H-plane. It can be seen from Fig. 4.7 that symmetrical radiation patterns are obtained in both the E- and H-plane when the proposed antenna operates with HP (in this case, differential port d1 is excited). In addition, this antenna also shows broad -3 dB beamwidth, which is 86° in both the E- and H-plane. Within this broad beamwidth, the XPD is higher than 46 dB . Similar radiation patterns are obtained when the differential port d2 is excited for VP, which is demonstrated in Fig. 4.8.

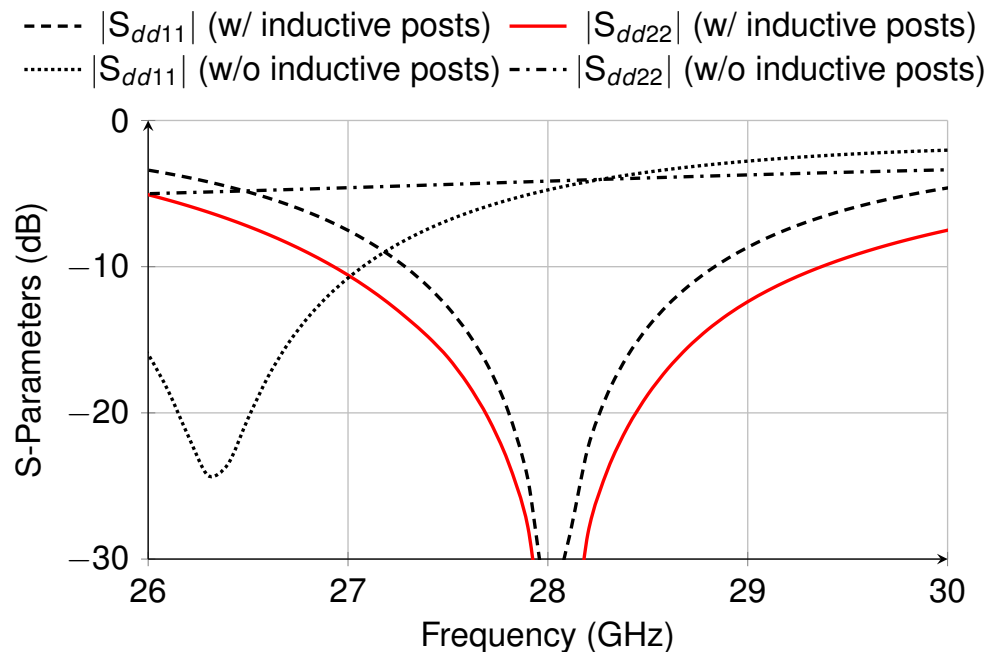


Fig. 4.9 Simulated S -parameters of the proposed differentially fed dual polarized patch antenna with or without the grounding vias.

In this proposed differentially fed dual polarized patch antenna, the four inductive grounding posts connecting the patch elements to the ground plane aid the impedance matching improvement. Fig. 4.9 shows the simulated S -parameters of the proposed antenna

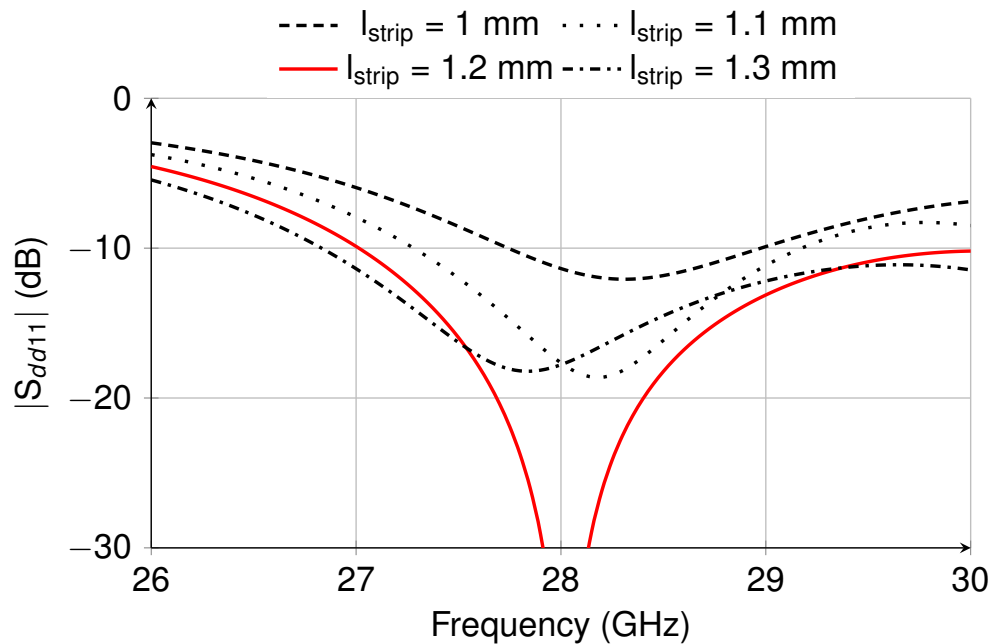


Fig. 4.10 Simulated S_{dd11} of the proposed differentially fed dual polarized patch antenna by varying the length of the feed strip.

with or without the inductive posts. Just as illustrated in this figure, the performance of $|S_{dd11}|$ and $|S_{dd22}|$ are significantly affected by the inductive posts. When the differential port d1 is excited, the resonance frequency of this antenna increases from 26.3 GHz to 28 GHz after introducing the inductive posts. However, it should be noted that if no inductive posts introduced there is no resonance over the operation bandwidth when the differential port d2 is excited. As can be seen from Fig. 4.10, the return loss at the differential port d1 is also significantly affected by varying the feed strip length l_{st} . The resonance frequency moves to the lower frequency as the feed strip length increases. This is because the electric current path of the antenna is extended with the increase of the feed strip length. The antenna resonates at 28 GHz with $|S_{dd11}| < -30$ dB when the feed strip length l_{st} equals 1.2 mm. Due to high isolation between the differential port d1 and d2, the presence of the feed strip is not detrimental to the performance of $|S_{dd22}|$.

4.3 2D Multibeam antenna array

This section will talk about the overall structure of the designed differentially fed dual polarized 2D multibeam antenna array based on the architecture shown in Fig. 4.1 and the antenna element designed in Section 4.2. For a passive 2D multibeam antenna array, the multibeam networks play a critically important role in determining the overall performance. However, one of the most commonly seen problems is high complexity and large size. Thus, in this section the simplification of overall structure will be repeatedly emphasized during the component designs.

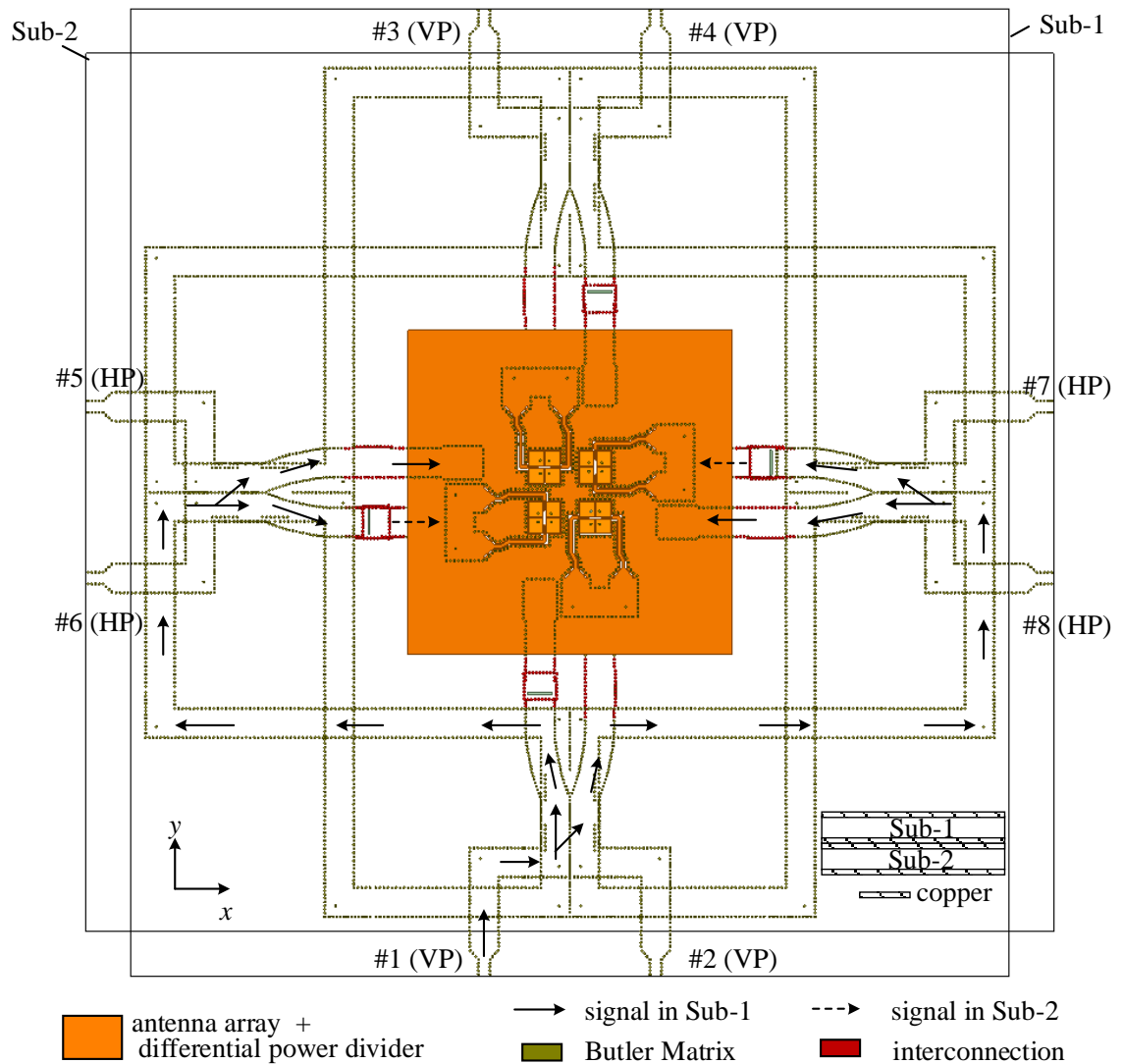


Fig. 4.11 Configuration of the proposed differentially fed dual polarized 2D multibeam antenna array.

4.3.1 Configuration

The configuration of the proposed differentially fed dual polarized 2D multibeam antenna array is illustrated in Fig. 4.11. The proposed 2D multibeam antenna array is composed of an antenna array with 2×2 elements, a pair of SIW Butler Matrices, eight differential power dividers, and four interconnection structures. In order to realize 2×2 tilted radiation beams with dual polarization, the pair of Butler Matrices are perpendicular to each other and they are situated in different laminates. The Butler Matrix with the feed ports #1–#4 serves as the multibeam network exciting VP radiation beams, and the Butler Matrix with the feed ports #5–#8 works as the multibeam network exciting HP radiation beams. To avoid congestion, the two Butler Matrices for HP and VP are implemented in the laminates Sub-2 and Sub-1, respectively. As a key component to realize differential feed, the differential power dividers are located around the antenna array aperture. The

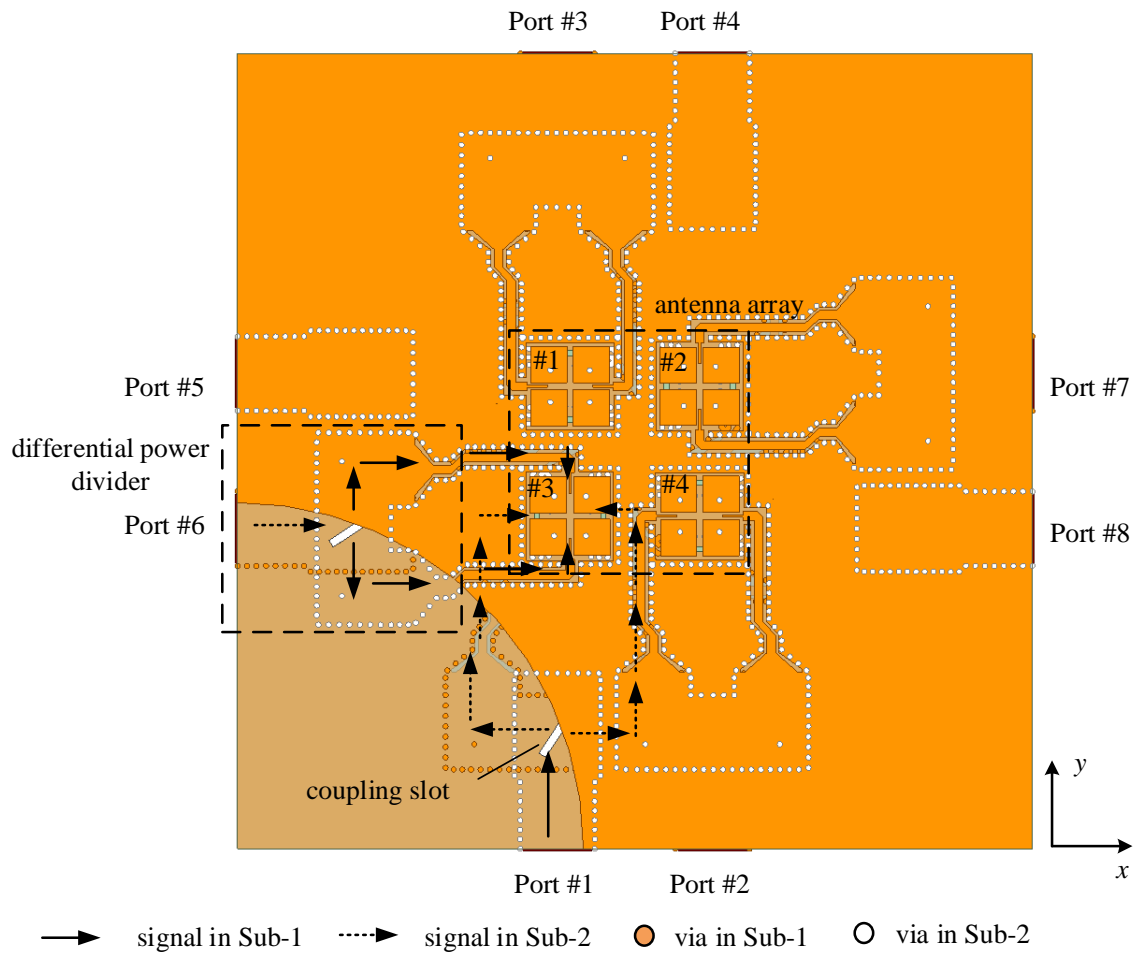


Fig. 4.12 Layout of the 2×2 antenna array and the differential power dividers.

interconnection structures, which connect the differential power dividers to the Butler Matrices, are designed to avoid intersection. To have a better understanding of the overall structure of this 2D multibeam antenna array, the signal paths from the feed port #1 to the radiators are also illustrated in Fig. 4.11. The flow directions of input signals are represented by arrows where the signals in the laminate Sub-1 is denoted as the solid arrows and the signals in Sub-2 is denoted by the dotted arrows. A close up view of the signals from the differential power dividers to the antenna elements is shown in Fig. 4.12. This figure also unveils the detailed stackup of the differential power divider and antenna array. As can be seen from this figure, the differential power divider connected to the feed port #1 is anti-symmetric with the one connected to the feed port #2 since the feed ports of the antenna elements for exciting different polarizations are designed in different laminates. The element separation of the antenna array in the x - and y -axis direction is set to 7.5 mm, which corresponds to $0.7\lambda_0$.

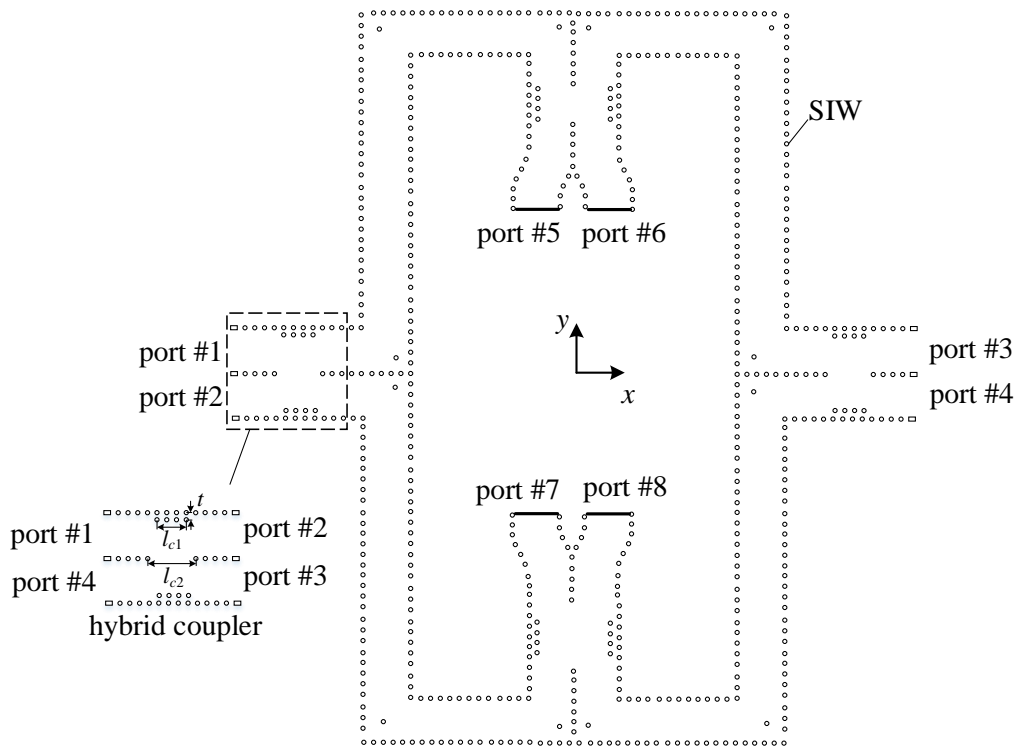


Fig. 4.13 Layout of the designed Butler Matrix and the $-3\text{dB}/90^\circ$ hybrid coupler.

4.3.2 Butler Matrix design

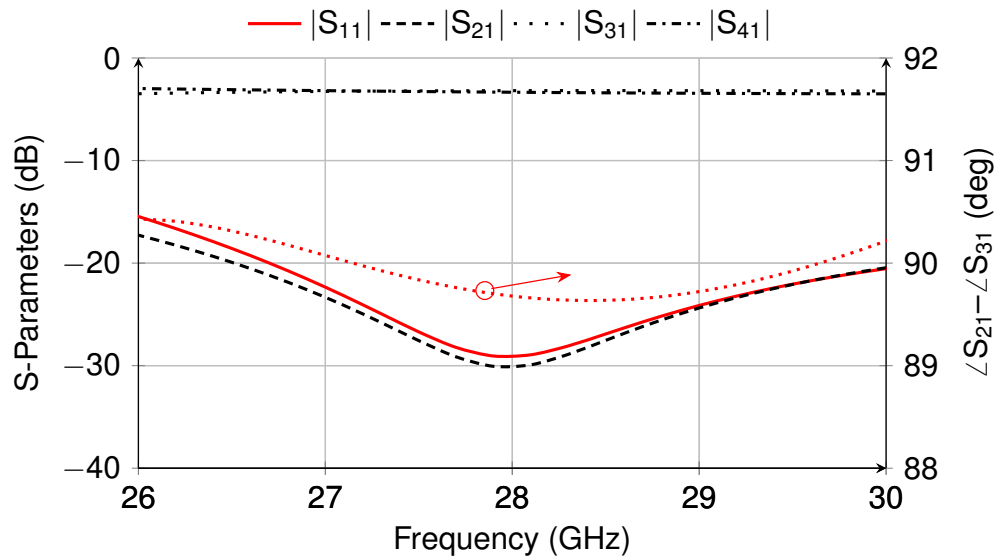
In the proposed antenna array, the Butler Matrix serves as the multibeam network feed the antenna array for tilted beams in 2D space domain. As can be seen from Fig. 4.13, it gives the layout of the Butler Matrix used in the design. The most key component in designing this Butler Matrix is the $-3\text{ dB}/90^\circ$ hybrid coupler, which can be regarded as the combination of an equal ratio power divider (-3 dB) and a 90° phase shifter. Four this kind of hybrid couplers are required and they are connected together by four bended SIWs. To improve the return loss, a metallized via is placed at each corner of the bended SIWs. These bended SIWs have equal electric length. Thus, the Butler Matrix used in this design

Table 4.2 Theoretical phase response of the designed Butler Matrix

	port #1	port #2	port #3	port #4
port #5	0°	-90°	-90°	180°
port #6	-90°	180°	0°	-90°
port #7	-90°	0°	180°	-90°
port #8	180°	-90°	-90°	0°
ϕ_x	-90°	-90°	90°	90°
ϕ_y	90°	-90°	90°	-90°

Table 4.3 Dimensions of the components used in the design of the multibeam antenna array

l_{c1}	l_{c2}	t	w_t	x_p	y_p	l_{s1}	w_{s1}
3.70 mm	5.40 mm	0.65 mm	3.60 mm	1.66 mm	1.46 mm	3.17 mm	0.30 mm
θ_1	m_1	s_p	l_5	l_6	l_{s2}	l_a	w_a
33.56°	0.70 mm	6.80 mm	3.00 mm	0.89 mm	3.63 mm	6.27 mm	0.20 mm


 Fig. 4.14 Simulated S -parameters and phase response of the designed SIW hybrid coupler.

requires no phase shifters. Ports #1–#4 are the feed ports, and ports #5–#8 are the output ports which are followed by the differential power dividers and the antenna array shown in Fig. 4.12. It can be easily derived that fixed phase differences are obtained between the output ports #5–#8 when any feed port is active. For the purpose of explicitness, Table 4.2 presents the theoretically derived phase response at the output ports #5–#8 when any feed port (#1–#4) is under excitation. The detailed parameters of the designed -3 dB/ 90° hybrid coupler are given in Table 4.3 and Fig. 4.14 presents the simulated S -parameters of the designed SIW -3 dB/ 90° hybrid coupler. The operation bandwidth for return loss $\|S_{11}\| > 15$ dB is in the frequency range 26–30 GHz. In this bandwidth, the insertion loss from the feed port #1 to the direct port #2 or the coupling port #3 is 3.2 ± 0.4 dB. In addition, port #4 keeps well isolated to port #1. The simulated phase difference between the ports #2 and #3 when the feed port #1 is excited is also included in Fig. 4.14 where $\angle S_{21} - \angle S_{31}$ is in the range $90 \pm 0.5^\circ$ over the operation bandwidth.

The simulated performance of the designed SIW Butler Matrix is illustrated in Fig. 4.15 and Fig. 4.16. As can be seen from Fig. 4.15, this Butler Matrix shows wide impedance bandwidth, which is larger than 14% (from 26.3 GHz–29.8 GHz) for $|S_{11}| < -20$ dB. In

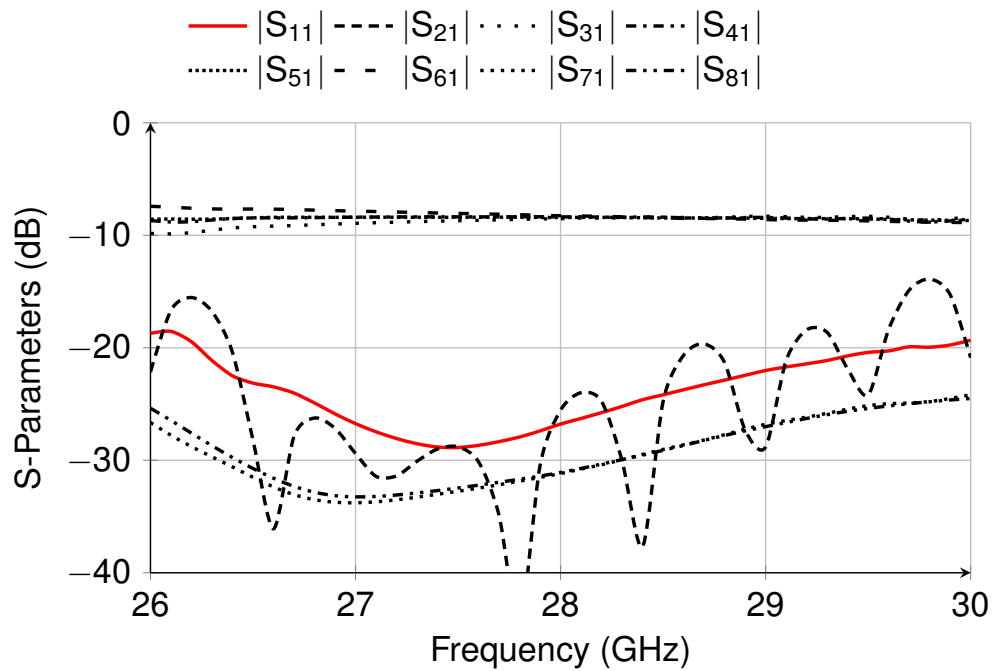


Fig. 4.15 Simulated S -parameters of the designed SIW Butler Matrix.

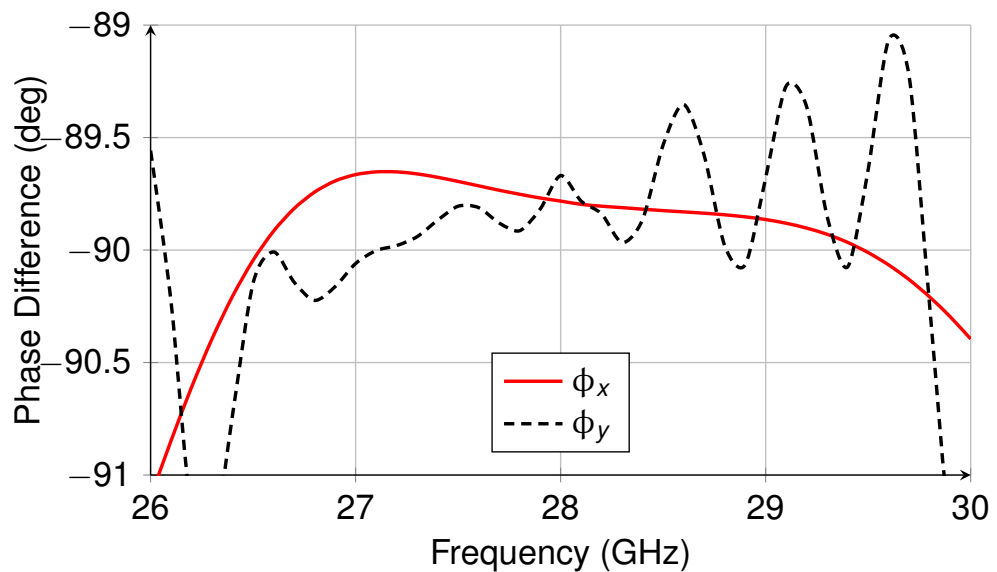


Fig. 4.16 Simulated phase response of the designed SIW Butler Matrix.

addition, the designed Butler Matrix also exhibits excellent isolation between any two feed ports. The port isolation between port #1 to ports #2–#4 is higher than 15 dB over the frequency range 26–30 GHz. The transmission loss caused by the dielectric, return loss and metallic loss is no more than 1.6 dB over the bandwidth from 26.8 GHz to 29.2 GHz. As shown in Fig. 4.16, the variation of phase differences between any two output ports #5–#8 is in the range $-90 \pm 1^\circ$ over the bandwidth 26–30 GHz, which indicates that the obtained

phase response of the designed Butler Matrix is quite close to the expected response shown in Table 4.2.

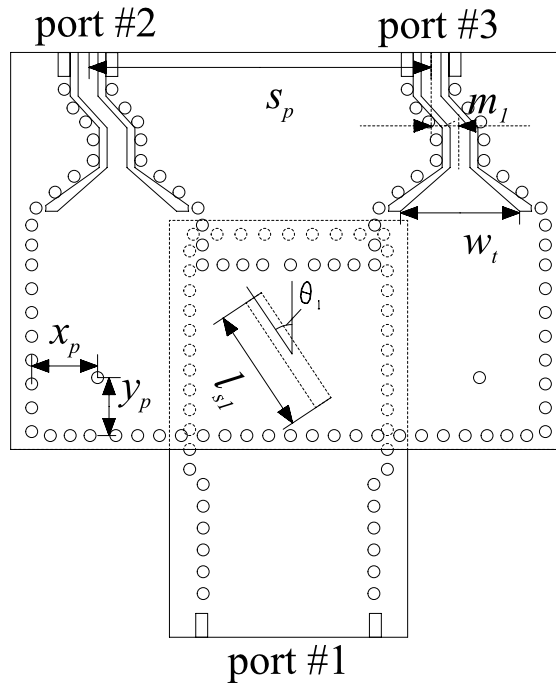


Fig. 4.17 Layout of the differential power dividers.

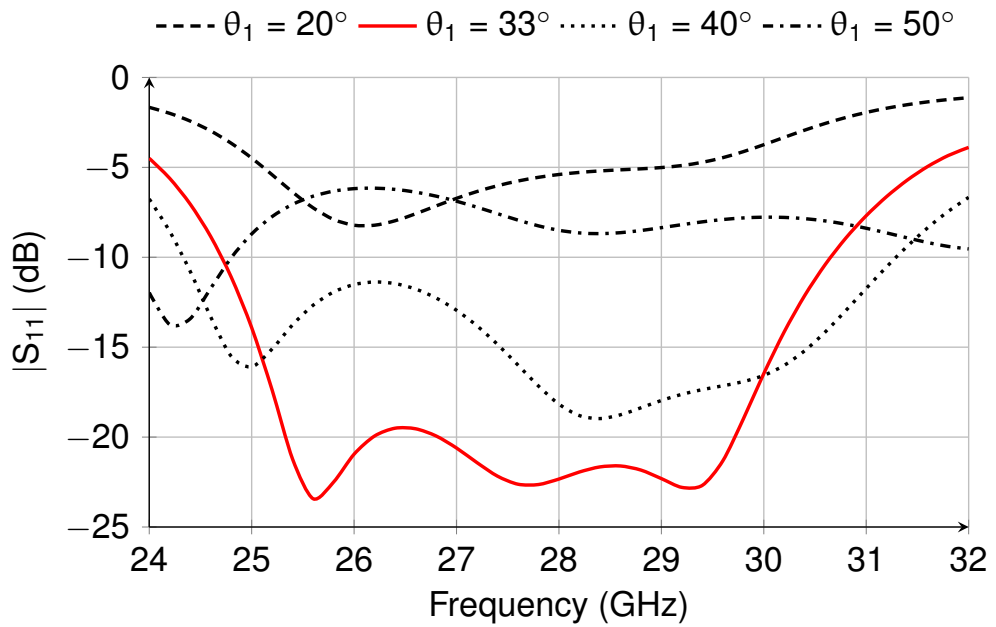


Fig. 4.18 Simulated $|S_{11}|$ of the designed differential power divider with different slant slot angles.

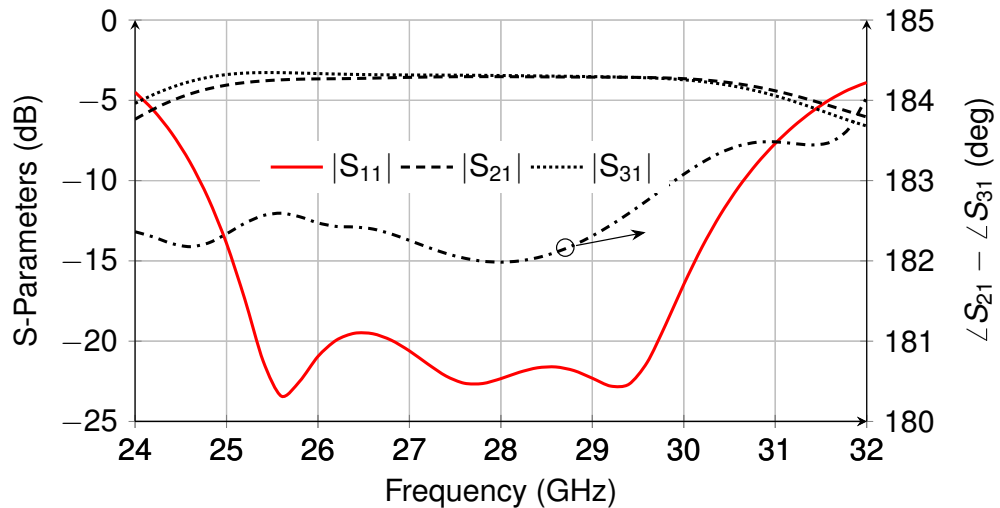


Fig. 4.19 Simulated S -parameters and phase difference between port #2 and #3 of the designed differential power divider when port #1 is excited.

4.3.3 Differential power divider

In this 2D multibeam antenna array, the differentially fed patch antenna is designed to achieve high XPD when beams scan off the boresight. Thus, differential feed structures with high performance should be incorporated into the design of the proposed 2D multibeam antenna array. Basically, it is required that the designed differential feed structure must have wide impedance bandwidth (larger than the bandwidth of dual polarized antenna element) and excellent differential response at the output ports. The configuration of the adopted differential structure is shown in Fig. 4.17, which can be considered as a differential power divider. It is realized on two laminates with compactness and simple configuration. The input port #1 is located on the bottom laminate and the output ports #2 and #3 are designed on the top laminate. Ideally, by exciting port #1, ports #2 and #3 can receive voltage of equal magnitude having a phase difference of 180° . Signals are coupled between two laminate layers through a slot etched on their shared ground plane. The coupling slot is slanted with an angle of θ_1 to improve the impedance matching and coupling efficiency. It should be noted that the meandered three-stage GCPWs are used to avoid overlapping between the two neighbouring differential power dividers. The offset of the meandered GCPWs is $m_1 = 0.7$ mm away from the centre line. As shown in Fig. 4.12, the two neighbouring differential power dividers are rotationally symmetrical with respect to the xoz -plane. The only difference between them lies in the distance s_p between the output ports. The detailed parameters of the designed differential power divider are given in Table 4.3. Fig. 4.18 shows the simulated $|S_{11}|$ of the designed differential power divider with different slant slot angles. As can be seen from this figure, the $|S_{11}|$ is very sensitive to the slant angle of the coupling slot. With the slant angle θ_1 increasing from 20° to 50° , the $|S_{11}|$ decreases firstly then increases after reaching the maximum -23 dB when

$\theta_1 = 33^\circ$. The simulated results of the designed differential power divider is shown in Fig. 4.19. The return loss at port #1 is higher than 20 dB over the frequency range from 26.8 GHz to 29.2 GHz. The power dividing ratio between the output ports #2 and #3 is in the range of -3.3 ± 0.15 dB over this operation bandwidth. When port #1 is excited, the phase difference between the two output ports is in the range of $182.5 \pm 0.5^\circ$ in the aforementioned impedance bandwidth. This indicates that the differential excitation to the antenna element is obtained in the designed power divider.

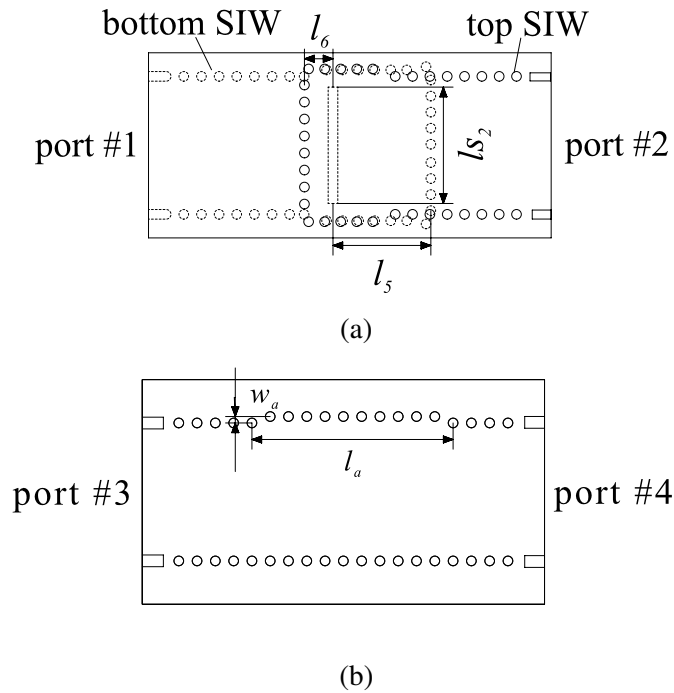


Fig. 4.20 Layout of (a) interconnection and (b) reference SIW.

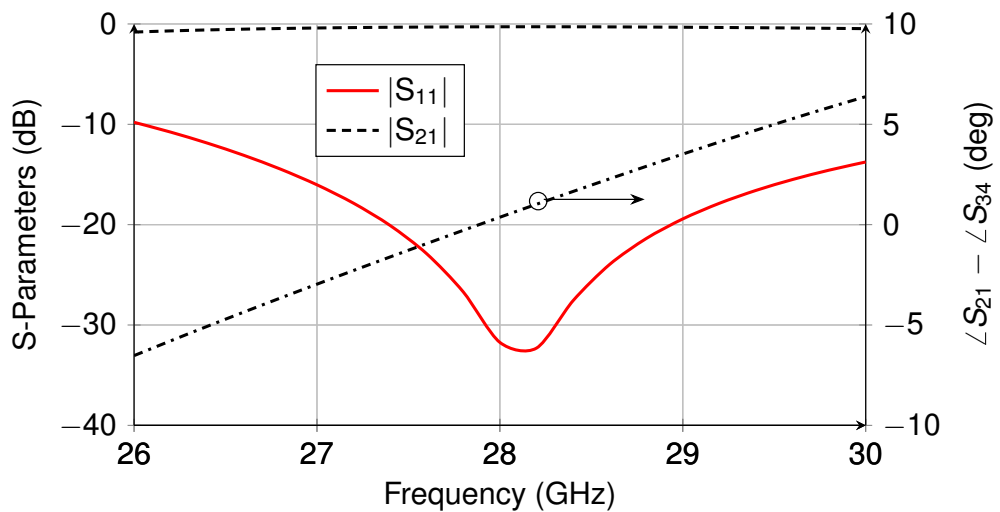


Fig. 4.21 Simulated S -parameters of the SIW interconnection and phase difference between the SIW interconnection and the reference SIW.

4.3.4 Interlayer transmission

The interconnection structure is another key component in designing the proposed differentially fed dual polarized 2D multibeam antenna array. It enables interlayer transmission and ensures that the feed networks for exciting orthogonal polarizations are situated in different laminate layers without congestion. The configuration of the designed interconnection structure is shown in Fig. 4.20(a), which is composed of two SIWs designed in two different laminate layers. In this structure, interlayer transmission is achieved by a transverse slot cut out from the common ground plane of the two SIWs. The coupling efficiency can be tuned by varying l_5 and l_6 . l_5 represents the distance between the transverse slot and the short end wall of the bottom SIW, and l_6 is the distance between the transverse slot and the short end wall of the top SIW. To cancel the additional phase introduced by the interconnection structure, an equal length unequal width reference SIW is designed, which is shown in Fig. 4.20(b). The detailed parameters of the designed interconnection structure and the reference SIW are given in Table 4.3. The desired 0° phase difference between the interconnection and the reference SIW can be realized by changing the length l_a and the unequal width w_a . The simulated results of the interconnection and the reference SIW are shown in Fig. 4.21. The impedance bandwidth of the interconnection structure for $|S_{11}|$ less than -10 dB is from 26 GHz to 30 GHz. The insertion loss of this interconnection structure is in the range from -0.52 dB to -0.28 dB over this bandwidth. The phase shift between the interconnection structure and the reference SIW is characterized by $\angle S_{21} - \angle S_{34}$. As can be seen from this figure, the obtained phase shift between the two structures has a deviation of $0.2 \pm 6.6^\circ$ over the bandwidth 26–30 GHz.

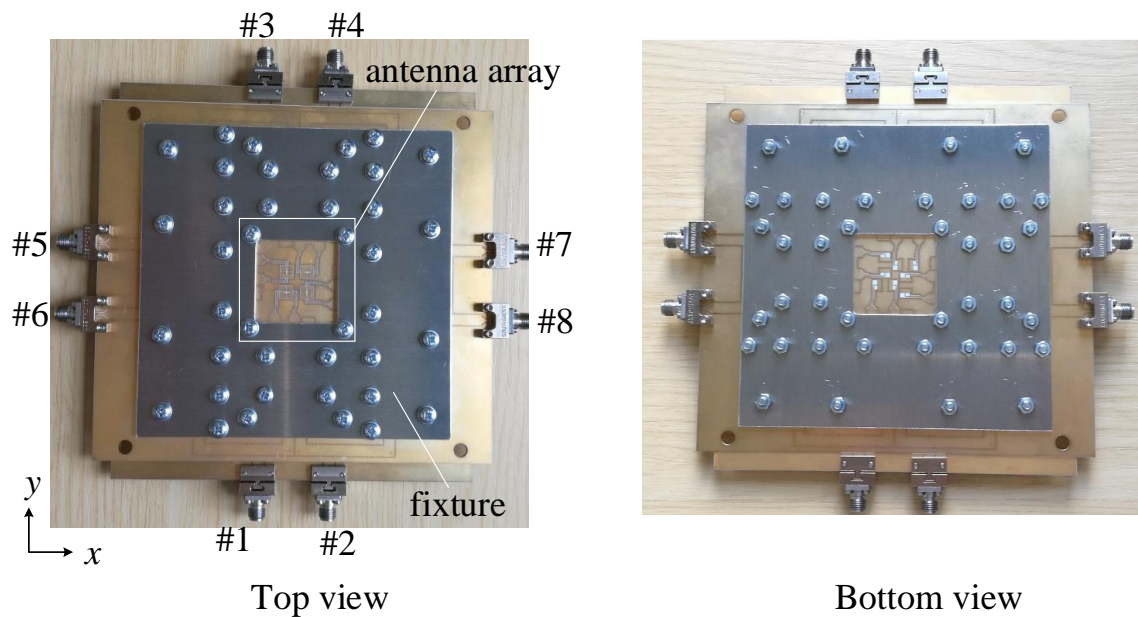


Fig. 4.22 Top view and bottom view of the fabricated prototype of the designed differentially fed dual polarized 2D multibeam antenna array.

4.4 Experiment and results

The designed differential fed dual polarized 2D multibeam antenna array is realized with two laminate layers, and it can be fabricated by using PCB processing technology with low cost. Fig. 4.22 presents the fabricated prototype of the proposed multibeam antenna array. The two Rogers RO4003C laminates are tightly sandwiched between two aluminium fixtures to avoid the air gap and ensure good interlayer transmission. The S -parameters measurements are carried out by using the vector network analyzer (VNA) Anritsu 37397C. This VNA is able to operate from 40 MHz to 65 GHz. The officially released document [233] shows that the system dynamic range of this VNA is in the range from -95 dB to -88 dB from 20 GHz to 40 GHz.

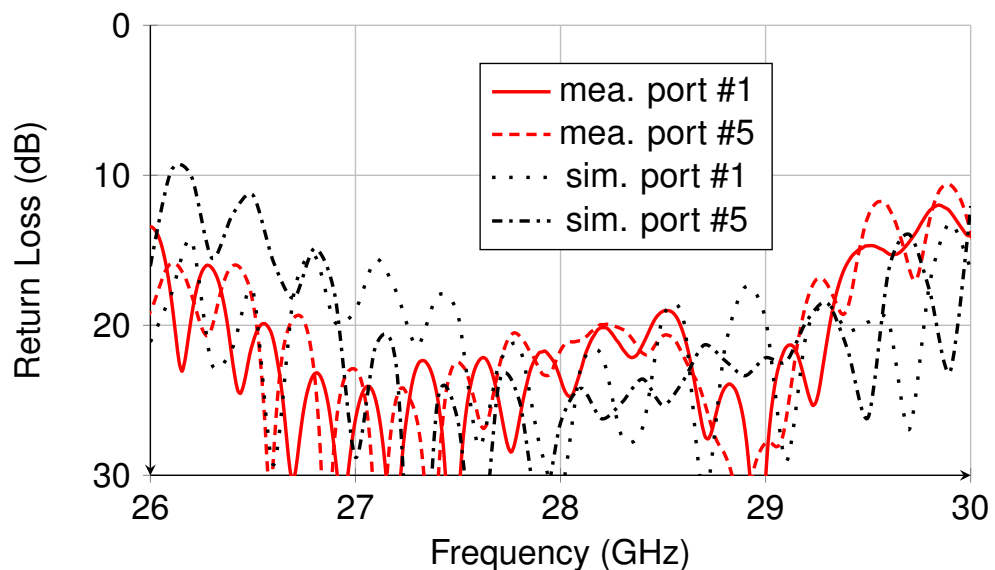


Fig. 4.23 Measured and simulated return loss of the designed differentially fed dual polarized 2D multibeam antenna array at the feed port #1 and #5.

4.4.1 Return loss and port isolation

The measured and simulated return loss at the feed ports #1 and #5 are shown in Fig. 4.23. Thanks to the symmetry of the proposed 2D multibeam antenna array, the performance of other ports is similar to the ports #1 and #5. Ports #1–#4 are the feed ports for exciting VP, and ports #5–#8 are the feed port for exciting HP. As shown in Fig. 4.23, the measured and simulated return losses at ports # 1 and #5 are well agreed with each other. The measured impedance bandwidth for return loss higher than 10 dB is from 26 GHz to 30 GHz, which corresponds to 14.3% of the fractional bandwidth. The measured and simulated impedance bandwidths of the antenna array are slightly larger when compares it with the operation bandwidth of the designed antenna element. The bandwidth extension is mainly caused

by the propagation loss from the multibeam feed networks and incomplete mismatching outside the bandwidth of the antenna element.

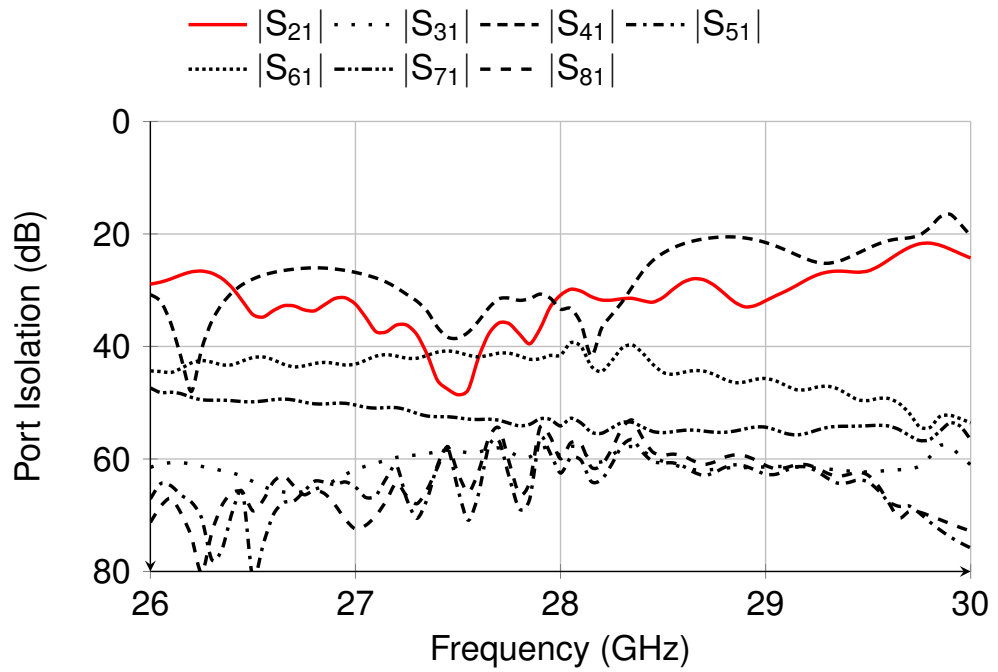


Fig. 4.24 Simulated isolation between port #1 and #8 of the designed 2D multibeam antenna array.

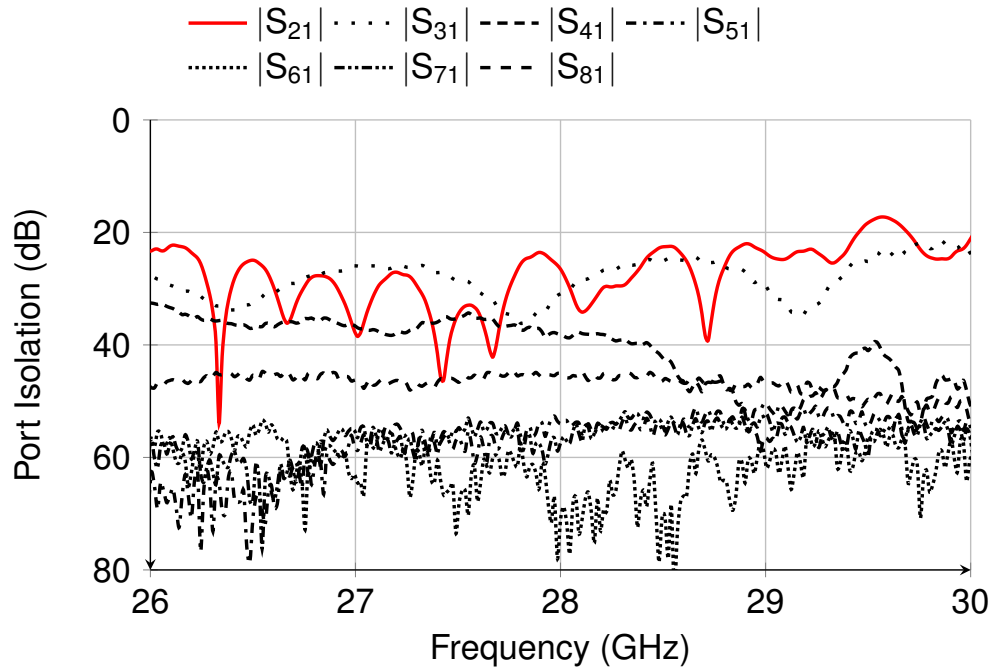


Fig. 4.25 Measured isolation between port #1 and #8 of the designed 2D multibeam antenna array.

Fig. 4.24 and Fig. 4.25 present the measured and simulated isolations between the feed port #1 and ports #2 to #8. It is shown that the measured and simulated port isolations are in reasonable agreement. The designed 2D multibeam antenna array achieves high port isolations. The measured isolations between the ports for exciting the same polarized waves, namely $\|S_{21}\|$ to $\|S_{41}\|$, are greater than 21.4 dB over the operation bandwidth of the antenna element 26.8 GHz–29.2 GHz. The measured isolations between the ports for exciting different polarized waves, namely $\|S_{51}\|$ to $\|S_{81}\|$, are larger than 46.3 dB over this bandwidth.

4.4.2 Radiation patterns

The measurement of far field radiation patterns of the fabricated antenna prototype was performed in the anechoic chamber. As given in [234], the beam pointing angles of a 2D phased antenna array or a 2D multibeam antenna array can be written and obtained by the following equations

$$\theta_0 = \arcsin \sqrt{\left(\frac{\phi_x}{kd_x}\right)^2 + \left(\frac{\phi_y}{kd_y}\right)^2}, \varphi_0 = \arctan\left(\frac{\phi_x d_x}{\phi_y d_y}\right) \quad (4.4)$$

In (4.4), θ_0 is the elevation angle measured off the z -axis, and φ_0 is the azimuth angle of spherical coordinates in antenna patterns, which is measured counter-clockwise off the x -axis. ϕ_x and ϕ_y are the progressive phase differences along the x - and y -axis direction, and their relationship with the feed ports of the designed Butler Matrix has already been tabulated in Table. 4.2. The separations of the antenna elements along the x - and y -axis direction are denoted as d_x and d_y in (4.4). To avoid intersection of the differential power dividers, the separations of the antenna elements are set to $d_x = d_y = 7.5$ mm, which correspond to $\approx 0.7\lambda_0$. k is the wave number in free space. In this proposed multibeam antenna array, 2×2 HP or VP tilted beams can be obtained in 2D space by exciting the feed ports #5–#8 or #1–#4, respectively. From (4.4), the theoretical beam pointing angles of these tilted beams are $(\theta_0, \varphi_0) = (30^\circ, 45^\circ), (30^\circ, 135^\circ), (30^\circ, 225^\circ)$ and $(30^\circ, 315^\circ)$ in the spherical coordinate when port #1 – #4 is excited, respectively.

As the radiation patterns tilt at the specific angles in 2D space by exciting different feed ports, the standard E- and H-plane defined as the vertical plane or horizontal plane cannot simply be applied to the measurement of the radiation patterns of this 2D multibeam antenna array. In view of this, the definitions of quasi E-plane and quasi H-plane given in [235] are introduced in the far field measurement. Fig. 4.26 and Fig. 4.27 present the measured and simulated radiation patterns at three most representative frequencies, 26.8 GHz, 28 GHz and 29.2 GHz. The frequency 28 GHz is the centre operation frequency, and 26.8 GHz and 29.2 GHz are the two edge frequencies of the designed antenna element. As can be seen from these figures, the measured radiation patterns are reasonably agreed

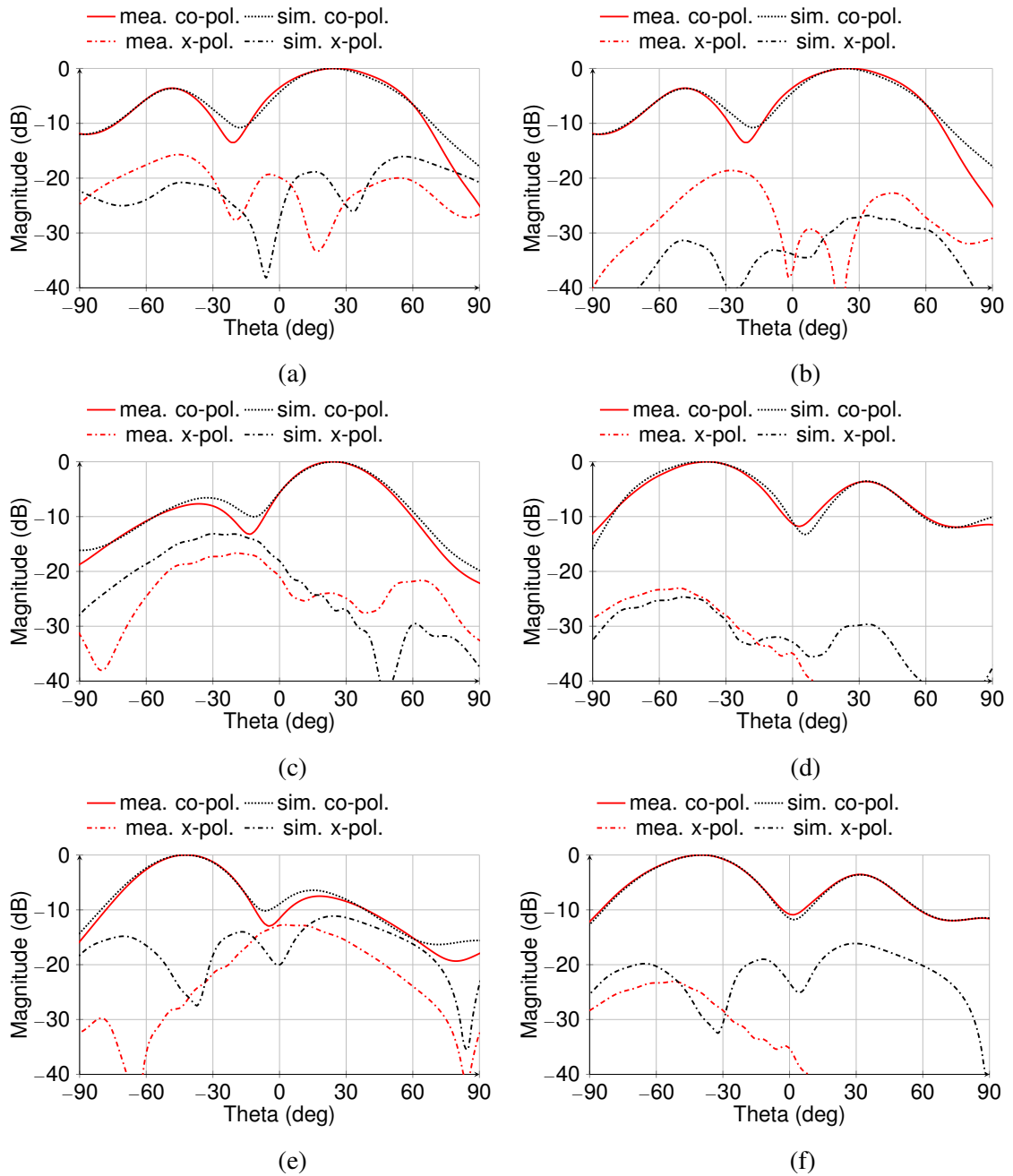


Fig. 4.26 Measured and simulated normalized far field radiation patterns of the proposed differentially fed dual polarized 2D multibeam array antenna with VP when port #1 is excited. (a) 26.8 GHz at quasi E-plane. (b) 28 GHz at quasi E-plane. (c) 29.2 GHz at quasi E-plane. (d) 26.8 GHz at quasi H-plane. (e) 28 GHz at quasi H-plane. (f) 29.2 GHz at quasi H-plane.

with the simulated ones. The co-polarization radiation patterns keep stable at different frequencies when beams scan to the maximum pointing angles. In addition, by comparing Fig. 4.26 and Fig. 4.27, it is also shown that the radiation patterns in the quasi E-plane or quasi H-plane agree well with each other at different frequencies. In addition, it can be obtained from the radiation patterns that the measured beam pointing angle at 28 GHz

is $(28^\circ, 41^\circ)$ when port #1 is excited for VP and the measured beam pointing angle is $(34^\circ, -43^\circ)$ when port #5 is excited for HP. The measured beam pointing angles differ slightly from the theoretical angles $(\pm 30^\circ, \pm 45^\circ)$ calculated from (4.4), as the beam pointing angles of the designed multibeam array antenna are significantly affected by the fabrication tolerance and the existence of the ground plane presented by the multibeam feed networks. When beams scan to the maximum point angles, the SLLs of the co-polarization radiation patterns are about 4 dB less than the main beam level.

4.4.3 XPD and gain

As can be seen from Fig. 4.26 and Fig. 4.27, the cross polarized radiations are maintained at relatively low level when beams scan to the maximum pointing angles. At the centre frequency 28 GHz, the XPDs are higher than 28 dB at the quasi E-plane and quasi H-plane when either port #1 or #5 is excited. To have a better understanding of the XPD performance, the minimum XPDs of the designed 2D multibeam antenna array at different frequencies are summarized in Fig. 4.28. As can be seen from this figure, high XPDs are achieved in the operation bandwidth 26.8–29.2 GHz when beams scan to the maximum pointing angles. Over this operation frequency band, the XPDs are higher than 25.2 dB which is achieved at the edge frequency 26.8 GHz. The XPD is slightly dropped when the antenna array works off the centre frequency. This is mainly because the phase error originated from the interconnection is not completely compensated by the reference SIW off the centre frequency, as shown in Fig. 4.21. Thus, strictly speaking, the antenna elements are not differentially excited at the edge frequencies. However, comparing the XPDs of this multibeam antenna array with the XPDs of the reported works, it can be confirmed that the cross polarized radiation in this multibeam antenna array is significantly contained due to the use of the differential feed structures.

Fig. 4.29 shows the measured and simulated gain and the directivity of the designed 2D multibeam antenna array when the feed port #1 or #5 is excited. The simulated realized gain climbs from 8.4 dBi to 10.8 dBi over the operation frequency bandwidth from 26.8 GHz to 29.2 GHz. The measured realized gain ranges from 7.6 dBi to 10.5 dBi, which is slightly decreased when compared with the simulated one. Over the the frequencies from 26.8 GHz to 29.2 GHz, the simulated directivity increases from 10.5 dBi to 12.1 dBi. Thus, the simulated efficiency of this 2D multibeam antenna array at the centre frequency 28 GHz is approximately 55%. The efficiency degradation is mainly because of the high loss ($\tan \delta \approx 0.0075$ at 28 GHz) laminates Rogers 4003C and the fabrication tolerance. Besides, the loss caused by the connectors are not calibrated in the measurement. When the feed port #5 is under excitation, the simulated and measured gain are very close to the gain when port #1 is excited. The measured gain slightly differs to the simulated one, due to the uncertainty of the dielectric loss of the used substrates at the mmWave frequencies.

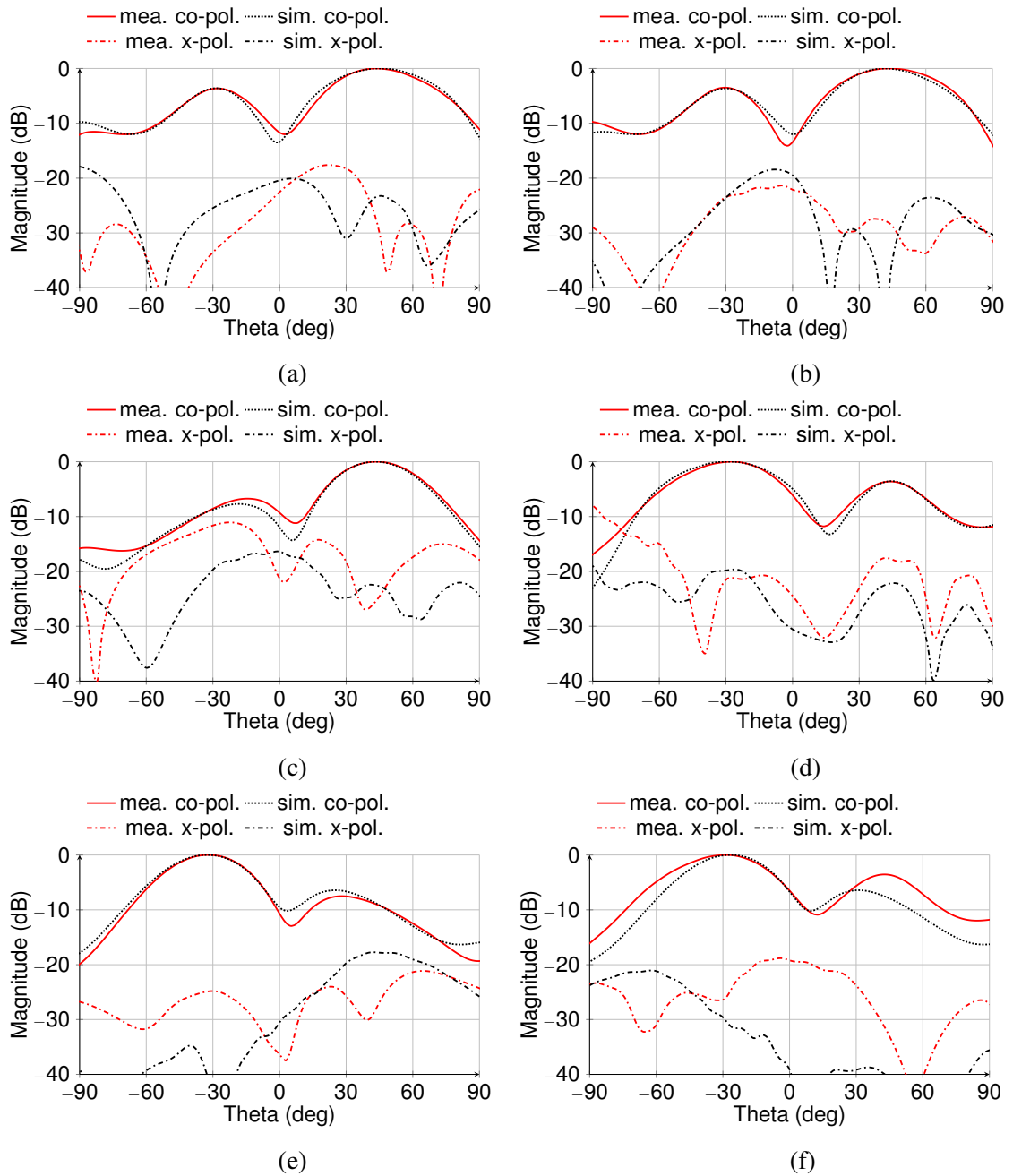


Fig. 4.27 Measured and simulated normalized far field radiation patterns of the proposed differentially fed dual polarized 2D multibeam array antenna with HP when port #5 is excited. (a) 26.8 GHz at quasi E-plane. (b) 28 GHz at quasi E-plane. (c) 29.2 GHz at quasi E-plane. (d) 26.8 GHz at quasi H-plane. (e) 28 GHz at quasi H-plane. (f) 29.2 GHz at quasi H-plane.

4.4.4 Discussion and comparison

Table 4.4 compares the proposed multibeam antenna array with the reported works. By applying magnitude tapering, low SLLs are achieved in the antenna array reported in [102], but this antenna array has very narrow bandwidth and its XPD is lower than 10 dB. The antenna arrays reported in [134], [135], and [137] can operate in a relatively wide

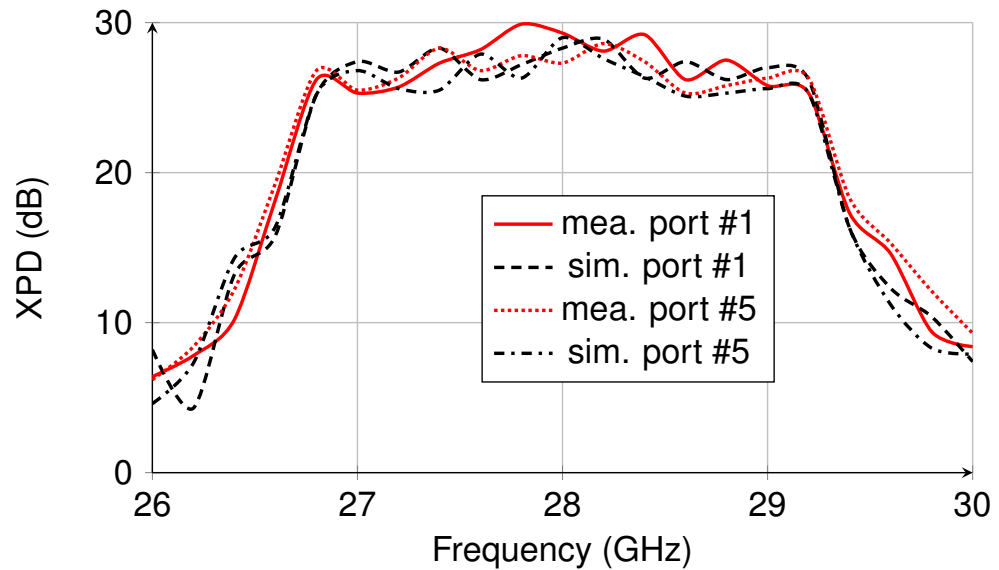


Fig. 4.28 Measured and simulated XPD of the designed 2D multibeam antenna array at the feed port #1 and #5.

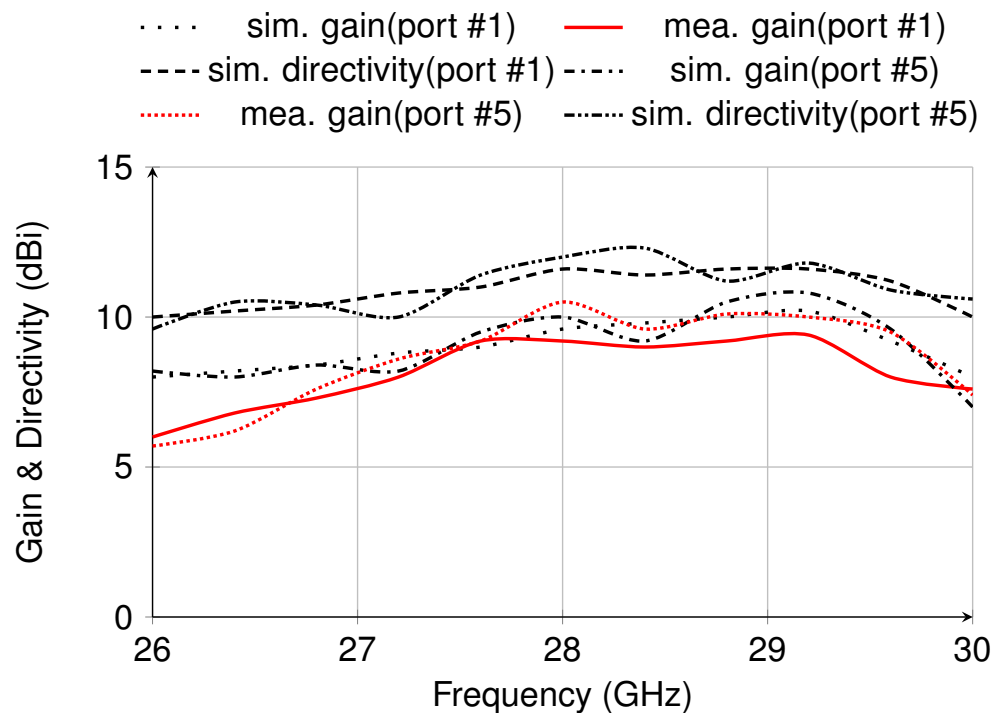


Fig. 4.29 Measured and simulated realized gain, and simulated directivity of the designed 2D multibeam antenna array at the feed port #1 and #5.

bandwidth, but these antennas are only capable of working with a single polarization and they also suffer low XPD not higher than 15 dB. Different from the above reported works, the antenna array presented in [207] can work with dual polarization in a wide bandwidth. Despite that, this antenna array also has very low XPD, which is less than 10 dB when beams scan to the maximum pointing angles. In contrast, this proposed 2D multibeam

Table 4.4 Comparison between this multibeam array antenna and the reported works

Ref.	Ant. Type	Pol.	XPD	B	h/λ	Layers	Spacing	SLL
[102]	slot	single	10dB	3.61%	0.07	3	n.a.	-13dB
[134]	patch	single	10dB	16.73%	n.a.	2	$0.5\lambda_0 \times 0.6\lambda_0$	-5dB
[135]	cavity-backed patch	single	15dB	36.2%	0.25	4	$0.6\lambda_0 \times 0.6\lambda_0$	-4dB
[137]	ME-dipole	single	12dB	16.42%	0.23	4	$0.6\lambda_0 \times 0.6\lambda_0$	-6dB
[207]	ME-dipole	dual	10dB	22.13%	0.21	3	$0.6\lambda_0 \times 0.6\lambda_0$	-7dB
This work	cavity-backed shorted patch	dual	28 dB	8.64%	0.09	2	$0.7\lambda_0 \times 0.7\lambda_0$	-4dB

antenna array can not only operate with dual polarization, but also achieve high XPD with beams scanning to the maximum pointing angles due to differential feed applied to each antenna element. Besides, the proposed dual polarized 2D multibeam antenna array can be physically implemented with only two laminates, since the multibeam network for exciting VP is realized with the 2×2 antenna array on the top laminate layer. Thus, the designed antenna array also offers benefits in terms of ease of fabrication and reduced cost.

The proposed antenna array is realized with very thin substrates, which has a thickness of 0.09λ (λ is the wavelength in the substrate). Thus, the proposed antenna array does not operate in a wide bandwidth when compare it with the antenna arrays reported in [134], [135], [137] and [207]. However, the operation bandwidth can be enhanced by thickening the substrates or using the substrates with lower dielectric constant, just as the reported works in [134], [135], [137] and [207]. Because the element spacing of the antenna array is set to $0.7\lambda_0$ along the x - and y -axis direction, the SLL of the proposed multibeam antenna array is deteriorated, which is about -4 dB when beams scan to the maximum pointing angles. This side effect can be eased by reducing the element separation or tuning the excitation if low SLL is required in some specific applications.

4.5 Summary

In this chapter, a new architecture of differentially fed dual polarized 2D multibeam antenna array was developed for the purpose of achieving compact size and high XPD when beams scan to the maximum pointing angles. Based on the concept depicted in the new architecture, a differentially fed dual polarized 2D multibeam antenna array was proposed and designed. At first, to implement differential feed to the multibeam antenna array, a differentially fed dual polarized cavity backed shorted patch antenna was developed as the antenna element. It was strictly analysed by using the Huygens' principle and the theory of the cavity mode method. To illustrate the design process of the proposed antenna element, two reference antennas were designed, analysed and compared with

the proposed one. It was shown that the proposed antenna element had an overlapped impedance bandwidth from 26.8 GHz to 29.2 GHz, XPD higher than 70 dB and realized gain ranging 6.2–7 dBi over the bandwidth. Then, the entire configuration of the proposed differentially fed dual polarized 2D multibeam antenna array was presented and followed by the design details of the essential components such as the Butler Matrix, the differential power divider, and the interconnection structures. Finally, the prototype of the differentially fed dual polarized 2D multibeam antenna array was fabricated and measured. The overall structure of this multibeam antenna array was physically realized with only two laminates by using low cost PCB processing technology. The measured results, which include the *S*-parameters, radiation patterns, XPD and realized gain, were well agreed with the simulated ones. The measured XPDs of this multibeam antenna array are higher than 25 dB over the operation frequency bandwidth 26.8–29.2 GHz. It is confirmed that the cross polarized radiation in this multibeam antenna array is significantly contained when beams scan to the maximum pointing angles, due to the use of the differential feed structures. A comparison between the proposed 2D multibeam antenna array and the reported works were carried out. It was concluded that the proposed 2D multibeam antenna array features in dual polarization capability, high XPDs, low profile, simple structure and low cost.

Chapter 5

Frequency-Scanning Dual Polarized Cross Slot Antenna Array

Frequency-controlled beam-scanning antenna array has been widely used in modern communication systems. The beam scanning is achieved by varying the frequency of the signal source and without any additional phase shifter. It has very low cost when compare it with the active electronically scanned array. In traditional frequency-controlled beam-scanning antennas, small beam scanning range must be realized in a large frequency bandwidth [236]. In addition, most of them cannot operate with dual polarization and be realized on a single laminate with simple configuration. In this chapter, a dual polarized frequency-scanning antenna array is developed. To avoid congestion of the feed networks, the crossover structure is introduced, which is realized by placing four metallized vias around the junction of two perpendicular SIWs. The design procedure and working principle of the antenna array are detailed. The designed antenna array is prototyped and measured. Compared with other reported frequency-scanning antenna arrays, the proposed one exhibits high XPD, high gain, high aperture efficiency, wide frequency-scanning range and low complexity.

5.1 Architecture of antenna array

Fig. 5.1 shows the concept architecture of the proposed dual polarized antenna array realized on a single laminate layer. As can be seen from this figure, the antenna array is composed of $m \times m$ dual polarized antenna elements. The coordinate (i, j) represents the antenna element in the i th row (x -axis direction) and the j th column (y -axis direction). It should be noted that the antenna elements in each row or column are serially connected. They are corporately fed at the terminal ports, Feed-1 to Feed-4. Between two orthogonal ports of the antenna elements, the coupling is reduced to a low level, which leads to low cross polarization level. Feed-1 and Feed-2 are the feed ports for exciting HP radiation beams, and Feed-3 and Feed-4 are used for exciting VP radiation beams. The radiation

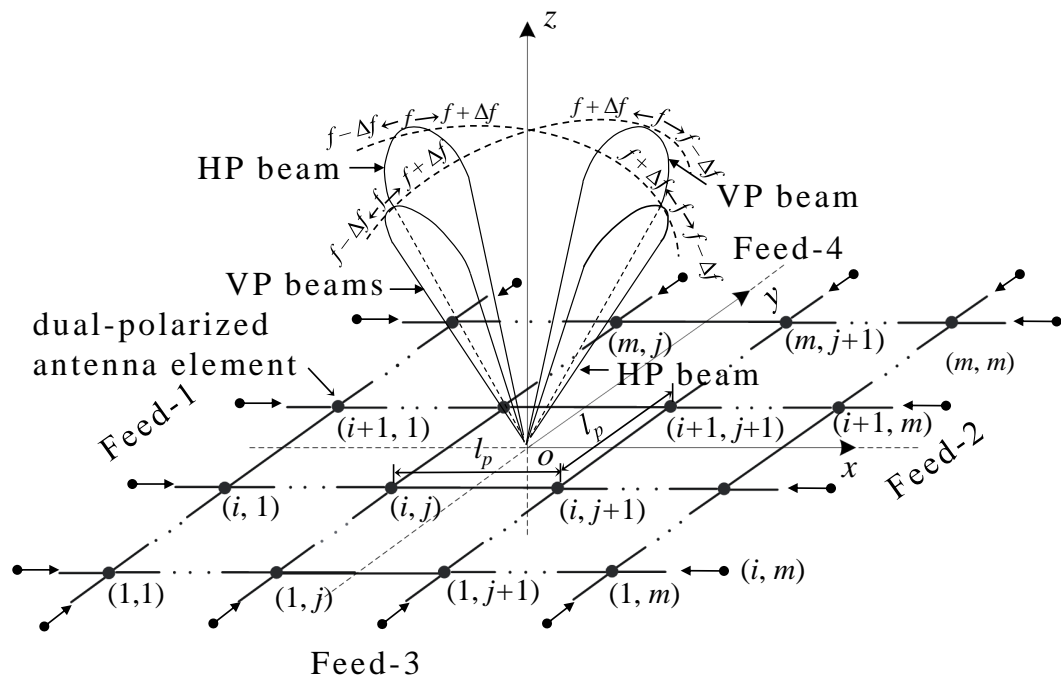


Fig. 5.1 Concept diagram of the dual polarized antenna array designed on a single laminate.

beams of this antenna array is frequency dependent. By imposing excitation to any feed port, a series of backward scanning beams varying with frequencies can be obtained.

5.2 Configuration of antenna array

To have a better understanding of this design, the overall structure of the designed antenna array is firstly presented in this section. Fig. 5.2 shows the configuration of the designed dual polarized antenna array. In this design, Rogers RT/duroid 5880 laminate with a thickness of 0.508 mm, a relative dielectric constant of 2.2 and loss tangent of 0.0009 is used. The developed array antenna can be considered as a combination of three parts including the antenna array aperture, the ten-way power dividers and the SIW-to-GCPW (grounded co-planar waveguide) transitions. For the antenna array aperture, it is composed of 10×10 dual polarized antenna elements. The proposed antenna array can be regarded as ten parallel serially-fed antenna arrays being placed perpendicularly to another ten linear antenna arrays. These parallel linear antenna arrays are then combined by the ten-way equal power dividers and are fed through the SIW-to-GCPW transition located at different positions. Thanks to high isolation between the orthogonal ports of each antenna element, it can be considered that virtual electric walls are placed between the linear antenna arrays. The electromagnetic waves in each linear antenna array can travel and radiate along their paths without crosstalk from other linear antenna arrays. This unique feature enables this array antenna being realized on a single laminate. HP radiations are realized by exciting

port #1 or #2, and VP radiations can be obtained by exciting port #3 or #4. The difference between port #1 and #2 excitations (or port #3 and #4) lies in the direction of radiation beams in the coordinate system. In this design, backward radiations relative to the direction of the wave travelling inside the antenna array are obtained with different port excitations, which have been illustrated in Fig. 5.1.

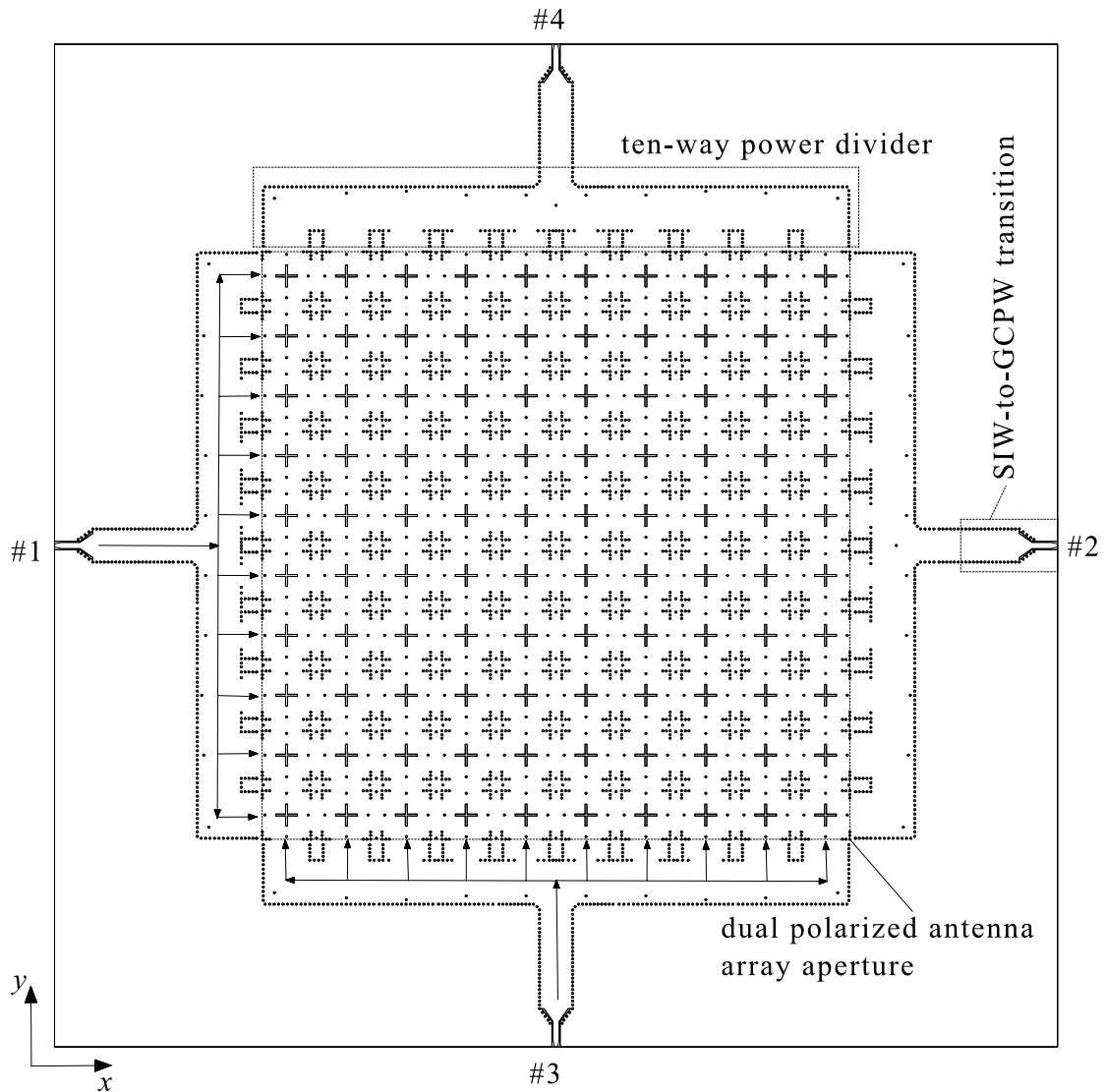


Fig. 5.2 Illustration of the radiation principle of a serially fed linear antenna array.

As can be seen from Fig. 5.2, the antenna element number of the linear antenna arrays in each row or column is set to $m = 10$. It is assumed that the radiated power P_{rad} from each linear antenna array is $0.95P_0$ where P_0 is the total power injected to the linear antenna array. For convenience of analysis, the radiation efficiency of an antenna element in the linear antenna array is assumed to be η . Fig. 5.3 illustrates the radiation principle of a serially fed linear antenna array. As can be seen from this figure, the radiated power P_{i_rad}

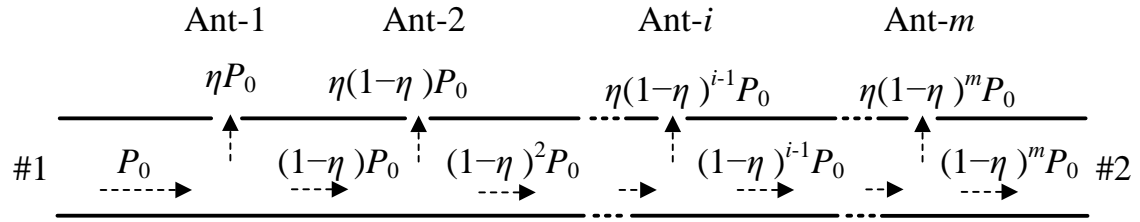


Fig. 5.3 Illustration of the radiation principle of a serially fed linear antenna array.

($i = 1, 2, \dots, m$) of the i th antenna element of the linear antenna array can be written as

$$P_{i_rad} = \eta(1 - \eta)^{i-1} P_0 \quad (5.1)$$

The total radiated power is the summation of radiated power from the antenna elements, which can be expressed as

$$P_{rad} = \sum_{i=1}^n P_{i_rad} = \sum_{i=1}^n \eta(1 - \eta)^{i-1} P_0 = 0.95P_0 \quad (5.2)$$

The desired radiation efficiency of the antenna elements in the linear antenna array can be obtained by solving (5.2), which is approximately 26%. In this design, each dual polarized antenna element can be considered as a five-port network because it is excited from two orthogonal directions. Based on this fact, the radiation efficiency of the antenna element can be obtained from the S -parameters of the corresponding four-port network, which is given by the following equation

$$\eta = \frac{1 - |S_{11}|^2 - |S_{21}|^2 - |S_{31}|^2 - |S_{41}|^2}{1 - |S_{11}|^2} \times 100\% \quad (5.3)$$

In (5.3), the ohmic loss from the absorption by the metals is not considered since it is small and negligible. However, it should be noted that the dielectric loss of the antenna element is included in this equation. This is because the S -parameters of the antenna element obtained from full-wave simulation include the dielectric loss from the used laminate Rogers RT/duroid 5880.

5.3 Dual-polarized cross slot antenna and antenna array design

In this section, the configuration and working mechanism of the dual polarized antenna element used in designing the antenna array of Fig. 5.2 will be presented. The design

of this dual polarized antenna is based on a crossover structure realized by placing four metallized posts around the junction of two perpendicular SIWs. To facilitate the analysis, the evolution process from two perpendicular SIWs to the designed antenna will be also detailed in this section. Followed by the antenna element design, two adjoint subarray antennas are illustrated to exemplify the antenna element performance. The designs of ten-way power divider and SIW-to-GCPW transition are also included in this section for the purpose of integrity.

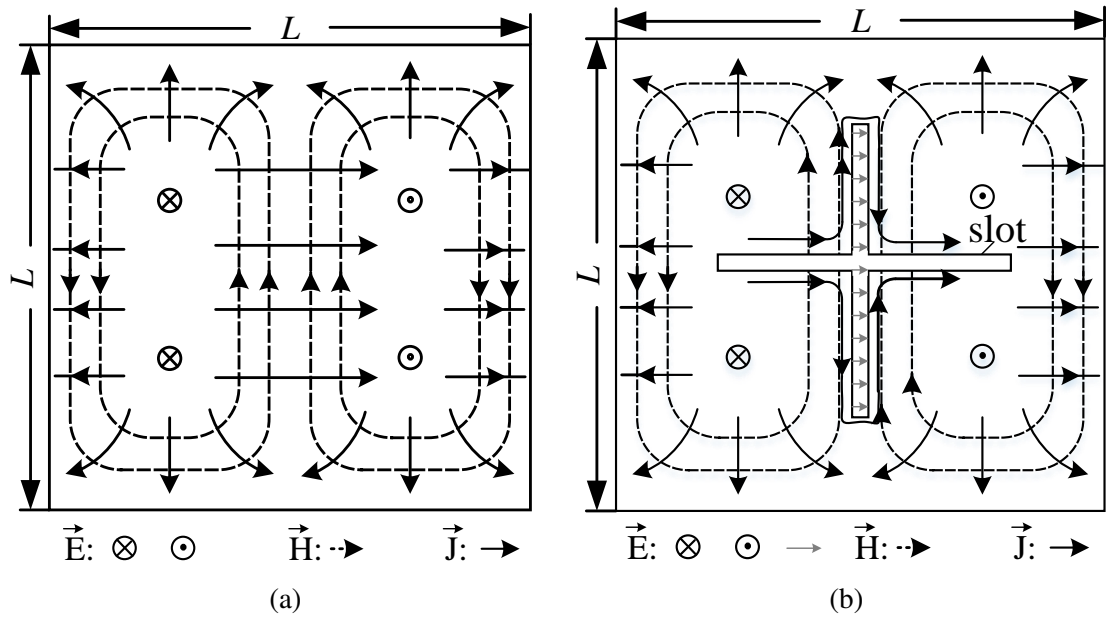


Fig. 5.4 Field distribution of (a) conventional square SIW cavity and (b) cross slot antenna designed by using the conventional square SIW cavity.

5.3.1 Configuration of antenna element

To realize dual polarization, the designed antenna element is developed by using a cavity that supports TE_{120} and TE_{210} modes. Fig. 5.4(a) and (b) show the layout and field patterns of a conventional square TE_{120} and TE_{210} mode cavity and a cross slot antenna designed by using this cavity, respectively. The physical dimension L of an SIW cavity supporting TE_{mn0} mode can be obtained from

$$f_{mn0} = \frac{c_0}{2\sqrt{\epsilon_r}} \sqrt{\frac{m^2 + n^2}{(L - d^2/0.95s)^2}} \quad (5.4)$$

where f_{mn0} is the resonance frequency excited in this cavity; c_0 is the velocity of electromagnetic wave in free space; ϵ_r is the relative permittivity of the filled dielectric material; m and n are the mode indexes; d is the diameter of metallized vias and s is the separation between the adjacent metallized vias. In the case shown from Fig. 5.4(b), the cross

slot etched over the square cavity can radiate HP beam. Generally speaking, the feed structures that can be used to feed the cavity-backed slot antenna are roughly divided into three categories: probes [237, 238], inset microstrip lines [239, 240] and slot apertures [241, 242]. However, the probe-fed cavity-backed antennas are complicated in structure and are difficult to be integrated with the feed networks. As to the cavity-backed antennas fed by inset microstrips, they suffer high insertion loss and severe parasitic radiation at high frequency bands. For the slot coupled cavity-backed slot antennas, they must be realized with at least two laminates. In view of these facts, it would be more beneficial to designing a cavity-backed slot antenna with a closed-form feed structure, such as SIWs or rectangular waveguides.

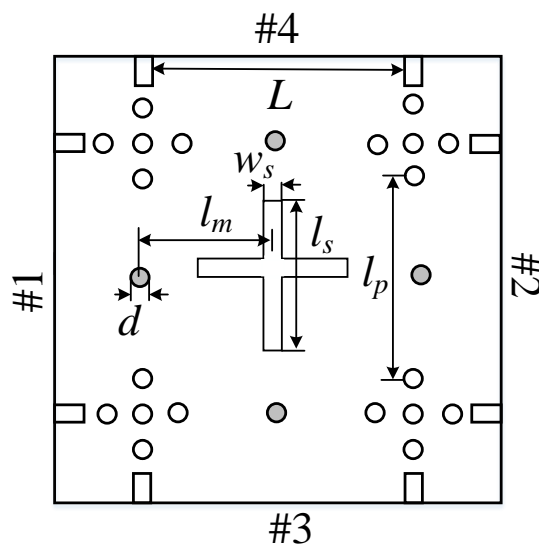


Fig. 5.5 Configuration of the proposed dual polarized cavity-backed cross slot antenna element.

Table 5.1 Dimensions of the designed dual polarized cavity-backed cross slot antenna: mm

L	d	l_m	l_s	w_s	l_p
7.00	0.30	3.48	3.00	0.30	5.00

Fig. 5.5 shows the configuration of the designed dual polarized cavity-backed cross slot antenna element. The cavity used in designing this antenna element differs from the conventional TE_{120} and TE_{210} mode cavity shown in Fig. 5.4. It is designed by placing four metallized vias around the cross junction of two perpendicular SIWs. The position l_m and the size d of the four metallized vias can be tuned to achieve high return loss and improved port isolation. The proposed structure can be considered as a planar SIW crossover in which the orthogonal channels are isolated to each other. In this design, the synthesized size of the cavity are smaller than the cavity size derived from (5.4). This is mainly because the cavity used in this design is not completely enclosed, resulting in

its equivalent cavity size larger than the cavity size calculated from (5.4). The cross slot, located at the centre, is etched over the cavity to enable dual polarization radiation. The antenna element can work with HP when port #1 or #2 is under excitation. In this case, ports #3 and #4 are well isolated. VP is realized by exciting port #3 or #4, in which case ports #1 and #2 are isolated.

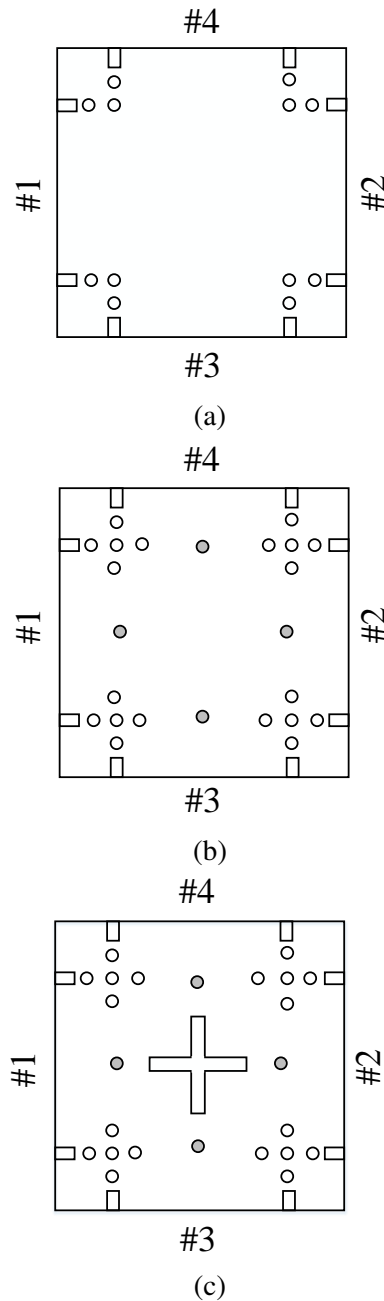


Fig. 5.6 Evolution process toward the developed dual polarized cavity-backed cross slot antenna element. (a) Two perpendicular SIWs. (b) Proposed SIW cavity supporting TE_{120} and TE_{210} modes. (c) Proposed dual polarized cross slot antenna.

5.3.2 Design procedure

The designed dual polarized cavity-backed cross slot antenna element is evolved from two SIWs placed perpendicularly with each other. As shown in Fig. 5.6(a), the cross junction formed by the two SIWs can be regarded as a cavity with four metallized vias located at its corners. However, it is observed from Fig. 5.7 that this structure suffers very low isolation between port #1 and #3 which is less than 10 dB over the frequency bandwidth from 24 GHz to 26 GHz. In order to improve the port isolation, an SIW cavity that supports TE_{120} and TE_{210} modes is constructed by placing four metallized vias around the junction of the crossed SIWs, as shown in Fig. 5.6(b). The port isolation can be also improved by changing the window width l_p in a certain degree. The dominant modes of the cavity is determined by the cavity size, which is evaluated from (5.4). In this cavity, the return loss and port isolation can be significantly improved. As seen from Fig. 5.7, the isolation between ports #1 and #3 is decreased to higher than 26 dB over the entire frequency bandwidth 24–26 GHz. Based on these facts, the proposed dual polarized antenna is realized by etching a cross slot over the cavity, which is shown in Fig. 5.6(c). Compared with the port isolation in the proposed TE_{120} and TE_{210} mode cavity, the port isolation in the propose antenna can be maintained at the same level (higher than 26 dB) from 24 GHz to 26 GHz. In addition, dual polarization is achieved in the proposed cavity-backed cross slot antenna by exciting it from the orthogonal ports.

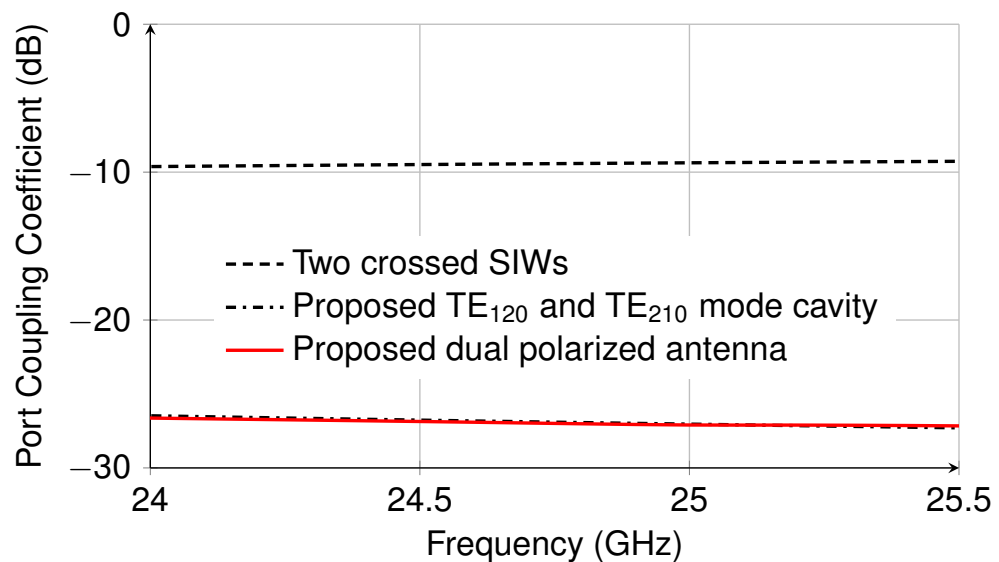


Fig. 5.7 Simulated coupling coefficients between port #1 and #3 in different structures shown in Fig. 5.6.

In this proposed dual polarized antenna, high port isolation is realized due to the orthogonality between the TE_{120} and TE_{210} modes inside the SIW cavity. In order to have a better understanding of the working mechanism of this antenna, the field and current distributions of the three structures are investigated, which are shown in Fig. 5.8. As can

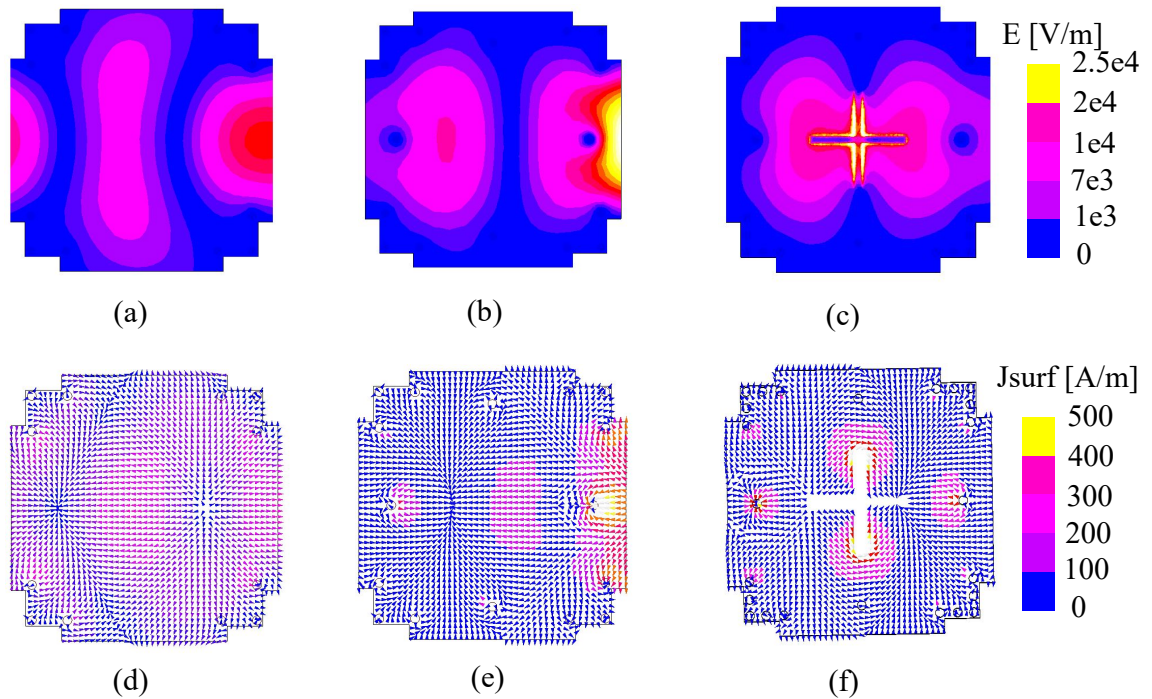


Fig. 5.8 Magnetic field inside the cylindrical cavities of the designed dual-polarized subarray antenna.

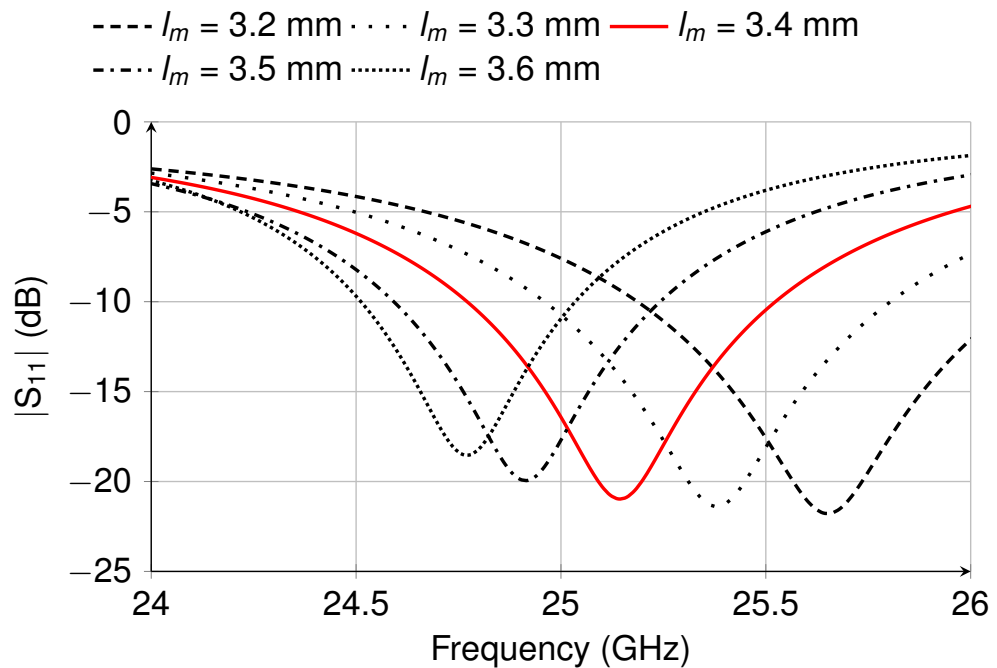


Fig. 5.9 Simulated reflection coefficients at port #1 of the proposed dual polarized antenna with different position l_m of the metallized vias.

be seen from Fig. 5.8(a), the electric field is observed at ports #3 and #4 when port #1 is excited. This is because no structures are designed to constrain the field behaviour at the junction of the cross SIWs, resulting in strong coupling between ports #1 and #3 or #4.

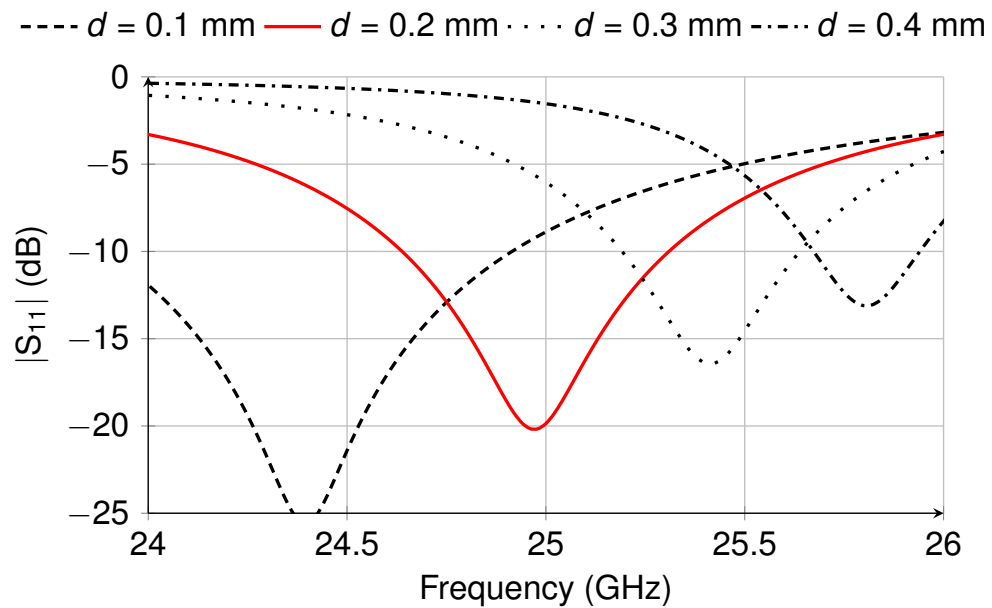


Fig. 5.10 Simulated reflection coefficients at port #1 of the proposed dual polarized antenna with different size d of the metallized vias.

By placing the metallized vias around the junction to shape a cavity supporting TE_{120} and TE_{210} modes, most of electric field is restrained to propagate along the horizontal direction, as illustrated in Fig. 5.8(b). However, it should be noted that the TE_{210} mode field inside the junction are not odd symmetric with respect to the centre line of the structure. This will spoil the polarization purity if the antenna is realized with this structure. To address this problem, it is necessary to introduce additional perturbation into the cavity. In this proposed antenna, the cross slot acts as not only a dual polarized radiator but also a perturbation used to improve the symmetry of the modes inside the cavity. Fig. 5.8 shows the rectified TE_{210} mode field inside the cavity. It is seen that the TE_{210} mode electric fields beside the centre line along the y -axis are equal in magnitude but opposite in phase. The electromagnetic waves are well restrained to propagate and radiate along the horizontal direction. With port #1 or #2 excited, the transverse slot can be excited to radiate HP waves since the electric fields on both sides of the transverse slot are out-of-phase. Besides, as illustrated in Fig. 5.8(c) and (f), almost no field is distributed at ports #3 and #4. This demonstrates that high port isolation is achieved in this proposed antenna.

In the proposed dual polarized cavity-backed cross slot antenna, the position l_m and size d of the four metallized vias introduced in this design have an effect on the resonance frequency and port isolation of the antenna. Fig. 5.9 and Fig. 5.10 illustrate the simulated reflection coefficients at port #1 with different l_m and d . The resonance frequency of this antenna moves to the lower frequency band by increasing l_m , as shown in Fig. 5.9. This is because the effective size of the TE_{120} and TE_{210} mode cavity is enlarged. At the resonance frequencies, the small variation of the reflection coefficients at port #1 with different l_m shows that the location of the four metallized vias mainly affect the resonant

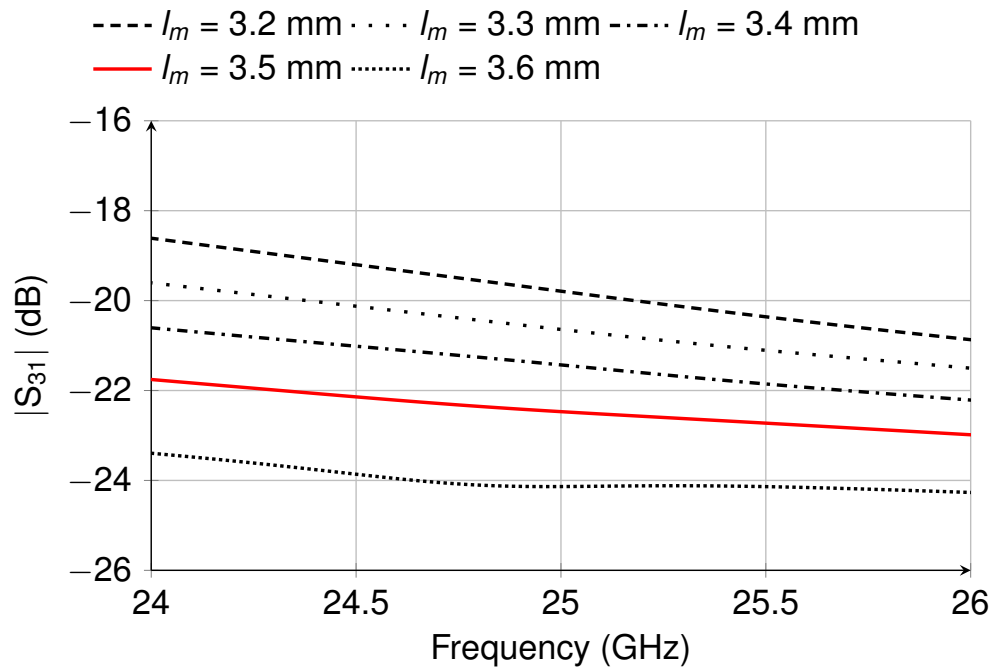


Fig. 5.11 Simulated port coupling coefficients of the proposed dual polarized antenna with different position l_m of the metallized vias.

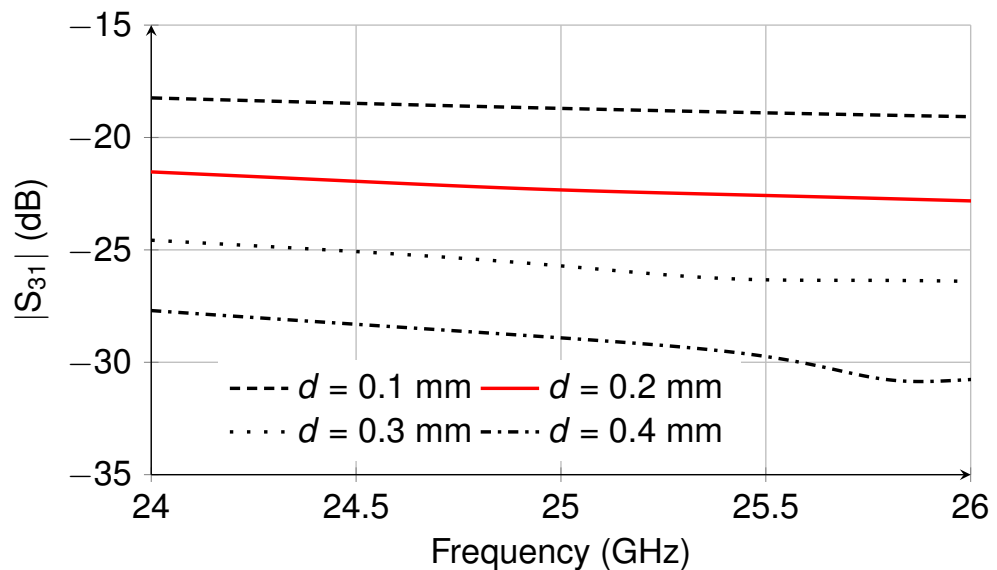


Fig. 5.12 Simulated port coupling coefficients of the proposed dual polarized antenna with different size d of the metallized vias.

frequency while the return loss at the resonance frequency remains stable. From Fig. 5.10, it is seen that the resonance frequency and the return loss at the resonance frequency are significantly affected by the size of the metallized vias. The resonance frequency of the proposed antenna shifts to the higher frequency band by increasing the size of the metallized vias, and the return loss at these resonant frequencies is decreased significantly when the size of the metallized vias is increased.

Besides, the position and size of the metallized vias also affect the port isolation of the designed antenna. As shown in Fig. 5.11, the isolation between ports #1 and #3 increases with l_m . From Fig. 5.12, it is seen that the port isolation is decreased by enlarging the metallized vias. The desired radiation efficiency of this proposed antenna can be obtained by varying the slot width w_s . As can be seen from Fig. 5.13, with the increase of w_s , the peak radiation efficiency is increased and its centre frequency moves toward the lower frequency band.

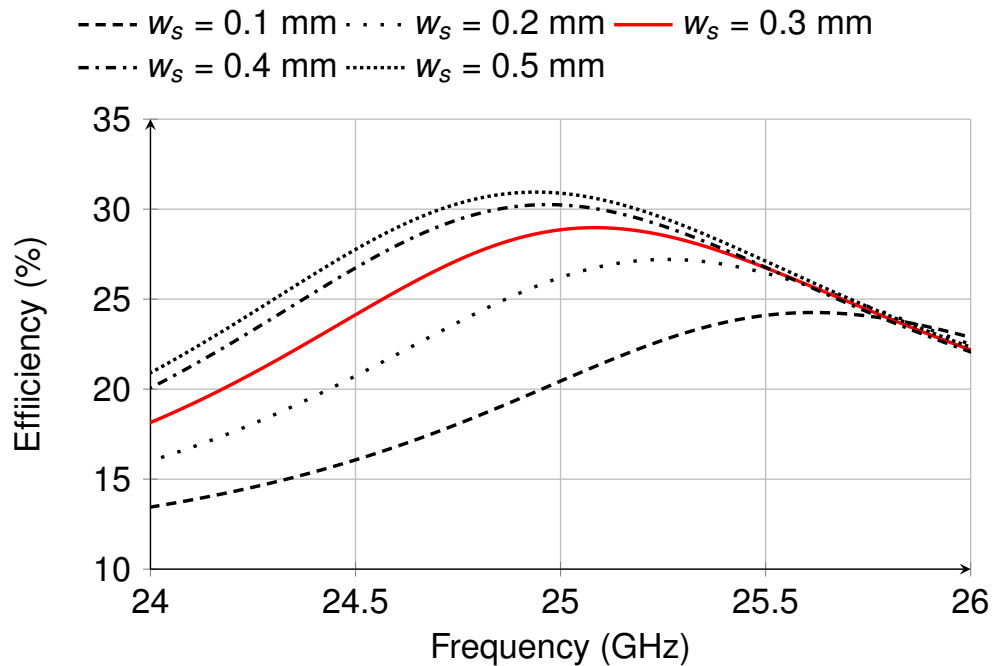


Fig. 5.13 Radiation efficiency of the designed dual polarized cavity-backed cross slot antenna with different slot width w_s .

5.3.3 Performance of antenna element

The performance of the dual polarized antenna element is optimized by varying the design parameters l_m , d and w_s , l_s and l_p . The optimized dimensions are given in Table 5.1. Fig. 5.14 shows the simulated S -parameters and radiation efficiency of the proposed antenna. It is seen that the proposed design can achieve high return loss and good port isolation at the same time. The impedance bandwidth for $|S_{11}|$ less than -10 dB is 700 MHz, 24.6 GHz to 25.3 GHz. The isolation between ports #1 and #3 is higher than 22 dB. The peak radiation efficiency at the centre frequency is 26.3%, which is very close to the desired value calculated from (5.2). Fig. 5.15 presents the simulated radiation patterns of the designed antenna at the centre frequency 25 GHz. Symmetrically unidirectional patterns are obtained in both the E- and H-plane. High XPD is achieved, which is higher than 40 dB. This indicates that good dual polarized radiation is realized in the developed antenna element.

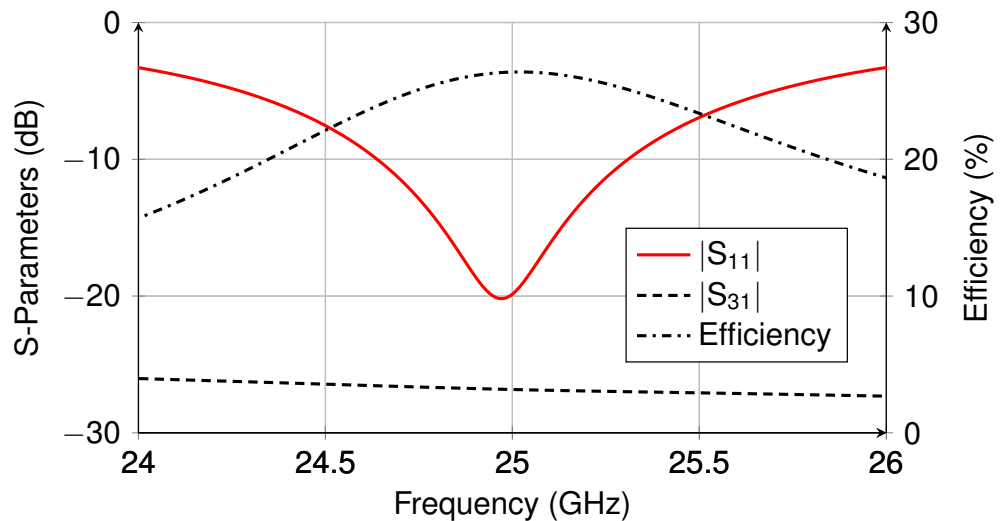


Fig. 5.14 Simulated S -parameters and radiation efficiency of the designed dual polarized antenna.

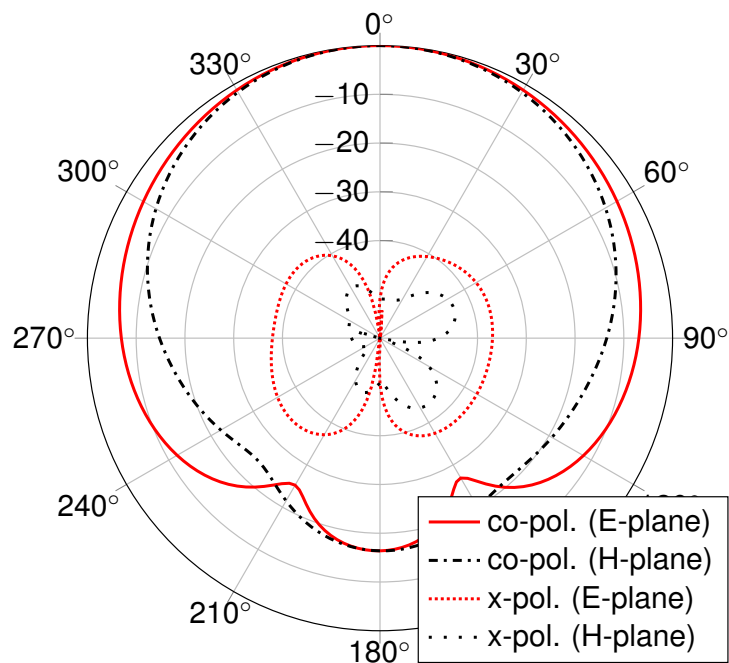


Fig. 5.15 Simulated normalized radiation patterns of the designed dual polarized antenna.

5.3.4 Subarray antenna

Based on the developed dual polarized antenna element, a subarray composed of two linear arrays is investigated, as shown in Fig. 5.16(a). The separations between the adjacent antenna elements in the x - and y -axis direction are 9.4 mm which corresponds $0.78\lambda_0$ at the centre frequency 25 GHz. In this subarray, ports #1 and #2 are excited simultaneously with equal amplitude and same phase. Ports #A1 – #A10 and ports #B1 – #B10 are the ports connected to the subsequent linear arrays. In the simulation, all these ports together

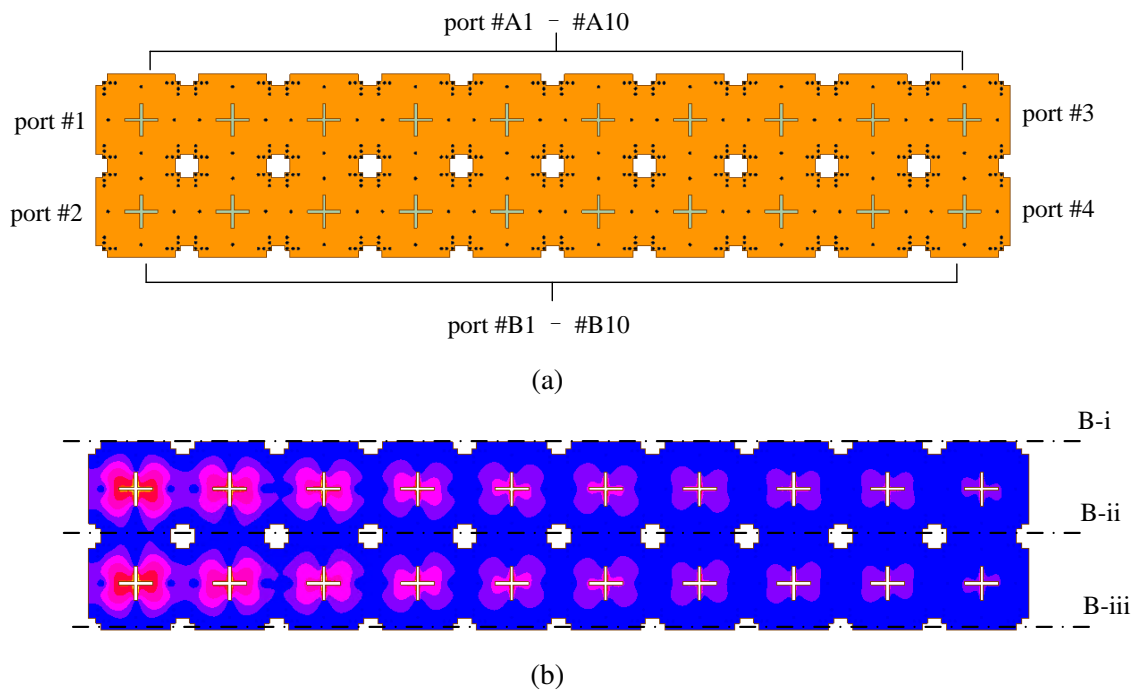


Fig. 5.16 Subarray composed of two linear antenna arrays. (a) Configuration. (b) Field distribution with port #1 and #2 excited simultaneously.

with ports #3 and #4 are terminated with a matched load. Fig. 5.16(b) shows the simulated electric field distribution of the subarray at 25 GHz. It is observed that the field strength is reduced to a low level at Boundary B-i to B-iii, indicating that the waves in the two linear arrays are bounded by three virtual electric walls. The signals can independently travel along the two linear arrays without interference. The electric field is gradually radiated and decayed along each linear antenna array. Similar field distribution can be obtained when excitation is imposed from the vertical ports. Hence, the designed planar antenna array consisting of the proposed dual polarized antenna element can be driven from orthogonal directions to realize dual polarization on a single laminate board.

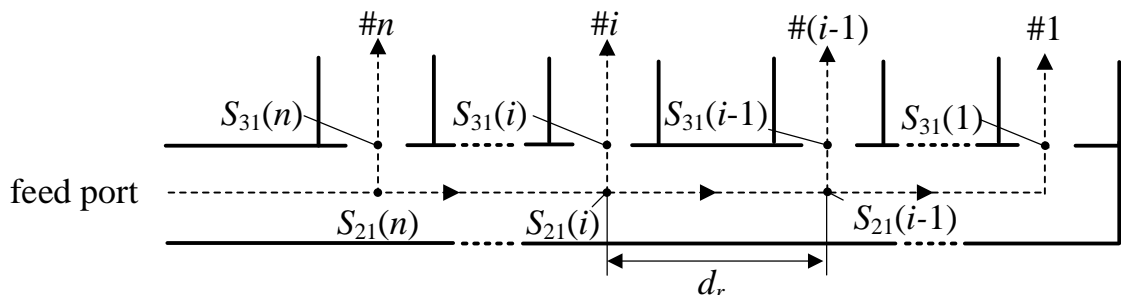


Fig. 5.17 Diagram of half a power divider.

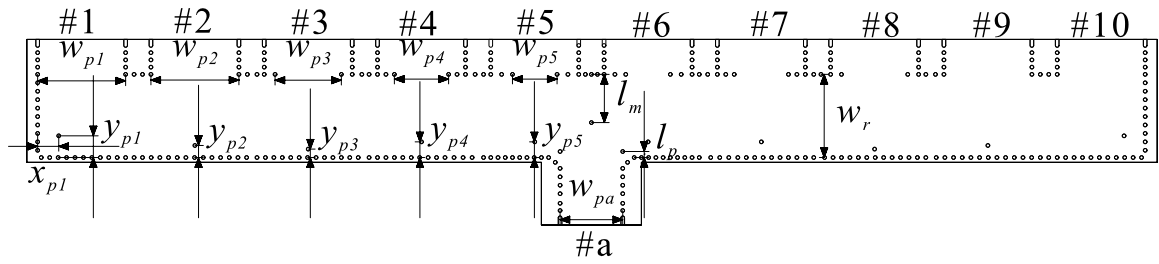


Fig. 5.18 Layout of the designed ten-way power divider.

5.3.5 Ten-way power divider

As can be seen from Fig. 5.2, the ten-way power dividers are used to excite the dual polarized antenna array aperture uniformly. Fig. 5.17 shows the diagram of half a power divider. The desired power at the output port $\#i$ ($i = 1, 2, \dots, n$) is also known as the coupling factor η , which can be obtained from $|S_{31}|^2$. In order to make sure the signals output from ports $\#i$ and $\#(i-1)$ have the same phase, $\angle S_{31}$ and $\angle S_{21}$ should satisfy the following derivation [243]

$$\angle S_{31}(i) = \angle S_{21}(i) - \frac{360^\circ d_r}{\lambda_g} + \angle S_{31}(i-1) + 360^\circ \quad (5.5)$$

In (5.5), d_r is the spacing between the adjacent output ports, which equals to the separation of the antenna elements of the antenna array. Therefore, once $\angle S_{31}(1)$ is given, the desired $\angle S_{31}(k)$ of all the output ports can be obtained. The preliminary simulation shows that the value of $\angle S_{31}(1)$ is 74.4° . Based on that, a model of ten-way power divider is constructed, which is shown in Fig. 5.18. By varying the positions y_{p1} to y_{p5} of the inserted vias and the width w_{p1} to w_{p5} of coupling windows, the signals with the same magnitude and phase can be obtained at the output ports $\#1$ to $\#10$.

Table 5.2 Dimensions of the designed ten-way power divider: mm

w_{p1}	w_{p2}	w_{p3}	w_{p4}	w_{p5}	x_{p1}	y_{p1}
7.30	7.30	5.50	4.50	3.70	1.75	1.80
y_{p2}	y_{p3}	y_{p4}	y_{p5}	l_p	l_m	w_{pa}
1.00	0.70	1.30	1.30	0.50	4.00	5.20

Fig. 5.19 shows the simulated coupling factor from port $\#a$ to ports $\#1$ – $\#5$. At the output ports, the coupling factors at the centre frequency 25 GHz are in the range from 8.9% to 10.9%, which are very close to the theoretical value 10%. Fig. 5.20 shows the phase differences between any two adjacent output ports. It is seen that the phase differences between these ports are in the range from -1° to 7° . Based on these simulated results, it can be concluded that the linear antenna arrays of the planar antenna array are excited with

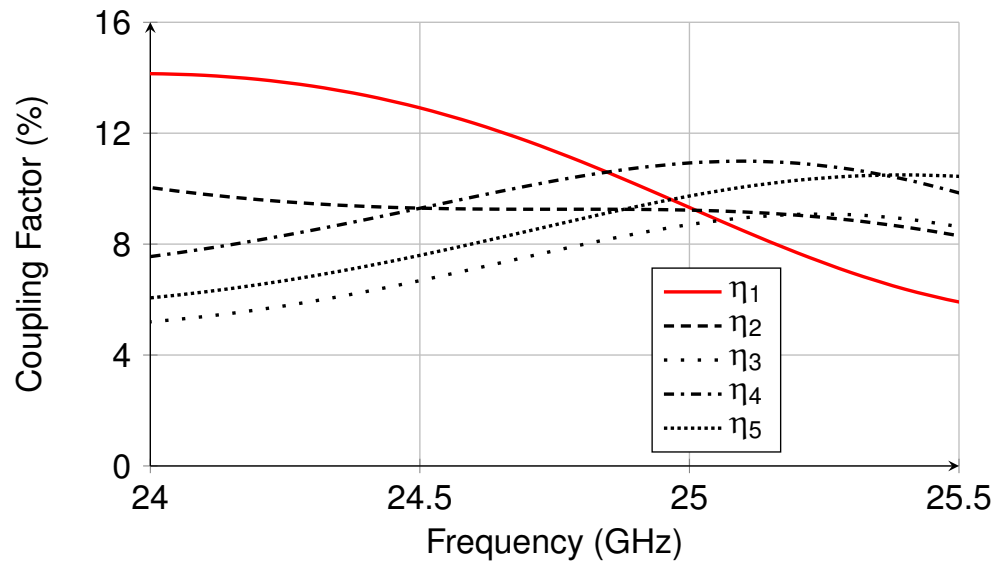


Fig. 5.19 Simulated coupling factors at output ports #1 to #5 of the ten way power divider.

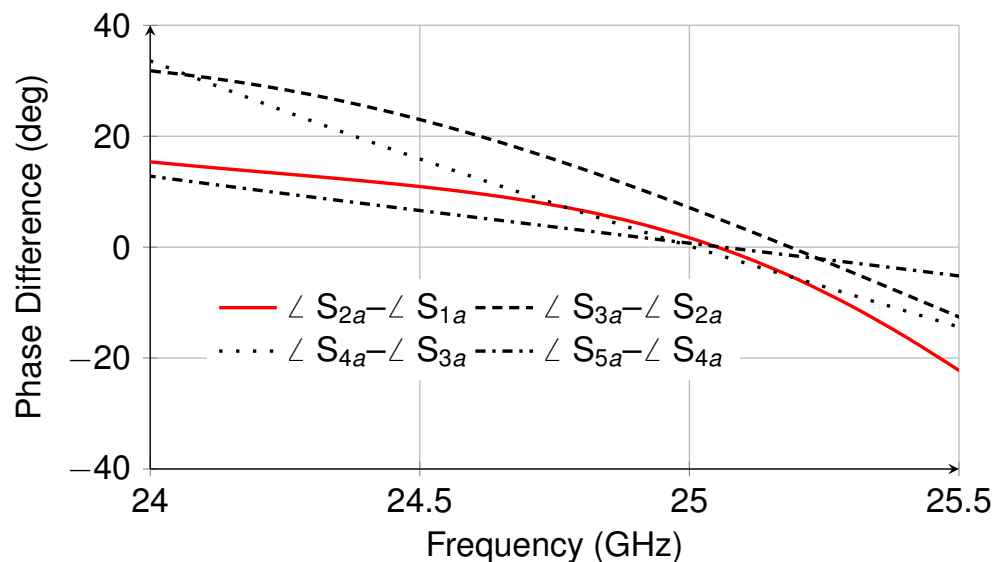


Fig. 5.20 Simulated phase differences between the adjacent output ports of the designed ten-way power divider.

the same magnitude and phase near the centre frequency. Due to the dispersion property of SIWs, the designed ten-way power divider can achieve equal magnitude and same phase output within a relatively narrow bandwidth.

5.3.6 SIW-to-GCPW transition

As well known, the feed pin of a connector used in sub-mmWave and mmWave applications is usually very small. Even though the SIW-to-microstrip transition has been widely used in designing a wide range of passive components and antennas due to its wide operation

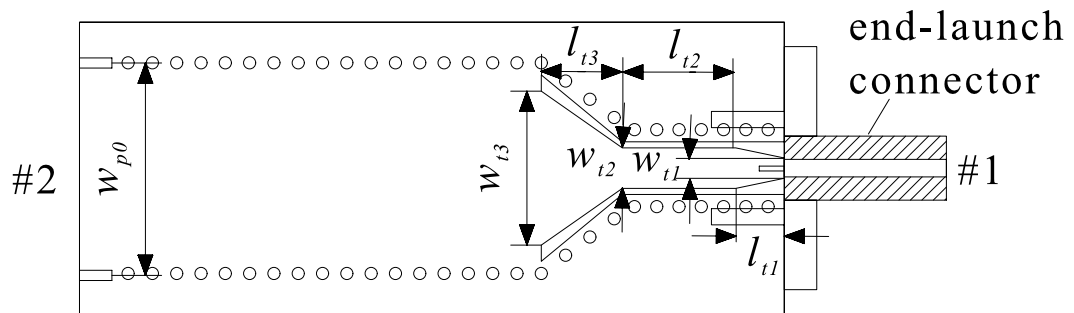


Fig. 5.21 Layout of the designed SIW-to-GCPW transition.

bandwidth, simple structure and ease of fabrication, it cannot be simply applied in some sub-mmWave and mmWave application because of excessively wide microstrip when the laminate used in the design has high thickness or low permittivity. It would result in significant impedance mismatching between the microstrip and the connector if a SIW-to-microstrip transition is used in sub-mmWave or mmWave applications. In contrast, the SIW-to-GCPW transition would be more preferable since the GCPW has smaller width compared with the microstrip line having the same characteristic impedance.

Table 5.3 Dimensions of the designed SIW-to-GCPW transition: mm

w_{p0}	w_{t3}	w_{t2}	w_{t1}	l_{t3}	l_{t2}	l_{t1}
5.20	3.80	1.00	0.50	2.00	2.80	1.20

Fig. 5.21 shows the layout of the designed SIW-to-GCPW transition. The structure of the end-launch connector is included in the simulation. Port #1 is connected to the network analyser for measurement, port #2 is connected to the input port of the designed ten-way power divider. The GCPW has three stages where the stage with a length of l_{t3} is a quarter-wavelength transformer, the second stage with a length of l_{t2} has a characteristic impedance of 50Ω and the stage with a length of l_{t1} helps further improve the impedance matching between the GCPW and connector. The detailed design parameters of this transition are shown in Table 5.3. Fig. 5.22 presents the simulated S -parameters of the designed SIW-to-GCPW transition. It is seen that the simulated return loss at 25 GHz are 26 dB. The impedance bandwidth for return loss higher than 20 dB is in the frequency range from 23.8 GHz to 26.8 GHz. Over this bandwidth, the insertion loss from port #1 to #2 is varied from 0.16 dB to 0.3 dB.

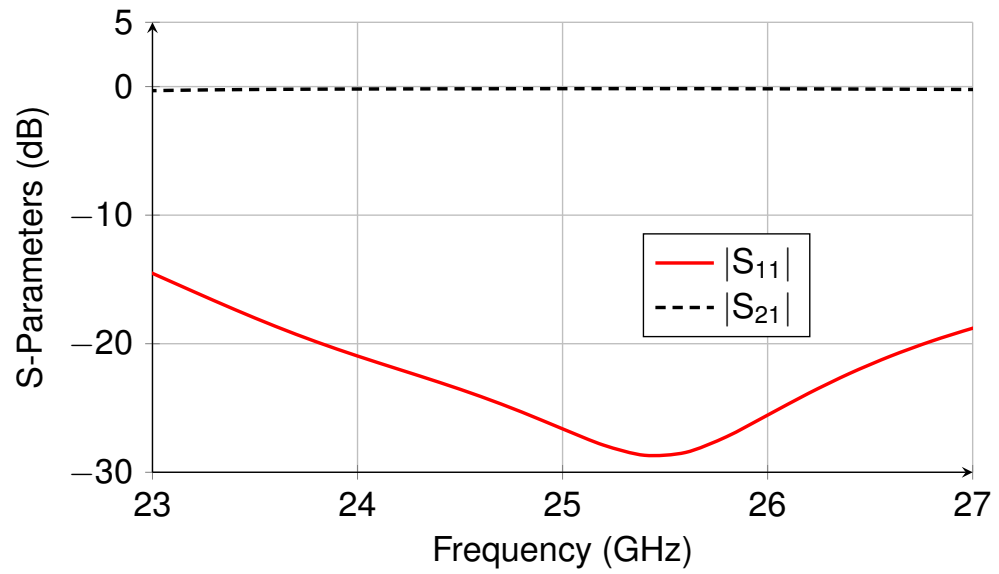


Fig. 5.22 Simulated S -parameters of the designed SIW-to-GCPW transition.

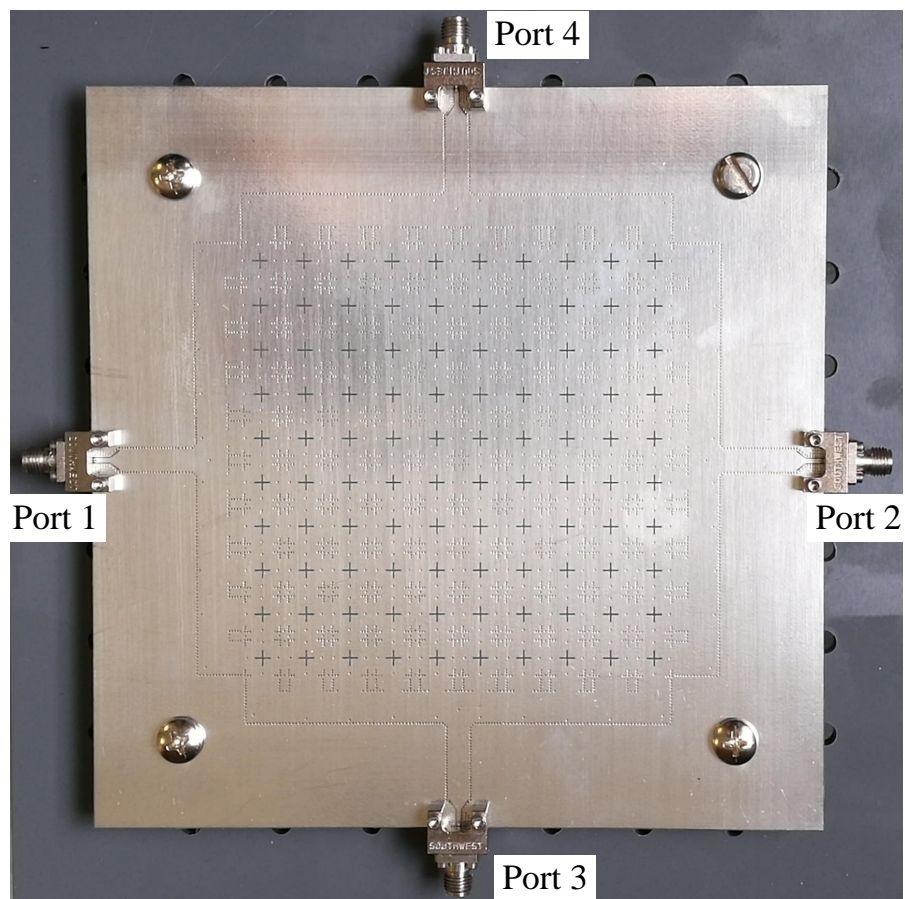


Fig. 5.23 Fabricated prototype of the designed dual polarized cross slot antenna array.

5.4 Experiment and results

In this section, the designed dual polarized cross slot antenna array is fabricated, tested and compared with other reported dual polarized antenna arrays. The fabricated prototype of the designed antenna array is shown in Fig. 5.23. The overall dimension of this antenna array prototype is $157.4 \text{ mm} \times 157.4 \text{ mm} \times 0.508 \text{ mm}$, and the dimension of the antenna array aperture is $94 \text{ mm} \times 94 \text{ mm}$. Four 2.92 mm end-launch connectors are used to connect the antenna to the test equipment, and four screws are applied to fix the fabricated antenna on the test platform.

5.4.1 Return loss and port isolation

Fig. 5.24 shows the measured and simulated reflection coefficients of the fabricated antenna array. The measured results are in good agreement with the simulated ones. The simulated impedance bandwidth for $|S_{11}|$ higher than 10 dB is in the frequency bandwidth from 24.2 GHz to 25.15 GHz. The reflection coefficient at different feed ports is very similar to each other since the designed antenna array is symmetric in structure. The overlapped impedance bandwidth for measured return loss high than 10 dB is from 24.3 GHz to 25.25 GHz. It is worth noting that the centre operation frequency shown in this figure is 24.75 GHz which is 250 MHz less than the desired centre operation frequency at 25 GHz because of complicated multi-reflection in the planar antenna array.

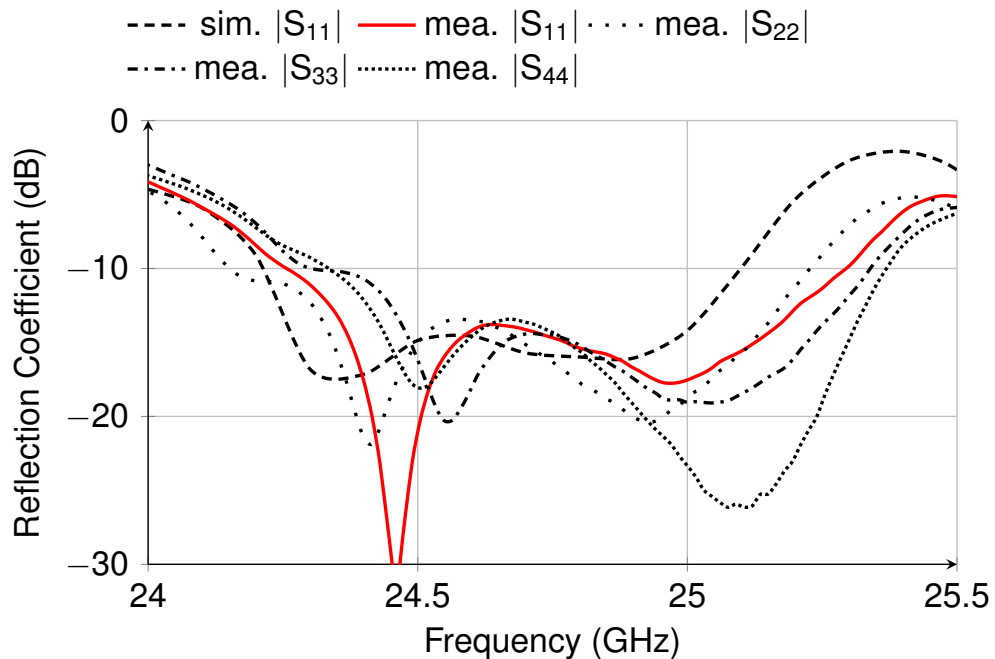


Fig. 5.24 Measured and simulated reflection coefficients of the designed dual polarized cross slot antenna array.

Fig. 5.25 presents the measured and simulated port coupling coefficients of the designed dual polarized cross slot antenna array. It is seen that the simulated $|S_{21}|$ is about -13 dB which is very close to the designed residual power $0.05P_0$. The simulated port coupling coefficient between port #1 and #3 are less than -30 dB within the frequency bandwidth from 24 GHz to 25.5 GHz, and the measured one is lower than -42 dB. Due to the loss from the connectors, the measured port coupling coefficients are lower than the simulated ones. These results indicate that high isolation between ports for exciting different polarizations is obtained in the designed antenna array.

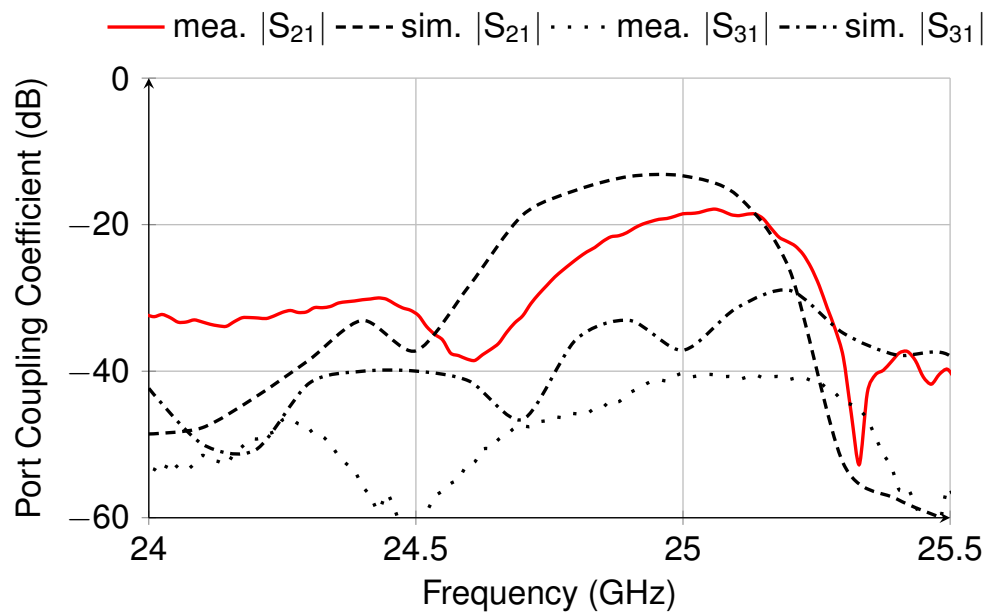


Fig. 5.25 Measured and simulated port coupling coefficients of the designed dual polarized cross slot antenna array.

5.4.2 Radiation patterns

Fig. 5.26 shows the measured and simulated co-polarization patterns at 24.8 GHz, 25 GHz and 25.2 GHz when ports #1 and #2 are excited. The measurements agree well with the simulations. The antenna array shows a frequency scanning range of 36° where the beam scanning range from -18° to 0° is obtained by exciting port #1 and the beam scanning range from 0° to 18° is obtained by exciting port #2. The SLLs of the designed antenna array at different frequencies are less than -9.3 dB. The designed antenna also shows stable -3 dB beamwidth at different frequencies, which is about 8° in average. The overlapped levels among these co-polarization radiation patterns are higher than -2.9 dB. Fig. 5.27 gives the measured and simulated cross polarization patterns at different frequencies when port #1 is excited. The designed antenna array shows high XPDs over the frequency bandwidth since high polarization purity and high port isolation is achieved in the dual

polarized cross slot antenna element. For example, the XPD measures 26 dB at 25 GHz, which is slightly lower than the simulated one, 35 dB.

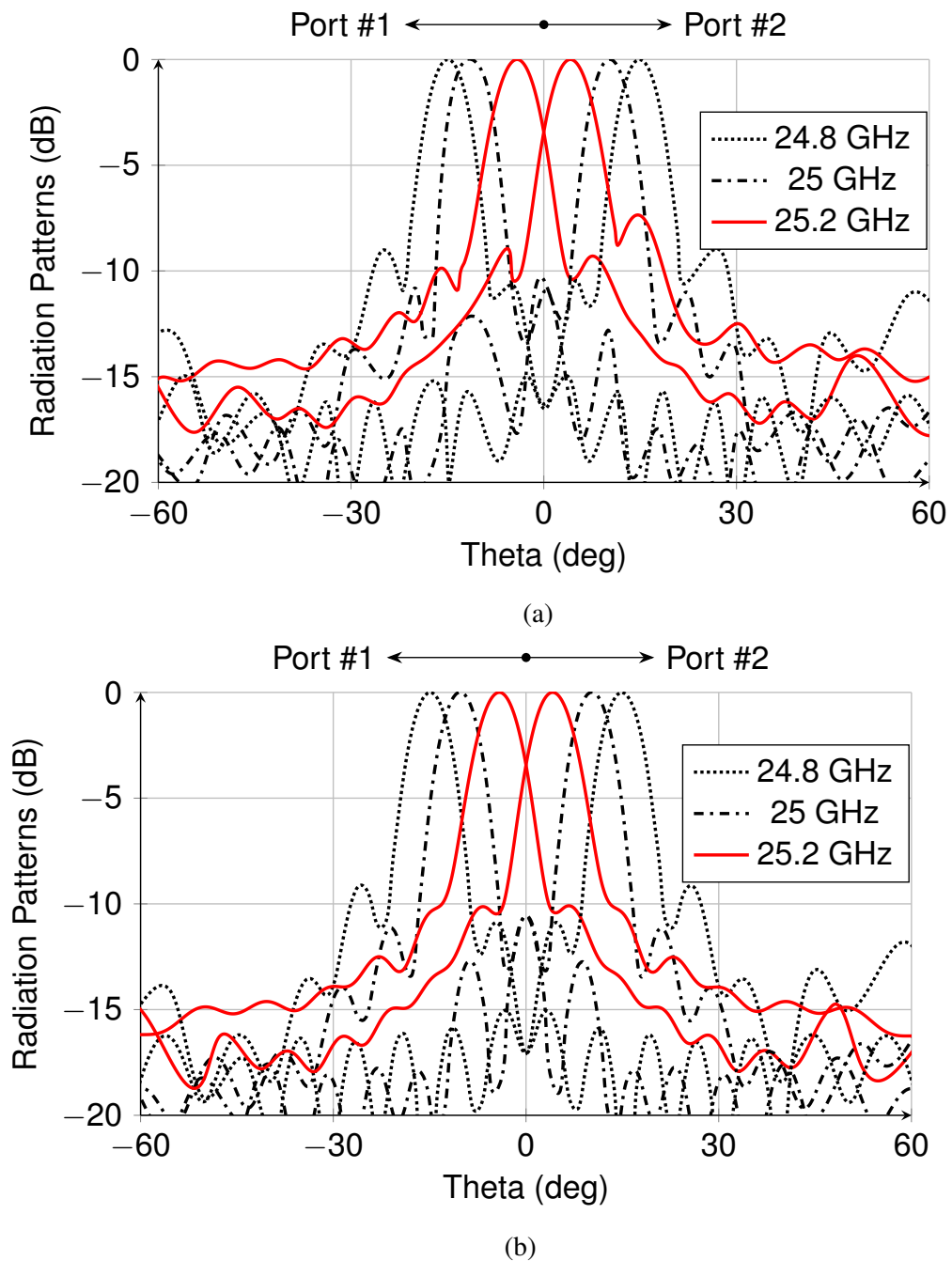


Fig. 5.26 Normalized co-polarization radiation patterns at different frequencies. (a) Measured. (b) Simulated.

5.4.3 Gain and radiation efficiency

Fig. 5.28 shows the gain and efficiency of the designed dual polarized cross slot array antenna with port #1 excited. It is seen that the antenna has a high gain from 24.6 GHz to

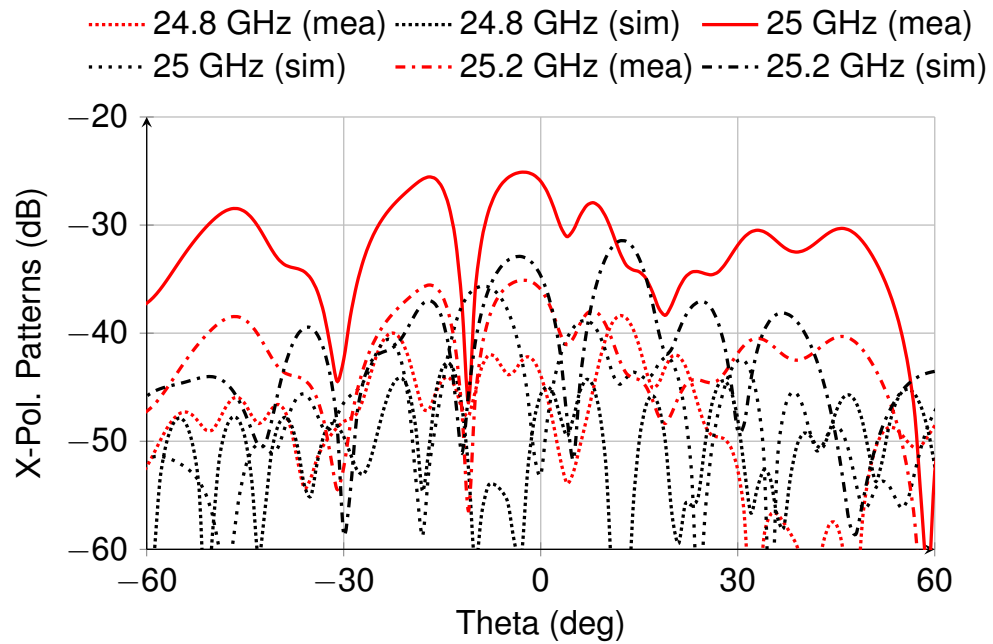


Fig. 5.27 Measured and simulated cross-polarization radiation patterns of the designed antenna array at different frequencies when port #1 is excited.

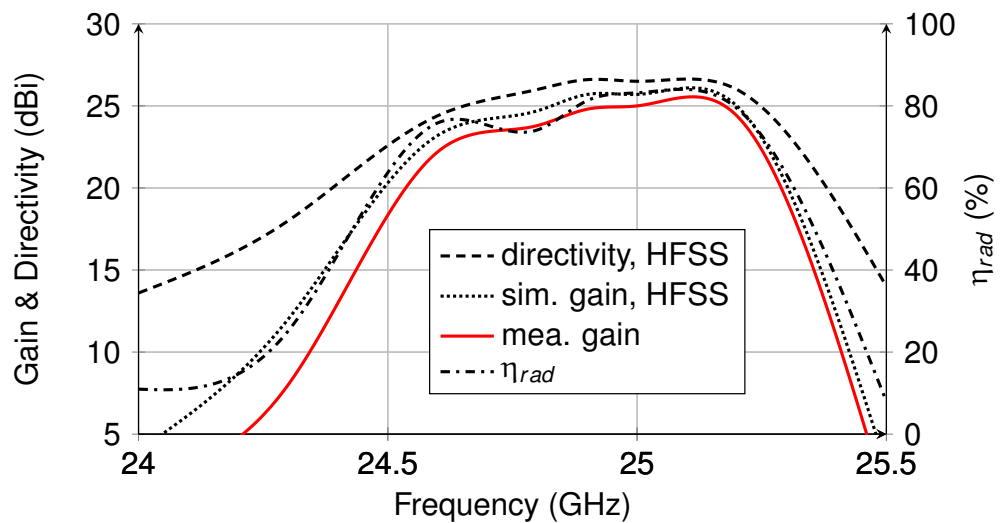


Fig. 5.28 Gain, directivity and radiation efficiency of the designed dual polarized cross slot antenna array.

25.3 GHz. The simulated gain is up to 25.7 dBi, and it has a variation of 2.8 dB over the bandwidth. The maximum measured gain is 24.9 dBi. The measured gain is about 0.8 dB lower than the simulated counterpart in the bandwidth. The slight discrepancy between the measured and simulated gain is mainly because 1) the insertion loss of the used connectors was calibrated in the measurement; 2) fabrication and the uncertainty of the dielectric loss of the laminate. The efficiency is calculated from the simulated directivity and gain, which is higher than 76% in the range from 24.6 GHz to 25.3 GHz.

Table 5.4 Comparison between this work and other frequency-scanning array antennas

Ref.	$B(\text{GHz})$	No. Sub.	Scanning Range	Pol.	XPD(dB)	Array Type	η_{ap}
[163]	2.40-2.48	1	n.a.	dual	16	planar	11%
[164]	33.12-39.23	1	(1°,35°)	dual	18	linear	34%
[165]	2.72-3.03	3	(70°,88°)	dual	30	linear	14%
[166]	8.52-14.13	3	(-17°,52°)	single	n.a.	linear	34%
[167]	8.92-10.63	3	(-28°,46°)	single	n.a.	linear	20%
[244]	13.52-13.93	1	(2°,37°)	single	n.a.	linear	17%
[245]	28.12-32.32	2	(4°,20°)	single	27	linear	28%
This work	24.82-25.24	1	(-18°,18°)	dual	26	planar	40%

5.4.4 Comparison and discussion

Table. 5.4 compares the designed dual polarized cross slot antenna array and the recently reported frequency-scanning antenna arrays. The antenna array reported in [165] can work with dual polarization and has high XPD, but it has very limited frequency-scanning range and low aperture efficiency. The antenna arrays reported in [163] and [164] can also operate with dual polarization and be realized with a single laminate. However, they suffers low XPD and low aperture efficiency which is not higher than 34% since their orthogonally polarized antenna elements are separated in different rows. Compared with the above reported works, the antenna arrays in [166] and [167] have relatively wide frequency-scanning range, but they can be only able to operate with a single polarization and cannot be applied to planar antenna arrays. In addition, these antenna arrays must be realized with multiple laminates. The antenna arrays in [244] and [245] can only operate with single polarization and have narrow frequency scanning range. In contrast, the proposed cross slot antenna array can not only work with dual polarization but also be implemented on a single laminate. The designed antenna array has a frequency-scanning range from -18° to 18° . In addition, the designed antenna array also shows advantages in terms of high aperture efficiency (40%) and high XPD (26 dB) when compared it with other reported frequency-scanning array antennas. Limited operation bandwidth in the proposed antenna array is mainly caused by the thin substrate used in the design. The proposed antenna array has very low cost since it only has one laminate and can be processed with the low cost PCB technology.

5.5 Summary

In this chapter, a planar dual polarized cross slot array antenna was proposed, designed, prototyped and measured. In order to achieve high port isolation and excite the antenna element from orthogonal directions, the crossover with four metallized vias placed around

the cross junction was introduced in designing the antenna element. Dual polarization radiation was realized by etching a cross slot over the crossover structure. In the designed antenna array, the measured isolation between the ports for different polarization is higher than 42 dB. The antenna array shows a frequency scanning range from -18° to 18° . The maximum gain measures 24.9 dBi and the measured XPD is higher than 26 dB over the operation bandwidth. The radiation efficiency and aperture efficiency of the designed dual polarized antenna array are higher than 76% and 40%, respectively. Compared with other reported frequency-scanning antenna arrays, the proposed one shows the advantages of low complexity, high XPD, high gain, high aperture efficiency and wide frequency-scanning range.

Chapter 6

Dual Polarized SIW Antenna Array With Orthomode Transducer

Dual polarized antenna arrays with high gain and high integration are highly required in applications such as 5G mmWave base stations and satellite communications. However, most of the reported antenna arrays related to this topic have high complexity, high profile and low integration. They also suffer degraded performance such as low XPD, high loss and unstable radiation patterns/gain, etc. In this chapter, a hybrid design scheme is developed to reduce the complexity of the dual polarized antenna array. Different from traditional dual polarized antenna arrays with series-corporate feed networks, the proposed one incorporates the series feed networks into the design of the dual polarized subarray antenna. In addition, the dual polarized antenna array aperture is differentially excited. Due to its ability of common mode suppression and anti-interference with high order harmonics, the differential feed technique has been widely applied in modern antenna designs for the purpose of achieving high XPD, high port isolation and symmetrical radiation patterns, etc [246–248]. Besides that, from the systematic perspective, the differentially fed antennas are available to be integrated with the differential RF front ends, which will significantly reduce system loss and physical size as a result. Differential excitation is achieved from a planar orthomode transducer. To test and verify the design concept, a dual polarized antenna array with 8×8 antenna elements are designed, fabricated and measured. Thanks to the hybrid approach applied, the developed dual polarized antenna array has simple configuration, compact size and low profile. In addition, the designed antenna array also shows advantages in terms of high XPD, high port isolation and high realized gain.

6.1 Architecture of the antenna array

The architecture of the proposed differentially fed dual-polarized antenna array is shown in Fig. 6.1(a), where each antenna element is serially connected to each other in two dimensions and the whole antenna array is differentially driven at the edges of the antenna

aperture to improve the XPD. Differential feed #1⁺ and differential feed #1⁻ are denoted as the differential feed pair for exciting horizontal polarization, and differential feed #2⁺ and differential feed #2⁻ are denoted as the differential feed pair for exciting vertical polarization. The horizontal ports #1 and #2 of the antenna element illustrated in Fig. 6.1(b) are expected to be well isolated from the vertical ports #3 and #4. Thus, signals are enabled to travel along the horizontal and vertical direction without interference. In this design, a corporate power divider is connected to each edge of array aperture. Following these power dividers, a planar orthomode transducer is designed on the lower layers to generate differential excitations for the antenna array.

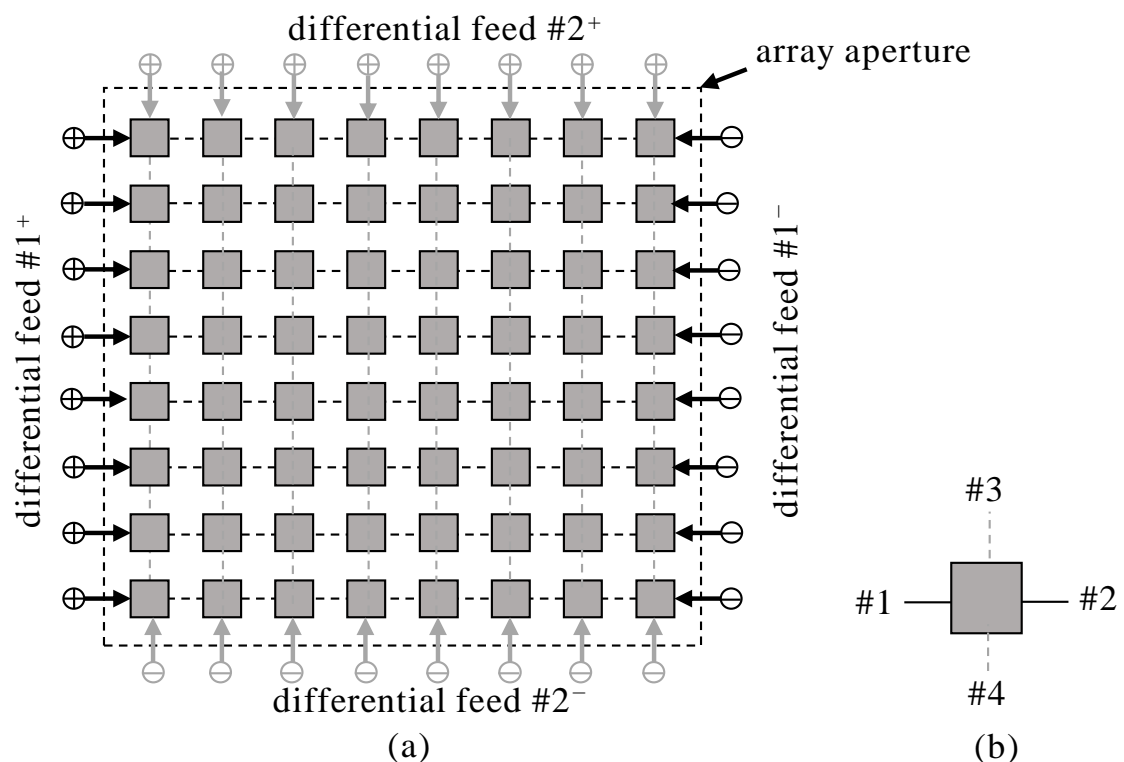


Fig. 6.1 Architecture of the proposed differentially fed dual polarized antenna array.

To have a better understanding of the working mechanism of the proposed differentially fed dual-polarized antenna array, the architecture of the antenna array is represented by a brief diagram shown in Fig. 6.2. The yo z -plane can be regarded as a perfect electric wall with the differential excitation introduced at the differential port #1 for horizontal polarization. This is because the differentially fed dual-polarized antenna array is completely symmetric with respect to the yo z -plane. In the present case, differential port #2 is infinitely isolated to the differential-mode signal injected from differential port #1. Differential port #2 is also not affected by the common-mode signal since the differential port #2 is strictly positioned across the perfect electric wall in the yo z -plane. In other words, high isolation between the differential ports #1 and #2 can be obtained in this antenna array. The radiated waves of cross polarization are equal in magnitude but opposite in phase with

respect to the electric walls in the yoz - and xoz -plane due to perfectly symmetric structure and differential feed applied. This will result in destruction of cross-polarization radiations in the far field; hence the XPD of the proposed antenna array can be significantly improved.

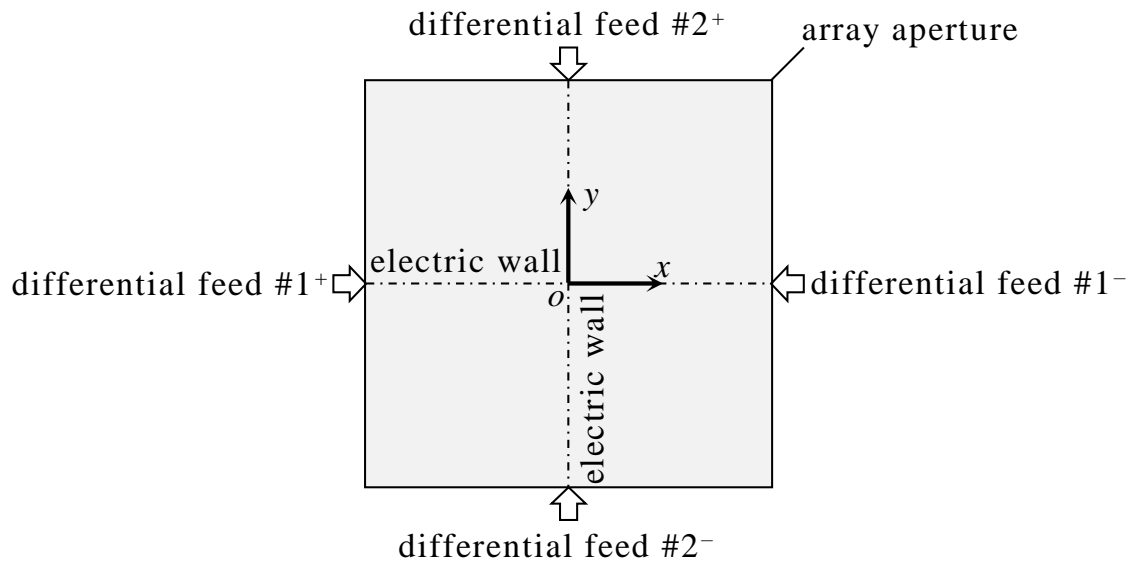


Fig. 6.2 Architecture of the proposed differentially fed dual polarized antenna array.

6.2 Dual polarized 2×2 -element subarray antenna

The proposed antenna array consists of 4×4 subarray antennas, and each subarray antenna has 2×2 antenna elements. In order to facilitate the analysis of the design procedure and working mechanism of the antenna array, the 2×2 -element subarray is modelled and synthesised. In this section, the configuration of the subarray antenna will be firstly presented and analysed. Then, as a key component in designing the subarray antenna, the via-loaded crossover structure will be discussed. The resonances of the designed subarray antenna, which are originated from the patch, the cross slot and the cylindrical cavity respectively, will be also discussed in this section. At last, a linear antenna array composed of four 2×2 -element subarray antennas will be designed to exemplify the performance of the 2×2 -element subarray.

6.2.1 Configuration

The configuration of the designed dual-polarized 2×2 -element subarray antenna is shown in Fig. 6.3. Three doubled-sided Rogers RO4003C laminates, Sub-1 to Sub-3, are used to design this subarray antenna. M1 to M6 are the copper layers of the laminates. The subarray antenna is composed of four resonant patches. Each patch is designed with four

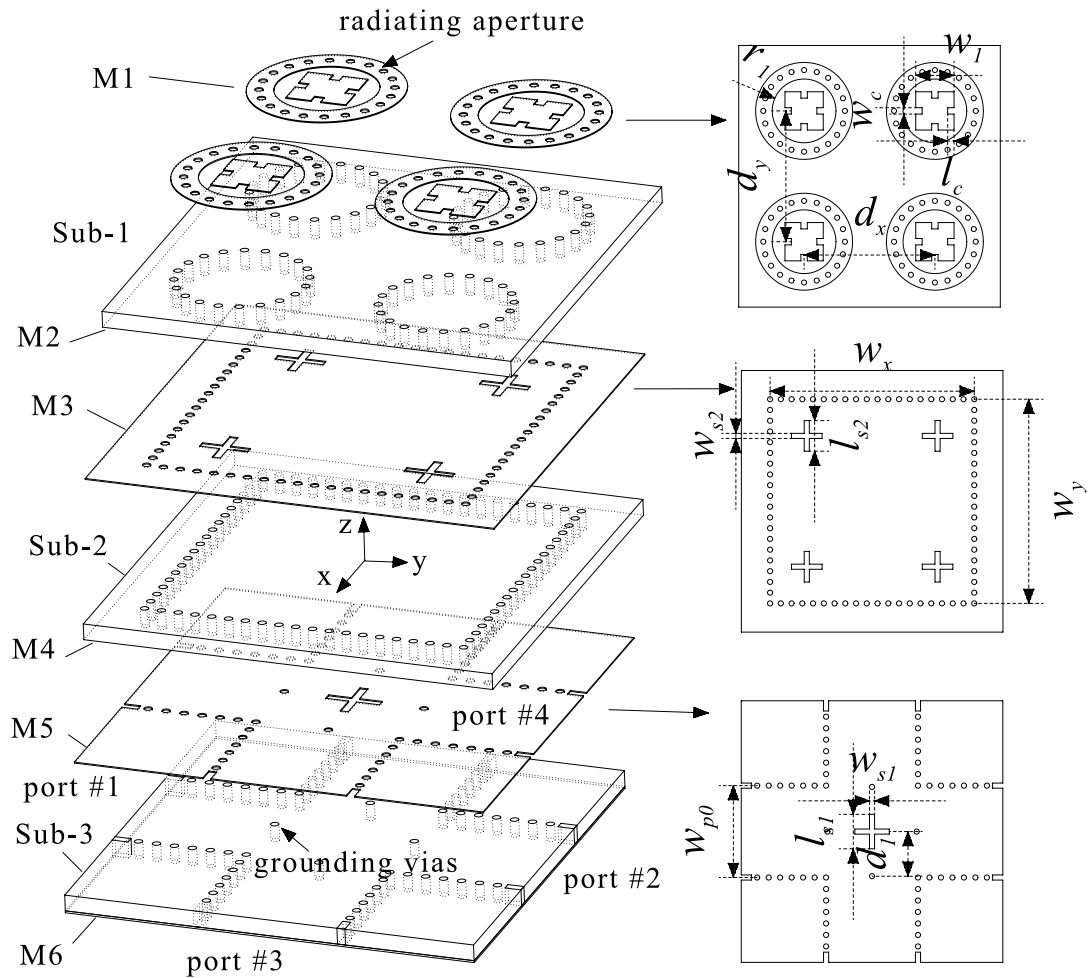


Fig. 6.3 Configuration of the designed dual polarized 2×2 -element subarray antenna.

short slit cut along the centre line of the patch. The resonant patch is placed inside a cylindrical cavity with a radius of r_1 . The spacings of the 2×2 antenna elements along the x - and y -axis direction are $d_x = d_y = 0.68\lambda_0$. The patch antennas are driven by the cross slots cut out from the copper layers M2 and M3. Under these copper layers, a SIW cavity supporting TE_{140} and TE_{410} modes is designed in Sub-2 to act as an four-way equal power splitter and excite the cross slots. The SIW cavity supporting TE_{140} and TE_{410} modes is driven by a cross slot with the length of l_{s1} and the width of w_{s1} . This cross slot is etched in the copper layers M4 and M5, and beneath which there is a crossover structure to enable the subarray antenna to be excited from the x -axis and y -axis direction for dual-polarization. In order to realize high port isolation just as illustrated in Fig. 6.1(b), four metallized vias are placed around the junction of the crossover. To obtain the impedance characteristics of the subarray antenna, port #2 is short-circuited with port #1 excited in the simulation [249]. Considering the mutual couplings between the subarrays, the periodic boundary condition is imposed to the subarray simulation. The design parameters of the 2×2 -element subarray antenna are given in Table. 6.1.

Table 6.1 Dimensions of the designed 2×2 -element subarray antenna: mm

w_{p0}	l_{s1}	w_{s1}	d_1	l_{s2}	w_{s2}	w_x	w_y	r_1	w_1	l_c	w_c	d_x	d_y
7.20	2.90	0.40	3.50	2.40	0.40	16.00	16.00	3.20	3.00	0.50	0.4	10.25	10.25

6.2.2 Simulated results

Based on the model shown in Fig. 6.3, the simulated S -parameters and the realized gain of the designed 2×2 -element subarray antenna are shown in Fig. 6.4. Three resonances are observed at 19.4 GHz, 19.8 GHz and 20.3 GHz, respectively. The impedance bandwidth for the reflection coefficient $|S_{11}|$ less than -10 dB is in the range of 19.3–20.5 GHz. The designed subarray antenna shows good isolation between port #1 and #3 or #4. As can be seen from this figure, the isolation is higher than 30 dB for frequency larger than 19.2 GHz. Within the operation bandwidth 19.3–20.5 GHz, stable gain varying from 10.8 dBi to 12.2 dBi is obtained in this subarray antenna. The realized gain drops to less than 0 dBi at the frequencies 18.8 GHz and 21.2 GHz.

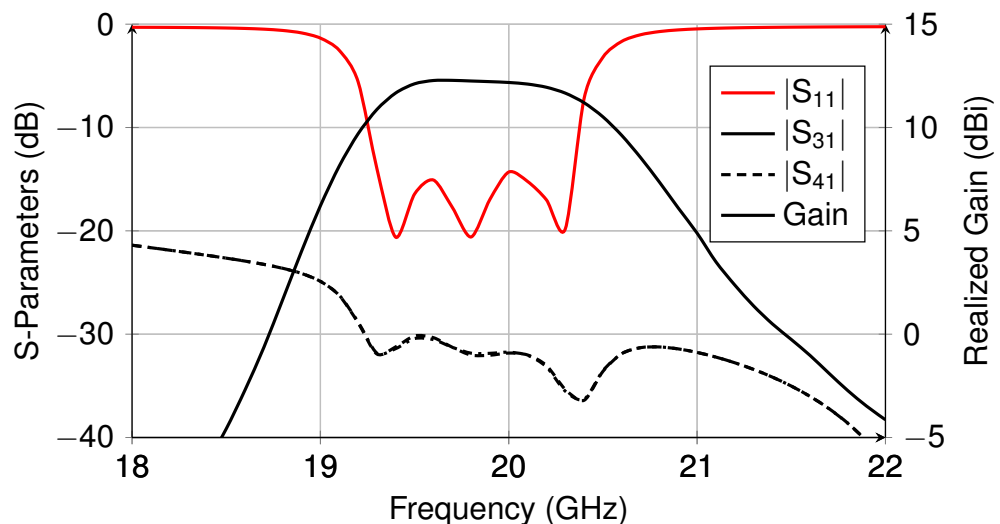


Fig. 6.4 Simulated S -parameters and realized gain of the designed dual polarized 2×2 -element subarray antenna.

Fig. 6.5 presents the simulated radiation patterns of the designed 2×2 -element subarray antenna. Symmetric co-polarization radiation patterns are obtained in both the E-plane ($yo z$ -plane) and H-plane (xoz -plane). Due to the unique radiation characteristic of the slot antennas, the -3 dB beamwidth of the co-polarization radiation pattern in the H-plane is wider than that in the E-plane. In addition, the subarray antenna also shows high XPD which is 58 dB at the boresight. The front-to-back ratios (FBRs) of the co-polarization radiation patterns are higher than 17 dB in the E- and H-plane.

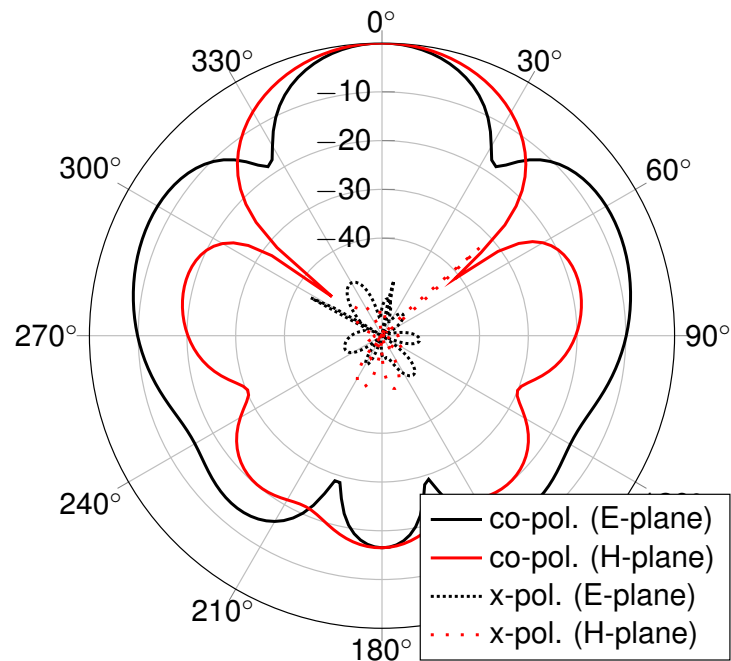


Fig. 6.5 Simulated normalized far field radiation patterns of the designed dual polarized 2×2 -element subarray antenna..

6.2.3 Via-loaded crossover

The crossover structure, situated in the laminate Sub-3, plays a critically important role in designing the 2×2 -element subarray antenna. It makes possible for the signals travelling through the linear subarray antennas without interference from other parallel linear subarrays. As can be seen from Fig. 6.3, the designed crossover structure is built by using two perpendicular SIWs with a width of w_{p0} . Around the cross junction, an SIW cavity is constructed by placing four metallized vias with a diameter of 0.3 mm. In order to achieve high isolation between the ports for exciting different polarizations, the SIW cavity can only support the degenerate modes, TE_{210} and TE_{120} . The fundamental mode TE_{110} and other higher order modes are prevented within the operation bandwidth by tuning the position d_1 of the four metallized vias. The effective size of this SIW cavity is $2d_1 \times 2d_1 = 7 \text{ mm} \times 7 \text{ mm}$, which is smaller than a completely enclosed TE_{210} and TE_{120} mode SIW cavity supporting TE_{210} operating at the same frequency.

The electric field pattern inside this via-loaded crossover with port #1 excited is given in Fig. 6.6(a). Thanks to the existence of the four metallized vias, it is seen that the TE_{210} mode field is distributed inside the junction of the crossover. When port # 1 is excited, the electromagnetic waves can travel through the cross junction without interfering ports #3 and #4. Thus, high isolation between ports #1 and port #3 is obtained as the waves are well constrained to travel in the horizontal direction.

Fig. 6.7 shows the simulated isolation between ports #1 and #3 of the crossover structure implemented with and without the four metallized vias placed around the junction.

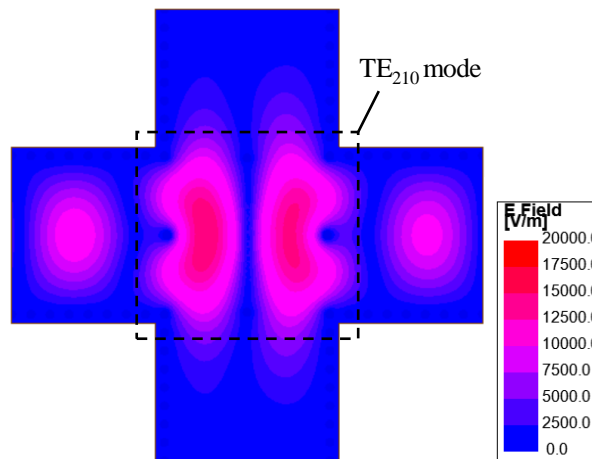


Fig. 6.6 Simulated electric field pattern inside the via-loaded crossover structure.

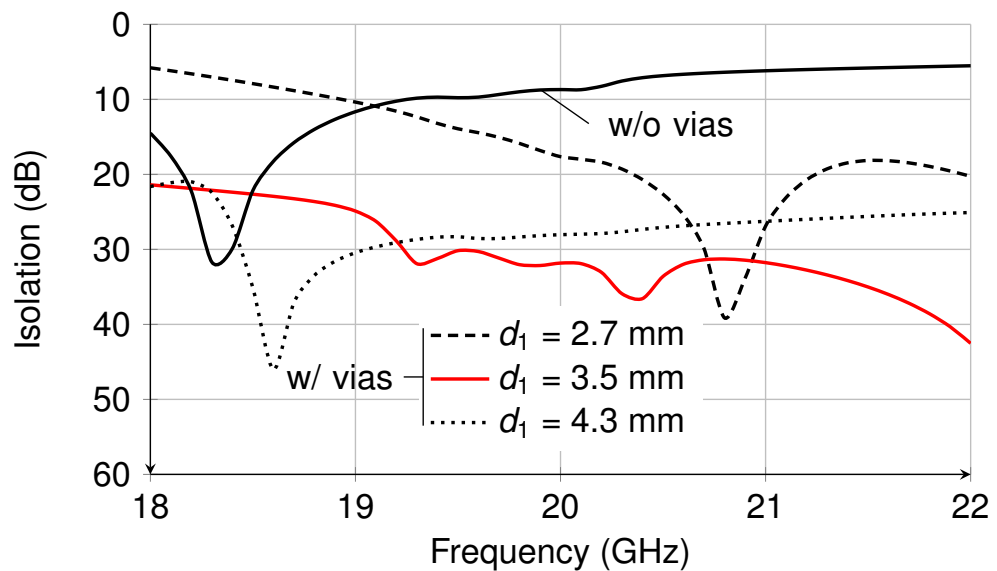


Fig. 6.7 Simulated port isolation of the designed crossover without the grounding vias and with different position of ground vias.

The isolation between ports #1 and #3 is less than 10 dB over the operation bandwidth of the antenna when the crossover structure is realized with no metallized vias inserted around the cross junction. In this case, the port isolation can be improved by reducing the size of the cross junction, but it will degrade the impedance matching of the subarray antenna. In our design, the port isolation of this crossover structure is significantly increased by introducing four metallized vias around the cross junction. As can be seen from Fig. 6.7, when the position of the four metallized vias is located at $d_1 = 3.5$ mm, the port isolation is improved to higher than 30 dB over the operation bandwidth of the antenna. Considering that the mode fields inside the cross junction are dramatically affected by the position of the four metallized vias, the port isolations with different d_1 are also studied in Fig. 6.7.

By increasing d_1 from 2.7 mm to 4.3 mm, the port isolation increases firstly then falls off after maximizing to 31 dB when $d_1 = 3.5$ mm.

6.2.4 Triple resonance

As discussed in Section 6.2.2, the designed 2×2 -element subarray antenna has three resonances over its operation bandwidth. The first resonance at 19.5 GHz is originated from the cylindrical cavity which encloses the patch element. As evidenced in [250], a cylindrical cavity can function as an aperture radiator if the field inside the cavity works as the TM_{110} mode. From the cavity theory conceived in [251] and [252], for a cylindrical cavity with a radius of r_1 and a height of h , the wave functions can be expressed as

$$\psi_{\text{TE}_{mnp}} = J_m \left(\frac{x_{mn}}{r_1} n \right) \begin{Bmatrix} \sin m\phi \\ \cos m\phi \end{Bmatrix} \sin \left[\frac{(2p+1)\pi}{2h} z \right] \quad (6.1)$$

$$\psi_{\text{TM}_{mnp}} = J_m \left(\frac{x'_{mn}}{r_1} n \right) \begin{Bmatrix} \sin m\phi \\ \cos m\phi \end{Bmatrix} \cos \frac{(2p+1)\pi z}{2h} \quad (6.2)$$

where J_m is the Bessel function of the first kind. x_{mn}/r_1 is the n^{th} root of $J_m(x) = 0$ for TE modes, and x'_{mn}/r_1 is the n^{th} root of $J'_m(x) = 0$ for TM modes. The resonance frequency f_{mnp} is governed by the separation equation

$$f_{mnp} = \frac{1}{2\pi r_1 \sqrt{\mu_r \epsilon_r}} \sqrt{\begin{Bmatrix} x_{mn}^2 \\ x'_{mn}^2 \end{Bmatrix} + \left[\frac{\pi r_1}{2h} (2p+1) \right]^2} \quad (6.3)$$

The order of modes inside the cylindrical cavity is determined by its radius r_1 and height h . In order to achieve compact size and avoid intersection between the adjacent antenna elements, the diameter of the cylindrical cavity is set to less than half a wavelength. This makes that only TM_{110} mode can be allowed in this cylindrical cavity. Besides, in order to suppress potential surface waves from propagation, the thickness of the laminate used to design the cylindrical cavity is less than half a wavelength in consideration of practical use. For this reason, this cylindrical cavity cannot support the TE and TM modes along the z -axis direction. From the above analysis, the initial cavity size and resonance frequency of the TM_{110} mode can be obtained by solving (6.3).

To verify the above calculation, the magnetic field patterns inside the four cylindrical cavities of the subarray antenna are presented in Fig. 6.8. It is clearly observed that the TM_{110} mode field patterns appear inside the cavities and all of these patterns have a rotation angle of $+45^\circ$ or -45° with regard to the centre of each cavity. Due to the anti-symmetry of the magnetic field among the cylindrical cavities, the co-polarization

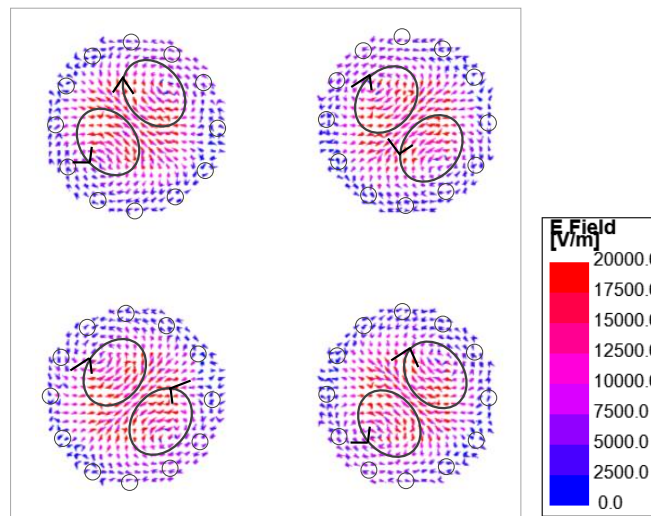


Fig. 6.8 Magnetic field inside the cylindrical cavities of the designed dual-polarized subarray antenna.

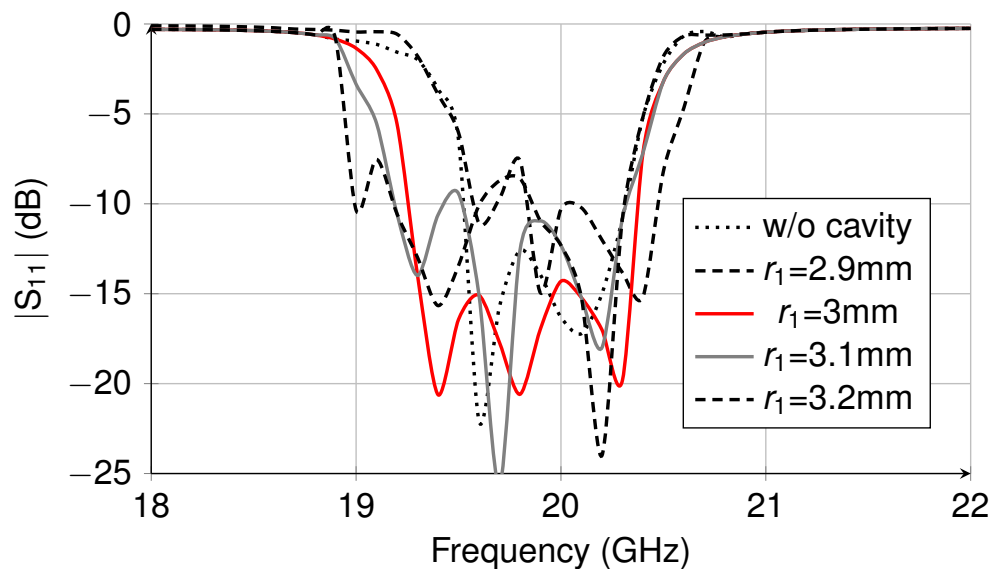


Fig. 6.9 Simulated reflection coefficient $|S_{11}|$ of the designed subarray antenna without the cylindrical cavity and with different size of the cylindrical cavity.

radiation pattern can be obtained at the boresight. The cylindrical cavity aids in producing a new resonance and the cavity size affects the resonance frequency. To demonstrate these impacts, Fig. 6.9 presents the reflection coefficient at port #1 when the subarray antenna is implemented without the cylindrical cavity and with different cavity size r_1 . As can be seen from this figure, without the cylindrical cavity, the subarray antenna only resonates at two frequency points 19.6 GHz and 20.1 GHz. They are originated from the patch and the cross slot beneath the patch, respectively. In this instance, the designed subarray antenna exhibits good performance in a relatively narrow bandwidth. In contrast, the operation bandwidth is improved by introducing the cylindrical cavity surrounding the patch since a

new resonance is created by the cavity. It is shown from Fig. 6.9 that the new resonance shifts to the lower frequency band with the increasing of the cavity size. In addition, the cylindrical cavity also has an effect on the resonances originated from the patch and the cross slot due to the very close distance between these structures. As the size of the cylindrical cavity is increased, the two resonance frequencies move to the lower frequency band. When r_1 equals to 3 mm, the maximum impedance bandwidth for $|S_{11}|$ less than -10 dB is obtained over the frequency range from 19.3 GHz to 20.5 GHz.

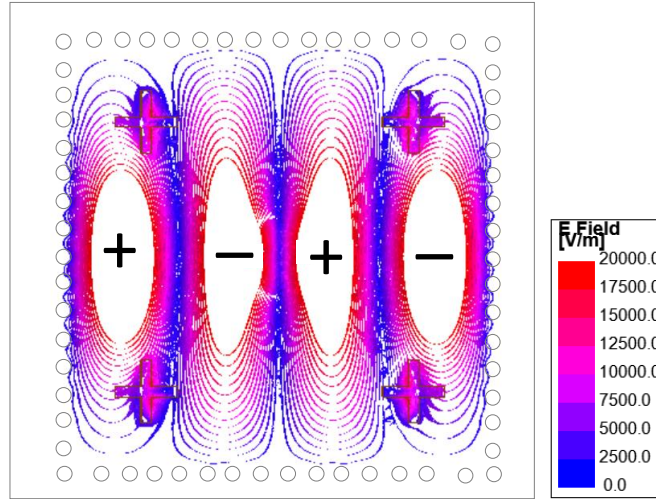


Fig. 6.10 Simulated reflection coefficient $|S_{11}|$ of the designed subarray antenna without the cylindrical cavity and with different size of the cylindrical cavity.

As aforementioned, the patch inside the cylindrical cavity and the cross slot beneath the patch result in the other two resonances at 19.8 GHz and 20.3 GHz, respectively. In regards to the patch, four narrow slots having the size of $w_c \times l_c$ are removed from the centre line of the patch. This can lengthen the meandering path of the currents effectively, thus reducing the physical dimension of the patch. As to the cross slots beneath the patches, they are cut out from the top copper layer of the square SIW cavity containing the TE_{410} and TE_{140} modes in the laminate Sub-2. They are designed with the length of l_{s2} and the width of w_{s2} . They are located at the position of $(\pm 0.34\lambda_0, \pm 0.34\lambda_0)$ relative to the centre of the square SIW cavity in the x - and y -axis direction. As demonstrated in [223], a rectangular or square SIW cavity allowing the designated TE_{mnp} mode can be resonant at the frequency

$$f_{mnp} = \frac{c}{2\pi\sqrt{\epsilon_r}} \sqrt{\left(\frac{m\pi}{w_x}\right)^2 + \left(\frac{n\pi}{w_y}\right)^2} \quad (6.4)$$

In this formula, w_x and w_y represent the physical dimensions of the SIW cavity in the x - and y -axis direction, respectively. Because the two orthogonal components of the designed antenna array have the same operation frequencies, the SIW cavity used in this design

must be a square one ($w_x = w_y$) so as to guarantee that the TE_{410} and TE_{140} mode fields resonance frequencies are overlapped. The initial size of the square SIW cavity can be achieved by replacing the resonance frequency in (6.4) with 20 GHz. From Fig. 6.10, it is clearly seen that the TE_{410} mode field is excited inside the square SIW cavity based on the calculated cavity size $w_x = w_y = 16.4$ mm. In this figure, the signs '+' and '-' represent the directions of the TE_{410} mode field along the z -axis. The cross slots etched over this cavity can be resonant with equal magnitude and same phase, because they have the same position relative to the centre of the cavity. By tuning the design parameters r_1 , l_c and l_{s2} , the designed 2×2 -element subarray antenna can achieve good impedance matching over the improved operation bandwidth from 19.3 GHz to 20.5 GHz.

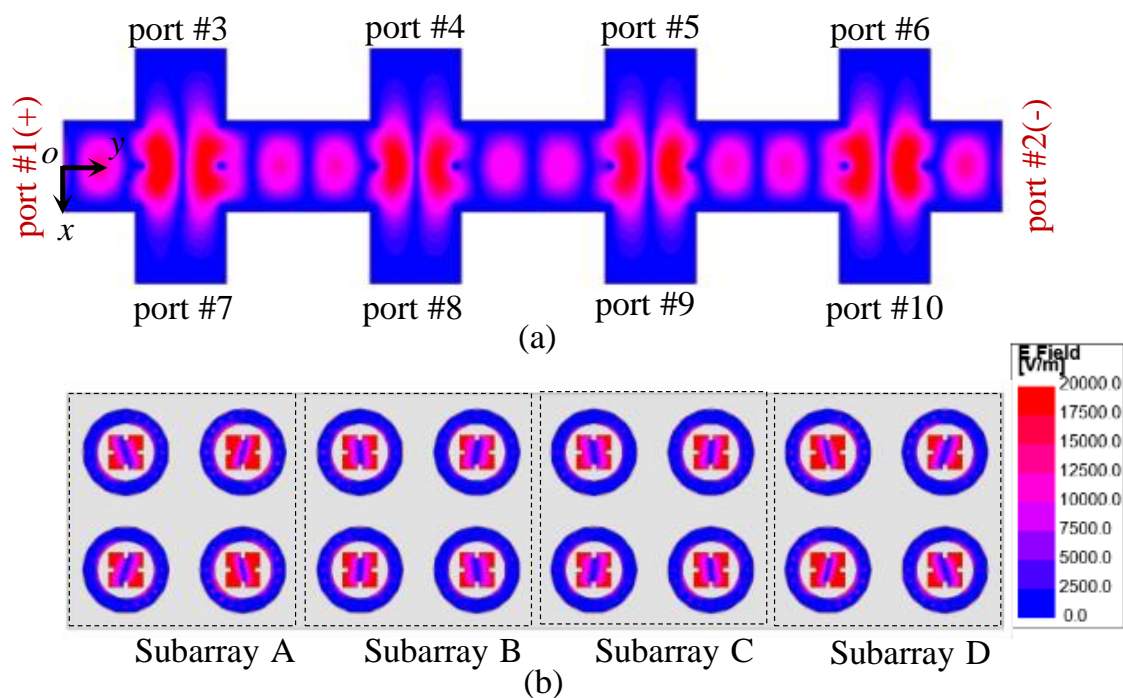


Fig. 6.11 Simulated electric field of (a) inside the crossover structures and (b) over the patch radiators of the four subarray antennas.

6.2.5 2×8 antenna array with four subarrays

As can be learnt from above analysis, the designed 2×2 -element subarray antenna has port isolation higher than 30 dB and thus it can be excited from the orthogonal directions for dual polarization. To validate its performance in the antenna array design, four 2×2 -element subarray antennas with a series combination are investigated. Fig. 6.11 shows the simulated electric field inside the crossover structures and over the patch radiators of the four subarray antennas. In this 2×8 antenna array, ports #1 and #2 are the differential feed pair, and ports #3 to #10 are connected to a matched load. The spacing between the

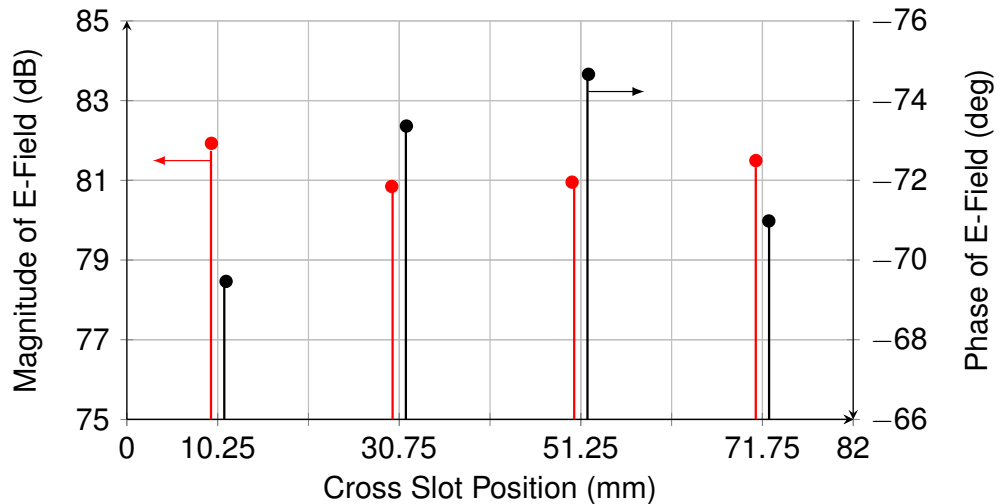


Fig. 6.12 Simulated magnitude and phase of the electric fields \vec{E}_y at the centre of the cross slots.

adjacent antenna elements are designed to be $0.7\lambda_0$, which is larger than $0.5\lambda_0$. This is mainly because of the following two reasons:

- In order to excite TE_{410} and TE_{140} modes within the frequency band of interest, the dimension of the square SIW cavity must be more than $1\lambda_0$;
- To make sure that all the antenna elements are excited with the same magnitude and phase, the length of SIW connected to the via-loaded crossover should be extended. As a consequence, the spacing between the adjacent antenna elements needs to be increased further.

Fig. 6.11(a) presents the simulated electric pattern inside the crossover structures of the 2×8 antenna array. It is seen that with the differential feed placed at ports #1 and #3 the electromagnetic waves inside the crossovers are constrained to travel along the y-axis direction and ports #3 to #10 are isolated effectively. In addition, the TE_{120} mode field is observed inside each junction of the via-loaded crossover structures. It can be concluded from the above results that the electromagnetic waves can freely propagate along the crossover structures in the y-axis direction and they cannot be coupled to other parallel antenna arrays.

To obtain broadside radiation and achieve high gain, the antenna elements of the antenna array must be excited with the same magnitude and phase. In the simulation, a field probe is placed at the centre of each cross slot etched over the crossover structure. The extracted magnitude and phase of the electric fields \vec{E}_y at the centre of the cross slots are shown in Fig. 6.12. The four cross slots etched over the crossovers are at the positions of $y = 10.25$ mm, $y = 30.75$ mm, $y = 51.25$ mm and $y = 71.75$ mm, respectively. Differential feed ports #1 and #2 are located at $y = 0$ mm and $y = 82$ mm, respectively. It is seen

from Fig. 6.12 that at these locations the magnitudes of the electric fields are 81.74 dB, 80.85 dB, 80.94 dB and 81.33 dB, respectively. In addition, the phase of the electric fields at these positions are -69.54° , -73.45° , -74.64° and -70.87° , respectively. Thus, one can conclude from the above obtained electric fields that these subarray antennas are excited with almost the equal magnitude and the same phase. These cross slots couple electromagnetic waves to feed the square cavity containing TE_{140} and TE_{410} modes and then drive the patch antenna printed on the copper layer M1. As shown in Fig. 6.11(b), uniform electric field patterns are achieved among the patch antenna elements.

6.3 Differentially fed planar antenna array with dual polarization

In this section, the differentially fed dual polarized antenna array will be developed by using the designed 2×2 -element subarray antenna. The designed antenna array is based on the architecture illustrated in Fig. 6.1. In this section, the configuration of the antenna array will be discussed firstly. Then, the design produces and performance of three key components including the orthomode transducer, four-way power divider, and 180° SIW elbow will be detailed.

6.3.1 Configuration of antenna array

The configuration of the developed differentially fed dual polarized antenna array is illustrated in Fig. 6.13. Fig. 6.14 shows the detailed structures of the developed antenna array in different layers. Fig. 6.15 shows the stack-up of the laminates used in designing this antenna array. It is seen that this antenna array is realized by using five double-sided laminates where the antenna elements are implemented on the upper three laminate layers and the feed networks are situated on the lower two laminates. When prototyping this antenna array, all the laminate layers are closely pressed and screwed together with nylon screws for convenience of assembling. In Fig. 6.15, the dielectric layers are Sub-1 to Sub-5, and the copper layers are M1 to M10. As seen from Fig. 6.13, the designed antenna array has 8×8 radiating elements and they are printed on the copper layer M1. As discussed in the last section, these antenna elements can operate with HP and VP, they are arranged with uniform distance in the x -axis and y -axis direction. Every 2×2 radiators is grouped as a subarray antenna and they are placed over an square SIW cavity that allows TE_{410} and TE_{140} modes in laminate Sub-2. For each square SIW cavity, four cross slots are cut out from the top copper layer of laminate Sub-2. They couple the electromagnetic waves inside the square cavity to drive the patch elements. The cavity supporting TE_{410} and TE_{140} modes is excited by a cross slot etched on the copper layers M4 and M5. Four horizontal and four vertical SIWs are placed perpendicularly to each other in the laminate

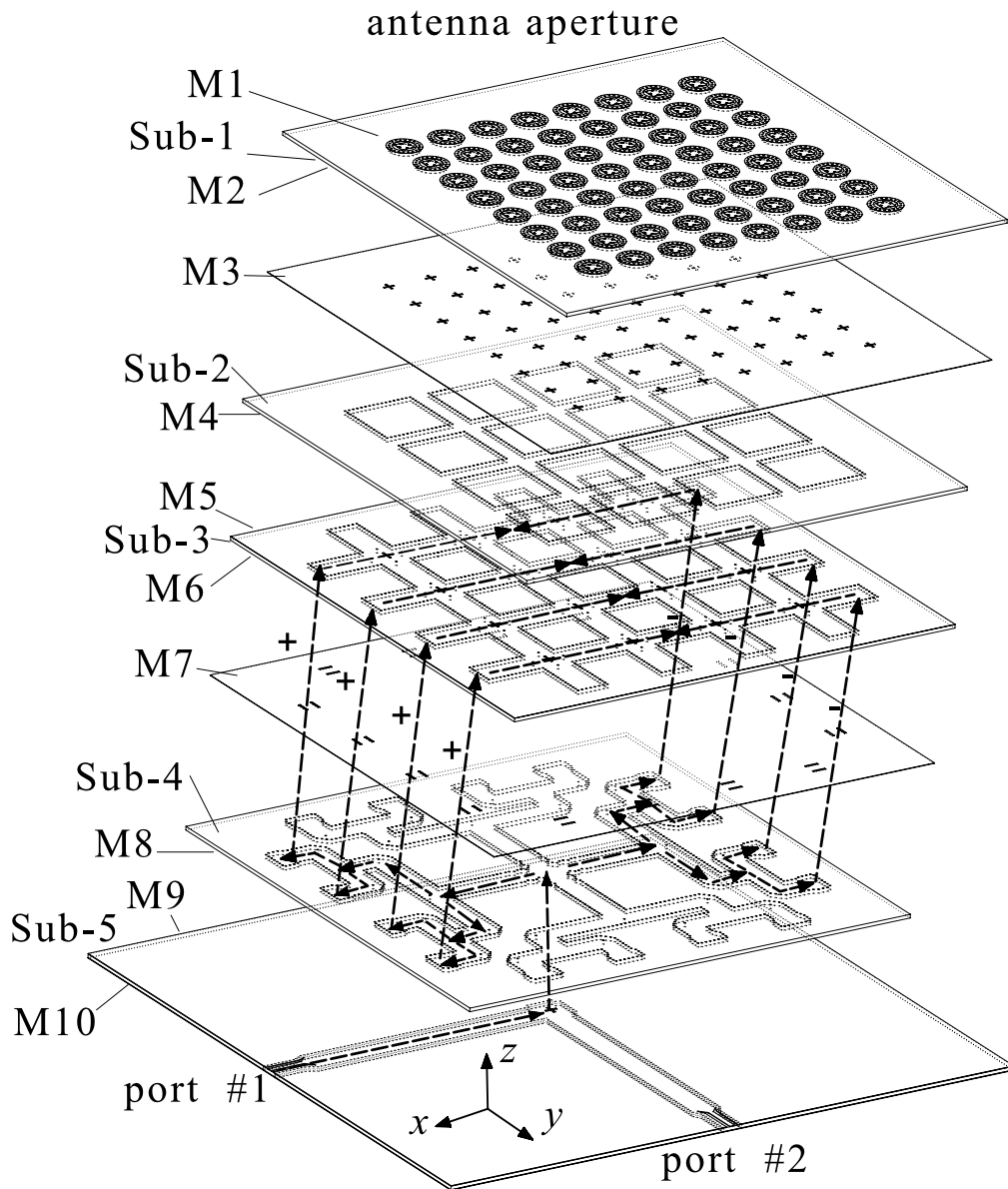


Fig. 6.13 Configuration of the proposed differentially fed dual polarized planar antenna array.

Sub-3. In fact, they are composed of 4×4 via-loaded crossovers. Because four metallized vias are inserted around each junction of the crossovers, the electromagnetic waves are enabled to propagate inside the parallel SIWs without interference from the orthogonal SIWs. In Fig. 6.13, the dashed arrows denote the signal travelling paths from feed port #1 to the parallel SIWs in laminate Sub-3. The signals input from feed port #1 are coupled to laminate Sub-4 through a cross slot cut out from the copper layers M8 and M9. The input signals are equally divided by a orthomode transducer in the laminate Sub-4. Then,

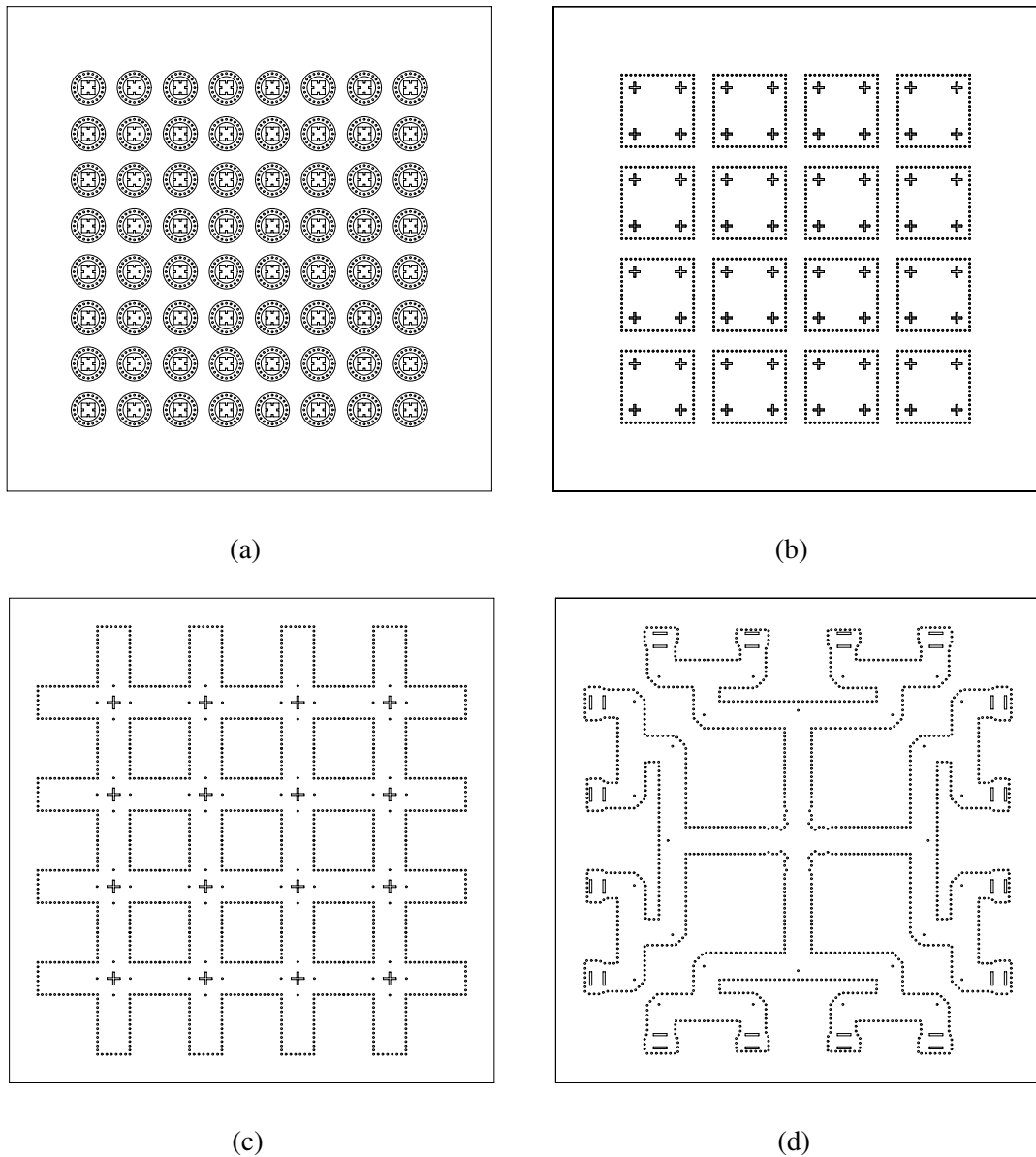


Fig. 6.14 Detailed structures of the designed differentially fed dual polarized antenna array on different layers. (a) Antenna array aperture. (b) TE_{410} and TE_{140} SIW cavities. (c) Via-loaded crossover structures. (d) Power dividers and orthomode transducer.

the signals travel to the four-way power dividers along the x -axis direction with opposite phase. Differential signals are coupled to feed the antenna array through the transverse slots designed in 180° SIW elbows. In this design, the antenna array and its feed networks are designed by using the low cost hydrocarbon ceramic laminates Rogers RO4003C which has a relative dielectric constant ϵ_r of 3.55, loss tangent $\tan \delta$ of 0.0027, a thickness of 0.813 mm and 1 oz copper foil.

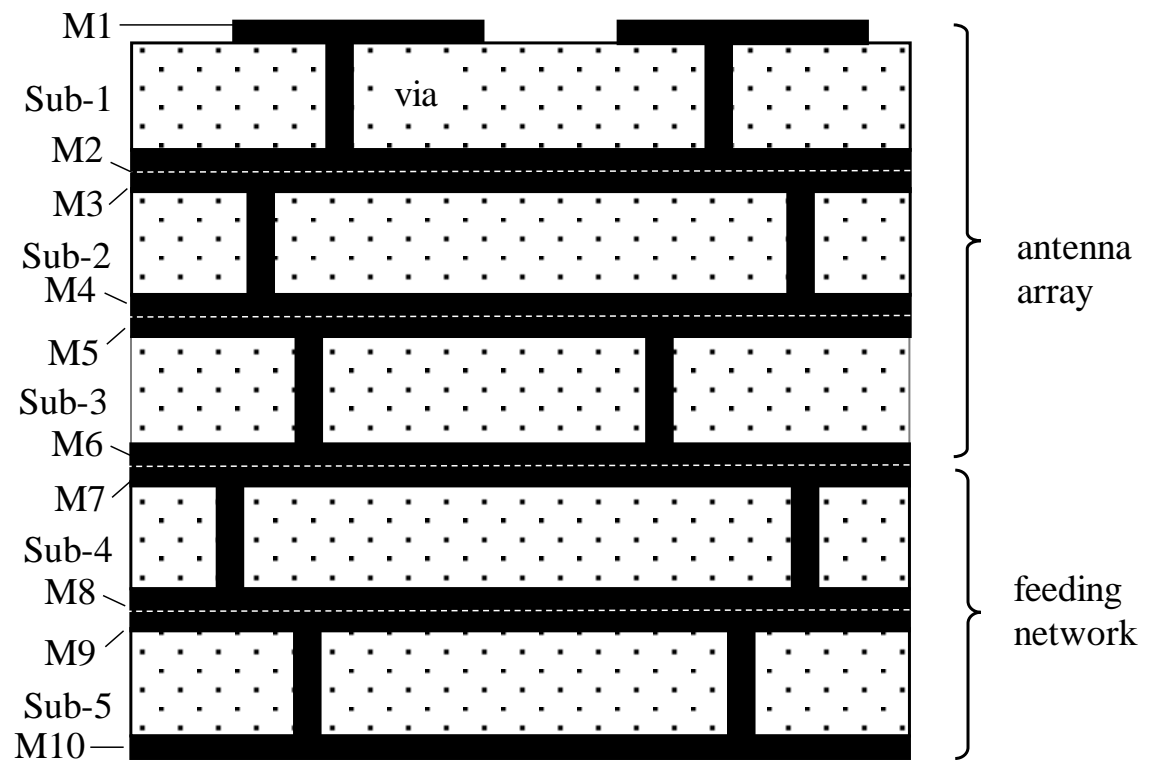


Fig. 6.15 Stackup diagram of the designed differentially fed dual polarized antenna array.

6.3.2 Planar orthomode transducer

An orthomode transducer can be regarded as a polarization duplexer or a six-port differential network [187, 216, 253]. It is usually found in the applications such as combining or splitting dual-polarized electromagnetic waves which are received by or transmitted from a differentially fed antenna with dual-polarization. The configuration of the planar orthomode transducer used in this design is given in Fig. 6.16. The designed orthomode transducer is implemented with two laminates. Two feed ports placed orthogonally and a semi-open SIW cavity that supports TE_{120} and TE_{210} modes are designed in the bottom layer. In the top laminate, the output ports #3 to #6 are connected with a cross junction. Electromagnetic waves are coupled from the bottom laminate to the top laminate through a cross slot cut out from the copper layer between the two laminates. The working mechanism of the designed orthomode transducer can be described as follows: when port #1 is excited, electromagnetic waves are coupled to the top laminate through the cross slot, and they are equally divided by the cross junction, then they get out at ports #3 and #4 with equal magnitude and opposite phase. In this case, ports #2, #5 and #6 are isolated to feed port #1. When feed port #2 is excited, the electromagnetic waves exit at ports #5 and #6 with equal magnitude and opposite phase, and ports #1, #3, and #4 are isolated. Thus, the antenna or antenna array connected to the output ports #3 to #6 can be differentially

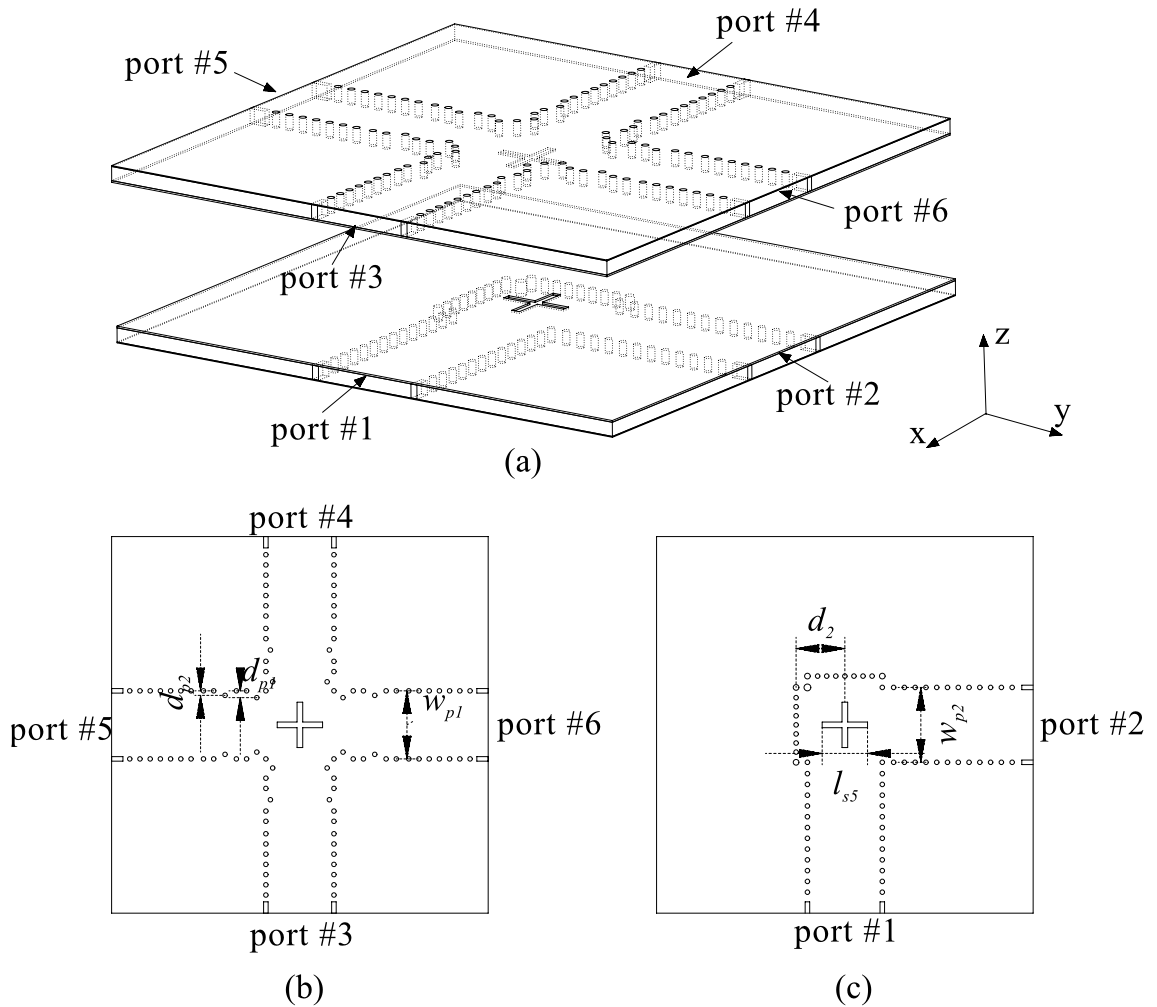


Fig. 6.16 Configuration of the designed planar orthomode transducer. (a) Exploded view. (b) Top layer. (c) Bottom layer.

excited for dual-polarization. The detailed dimensions of the design parameters used in designing this orthomode transducer are listed in Table 6.2.

Fig. 6.17 presents the simulated performance of the designed orthomode transducer. The impedance bandwidth of $|S_{11}|$ less than -15 dB is in the frequency range from 19.1 GHz to 20.7 GHz, which is larger than the operation bandwidth of the designed 2×2 -element subarray antenna. The simulated isolation between feed ports #1 and #2 higher than 15 dB is in the frequency range from 19 GHz to 21.6 GHz, and it is higher than 20 dB at 20 GHz. The isolation between the feed ports #1 and #2 is improved by optimizing the cross slot length and the semi-open cavity size. The simulated isolation between the feed port #1 and the output ports #5 and #6 are higher than 20 dB over the frequency range 19–22 GHz, which is improved by changing the cross junction size and the positions of metallized vias d_{p1} and d_{p2} . Fig. 6.17 also includes the simulated phase responses at the output ports #3 to #6. In this figure, the phase difference between the output ports #3 and #4 when feed ports #1 is excited is characterized as $\angle S_{41} - \angle S_{31}$;

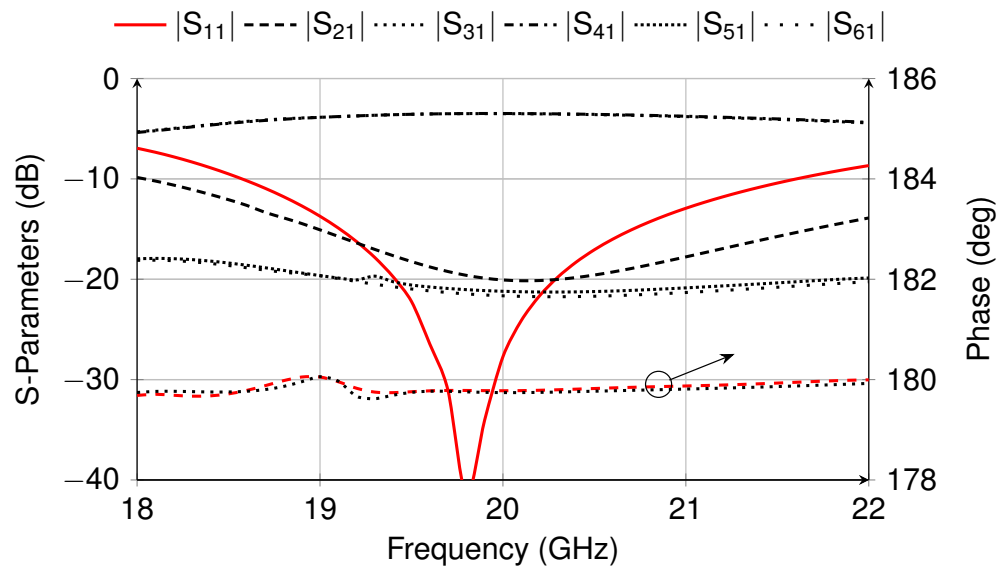


Fig. 6.17 Simulated S -parameters and phase differences between the output ports of the designed orthomode transducer.

Table 6.2 Dimensions of the components used in designing the feed network: mm

w_{p1}	d_{p1}	d_{p2}	w_{p2}	d_1	l_{s5}	w_{p1}	w_{int}	l_{int}	d_{p3}
6	2.2	0.94	0.53	6.6	4.76	4.8	6	7.2	3.2
l_{s3}	l_{s4}	s_1	w_{p0}	w_{p1}	l_{y1}	l_{x2}	l_{y2}	l_{x3}	l_{y3}
3.00	3.00	2.95	7.20	6	2.82	2.30	2.30	2.30	2.30

the phase difference between the output ports #5 and #6 when feed ports #2 is excited is characterized as $\angle S_{61} - \angle S_{51}$. As can be seen from this figure, when feed port #1 is excited the output ports #3 and #4 has almost the same phase response as the output ports #5 and #6 with feed port #2 excited. The simulated phase differences at the two output port pairs are varied from 179.6° to 180.1° over the frequency range 18–22 GHz. This demonstrates that differential excitations to the antenna array for dual-polarization are obtained.

6.3.3 Four-way power divider

As can be seen from Fig. 6.13, the four-way power dividers are located between the orthomode transducer and the 180° SIW elbow. It is used to equally split the power output from the orthomode transducer and pass the split power to the 180° SIW elbow. The layout of the designed four-way power divider is shown in Fig. 6.18 where port #1 is the feed port, and ports #2–#5 are the output ports. A metallized via is placed at each right angled corner in order to improve the impedance matching of the power divider in a relatively wide bandwidth. The detailed dimensions of the design parameters used in designing the four-way power divider are given in Table 6.2.

Fig. 6.19 presents the simulated reflection coefficient at port #1 and the transmission coefficients from port #1 to ports #2–#5. The designed four-way power divider has wide operation bandwidth. Good impedance matching for $|S_{11}|$ less than -20 dB is achieved in the frequency range from 18.3 GHz to 21.8 GHz. The transmission coefficients from feed port #1 to output ports #2–#5 are varied from -6.8 dB to -6.6 dB over the bandwidth 18.3–21.8 GHz. Low propagation loss is achieved in this power divider, which is less than 0.8 dB.

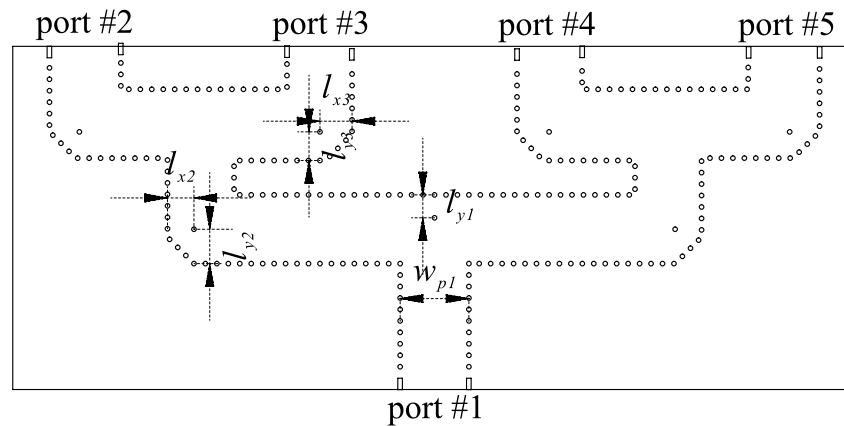


Fig. 6.18 Layout of the designed SIW four-way power divider.

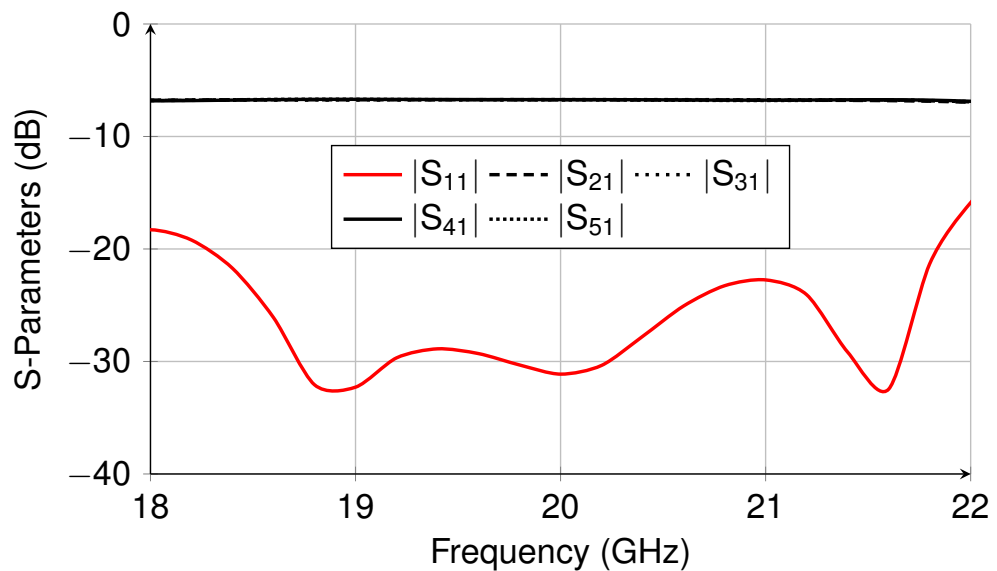


Fig. 6.19 Simulated reflection coefficient at feed port #1 and transmission coefficients from port #1 to ports #2–#5 of the designed four-way power divider.

6.3.4 180° SIW elbow

The interconnection between the four-way power divider and the antenna array is realized with a 180° SIW elbow, as shown from Fig. 6.13. The 180° SIW elbow also acts as an

interlayer transmission structure which allows signals couple from Sub-4 to Sub-3. Fig. 6.20 shows the configuration of the designed 180° SIW elbow. It is implemented with two laminate layers. Port #1 located in the bottom laminate is connected to one of the ports of the four-way power divider, and port #2 is followed by one of the feed ports of the antenna array. Two transverse slots, which enable interlayer transmission, are cut out from the copper layer between the two laminates. To improve the impedance matching over an increased operation bandwidth, the distance between the two transverse slots should be around $\lambda/4$ where λ is the wavelength in the laminates. The simulation shows that the 180° SIW elbow with two transverse slots exhibits wider operation bandwidth and lower insertion loss than the 180° elbow with only one slot. In order to decrease the return loss, the width of the SIW close to the end short wall in the bottom laminate is broadened from w_{p1} to w_{int} . The dimensions of the design parameters used in designing this 180° SIW elbow are shown in Table 6.2. Fig. 6.21 shows the simulated S -parameters of the designed 180° elbow. It is seen that the impedance bandwidth for $|S_{11}|$ less than -30 dB is in the range from 19 GHz to 21 GHz. The designed 180° elbow also shows lower insertion loss from port #1 to #2, which is less than 0.22 dB over the bandwidth from 18 GHz to 22 GHz.

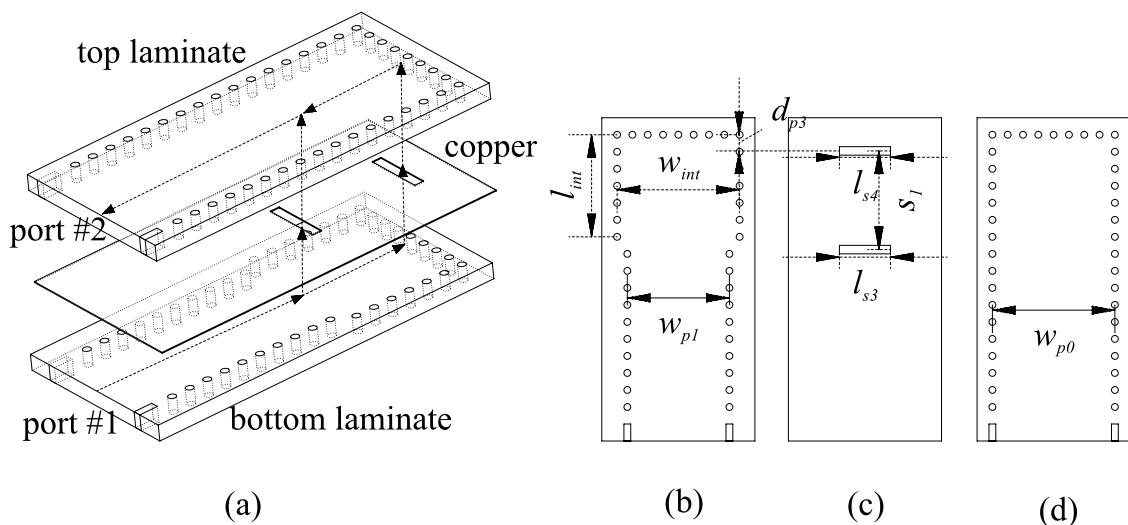


Fig. 6.20 Configuration of the designed SIW elbow. (b) Bottom layer. (b) Transverse slots on the ground plane. (c) Top layer.

Fig. 6.22 shows the simulated electric field pattern in the structures including the orthomode transducer, the four-way power dividers and the 180° SIW elbows when feed port #1 of the orthomode transducer is excited. Strong field distribution is observed in the SIWs of the orthomode transducer, the power dividers and the 180° SIW elbow along the x -axis direction. The structures along the y -axis direction are well isolated. In this case, the antenna array sitting at the centre can be differentially excited for horizontal polarization.

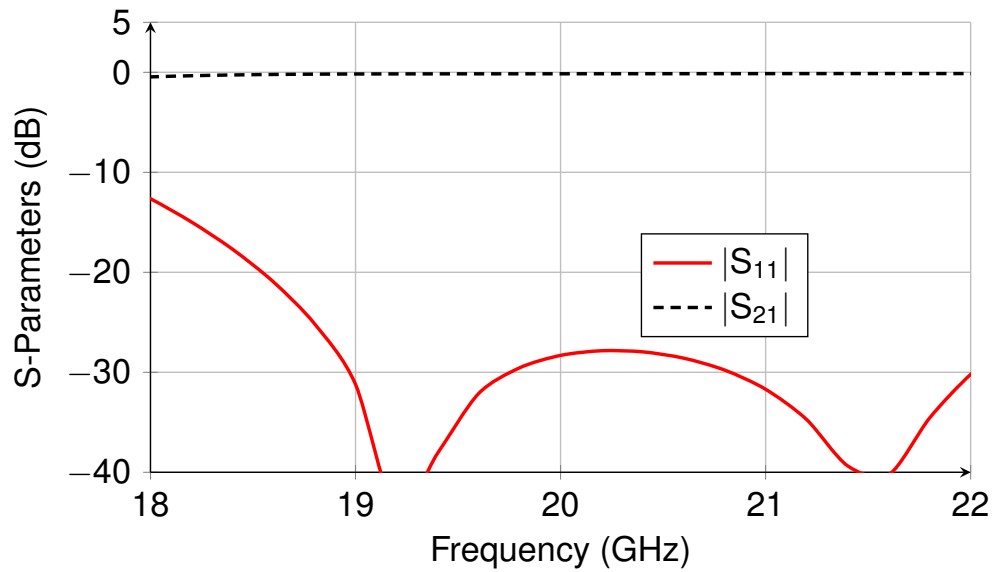


Fig. 6.21 Simulated reflection coefficient $|S_{11}|$ and transmission coefficient $|S_{21}|$ of the designed SIW 180° elbow.

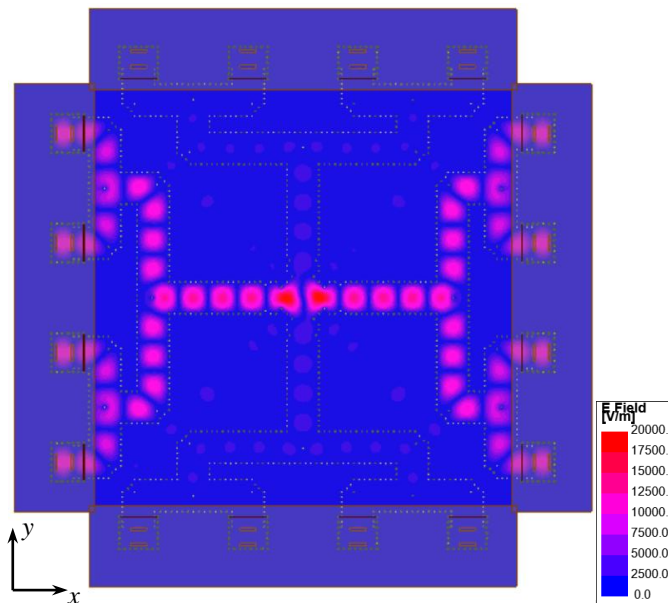


Fig. 6.22 Simulated electric field pattern inside the cascaded structure including the orthomode transducer, the four-way power dividers and the 180° SIW elbows.

6.4 Fabrication and experimental results

In the last two sections, the working mechanisms, design procedures, simulated results of the 2×2 -element subarray antenna, dual-polarized antenna array and three key components used in designing the antenna array are detailed. Based on these fundamentals, a prototype of the designed antenna array is fabricated. In this section, the fabrication of this antenna array, and its measured results including the S -parameters, radiation patterns and realized gain will be given and discussed.

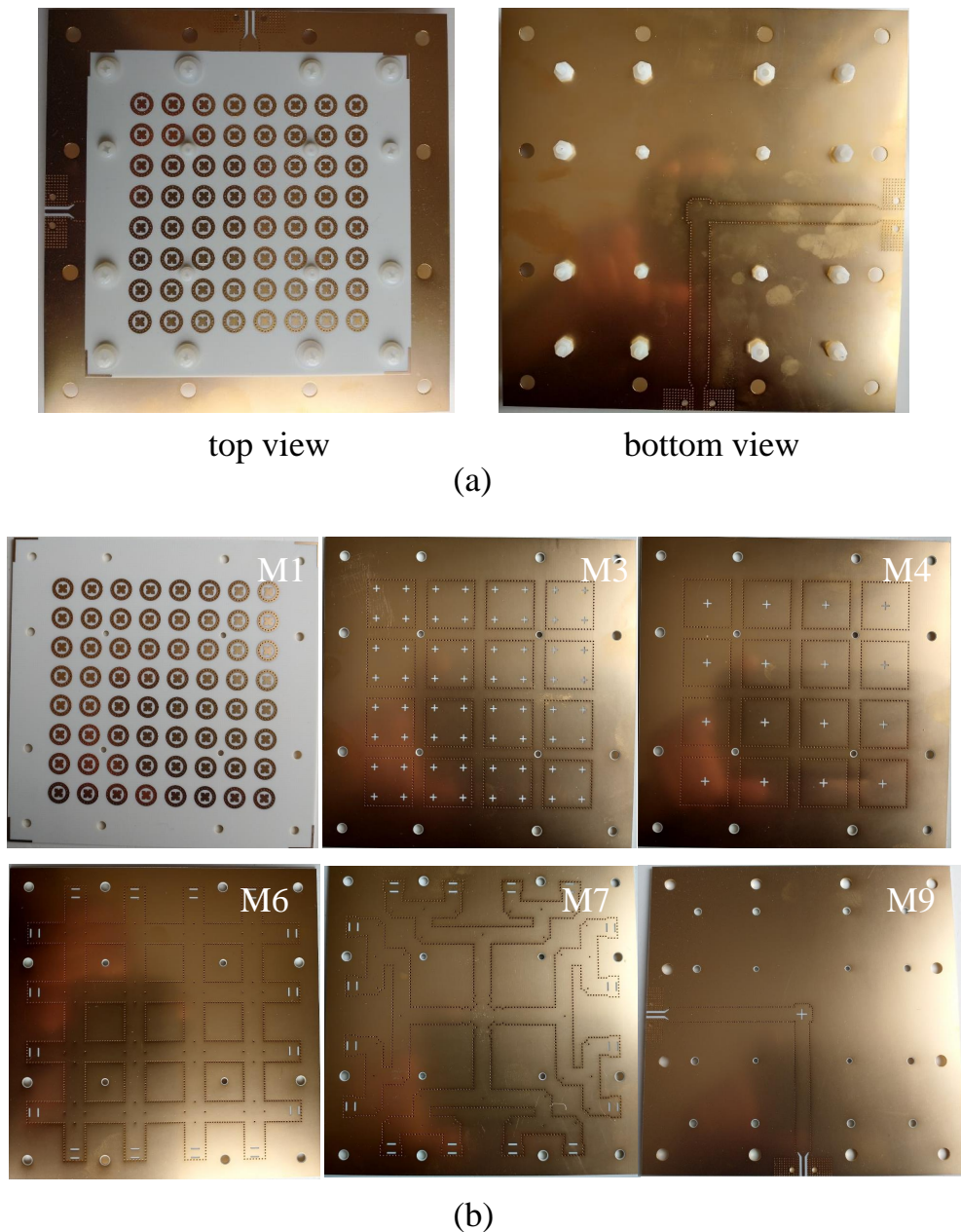


Fig. 6.23 Fabricated prototype of the designed differentially fed dual polarized antenna array. (a) Top and bottom view. (b) Different copper layers of the antenna array.

6.4.1 Fabricated prototype

To validate the design, the proposed differentially fed dual-polarized antenna array is fabricated and tested. The designed antenna array is fabricated by standard PCB processing technology with low cost. The fabricated prototype of this antenna array is shown in Fig. 6.23. Fig. 6.23(a) shows the top and bottom view of the fabricated array antenna. As can be seen from this figure, all the double-sided PCB laminates are stacked up and then screwed tightly with nylon screws. To minimize the misalignment among these laminates as much as possible, densely enough screw holes and proper alignment marks are included

in each laminate layers before the fabrication. Fig. 6.23(b) shows the patterns on different copper layers constructing the design. Because the same etched patterns are found on the back-to-back copper layer, only the copper layers M1, M3, M4, M6, M7 and M9 are illustrated in Fig. 6.23(b). The S -parameter measurement of this prototyped antenna array is carried out by using the vector network analyser Anritsu 37397C, and the far field radiation patterns and the realized gain are obtained in the anechoic chamber.

6.4.2 Reflection and port coupling coefficient

Fig. 6.24 shows the measured and simulated reflection coefficients and the port coupling coefficients. The measured results are in good agreement with the simulations. The measured reflection coefficients for $|S_{11}|$ and $|S_{22}|$ less than -10 dB are in the frequency bandwidth from 19.2 GHz to 20.7 GHz, which is slightly wider than the simulated operation bandwidth of the 2×2 -element subarray antenna due to the presence of the feed networks. The measured coupling coefficient $|S_{21}|$ between feed ports #1 and #2 are less than -20 dB over the impedance bandwidth 19.2–20.7 GHz.

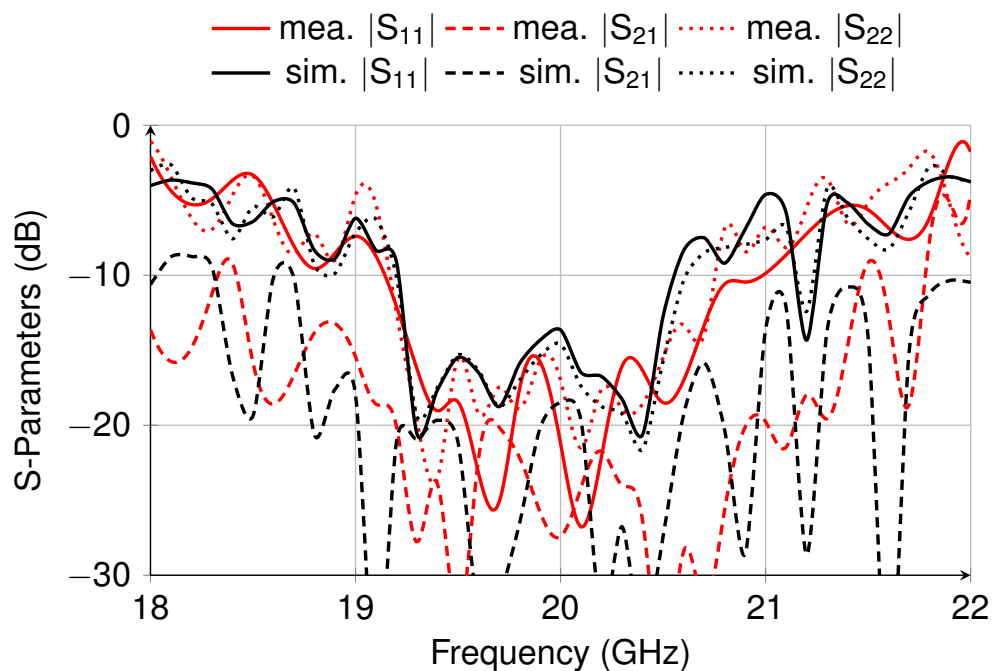


Fig. 6.24 Measured and simulated reflection coefficients $|S_{11}|$ and $|S_{22}|$, and the port coupling coefficient $|S_{21}|$.

6.4.3 Radiation patterns and gain

Fig. 6.25 gives the measured and simulated normalized far field radiation patterns of the designed differentially fed dual-polarized antenna array with different port excitations. The radiation patterns at three frequencies 19.2 GHz, 20 GHz and 20.6 GHz are illustrated

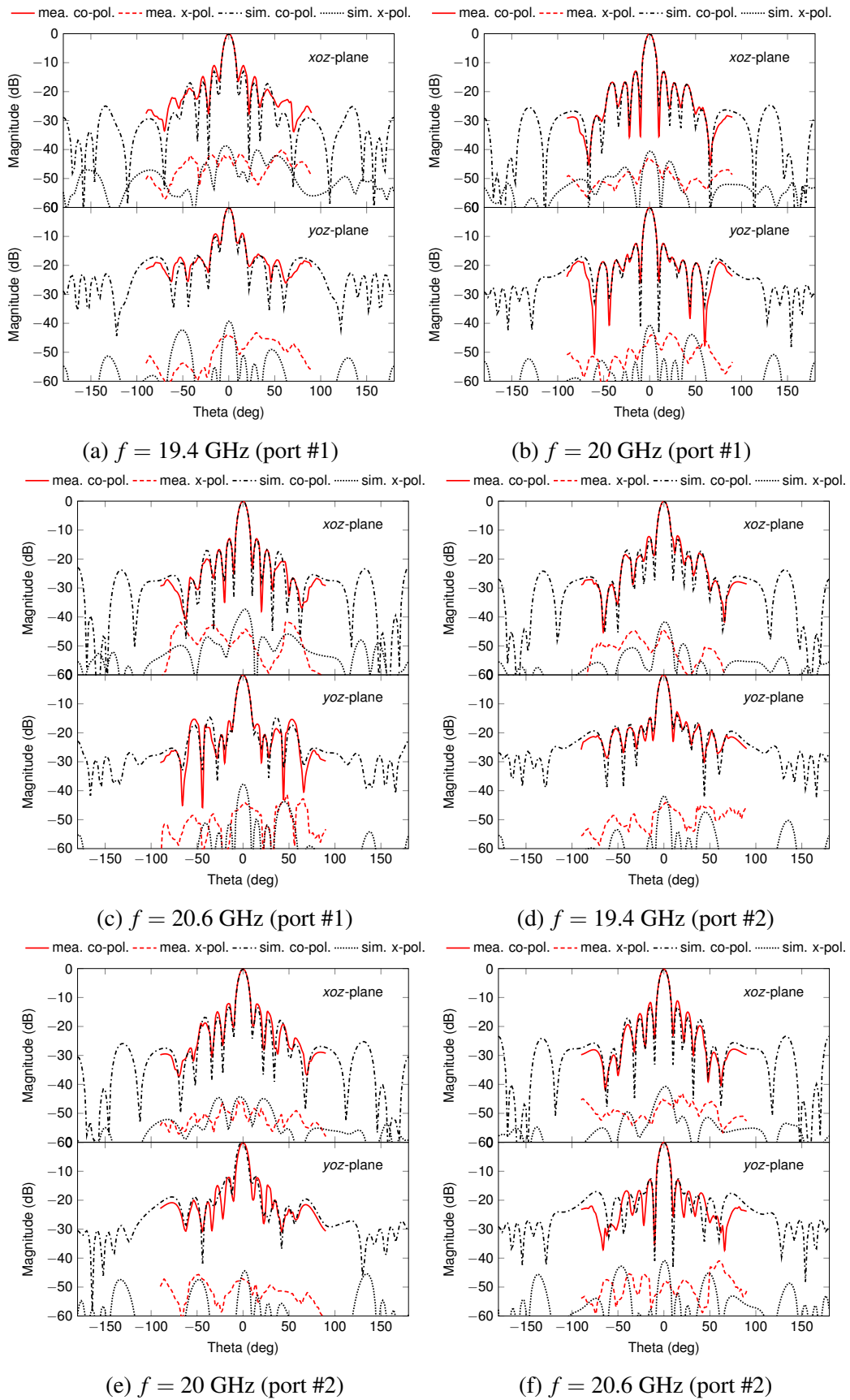


Fig. 6.25 Normalized far-field radiation patterns at the frequencies 19.4 GHz, 20 GHz and 20.6 GHz when port #1 or port #2 is excited.

in this figure. When feed port #1 and #2 is excited, the designed antenna array works with VP and HP, respectively. With different port excited, the measured radiation patterns agree well with the simulated ones in both the xoz - and yoz -plane. In the far field measurement, the radiation patterns out of the range from -90° to 90° are not obtained because of the limitation of the measurement system in the anechoic chamber. It is seen that the designed antenna array shows excellent radiation performance with the main beam pointing to the broadside. Besides, the measured and simulated radiation patterns in both the xoz - and yoz -plane look very similar to each other and the radiation patterns almost keep constant at different operation frequencies of the antenna array. The measured XPDs in the two planes are about 43 dB at the centre frequency 20 GHz. The first SLLs are less than -14 dB in both the xoz - and yoz -plane. Thanks to high symmetry of the designed antenna array, similar far field radiation patterns in the xoz - and yoz -plane at different frequencies are observed when feed port #2 is excited for HP.

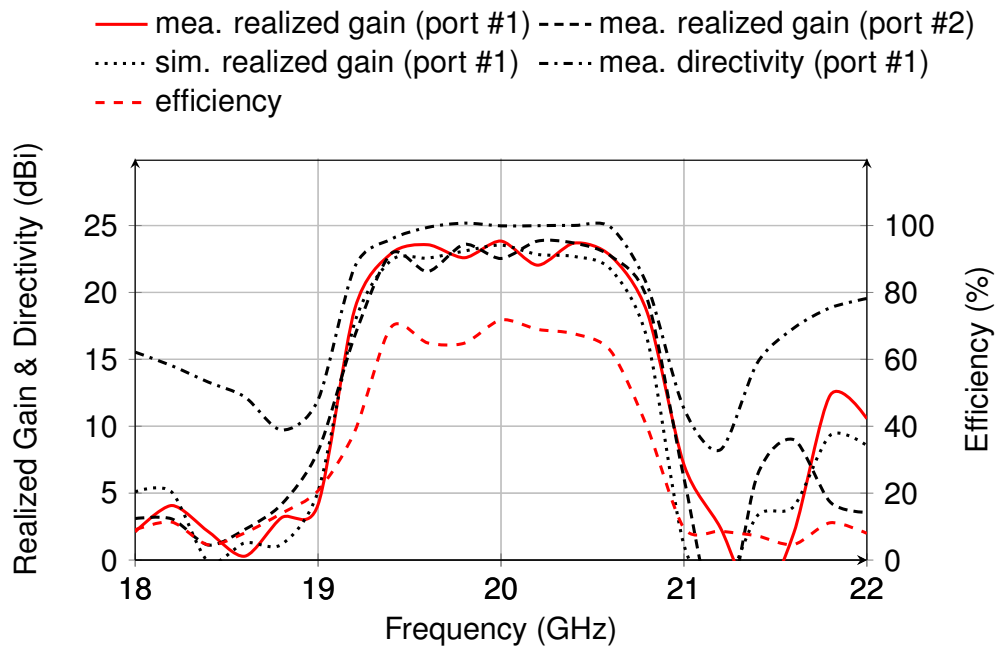


Fig. 6.26 Measured and simulated gain, directivity and radiation efficiency of the designed differential fed dual polarized antenna array.

The measured and simulated realized gains of the designed antenna array are presented in Fig. 6.26. The measured results agree well with the simulations. It is seen that the maximum realized gain measures 22.8 dBi at the frequency 19.9 GHz when port #1 is excited. Over the frequency bandwidth from 19.2 GHz to 20.6 GHz, the designed antenna array shows stable gain, which is on an average of 22.2 dBi. The measured and simulated realized gain are decreased to lower than 5 dBi at the frequency points 19 GHz and 21.1 GHz, which indicates the designed antenna array also has good frequency selectivity. The antenna array shows similar tendency of the realized gain varying with the frequencies with port #2 excited. The maximum simulated directivity of this antenna

Table 6.3 Comparison between this antenna and the reported dual-polarized antenna arrays

Ref.	B	XPD	No. of Elements	G_{max}	Feed Network	Fab.	h	η_{ap}
[48]	13.2%	27 dB	8×8	26.1 dBi	series-corporate	CNC	$2.70\lambda_0$	75%
[76]	1.5%	25 dB	11×12	22.2 dBi	series-corporate	PCB	$0.14\lambda_0$	22%
[186]	17.1%	20 dB	8×8	22.3 dBi	full-corporate	PCB	$0.47\lambda_0$	46%
[187]	23.3%	15 dB	8×8	25.8 dBi	full-corporate	PCB	$0.70\lambda_0$	69%
[188]	12.2%	30 dB	8×8	19.6 dBi	full-corporate	LTCC	$0.29\lambda_0$	50%
[190]	1.1%	n.a.	15×15	26.3 dBi	series-corporate	PCB	$0.32\lambda_0$	30%
[254]	22.2%	18 dB	8×8	n.a.	probe feed	CNC	$1.10\lambda_0$	n.a.
This work	7.5%	43 dB	8×8	22.8 dBi	series-corporate	PCB	$0.27\lambda_0$	51%

array is about 25 dBi. In this figure, the simulated radiation efficiency of this antenna array is calculated by using the simulated directivity and the simulated realized gain. It is seen that the radiation efficiency of the designed antenna array reaches to its maximum 71% at 19.9 GHz and the radiation efficiency is higher than 61% over the operation bandwidth, 19.2–20.6 GHz.

6.4.4 Comparison and discussion

The designed dual-polarized antenna array is differentially fed by an orthomode transducer to realize low complexity and high XPD. A comparison between this proposed antenna array with other recently reported dual-polarized antenna arrays working at sub-mmWave and mmWave frequencies is carried out in Table. 6.3. In this table, the aperture efficiency η_{ap} of an antenna array is calculated by using (3.7). G_{max} represents the maximum realized gain and $h(\lambda_0)$ is the profile of the antenna array in wavelength. The dual polarized antenna array reported in [76] can be realized with its feed networks on a single laminate layer, but it is very bulky and suffers very low aperture efficiency due to its orthogonal antenna elements are interleaved with each other. The dual polarized antenna array designed in [254] suffers low XPD and has very high profile, although it can operate in a wide bandwidth. The dual-polarized antenna arrays reported in [48, 186, 188] are very complicated in structure, since the feed networks for exciting the orthogonal polarizations are implemented on different

laminated layers in order to prevent congestion of the feed networks. The complexity of the antenna arrays reported in [187] and [190] is much reduced. Thus, compared with the aforementioned antenna arrays, these antennas can be realized with less difficulty and low cost. However, the antenna array designed in [187] has low XPD which is not higher than 15 dB, and the antenna array reported in [190] can operate in a very limited bandwidth and it has low aperture efficiency as well. In contrast, the proposed dual-polarized antenna array has simple configuration because the series feed networks are considered in the design of the 2×2 -element subarray antenna. Compared with the reported works in [48, 186, 188] in which the feed networks for different polarizations are realized on separate laminated layers, the proposed antenna array can be implemented with less laminated layers. Besides that, the proposed antenna array also exhibits substantial enhancement in performance when compared with the other reported antenna arrays. As tabulated in Table 6.3, the designed dual-polarized antenna array has advantages in terms of high XPD (43 dB), high aperture efficiency (51%), low profile ($0.27\lambda_0$) and ease of fabrication.

6.5 Summary

In this chapter, a dual-polarized planar antenna array differentially fed by an orthomode transducer was developed. Compared with the traditional dual-polarized antenna arrays, the developed antenna array has simple configuration and can be realized with less laminated layers since the series feed networks are considered in the design of its 2×2 -element subarray antenna. Low complexity of the designed antenna array is enabled by using a via-loaded crossover structure. The antenna array can operate in the frequency bandwidth 19.2–20.7 GHz. The operation bandwidth of this antenna is enhanced by introducing triple resonance in the 2×2 -element subarray antenna. In this chapter, the working mechanism, design produces and three key components of this dual-polarized antenna array are synthesised and described in detail. The antenna array was fabricated, measured and compared with the reported dual-polarized antenna array working at sub-mmWave and mmWave frequencies. The measure results demonstrate that the designed antenna array features in high XPD (43 dB), high gain (22.8 dBi), stable radiation patterns and high aperture efficiency (51%). Besides, the designed antenna array can be easily fabricated by using standard PCB processing technology with low cost. Thus, the designed dual-polarized antenna array differentially fed by an orthomode transducer is a potential candidate for geostationary satellite communications that can radiate fixed beams illuminating areas with high density of users and devices.

Chapter 7

Conclusion and Future Work

7.1 Conclusion

Sub-mmWave and mmWave technology have been evaluated the best candidate frequencies for use in future mobile communications since more bandwidth can be allocated to deliver faster, higher quality video, multimedia content and services. They stimulate extensive research on wireless systems with high integration, small size, multi-functionality, and low cost. The antennas working with dual polarization are considered as an effective solution to achieve high channel capacity and high system reliability. In addition, they could also significantly reduce the volume/size and cost of wireless systems.

In this thesis, four antenna arrays having high XPD, high port isolation and low complexity are designed. To achieve high integration, small size and low loss, the feed networks were seriously considered and included in the antenna element/array design. In addition, to fulfil the requirements from different applications, the antenna complexity, substrate layers, fabrication cost were also taken into consideration. Different dual polarized antennas having different functions were developed in this thesis in order to tailor the needs from potential application scenarios. The antenna gain improvement and operation bandwidth were also studied in the designs.

In this thesis, the design approaches of dual polarized antenna arrays were firstly discussed, and then the state of the art in dual polarized mmWave antenna arrays were detailed. In Chapter 3, a $\pm 45^\circ$ dual slant polarized antenna arrays working at 28 GHz was proposed for mmWave base station applications. The proposed dual slant polarized antenna was designed by using a corner-fed SIW cavity that supports diagonal TE_{120} and TE_{210} modes in order to achieve high port isolation and high XPD. Bandwidth improvement in this antenna was achieved by placing four corner-truncated patches connected by a cross strip over the SIW cavity. The antenna was well synthesised in terms of the beneficial effects originated from the corner-fed cavity, the cross strip and the corner truncation. Then, an antenna array with 2×8 dual slant polarized antenna elements was designed. In order to suppress the side effect caused by structure discontinuity, a new two-way power

divider and a new series feed network were developed. The grounded shorted patch was introduced in designing these feed networks. The proposed dual slant antenna array shows advantages in terms of high XPD, good aperture efficiency, compact size, low profile and simple configuration.

In Chapter 4, a new architecture of differentially fed dual polarized 2D multibeam antenna array was proposed for the purpose of achieving low complexity and high XPD when beams scan to the maximum pointing angles. Based on this concept, a differentially fed dual polarized antenna array was realized and prototyped. The antenna element was designed in the form of cavity backed shorted patch antenna. High XPD and wide -3 dB beamwidth were achieved in the designed antenna element. The multibeam networks in the design was realized by using two sets of SIW 4×4 Butler Matrix, and differential excitation was achieved by a differential power divider. The overall configuration of the designed dual polarized multibeam antenna array was implemented with only two laminates. The proposed dual polarized 2D multibeam antenna array features dual polarization, high XPD, low profile, low complexity and low fabrication cost.

In Chapter 5, a frequency-scanning dual polarized cross slot antenna array was proposed and designed. In this design, the crossover structure with four metallized vias placed around the cross junction was introduced to enable high port isolation and excite the antenna element from orthogonal directions. A cross slot was etched over the cross structure to realize dual polarization radiation. The working principle and design procedures of this antenna array were thoroughly synthesised and discussed. Compared with the reported works, this antenna array shows advantages of low complexity, high XPD, high gain, wide frequency-scanning range and high aperture efficiency.

In Chapter 6, a dual polarized planar antenna array differentially fed by an orthomode transducer was proposed and designed for geostationary satellite communications that produces fixed beams for areas with high density of users and devices. Compared with traditional dual polarized antenna arrays, the designed antenna array features simpler structure, less laminate layers and higher XPD. Structure simplification in this antenna array was achieved by incorporating the series feed networks into the design of the 2×2 -element subarray antenna. The via-loaded crossover was introduced in the design to achieve high port isolation. The operation bandwidth of this antenna was enhanced by introducing triple resonance in the 2×2 -element subarray antenna. The design of three key components which includes the orthomode transducer, four-way power divider and the 180° SIW elbow was also detailed in this chapter. The measured results show that the designed dual polarized antenna array has high XPD, high realized gain, stable radiation patterns and high aperture efficiency. Table 7.1 summaries the features and technical contributions of the developed dual polarized antenna arrays in this thesis.

Table 7.1 Summary of the developed dual polarized antenna arrays in this thesis

Antenna structure	Location	Performance	Profile	Advantages	Limitations	Application scenarios
Dual slant polarized cavity-backed corner-truncated patch antenna array	Chapter 3	port isolation > 20 dB, $B = 6.0\%$, $G_{max} = 16.7$ dBi, XPD > 25 dB, $\eta_{ap} = 39\%$, $\eta_{rad.} = 75\%$	$0.076\lambda_0$	improved port isolation, enhanced the bandwidth, low complexity, low profile	distorted radiation patterns due to board-to-board misalignment	5G mmWave outdoor base stations
Dual polarized 2D cavity-backed shorted patch antenna array with switched beams	Chapter 4	port isolation > 20 dB, $B = 8.6\%$, XPD > 28 dB	$0.09\lambda_0$	High port isolation, high XPD when beams scan to the maximum pointing angles, low complexity, low profile	only has 2×2 radiation beams, de-graded SLLs	5G mmWave indoor base stations
Dual polarized frequency controlled cross slot antenna array realized on a single laminate	Chapter 5	port isolation > 42 dB, $G_{max} = 24.9$ dBi, XPD > 26 dB, $\eta_{ap} = 40\%$, $\eta_{rad.} = 76\%$, scan angle = $(-18^\circ, 18^\circ)$	$0.042\lambda_0$	High port isolation, able to realized on a single laminate, low profile, low complexity, high gain, wide frequency-scanning angle	relatively narrow bandwidth	imaging, enclosed buildings and tunnels
Dual cavity backed slot-coupled patch antenna array	Chapter 6	port isolation > 20 dB, $B = 7.5\%$, $G_{max} = 22.8$ dBi, XPD > 43 dB, $\eta_{ap} = 51\%$, $\eta_{rad.} = 71\%$	$0.27\lambda_0$	High port isolation, enhanced bandwidth, flat gain, high XPD, low complexity, low profile	high loss from the laminates	geostationary satellite communications

7.2 Future work

In this research programme, four dual polarized sub-mmWave and mmWave antenna arrays have been completed. However, they are designed to address several specific problems and thus they can only be deployed in specific application scenarios. Dual polarized antenna arrays have other potential applications in future wireless communications. For example, dual circularly polarized sub-mmWave and mmWave antenna array are considered as a good candidate to achieve high data rate and high reliability in SOTM. The challenges in designing dual circularly polarized antenna array are high complexity, low radiation efficiency and high axial ratio when beams scan off the boresight, etc. Thus, how to design a dual circularly polarized antenna array that can address these problems and fulfil the requirement from satellite communications could be a new line of research.

In many applications, the antenna arrays are required to steer high gain beams for the purpose of achieving wide coverage and exploiting spatial diversity. Passive multibeam networks are widely used in beam scanning antenna array designs due to low cost and high design flexibility. However, it would be very tricky to design the passive multibeam networks for a mmWave dual polarized antenna array having a large number of antenna elements because of constraint space and high complexity. In addition, high cross polarization radiation can be excited when beams scan off the boresight in these antenna arrays. Thus, how to design a high XPD dual polarized beam scanning antenna array with large number of antenna elements would be another research topic in my future work.

Antenna arrays that can operate in multiple band are also significant in many application scenarios. For example, SOTM requires that the antenna array should operate at two different frequencies, 20 GHz for downlink and 30 GHz for uplink. In 5G or 6G mobile communications, it is required that base stations should operate at sub-6 GHz and mmWave frequencies simultaneously in order to reduce the cost, volume and weight of base station equipment. However, the dual band antenna array with large frequency ratio face challenges such as high mutual coupling, limited beam scanning angles, complicated feed networks, etc. Thus, how to design a dual band dual polarized antenna array that is free from these problems will be also considered in my future work.

Terahertz (THz) communications can provide massive frequency spectrum. Hence, it would be an attractive solution to realize ultra-high speed wireless communications by exploiting THz waves in the future. Most of the reported THz antennas are simply designed from mmWave antennas. Even though a lot of attention has been paid, the research of THz antennas is still in the preliminary stage. How to design high efficiency and high gain THz antennas/arrays with dual polarization and beam scanning capability will be another research work in the future.

References

- [1] C. E. Shannon, "A mathematical theory of communication," *The Bell System Technical Journal*, vol. 27, no. 3, pp. 379–423, 1948.
- [2] R. V. L. Hartley, "Transmission of information1," *Bell System Technical Journal*, vol. 7, no. 3, pp. 535–563, 1928.
- [3] T. Union, "International telecommunication union," *Yearbook of Statistics 1991–2000*, 2001.
- [4] E. U. T. R. Access, "User equipment (UE) radio transmission and reception," *3GPP TS*, vol. 36, p. V10, 2011.
- [5] C. Eklund, R. B. Marks, S. Ponnuswamy, K. L. Stanwood, and N. Waes, *Wireless-MAN@: Inside the IEEE 802.16 Standard for Wireless Metropolitan Area Networks*. IEEE Press, 2006.
- [6] W. Liu, T. Wei, Y. Huang, C. Chan, and S. Jou, "All-digital synchronization for SC/OFDM mode of IEEE 802.15.3c and IEEE 802.11ad," *IEEE Transactions on Circuits and Systems I: Regular Papers*, vol. 62, no. 2, pp. 545–553, 2015.
- [7] V. W. S. Wong, R. Schober, D. W. K. Ng, and L. C. Wang, *Key Technologies for 5G Wireless Systems*. Cambridge University Press, 2017.
- [8] X. Yi, G. Feng, Z. Liang, C. Wang, B. Liu, C. Li, K. Yang, C. C. Boon, and Q. Xue, "A 24/77 GHz dual-band receiver for automotive radar applications," *IEEE Access*, vol. 7, pp. 48053–48059, 2019.
- [9] V. Eiceg, H. Sampath, and S. Catreux-Erceg, "Dual-polarization versus single-polarization MIMO channel measurement results and modeling," *IEEE Transactions on Wireless Communications*, vol. 5, no. 1, pp. 28–33, 2006.
- [10] J. W. Wallace and M. A. Jensen, "Modeling the indoor MIMO wireless channel," *IEEE Transactions on Antennas and Propagation*, vol. 50, no. 5, pp. 591–599, 2002.
- [11] C. Oestges, V. Erceg, and A. J. Paulraj, "Propagation modeling of MIMO multipolarized fixed wireless channels," *IEEE Transactions on Vehicular Technology*, vol. 53, no. 3, pp. 644–654, 2004.
- [12] O. Jo, J. Kim, J. Yoon, D. Choi, and W. Hong, "Exploitation of dual-polarization diversity for 5G millimeter-wave MIMO beamforming systems," *IEEE Transactions on Antennas and Propagation*, vol. 65, no. 12, pp. 6646–6655, 2017.

- [13] A. Ludwig, "The definition of cross polarization," *IEEE Transactions on Antennas and Propagation*, vol. 21, no. 1, pp. 116–119, 1973.
- [14] A. Garcia-Aguilar, J. Inclan-Alonso, L. Vigil-Herrero, J. Fernandez-Gonzalez, and M. Sierra-Perez, "Low-profile dual circularly polarized antenna array for satellite communications in the X band," *IEEE Transactions on Antennas and Propagation*, vol. 60, no. 5, pp. 2276–2284, 2012.
- [15] M. Maqsood, S. Gao, T. W. C. Brown, M. Unwin, R. de vos Van Steenwijk, J. D. Xu, and C. I. Underwood, "Low-cost dual-band circularly polarized switched-beam array for global navigation satellite system," *IEEE Transactions on Antennas and Propagation*, vol. 62, no. 4, pp. 1975–1982, 2014.
- [16] M. Khan, Z. Yang, and K. Warnick, "Dual-circular-polarized high-efficiency antenna for Ku-band satellite communication," *IEEE Antennas and Wireless Propagation Letters*, vol. 13, pp. 1624–1627, 2014.
- [17] S. Mener, R. Gillard, and L. Roy, "A dual-band dual-circular-polarization antenna for Ka-band satellite communications," *IEEE Antennas and Wireless Propagation Letters*, vol. 16, pp. 274–277, 2017.
- [18] A. Elsherbini, J. Wu, and K. Sarabandi, "Dual polarized wideband directional coupled sectorial loop antennas for radar and mobile base-station applications," *IEEE Transactions on Antennas and Propagation*, vol. 63, no. 4, pp. 1505–1513, 2015.
- [19] F. Qin, S. S. Gao, Q. Luo, C. Mao, C. Gu, G. Wei, J. Xu, J. Li, C. Wu, K. Zheng, and S. Zheng, "A simple low-cost shared-aperture dual-band dual-polarized high-gain antenna for synthetic aperture radars," *IEEE Transactions on Antennas and Propagation*, vol. 64, no. 7, pp. 2914–2922, 2016.
- [20] B. G. Porter, L. L. Rauth, J. R. Mura, and S. S. Gearhart, "Dual-polarized slot-coupled patch antennas on duroid with teflon lenses for 76.5-GHz automotive radar systems," *IEEE Transactions on Antennas and Propagation*, vol. 47, no. 12, pp. 1836–1842, 1999.
- [21] R. V. S. R. Krishna and R. Kumar, "A dual-polarized square-ring slot antenna for UWB, imaging, and radar applications," *IEEE Antennas and Wireless Propagation Letters*, vol. 15, pp. 195–198, 2016.
- [22] M. Secmen, S. Demir, and A. Hizal, "Dual-polarised T/R antenna system suitable for FMCW altimeter radar applications," *IEE Proceedings - Microwaves, Antennas and Propagation*, vol. 153, no. 5, pp. 407–412, 2006.
- [23] R. G. Vaughan, "Polarization diversity in mobile communications," *IEEE Transactions on Vehicular Technology*, vol. 39, no. 3, pp. 177–186, 1990.
- [24] C. B. Dietrich, K. Dietze, J. R. Nealy, and W. L. Stutzman, "Spatial, polarization, and pattern diversity for wireless handheld terminals," *IEEE Transactions on Antennas and Propagation*, vol. 49, no. 9, pp. 1271–1281, 2001.

- [25] J. J. A. Lempiainen and J. K. Laiho-Steffens, "The performance of polarization diversity schemes at a base station in small/micro cells at 1800 MHz," *IEEE Transactions on Vehicular Technology*, vol. 47, no. 3, pp. 1087–1092, 1998.
- [26] W. Lee and Yu Yeh, "Polarization diversity system for mobile radio," *IEEE Transactions on Communications*, vol. 20, no. 5, pp. 912–923, 1972.
- [27] R. U. Nabar, H. Bolcskei, V. Erceg, D. Gesbert, and A. J. Paulraj, "Performance of multiantenna signaling techniques in the presence of polarization diversity," *IEEE Transactions on Signal Processing*, vol. 50, no. 10, pp. 2553–2562, 2002.
- [28] Y. J. Sung, "Reconfigurable patch antenna for polarization diversity," *IEEE Transactions on Antennas and Propagation*, vol. 56, no. 9, pp. 3053–3054, 2008.
- [29] P. Qin, Y. J. Guo, Y. Cai, E. Dutkiewicz, and C. Liang, "A reconfigurable antenna with frequency and polarization agility," *IEEE Antennas and Wireless Propagation Letters*, vol. 10, pp. 1373–1376, 2011.
- [30] R. K. Singh, A. Basu, and S. K. Koul, "A novel reconfigurable microstrip patch antenna with polarization agility in two switchable frequency bands," *IEEE Transactions on Antennas and Propagation*, vol. 66, no. 10, pp. 5608–5613, 2015.
- [31] N. Nguyen-Trong, L. Hall, and C. Fumeaux, "A frequency- and polarization-reconfigurable stub-loaded microstrip patch antenna," *IEEE Transactions on Antennas and Propagation*, vol. 63, no. 11, pp. 5235–5240, 2015.
- [32] S. Zhong, X. Yang, and S. Gao, "Polarization-agile microstrip antenna array using a single phase-shift circuit," *IEEE Transactions on Antennas and Propagation*, vol. 52, no. 1, pp. 84–87, 2004.
- [33] L. Ge, Y. Li, J. Wang, and C. Sim, "A low-profile reconfigurable cavity-backed slot antenna with frequency, polarization, and radiation pattern agility," *IEEE Transactions on Antennas and Propagation*, vol. 65, no. 5, pp. 2182–2189, 2017.
- [34] D. Lee and S. Pyo, "Dual-reconfigurable microstrip antenna for polarisation agility and diversity," *Electronics Letters*, vol. 51, no. 16, pp. 1226–1227, 2015.
- [35] S. B. Chakrabarty, F. Klefenz, and A. Dreher, "Dual polarized wide-band stacked microstrip antenna with aperture coupling for SAR applications," in *IEEE Antennas and Propagation Society International Symposium. Transmitting Waves of Progress to the Next Millennium. 2000 Digest. Held in conjunction with: USNC/URSI National Radio Science Meeting (C)*, vol. 4, pp. 2216–2219 vol.4, 2000.
- [36] K. Li, T. Dong, and Z. Xia, "A broadband shared-aperture L/S/X-band dual-polarized antenna for SAR applications," *IEEE Access*, vol. 7, pp. 51417–51425, 2019.
- [37] C. Mao, S. Gao, C. Tienda, T. Rommel, A. Patyuchenko, M. Younis, L. Boccia, E. Arneri, S. Glisic, U. Yodprasit, P. Penkala, M. Krstic, F. Qin, O. Schrape, A. Koczor, G. Amendola, and V. Petrovic, "X/Ka-band dual-polarized digital beamforming synthetic aperture radar," *IEEE Transactions on Microwave Theory and Techniques*, vol. 65, no. 11, pp. 4400–4407, 2017.

- [38] S. Gao, Y. Rahmat-Samii, R. E. Hodges, and X. Yang, "Advanced antennas for small satellites," *Proceedings of the IEEE*, vol. 106, no. 3, pp. 391–403, 2018.
- [39] S. Gao, Q. Luo, and F. Zhu, *Circularly Polarized Antennas*. New York: John Wiley & Sons, 2013.
- [40] Y. Yu, W. Hong, Z. H. Jiang, and H. Zhang, "E -band low-profile, wideband 45° linearly polarized slot-loaded patch and its array for millimeter-wave communications," *IEEE Transactions on Antennas and Propagation*, vol. 66, no. 8, pp. 4364–4369, 2018.
- [41] J. Xu, W. Hong, Z. H. Jiang, J. Chen, and H. Zhang, "A Q-band low-profile dual circularly polarized array antenna incorporating linearly polarized substrate integrated waveguide-fed patch subarrays," *IEEE Transactions on Antennas and Propagation*, vol. 65, no. 10, pp. 5200–5210, 2017.
- [42] Y. Zhang, Z. Song, W. Hong, and R. Mittra, "Wideband high-gain $\pm 45^\circ$ dual-polarised stacked patch antenna array for Ku-band back-haul services," *IET Microwaves, Antennas Propagation*, vol. 14, no. 1, pp. 53–59, 2020.
- [43] G. F. Hamberger, S. Trummer, U. Siart, and T. F. Eibert, "A planar dual-polarized microstrip 1-D-beamforming antenna array for the 24-GHz band," *IEEE Transactions on Antennas and Propagation*, vol. 65, no. 1, pp. 142–149, 2017.
- [44] S. Raman and G. M. Rebeiz, "Single- and dual-polarized millimeter-wave slot-ring antennas," *IEEE Transactions on Antennas and Propagation*, vol. 44, no. 11, pp. 1438–1444, 1996.
- [45] X. Wu, F. Yang, F. Xu, and J. Zhou, "Circularly polarized waveguide antenna with dual pairs of radiation slots at Ka-band," *IEEE Antennas and Wireless Propagation Letters*, vol. 16, pp. 2947–2950, 2017.
- [46] H. Chu and Y. Guo, "A filtering dual-polarized antenna subarray targeting for base stations in millimeter-wave 5G wireless communications," *IEEE Transactions on Components, Packaging and Manufacturing Technology*, vol. 7, no. 6, pp. 964–973, 2017.
- [47] T. Li, H. Meng, and W. Dou, "Design and implementation of dual-frequency dual-polarization slotted waveguide antenna array for Ka-band application," *IEEE Antennas and Wireless Propagation Letters*, vol. 13, pp. 1317–1320, 2014.
- [48] G. Huang, S. Zhou, T. Chio, C. Sim, and T. Yeo, "Waveguide-stripline series-corporate hybrid feed technique for dual-polarized antenna array applications," *IEEE Transactions on Components, Packaging and Manufacturing Technology*, vol. 7, no. 1, pp. 81–87, 2017.
- [49] A. E. I. Lamminen, J. Saily, and A. R. Vimpari, "60-GHz patch antennas and arrays on LTCC with embedded-cavity substrates," *IEEE Transactions on Antennas and Propagation*, vol. 56, no. 9, pp. 2865–2874, 2008.

- [50] Y. P. Zhang and D. Liu, "Antenna-on-chip and antenna-in-package solutions to highly integrated millimeter-wave devices for wireless communications," *IEEE Transactions on Antennas and Propagation*, vol. 57, no. 10, pp. 2830–2841, 2009.
- [51] Q. Liao, E. Rajo-Iglesias, and O. Quevedo-Teruel, "Ka-band fully metallic TE₄₀ slot array antenna with glide-symmetric gap waveguide technology," *IEEE Transactions on Antennas and Propagation*, vol. 67, no. 10, pp. 6410–6418, 2019.
- [52] P. Nayeri, M. Liang, R. A. Sabory-García, M. Tuo, F. Yang, M. Gehm, H. Xin, and A. Z. Elsherbeni, "3D printed dielectric reflectarrays: Low-cost high-gain antennas at sub-millimeter waves," *IEEE Transactions on Antennas and Propagation*, vol. 62, no. 4, pp. 2000–2008, 2014.
- [53] Y. Miura, J. Hirokawa, M. Ando, Y. Shibuya, and G. Yoshida, "Double-layer full-corporate-feed hollow-waveguide slot array antenna in the 60-GHz band," *IEEE Transactions on Antennas and Propagation*, vol. 59, no. 8, pp. 2844–2851, 2011.
- [54] D. Deslandes and K. Wu, "Integrated microstrip and rectangular waveguide in planar form," *IEEE Microwave and Wireless Components Letters*, vol. 11, no. 2, pp. 68–70, 2001.
- [55] Feng Xu and Ke Wu, "Guided-wave and leakage characteristics of substrate integrated waveguide," *IEEE Transactions on Microwave Theory and Techniques*, vol. 53, no. 1, pp. 66–73, 2005.
- [56] Y. Cassivi, L. Perreggrini, P. Arcioni, M. Bressan, K. Wu, and G. Conciauro, "Dispersion characteristics of substrate integrated rectangular waveguide," *IEEE Microwave and Wireless Components Letters*, vol. 12, no. 9, pp. 333–335, 2002.
- [57] M. Bozzi, A. Georgiadis, and K. Wu, "Review of substrate-integrated waveguide circuits and antennas," *IET Microwaves, Antennas Propagation*, vol. 5, no. 8, pp. 909–920, 2011.
- [58] B. Lindmark and M. Nilsson, "On the available diversity gain from different dual-polarized antennas," *IEEE Journal on Selected Areas in Communications*, vol. 19, no. 2, pp. 287–294, 2001.
- [59] Y. Gou, S. Yang, Q. Zhu, and Z. Nie, "A compact dual-polarized double E-shaped patch antenna with high isolation," *IEEE Transactions on Antennas and Propagation*, vol. 61, no. 8, pp. 4349–4353, 2013.
- [60] J. Deng, L. Guo, Y. Yin, J. Qiu, and Z. Wu, "Broadband patch antennas fed by novel tuned loop," *IEEE Transactions on Antennas and Propagation*, vol. 61, no. 4, pp. 2290–2293, 2013.
- [61] B. Q. Wu and K. Luk, "A broadband dual-polarized magneto-electric dipole antenna with simple feeds," *IEEE Antennas and Wireless Propagation Letters*, vol. 8, pp. 60–63, 2009.
- [62] M. Barba, "A high-isolation, wideband and dual-linear polarization patch antenna," *IEEE Transactions on Antennas and Propagation*, vol. 56, no. 5, pp. 1472–1476, 2008.

- [63] L. Wen, S. Gao, Q. Luo, Q. Yang, W. Hu, and Y. Yin, "A low-cost differentially driven dual-polarized patch antenna by using open-loop resonators," *IEEE Transactions on Antennas and Propagation*, vol. 67, no. 4, pp. 2745–2750, 2019.
- [64] Y. Zhu, Y. Chen, and S. Yang, "Decoupling and low-profile design of dual-band dual-polarized base station antennas using frequency-selective surface," *IEEE Transactions on Antennas and Propagation*, vol. 67, no. 8, pp. 5272–5281, 2019.
- [65] L. Wen, S. Gao, Q. Luo, C. Mao, W. Hu, Y. Yin, Y. Zhou, and Q. Wang, "Compact dual-polarized shared-dipole antennas for base station applications," *IEEE Transactions on Antennas and Propagation*, vol. 66, no. 12, pp. 6826–6834, 2018.
- [66] M. V. Komandla, G. Mishra, and S. K. Sharma, "Investigations on dual slant polarized cavity-backed massive MIMO antenna panel with beamforming," *IEEE Transactions on Antennas and Propagation*, vol. 65, no. 12, pp. 6794–6799, 2017.
- [67] T. Tomura, Y. Miura, M. Zhang, J. Hirokawa, and M. Ando, "A 45° linearly polarized hollow-waveguide corporate-feed slot array antenna in the 60-GHz band," *IEEE Transactions on Antennas and Propagation*, vol. 60, no. 8, pp. 3640–3646, 2012.
- [68] S. Sugawa, K. Sakakibara, N. Kikuma, and H. Hirayama, "Low-sidelobe design of microstrip comb-line antennas using stub-integrated radiating elements in the millimeter-wave band," *IEEE Transactions on Antennas and Propagation*, vol. 60, no. 10, pp. 4699–4709, 2012.
- [69] Y. Yang, B. Sun, G. Zhang, and L. Shen, "TFSIW-excited dual-polarized array antenna with 30° beam-pointing for millimeter-wave applications," *IEEE Transactions on Antennas and Propagation*, vol. 67, no. 8, pp. 5740–5745, 2019.
- [70] B. Liu, R. Zhao, Y. Ma, Z. Guo, X. Wei, W. Xing, and Y. Wang, "A 45° linearly polarized slot array antenna with substrate integrated coaxial line technique," *IEEE Antennas and Wireless Propagation Letters*, vol. 17, no. 2, pp. 339–342, 2018.
- [71] M. S. Abdallah, Y. Wang, W. M. Abdel-Wahab, and S. Safavi-Naeini, "Design and optimization of SIW center-fed series rectangular dielectric resonator antenna array with 45° linear polarization," *IEEE Transactions on Antennas and Propagation*, vol. 66, no. 1, pp. 23–31, 2018.
- [72] D. Kim, W. Chung, C. Park, S. Lee, and S. Nam, "A series slot array antenna for 45°-inclined linear polarization with SIW technology," *IEEE Transactions on Antennas and Propagation*, vol. 60, no. 4, pp. 1785–1795, 2012.
- [73] A. B. Guntupalli and K. Wu, "45° linearly polarized high-gain antenna array for 60-GHz radio," *IEEE Antennas and Wireless Propagation Letters*, vol. 13, pp. 384–387, 2014.
- [74] M. Sonkki, S. Myllymäki, N. Tervo, M. E. Leinonen, M. Sobocinski, G. Destino, and A. Pärssinen, "Linearly polarized 64-element antenna array for mm-Wave mobile backhaul application," in *12th European Conference on Antennas and Propagation (EuCAP 2018)*, pp. 1–5, 2018.

- [75] Y. J. Cheng, X. Y. Bao, and Y. X. Guo, "60-GHz LTCC miniaturized substrate integrated multibeam array antenna with multiple polarizations," *IEEE Transactions on Antennas and Propagation*, vol. 61, no. 12, pp. 5958–5967, 2013.
- [76] S. Park, Y. Okajima, J. Hirokawa, and M. Ando, "A slotted post-wall waveguide array with interdigital structure for 45° linear and dual polarization," *IEEE Transactions on Antennas and Propagation*, vol. 53, no. 9, pp. 2865–2871, 2005.
- [77] A. Bagheri, J. Petersson, A. Haddadi, and A. A. Glazunov, "A $\pm 45^\circ$ dual-polarized antenna for 5G mmWave applications based on gap waveguide technology," in *2019 International Symposium on Antennas and Propagation (ISAP)*, pp. 1–3, 2019.
- [78] S. Liao and Q. Xue, "Dual polarized planar aperture antenna on ltcc for 60-GHz antenna-in-package applications," *IEEE Transactions on Antennas and Propagation*, vol. 65, no. 1, pp. 63–70, 2017.
- [79] A. I. Sandhu, E. Arnieri, G. Amendola, L. Boccia, E. Meniconi, and V. Ziegler, "Radiating elements for shared aperture Tx/Rx phased arrays at K/Ka Band," *IEEE Transactions on Antennas and Propagation*, vol. 64, no. 6, pp. 2270–2282, 2016.
- [80] Y. R. Ding and Y. J. Cheng, "Ku/Ka dual-band dual-polarized shared-aperture beam-scanning antenna array with high isolation," *IEEE Transactions on Antennas and Propagation*, vol. 67, no. 4, pp. 2413–2422, 2019.
- [81] K. So, K. Luk, C. Chan, and K. Chan, "3D printed high gain complementary dipole/slot antenna array," *Applied Sciences*, vol. 8, no. 8, p. 1410, 2018.
- [82] V. F. Fusco, "Mechanical beam scanning reflectarray," *IEEE Transactions on Antennas and Propagation*, vol. 53, no. 11, pp. 3842–3844, 2005.
- [83] E. Gandini, M. Ettorre, M. Casaletti, K. Tekkouk, L. Le Coq, and R. Sauleau, "SIW slotted waveguide array with pillbox transition for mechanical beam scanning," *IEEE Antennas and Wireless Propagation Letters*, vol. 11, pp. 1572–1575, 2012.
- [84] H. Holter, "Dual-polarized broadband array antenna with BOR-elements, mechanical design and measurements," *IEEE Transactions on Antennas and Propagation*, vol. 55, no. 2, pp. 305–312, 2007.
- [85] G. Wu, S. Qu, and S. Yang, "Wide-angle beam-scanning reflectarray with mechanical steering," *IEEE Transactions on Antennas and Propagation*, vol. 66, no. 1, pp. 172–181, 2018.
- [86] G. Han, B. Du, W. Wu, and B. Yang, "A novel hybrid phased array antenna for satellite communication on-the-move in Ku-band," *IEEE Transactions on Antennas and Propagation*, vol. 63, no. 4, pp. 1375–1383, 2015.
- [87] H. Scott and V. F. Fusco, "360° electronically controlled beam scan array," *IEEE Transactions on Antennas and Propagation*, vol. 52, no. 1, pp. 333–335, 2004.
- [88] B. Rohrdantz, T. Jaschke, T. Reuschel, S. Radziejewski, A. Sieganschin, and A. F. Jacob, "An electronically scannable reflector antenna using a planar active array feed at Ka-band," *IEEE Transactions on Microwave Theory and Techniques*, vol. 65, no. 5, pp. 1650–1661, 2017.

- [89] A. I. Zaghloul and O. Kilic, "Hybrid beam former for distributed-aperture electronically steered arrays," *IEEE Antennas and Wireless Propagation Letters*, vol. 9, pp. 678–681, 2010.
- [90] N. Khandelwal and R. W. Jackson, "Active antenna module for low-cost electronically scanned phased arrays," *IEEE Transactions on Microwave Theory and Techniques*, vol. 56, no. 10, pp. 2286–2292, 2008.
- [91] R. A. Alhalabi and G. M. Rebeiz, "High-efficiency angled-dipole antennas for millimeter-wave phased array applications," *IEEE Transactions on Antennas and Propagation*, vol. 56, no. 10, pp. 3136–3142, 2008.
- [92] A. A. Eldek, "Ultrawideband double rhombus antenna with stable radiation patterns for phased array applications," *IEEE Transactions on Antennas and Propagation*, vol. 55, no. 1, pp. 84–91, 2007.
- [93] A. G. Toshev, "Multipanel concept for wide-angle scanning of phased array antennas," *IEEE Transactions on Antennas and Propagation*, vol. 56, no. 10, 2008.
- [94] E. Lier and A. Cherrette, "An intermodulation suppression technique for transmit active phased array satellite antennas with multiple shaped beams," *IEEE Transactions on Antennas and Propagation*, vol. 53, no. 5, pp. 1853–1858, 2005.
- [95] M. C. Viganó, D. Llorens del Río, F. Bongard, and S. Vaccaro, "Sparse array antenna for Ku-band mobile terminals using 1 bit phase controls," *IEEE Transactions on Antennas and Propagation*, vol. 62, no. 4, pp. 1723–1730, 2014.
- [96] K. Wincza, K. Staszek, I. Slomian, and S. Gruszczynski, "Scalable multibeam antenna arrays fed by dual-band modified Butler Matrices," *IEEE Transactions on Antennas and Propagation*, vol. 64, no. 4, pp. 1287–1297, 2016.
- [97] K. Tekkouk, J. Hirokawa, R. Sauleau, M. Ettorre, M. Sano, and M. Ando, "Dual-layer ridged waveguide slot array fed by a Butler Matrix with sidelobe control in the 60-GHz band," *IEEE Transactions on Antennas and Propagation*, vol. 63, no. 9, pp. 3857–3867, 2015.
- [98] P. Chen, W. Hong, Z. Kuai, J. Xu, H. Wang, J. Chen, H. Tang, J. Zhou, and K. Wu, "A multibeam antenna based on substrate integrated waveguide technology for MIMO wireless communications," *IEEE Transactions on Antennas and Propagation*, vol. 57, no. 6, pp. 1813–1821, 2009.
- [99] W. Yang, Y. Yang, W. Che, C. Fan, and Q. Xue, "94-GHz compact 2-D multibeam LTCC antenna based on multifolded SIW beam-forming network," *IEEE Transactions on Antennas and Propagation*, vol. 65, no. 8, pp. 4328–4333, 2017.
- [100] J. Lian, Y. Ban, Q. Yang, B. Fu, Z. Yu, and L. Sun, "Planar millimeter-wave 2-D beam-scanning multibeam array antenna fed by compact siw beam-forming network," *IEEE Transactions on Antennas and Propagation*, vol. 66, no. 3, pp. 1299–1310, 2018.

- [101] X. Wang, X. Fang, M. Laabs, and D. Plettemeier, "Compact 2-D multibeam array antenna fed by planar cascaded butler matrix for millimeter-wave communication," *IEEE Antennas and Wireless Propagation Letters*, vol. 18, no. 10, pp. 2056–2060, 2019.
- [102] J. Lian, Y. Ban, J. Zhu, J. Guo, and Z. Chen, "Planar 2-D scanning siw multibeam array with low sidelobe level for millimeter-wave applications," *IEEE Transactions on Antennas and Propagation*, vol. 67, no. 7, pp. 4570–4578, 2019.
- [103] C. Tsokos, E. Mylonas, P. Groumas, V. Katopodis, L. Gounaridis, R. B. Timens, R. M. Oldenbeuving, C. G. H. Roeloffzen, H. Avramopoulos, and C. Kouloumentas, "Analysis of a multibeam optical beamforming network based on Blass Matrix architecture," *Journal of Lightwave Technology*, vol. 36, no. 16, pp. 3354–3372, 2018.
- [104] S. Mosca, F. Bilotti, A. Toscano, and L. Vegni, "A novel design method for Blass matrix beam-forming networks," *IEEE Transactions on Antennas and Propagation*, vol. 50, no. 2, pp. 225–232, 2002.
- [105] H. Ren, H. Zhang, Y. Jin, Y. Gu, and B. Arigong, "A novel 2-D 3×3 Nolen Matrix for 2-D beamforming applications," *IEEE Transactions on Microwave Theory and Techniques*, vol. 67, no. 11, pp. 4622–4631, 2019.
- [106] T. Djerafi, N. J. G. Fonseca, and K. Wu, "Planar *ku*-band 4×4 Nolen Matrix in siw technology," *IEEE Transactions on Microwave Theory and Techniques*, vol. 58, no. 2, pp. 259–266, 2010.
- [107] N. J. G. Fonseca, "Printed S-band 4×4 Nolen Matrix for multiple beam antenna applications," *IEEE Transactions on Antennas and Propagation*, vol. 57, no. 6, pp. 1673–1678, 2009.
- [108] Y. Liu, H. Yang, Z. Jin, F. Zhao, and J. Zhu, "A multibeam cylindrically conformal slot array antenna based on a modified rotman lens," *IEEE Transactions on Antennas and Propagation*, vol. 66, no. 7, pp. 3441–3452, 2018.
- [109] Y. F. Wu, Y. J. Cheng, and Z. X. Huang, "Ka-band near-field-focused 2-D steering antenna array with a focused rotman lens," *IEEE Transactions on Antennas and Propagation*, vol. 66, no. 10, pp. 5204–5213, 2018.
- [110] K. K. Chan and S. K. Rao, "Design of a Rotman lens feed network to generate a hexagonal lattice of multiple beams," *IEEE Transactions on Antennas and Propagation*, vol. 50, no. 8, pp. 1099–1108, 2002.
- [111] L. Schulwitz and A. Mortazawi, "A compact dual-polarized multibeam phased-array architecture for millimeter-wave radar," *IEEE Transactions on Microwave Theory and Techniques*, vol. 53, no. 11, pp. 3588–3594, 2005.
- [112] Y. J. Cheng, W. Hong, and K. Wu, "Design of a substrate integrated waveguide modified R-KR lens for millimetre-wave application," *IET Microwaves, Antennas Propagation*, vol. 4, no. 4, pp. 484–491, 2010.

- [113] P. S. Hall and S. J. Vetterlein, "Review of radio frequency beamforming techniques for scanned and multiple beam antennas," *IEEE Proceedings H - Microwaves, Antennas and Propagation*, vol. 137, no. 5, pp. 293–303, 1990.
- [114] Q. Liao, N. J. G. Fonseca, and O. Quevedo-Teruel, "Compact multibeam fully metallic geodesic Luneburg Lens antenna based on non-euclidean transformation optics," *IEEE Transactions on Antennas and Propagation*, vol. 66, no. 12, pp. 7383–7388, 2018.
- [115] G. Thiele and R. Rudduck, "Geodesic lens antennas for low-angle radiation," *IEEE Transactions on Antennas and Propagation*, vol. 13, no. 4, pp. 514–521, 1965.
- [116] N. J. G. Fonseca, Q. Liao, and O. Quevedo-Teruel, "Equivalent planar lens ray-tracing model to design modulated geodesic lenses using non-euclidean transformation optics," *IEEE Transactions on Antennas and Propagation*, vol. 68, no. 5, pp. 3410–3422, 2020.
- [117] H. Lu, Z. Liu, Y. Liu, H. Ni, and X. Lv, "Compact air-filled luneburg lens antennas based on almost-parallel plate waveguide loaded with equal-sized metallic posts," *IEEE Transactions on Antennas and Propagation*, vol. 67, no. 11, pp. 6829–6838, 2019.
- [118] A. R. Weily and N. Nikolic, "Dual-polarized planar feed for low-profile hemispherical Luneburg Lens antennas," *IEEE Transactions on Antennas and Propagation*, vol. 60, no. 1, pp. 402–407, 2012.
- [119] M. Bosiljevac, M. Casaletti, F. Caminita, Z. Sipus, and S. Maci, "Non-uniform metasurface Luneburg Lens antenna design," *IEEE Transactions on Antennas and Propagation*, vol. 60, no. 9, pp. 4065–4073, 2012.
- [120] Y. Su and Z. N. Chen, "A flat dual-polarized transformation-optics beamscanning luneburg lens antenna using PCB-stacked gradient index metamaterials," *IEEE Transactions on Antennas and Propagation*, vol. 66, no. 10, pp. 5088–5097, 2018.
- [121] N. T. Nguyen, A. V. Boriskin, L. Le Coq, and R. Sauleau, "Improvement of the scanning performance of the extended hemispherical integrated lens antenna using a double lens focusing system," *IEEE Transactions on Antennas and Propagation*, vol. 64, no. 8, pp. 3698–3702, 2016.
- [122] M. K. Saleem, H. Vettikaladi, M. A. S. Alkanhal, and M. Himdi, "Lens antenna for wide angle beam scanning at 79 GHz for automotive short range radar applications," *IEEE Transactions on Antennas and Propagation*, vol. 65, no. 4, pp. 2041–2046, 2017.
- [123] A. Bisognin, N. Nachabe, C. Luxey, F. Giancesello, D. Gloria, J. R. Costa, C. A. Fernandes, Y. Alvarez, A. Arboleya-Arboleya, J. Laviada, F. Las-Heras, N. Dolatsha, B. Grave, M. Sawaby, and A. Arbabian, "Ball grid array module with integrated shaped lens for 5G backhaul/fronthaul communications in F-band," *IEEE Transactions on Antennas and Propagation*, vol. 65, no. 12, pp. 6380–6394, 2017.

- [124] D. Pasqualini and S. Maci, "High-frequency analysis of integrated dielectric lens antennas," *IEEE Transactions on Antennas and Propagation*, vol. 52, no. 3, pp. 840–847, 2004.
- [125] M. Ettorre, A. Neto, G. Gerini, and S. Maci, "Leaky-wave slot array antenna fed by a dual reflector system," *IEEE Transactions on Antennas and Propagation*, vol. 56, no. 10, pp. 3143–3149, 2008.
- [126] Y. J. Cheng, W. Hong, and K. Wu, "Millimeter-wave substrate integrated waveguide multibeam antenna based on the parabolic reflector principle," *IEEE Transactions on Antennas and Propagation*, vol. 56, no. 9, pp. 3055–3058, 2008.
- [127] D. M. Pozar, S. D. Targonski, and H. D. Syrigos, "Design of millimeter wave microstrip reflectarrays," *IEEE Transactions on Antennas and Propagation*, vol. 45, no. 2, pp. 287–296, 1997.
- [128] J. A. Encinar, "Design of two-layer printed reflectarrays using patches of variable size," *IEEE Transactions on Antennas and Propagation*, vol. 49, no. 10, 2001.
- [129] D. Berry, R. Malech, and W. Kennedy, "The reflectarray antenna," *IEEE Transactions on Antennas and Propagation*, vol. 11, no. 6, pp. 645–651, 1963.
- [130] C. G. M. Ryan, M. R. Chaharmir, J. Shaker, J. R. Bray, Y. M. M. Antar, and A. Ittipiboon, "A wideband transmitarray using dual-resonant double square rings," *IEEE Transactions on Antennas and Propagation*, vol. 58, no. 5, pp. 1486–1493, 2010.
- [131] C. Pfeiffer and A. Grbic, "Millimeter-wave transmitarrays for wavefront and polarization control," *IEEE Transactions on Microwave Theory and Techniques*, vol. 61, no. 12, pp. 4407–4417, 2013.
- [132] Y. J. Cheng, W. Hong, and K. Wu, "Millimeter-wave multibeam antenna based on eight-port hybrid," *IEEE Microwave and Wireless Components Letters*, vol. 19, no. 4, pp. 212–214, 2009.
- [133] D. Guan, Y. Zhang, Z. Qian, Y. Li, M. Asaadi, and C. Ding, "A novel 2-D multi-beam antenna without beamforming network," *IEEE Transactions on Antennas and Propagation*, vol. 64, no. 7, pp. 3177–3180, 2016.
- [134] W. F. Moulder, W. Khalil, and J. L. Volakis, "60-GHz two-dimensionally scanning array employing wideband planar switched beam network," *IEEE Antennas and Wireless Propagation Letters*, vol. 9, pp. 818–821, 2010.
- [135] I. M. Mohamed and A. Sebak, "60 GHz 2-D scanning multibeam cavity-backed patch array fed by compact SIW beamforming network for 5G applications," *IEEE Transactions on Antennas and Propagation*, vol. 67, no. 4, pp. 2320–2331, 2019.
- [136] M. M. M. Ali and A. Sebak, "2-D scanning magnetoelectric dipole antenna array fed by RGW Butler Matrix," *IEEE Transactions on Antennas and Propagation*, vol. 66, no. 11, pp. 6313–6321, 2018.

- [137] Y. Li, J. Wang, and K. Luk, "Millimeter-wave multibeam aperture-coupled magnetoelectric dipole array with planar substrate integrated beamforming network for 5G applications," *IEEE Transactions on Antennas and Propagation*, vol. 65, no. 12, pp. 6422–6431, 2017.
- [138] W. W. Hansen, "Radiating electromagnetic wave guide," 1940.
- [139] C. Walter, *Traveling Wave Antennas*. Dover Publications, 1970.
- [140] C. Balanis, *Antenna Theory: Analysis and Design*. John Wiley & Sons, 2012.
- [141] F. Zucker and J. Strom, "Experimental resolution of surface-wave antenna radiation into feed and terminal patterns," *IEEE Transactions on Antennas and Propagation*, vol. 18, no. 3, pp. 420–422, 1970.
- [142] D. R. Jackson, C. Caloz, and T. Itoh, "Leaky-wave antennas," *Proceedings of the IEEE*, vol. 100, no. 7, pp. 2194–2206, 2012.
- [143] J. Kraus and R. Marhefka, *Antennas for All Applications*. Tata McGraw-Hill, 2003.
- [144] Shiwen Yang, Soon Hie Tan, and J. S. Fu, "Short backfire antennas for wireless LAN applications at millimeter-waves," in *IEEE Antennas and Propagation Society International Symposium. Transmitting Waves of Progress to the Next Millennium. 2000 Digest. Held in conjunction with: USNC/URSI National Radio Science Meeting (C)*, vol. 3, pp. 1260–1263 vol.3, 2000.
- [145] A. Nestic, D. Nestic, V. Brankovic, K. Sasaki, and K. Kawasaki, "Antenna solution for future communication devices in mm-wave range," in *5th International Conference on Telecommunications in Modern Satellite, Cable and Broadcasting Service. TELSIKS 2001. Proceedings of Papers (Cat. No.01EX517)*, vol. 1, pp. 194–202 vol.1, 2001.
- [146] L. Goldstone and A. Oliner, "Leaky-wave antennas I: Rectangular waveguides," *IRE Transactions on Antennas and Propagation*, vol. 7, no. 4, pp. 307–319, 1959.
- [147] L. Goldstone and A. Oliner, "Leaky wave antennas II: Circular waveguides," *IRE Transactions on Antennas and Propagation*, vol. 9, no. 3, pp. 280–290, 1961.
- [148] A. A. Oliner and K. S. Lee, "The nature of the leakage from higher modes on microstrip line," in *1986 IEEE MTT-S International Microwave Symposium Digest*, pp. 57–60, 1986.
- [149] P. K. Pocharazu and D. R. Jackson, "Analysis and design of a leaky-wave EMC dipole array," *IEEE Transactions on Antennas and Propagation*, vol. 40, no. 8, pp. 950–958, 1992.
- [150] Yu-De Lin and Jyh-Wen Sheen, "Mode distinction and radiation-efficiency analysis of planar leaky-wave line source," *IEEE Transactions on Microwave Theory and Techniques*, vol. 45, no. 10, pp. 1672–1680, 1997.
- [151] A. Grbic and G. V. Eleftheriades, "Leaky CPW-based slot antenna arrays for millimeter-wave applications," *IEEE Transactions on Antennas and Propagation*, vol. 50, no. 11, pp. 1494–1504, 2002.

- [152] Pi-Wei Chen, Choon Sae Lee, and V. Nalbandian, "Planar double-layer leaky-wave microstrip antenna," *IEEE Transactions on Antennas and Propagation*, vol. 50, no. 6, pp. 832–835, 2002.
- [153] Wanchu Hong, Tai-Lee Chen, Chi-Yang Chang, J. . Sheen, and Yu-De Lin, "Broadband tapered microstrip leaky-wave antenna," *IEEE Transactions on Antennas and Propagation*, vol. 51, no. 8, pp. 1922–1928, 2003.
- [154] J. L. Gomez-Tornero, A. T. Martinez, D. C. Rebenaque, M. Gugliemi, and A. Alvarez-Melcon, "Design of tapered leaky-wave antennas in hybrid waveguide-planar technology for millimeter waveband applications," *IEEE Transactions on Antennas and Propagation*, vol. 53, no. 8, pp. 2563–2577, 2005.
- [155] Tianxia Zhao, D. R. Jackson, J. T. Williams, and A. A. Oliner, "General formulas for 2-D leaky-wave antennas," *IEEE Transactions on Antennas and Propagation*, vol. 53, no. 11, pp. 3525–3533, 2005.
- [156] J. L. Gomez-Tornero, G. Goussetis, A. P. Feresidis, and A. A. Melcon, "Control of leaky-mode propagation and radiation properties in hybrid dielectric-waveguide printed-circuit technology: Experimental results," *IEEE Transactions on Antennas and Propagation*, vol. 54, no. 11, pp. 3383–3390, 2006.
- [157] D. Deslandes and K. Wu, "Integrated microstrip and rectangular waveguide in planar form," *IEEE Microwave and Wireless Components Letters*, vol. 11, no. 2, pp. 68–70, 2001.
- [158] J. R. James and P. S. Hall, "Microstrip antennas and arrays. part 2: New array-design technique," *IEE Journal on Microwaves, Optics and Acoustics*, vol. 1, no. 5, pp. 175–181, 1977.
- [159] K. Solbach and B. Adelseck, "Dielectric image line leaky wave antenna for broadside radiation," *Electronics Letters*, vol. 19, no. 16, pp. 640–641, 1983.
- [160] M. Guglielmi and D. R. Jackson, "Broadside radiation from periodic leaky-wave antennas," *IEEE Transactions on Antennas and Propagation*, vol. 41, no. 1, pp. 31–37, 1993.
- [161] T. Kokkinos, C. D. Sarris, and G. V. Eleftheriades, "Periodic FDTD analysis of leaky-wave structures and applications to the analysis of negative-refractive-index leaky-wave antennas," *IEEE Transactions on Microwave Theory and Techniques*, vol. 54, no. 4, pp. 1619–1630, 2006.
- [162] P. Burghignoli, G. Lovat, and D. R. Jackson, "Analysis and optimization of leaky-wave radiation at broadside from a class of 1-D periodic structures," *IEEE Transactions on Antennas and Propagation*, vol. 54, no. 9, pp. 2593–2604, 2006.
- [163] Y. Li, Z. Zhang, C. Deng, Z. Feng, and M. F. Iskander, "2-D planar scalable dual-polarized series-fed slot antenna array using single substrate," *IEEE Transactions on Antennas and Propagation*, vol. 62, no. 4, pp. 2280–2283, 2014.

- [164] Y. J. Cheng, W. Hong, and K. Wu, "Millimeter-wave half mode substrate integrated waveguide frequency scanning antenna with quadri-polarization," *IEEE Transactions on Antennas and Propagation*, vol. 58, no. 6, pp. 1848–1855, 2010.
- [165] S. Karimkashi and G. Zhang, "A dual-polarized series-fed microstrip antenna array with very high polarization purity for weather measurements," *IEEE Transactions on Antennas and Propagation*, vol. 61, no. 10, pp. 5315–5319, 2013.
- [166] X. Yang, L. Di, Y. Yu, and S. Gao, "Low-profile frequency-scanned antenna based on substrate integrated waveguide," *IEEE Transactions on Antennas and Propagation*, vol. 65, no. 4, pp. 2051–2056, 2017.
- [167] L. Cui, W. Wu, and D. Fang, "Printed frequency beam-scanning antenna with flat gain and low sidelobe levels," *IEEE Antennas and Wireless Propagation Letters*, vol. 12, pp. 292–295, 2013.
- [168] Y. J. Cheng, Y. X. Guo, and Z. G. Liu, "W-band large-scale high-gain planar integrated antenna array," *IEEE Transactions on Antennas and Propagation*, vol. 62, no. 6, pp. 3370–3373, 2014.
- [169] J. Wu, Y. J. Cheng, and Y. Fan, "A wideband high-gain high-efficiency hybrid integrated plate array antenna for V-band inter-satellite links," *IEEE Transactions on Antennas and Propagation*, vol. 63, no. 4, pp. 1225–1233, 2015.
- [170] D. Kim, J. Hirokawa, M. Ando, J. Takeuchi, and A. Hirata, "64 × 64-element and 32 × 32-element slot array antennas using double-layer hollow-waveguide corporate-feed in the 120 GHz band," *IEEE Transactions on Antennas and Propagation*, vol. 62, no. 3, pp. 1507–1512, 2014.
- [171] L. Kong and X. Xu, "A compact dual-band dual-polarized microstrip antenna array for MIMO-SAR applications," *IEEE Transactions on Antennas and Propagation*, vol. 66, no. 5, pp. 2374–2381, 2018.
- [172] M. Takahashi, M. Ando, N. Goto, Y. Numano, M. Suzuki, Y. Okazaki, and T. Yoshimoto, "Dual circularly polarized radial line slot antennas," *IEEE Transactions on Antennas and Propagation*, vol. 43, no. 8, pp. 874–876, 1995.
- [173] Z. Zhang and K. Wu, "A wideband dual-polarized dielectric magnetoelectric dipole antenna," *IEEE Transactions on Antennas and Propagation*, vol. 66, no. 10, pp. 5590–5595, 2018.
- [174] L. Wen, S. Gao, Q. Luo, Q. Yang, W. Hu, Y. Yin, X. Ren, and J. Wu, "A compact wideband dual-polarized antenna with enhanced upper out-of-band suppression," *IEEE Transactions on Antennas and Propagation*, vol. 67, no. 8, pp. 5194–5202, 2019.
- [175] Y. Li, C. Wang, and Y. X. Guo, "A ka-band wideband dual-polarized magnetoelectric dipole antenna array on ltcc," *IEEE Transactions on Antennas and Propagation*, vol. 68, no. 6, pp. 4985–4990, 2020.

- [176] Y. Yang, B. Sun, G. Zhang, and L. Shen, "TFSIW-excited dual-polarized array antenna with 30° beam-pointing for millimeter-wave applications," *IEEE Transactions on Antennas and Propagation*, vol. 67, no. 8, pp. 5740–5745, 2019.
- [177] D. Kim, M. Zhang, J. Hirokawa, and M. Ando, "Design and fabrication of a dual-polarization waveguide slot array antenna with high isolation and high antenna efficiency for the 60 GHz band," *IEEE Transactions on Antennas and Propagation*, vol. 62, no. 6, pp. 3019–3027, 2014.
- [178] Y. Zhang and J. Li, "Differential-series-fed dual-polarized traveling-wave array for full-duplex applications," *IEEE Transactions on Antennas and Propagation*, vol. 68, no. 5, pp. 4097–4102, 2020.
- [179] Shun-Shi Zhong, Xue-Xia Yang, Shi-Chang Gao, and Jun-Hai Cui, "Corner-fed microstrip antenna element and arrays for dual-polarization operation," *IEEE Transactions on Antennas and Propagation*, vol. 50, no. 10, pp. 1473–1480, 2002.
- [180] Shun-Shi Zhong, M. Ahmed, and G. Qasim, "Low-cost corner-fed microstrip antenna array with dual polarization," in *1999 Asia Pacific Microwave Conference. APMC'99. Microwaves Enter the 21st Century. Conference Proceedings (Cat. No.99TH8473)*, vol. 3, pp. 928–931 vol.3, 1999.
- [181] J. Wu, Y. J. Cheng, H. B. Wang, Y. C. Zhong, D. Ma, and Y. Fan, "A wideband dual circularly polarized full-corporate waveguide array antenna fed by triple-resonant cavities," *IEEE Transactions on Antennas and Propagation*, vol. 65, no. 4, pp. 2135–2139, 2017.
- [182] W. Wang, J. Wang, A. Liu, and Y. Tian, "A novel broadband and high-isolation dual-polarized microstrip antenna array based on quasi-substrate integrated waveguide technology," *IEEE Transactions on Antennas and Propagation*, vol. 66, no. 2, pp. 951–956, 2018.
- [183] M. Ferrando-Rocher, J. I. Herranz-Herruzo, A. Valero-Nogueira, B. Bernardo-Clemente, A. U. Zaman, and J. Yang, "8 × 8 Ka -band dual-polarized array antenna based on gap waveguide technology," *IEEE Transactions on Antennas and Propagation*, vol. 67, no. 7, pp. 4579–4588, 2019.
- [184] S. Zhou, Z. Peng, G. Huang, J. Li, and C. Sim, "Design of wideband and dual polarized cavity antenna planar array," *IEEE Transactions on Antennas and Propagation*, vol. 64, no. 10, pp. 4565–4569, 2016.
- [185] S. Zhou, G. Huang, T. Chio, J. Yang, and G. Wei, "Design of a wideband dual-polarization full-corporate waveguide feed antenna array," *IEEE Transactions on Antennas and Propagation*, vol. 63, no. 11, pp. 4775–4782, 2015.
- [186] Z. Chen, H. Liu, J. Yu, and X. Chen, "High gain, broadband and dual-polarized substrate integrated waveguide cavity-backed slot antenna array for 60 GHz band," *IEEE Access*, vol. 6, pp. 31012–31022, 2018.
- [187] Y. Zhao and K. Luk, "Dual circular-polarized SIW-fed high-gain scalable antenna array for 60 GHz applications," *IEEE Transactions on Antennas and Propagation*, vol. 66, no. 3, pp. 1288–1298, 2018.

- [188] P. Li, S. Liao, Q. Xue, and S. Qu, "60 GHz dual-polarized high-gain planar aperture antenna array based on LTCC," *IEEE Transactions on Antennas and Propagation*, vol. 68, no. 4, pp. 2883–2894, 2020.
- [189] Y. Cheng, *Substrate Integrated Antennas and Arrays*. CRC Press, 2018.
- [190] Y. J. Cheng, J. Wang, and X. L. Liu, "94 GHz substrate integrated waveguide dual-circular-polarization shared-aperture parallel-plate long-slot array antenna with low sidelobe level," *IEEE Transactions on Antennas and Propagation*, vol. 65, no. 11, pp. 5855–5861, 2017.
- [191] X. Lu, H. Zhang, S. Gu, H. Liu, X. Wang, and W. Lu, "A dual-polarized cross-slot antenna array on a parallel-plate waveguide with compact structure and high efficiency," *IEEE Antennas and Wireless Propagation Letters*, vol. 17, no. 1, pp. 8–11, 2018.
- [192] J. S. Chieh, B. Pham, A. Pham, G. Kannell, and A. Pidwerbetsky, "Millimeter-wave dual-polarized high-isolation antennas and arrays on organic substrates," *IEEE Transactions on Antennas and Propagation*, vol. 61, no. 12, pp. 5948–5957, 2013.
- [193] T. H. Jang, H. Y. Kim, D. M. Kang, S. H. Kim, and C. S. Park, "60 GHz low-profile, wideband dual-polarized U-slot coupled patch antenna with high isolation," *IEEE Transactions on Antennas and Propagation*, vol. 67, no. 7, pp. 4453–4462, 2019.
- [194] T. Chaloun, V. Ziegler, and W. Menzel, "Design of a dual-polarized stacked patch antenna for wide-angle scanning reflectarrays," *IEEE Transactions on Antennas and Propagation*, vol. 64, no. 8, pp. 3380–3390, 2016.
- [195] Q. Luo, S. Gao, and L. Zhang, "Wideband multilayer dual circularly-polarised antenna for array application," *Electronics Letters*, vol. 51, no. 25, pp. 2087–2089, 2015.
- [196] N. Ashraf, A. R. Sebak, and A. A. Kishk, "Packaged microstrip line feed network on a single surface for dual-polarized 2N×2M ME-dipole antenna array," *IEEE Antennas and Wireless Propagation Letters*, vol. 19, no. 4, pp. 596–600, 2020.
- [197] J. Du, K. So, Y. Ra, S. Jung, J. Kim, S. Y. Kim, S. Woo, H. Kim, Y. Ho, and W. Paik, "Dual-polarized patch array antenna package for 5G communication systems," in *2017 11th European Conference on Antennas and Propagation (EUCAP)*, pp. 3493–3496, 2017.
- [198] S. J. Yang, Y. M. Pan, L. Shi, and X. Y. Zhang, "Millimeter-wave dual-polarized filtering antenna for 5G application," *IEEE Transactions on Antennas and Propagation*, vol. 68, no. 7, pp. 5114–5121, 2020.
- [199] K. Klionovski, M. S. Sharawi, and A. Shamim, "A dual-polarization-switched beam patch antenna array for millimeter-wave applications," *IEEE Transactions on Antennas and Propagation*, vol. 67, no. 5, pp. 3510–3515, 2019.
- [200] D. Liu, X. Gu, C. W. Baks, and A. Valdes-Garcia, "Antenna-in-package design considerations for Ka-band 5G communication applications," *IEEE Transactions on Antennas and Propagation*, vol. 65, no. 12, pp. 6372–6379, 2017.

- [201] T. Zhang, Y. Zhang, L. Cao, W. Hong, and K. Wu, "Single-layer wideband circularly polarized patch antennas for Q-band applications," *IEEE Transactions on Antennas and Propagation*, vol. 63, no. 1, pp. 409–414, 2015.
- [202] G. F. Hamberger, S. Späth, U. Siart, and T. F. Eibert, "A mixed circular/linear dual-polarized phased array concept for automotive radar—planar antenna designs and system evaluation at 78 GHz," *IEEE Transactions on Antennas and Propagation*, vol. 67, no. 3, pp. 1562–1572, 2019.
- [203] Shi-Chang Gao, Le-Wei Li, Mook-Seng Leong, and Tat-Soon Yeo, "Dual-polarized slot-coupled planar antenna with wide bandwidth," *IEEE Transactions on Antennas and Propagation*, vol. 51, no. 3, pp. 441–448, 2003.
- [204] S. Gao, L. W. Li, M. S. Leong, and T. S. Yeo, "A broad-band dual-polarized microstrip patch antenna with aperture coupling," *IEEE Transactions on Antennas and Propagation*, vol. 51, no. 4, pp. 898–900, 2003.
- [205] M. A. Islam and N. C. Karmakar, "A 4×4 dual polarized mm-wave ACMPA array for a universal mm-wave chipless RFID tag reader," *IEEE Transactions on Antennas and Propagation*, vol. 63, no. 4, pp. 1633–1640, 2015.
- [206] A. Dadgarpour, N. Bayat-Makou, M. A. Antoniadis, A. A. Kishk, and A. Sebak, "A dual-polarized magnetoelectric dipole array based on printed ridge gap waveguide with dual-polarized split-ring resonator lens," *IEEE Transactions on Antennas and Propagation*, vol. 68, no. 5, pp. 3578–3585, 2020.
- [207] Y. Li and K. Luk, "60-GHz dual-polarized two-dimensional switch-beam wideband antenna array of aperture-coupled magneto-electric dipoles," *IEEE Transactions on Antennas and Propagation*, vol. 64, no. 2, pp. 554–563, 2016.
- [208] J. Zhu, S. Li, S. Liao, Y. Yang, and H. Zhu, "60 GHz substrate-integrated-waveguide-fed patch antenna array with quadri-polarization," *IEEE Transactions on Antennas and Propagation*, vol. 66, no. 12, pp. 7406–7411, 2018.
- [209] J. Wu, Y. J. Cheng, H. B. Wang, Y. C. Zhong, D. Ma, and Y. Fan, "A wideband dual circularly polarized full-corporate waveguide array antenna fed by triple-resonant cavities," *IEEE Transactions on Antennas and Propagation*, vol. 65, no. 4, pp. 2135–2139, 2017.
- [210] S. Zhou, G. Huang, and T. Chio, "A lightweight, wideband, dual-circular-polarized waveguide cavity array designed with direct metal laser sintering considerations," *IEEE Transactions on Antennas and Propagation*, vol. 66, no. 2, pp. 675–682, 2018.
- [211] L. Schulwitz and A. Mortazawi, "Millimeter-wave dual polarized L-shaped horn antenna for wide-angle phased arrays," *IEEE Transactions on Antennas and Propagation*, vol. 54, no. 9, pp. 2663–2668, 2006.
- [212] H. Jin, Y. M. Huang, H. Jin, and K. Wu, "E-band substrate integrated waveguide orthomode transducer integrated with dual-polarized horn antenna," *IEEE Transactions on Antennas and Propagation*, vol. 66, no. 5, pp. 2291–2298, 2018.

- [213] M. Esquiús-Morote, M. Mattes, and J. R. Mosig, "Orthomode transducer and dual-polarized horn antenna in substrate integrated technology," *IEEE Transactions on Antennas and Propagation*, vol. 62, no. 10, pp. 4935–4944, 2014.
- [214] J. Hwang and Y. Oh, "Compact orthomode transducer using single-ridged triangular waveguides," *IEEE Microwave and Wireless Components Letters*, vol. 21, no. 8, pp. 412–414, 2011.
- [215] Z. Ahmad and J. Hesselbarth, "Dual-polarized antenna with orthomode transducer for 60 GHz communications," in *2016 10th European Conference on Antennas and Propagation (EuCAP)*, pp. 1–5, 2016.
- [216] A. Navarrini and R. L. Plambeck, "A turnstile junction waveguide orthomode transducer," *IEEE Transactions on Microwave Theory and Techniques*, vol. 54, no. 1, pp. 272–277, 2006.
- [217] S. J. Skinner and G. L. James, "Wide-band orthomode transducers," *IEEE Transactions on Microwave Theory and Techniques*, vol. 39, no. 2, pp. 294–300, 1991.
- [218] C. A. Balanis, *Antenna theory: analysis and design*. John Wiley & sons, 2016.
- [219] D. Pozar, *Microwave Engineering, 4th ed.* John Wiley & Sons, 2011.
- [220] J. Xu, Z. N. Chen, X. Qing, and W. Hong, "Bandwidth enhancement for a 60 GHz substrate integrated waveguide fed cavity array antenna on ltcc," *IEEE Transactions on Antennas and Propagation*, vol. 59, no. 3, pp. 826–832, 2011.
- [221] A. D. Nestic and D. A. Nestic, "Printed planar 8×8 array antenna with circular polarization for millimeter-wave application," *IEEE Antennas and Wireless Propagation Letters*, vol. 11, pp. 744–747, 2012.
- [222] S. Mukherjee and A. Biswas, "Substrate integrated waveguide (SIW) cavity backed slot antenna for polarization diversity application," in *2015 IEEE Applied Electromagnetics Conference (AEMC)*, pp. 1–2, 2015.
- [223] H. B. Wang and Y. J. Cheng, "Broadband printed-circuit-board characterization using multimode substrate-integrated-waveguide resonator," *IEEE Transactions on Microwave Theory and Techniques*, vol. 65, no. 6, pp. 2145–2152, 2017.
- [224] R. Garg, K. Gupta, and R. Sharan, "A thin wall leaky waveguide antenna," *IEEE Transactions on Antennas and Propagation*, vol. 23, no. 1, pp. 107–112, 1975.
- [225] J. Hu, Z. Hao, and W. Hong, "Design of a wideband quad-polarization reconfigurable patch antenna array using a stacked structure," *IEEE Transactions on Antennas and Propagation*, vol. 65, no. 6, pp. 3014–3023, 2017.
- [226] W. L. Stutzman and G. A. Thiele, *Antenna Theory and Design, 3rd ed.* Hoboken, NJ, USA: Wiley, 2012.
- [227] Q. Xue, S. W. Liao, and J. H. Xu, "A differentially-driven dual-polarized magneto-electric dipole antenna," *IEEE Transactions on Antennas and Propagation*, vol. 61, no. 1, pp. 425–430, 2013.

- [228] Y. P. Zhang and J. J. Wang, "Theory and analysis of differentially-driven microstrip antennas," *IEEE Transactions on Antennas and Propagation*, vol. 54, no. 4, pp. 1092–1099, 2006.
- [229] Y. P. Zhang, "Design and experiment on differentially-driven microstrip antennas," *IEEE Transactions on Antennas and Propagation*, vol. 55, no. 10, pp. 2701–2708, 2007.
- [230] D. Deslandes and Ke Wu, "Accurate modeling, wave mechanisms, and design considerations of a substrate integrated waveguide," *IEEE Transactions on Microwave Theory and Techniques*, vol. 54, no. 6, pp. 2516–2526, 2006.
- [231] W. R. Eisenstadt, R. Stengel, and B. M. Thompson, *Microwave Differential Circuit Design Using Mixed-Mode S-Parameters*. Boston, MA, USA: Artech House, 2006.
- [232] K. Carver and J. Mink, "Microstrip antenna technology," *IEEE Transactions on Antennas and Propagation*, vol. 29, no. 1, pp. 2–24, 1981.
- [233] A. Company, "Series 37XXXC vector network analyser operation manual." <https://dl.cdn-anritsu.com/en-us/test-measurement/files/Manuals/Operation-Manual/10410-00226b.pdf>. Accessed: 2020-08-24.
- [234] R. J. Mailloux, *Phased Array Antenna Handbook*. USA: Artech House, Inc., 3rd ed., 2017.
- [235] D. Kim, J. Hirokawa, and M. Ando, "Design of waveguide short-slot two-plane couplers for one-body 2-D beam-switching Butler Matrix application," *IEEE Transactions on Microwave Theory and Techniques*, vol. 64, no. 3, pp. 776–784, 2016.
- [236] A. Fackelmeier and E. M. Biebl, "Narrowband frequency scanning array antenna at 5.8 ghz for short range imaging," in *2010 IEEE MTT-S International Microwave Symposium*, pp. 1266–1269, 2010.
- [237] F. Zavosh and J. T. Aberle, "Single and stacked circular microstrip patch antennas backed by a circular cavity," *IEEE Transactions on Antennas and Propagation*, vol. 43, no. 7, pp. 746–750, 1995.
- [238] M. H. Awida, A. H. Kamel, and A. E. Fathy, "Analysis and design of wide-scan angle wide-band phased arrays of substrate-integrated cavity-backed patches," *IEEE Transactions on Antennas and Propagation*, vol. 61, no. 6, pp. 3034–3041, 2013.
- [239] H. Dashti and M. H. Neshati, "Development of low-profile patch and semi-circular SIW cavity hybrid antennas," *IEEE Transactions on Antennas and Propagation*, vol. 62, no. 9, pp. 4481–4488, 2014.
- [240] G. Srivastava and A. Mohan, "A differential dual-polarized SIW cavity-backed slot antenna," *IEEE Transactions on Antennas and Propagation*, vol. 67, no. 5, pp. 3450–3454, 2019.
- [241] T. Hong, Z. Zhao, W. Jiang, S. Xia, Y. Liu, and S. Gong, "Dual-band siw cavity-backed slot array using TM_{020} and TM_{120} modes for 5G applications," *IEEE Transactions on Antennas and Propagation*, vol. 67, no. 5, pp. 3490–3495, 2019.

- [242] S. A. Razavi, P. Kildal, L. Xiang, E. Alfonso Alós, and H. Chen, “ 2×2 -slot element for 60-GHz planar array antenna realized on two doubled-sided pcbs using SIW cavity and EBG-type soft surface fed by microstrip-ridge gap waveguide,” *IEEE Transactions on Antennas and Propagation*, vol. 62, no. 9, pp. 4564–4573, 2014.
- [243] J. Hirokawa and M. Ando, “Single-layer feed waveguide consisting of posts for plane TEM wave excitation in parallel plates,” *IEEE Transactions on Antennas and Propagation*, vol. 46, no. 5, pp. 625–630, 1998.
- [244] D. Guan, Q. Zhang, P. You, Z. Yang, Y. Zhou, and S. Yong, “Scanning rate enhancement of leaky-wave antennas using slow-wave substrate integrated waveguide structure,” *IEEE Transactions on Antennas and Propagation*, vol. 66, no. 7, pp. 3747–3751, 2018.
- [245] K. Mak, K. So, H. Lai, and K. Luk, “A magnetoelectric dipole leaky-wave antenna for millimeter-wave application,” *IEEE Transactions on Antennas and Propagation*, vol. 65, no. 12, pp. 6395–6402, 2017.
- [246] T. Y. Yang, W. Hong, and Y. Zhang, “Wideband millimeter-wave substrate integrated waveguide cavity-backed rectangular patch antenna,” *IEEE Antennas and Wireless Propagation Letters*, vol. 13, pp. 205–208, 2014.
- [247] Y. P. Zhang and J. J. Wang, “Theory and analysis of differentially-driven microstrip antennas,” *IEEE Transactions on Antennas and Propagation*, vol. 54, no. 4, pp. 1092–1099, 2006.
- [248] T. Yang, W. Hong, and Y. Zhang, “Balanced dual fed SIW slot antenna array for Q-Link PAN high gain application,” in *2013 IEEE International Wireless Symposium (IWS)*, pp. 1–4, 2013.
- [249] R. S. Elliot, *Antenna Theory and Design*. Hoboken: John Wiley & Sons, 1981.
- [250] M. Li, K. A. Hummer, and K. Chang, “Theoretical and experimental study of the input impedance of the cylindrical cavity-backed rectangular slot antennas,” *IEEE Trans. Antennas Propag.*, vol. 39, no. 8, pp. 1158–1166, 1991.
- [251] R. N. Bracewell, “Charts for resonant frequencies of cavities,” *Proc. IEEE*, vol. 35, no. 8, pp. 830–841, 1947.
- [252] S. Long, M. McAllister, and Liang Shen, “The resonant cylindrical dielectric cavity antenna,” *IEEE Transactions on Antennas and Propagation*, vol. 31, no. 3, pp. 406–412, 1983.
- [253] M. Esquius-Morote, M. Mattes, and J. R. Mosig, “Orthomode transducer and dual-polarized horn antenna in substrate integrated technology,” *IEEE Transactions on Antennas and Propagation*, vol. 62, no. 10, pp. 4935–4944, 2014.
- [254] H. Kähkönen, J. Ala-Laurinaho, and V. Viikari, “Dual-polarized Ka-band Vivaldi antenna array,” *IEEE Transactions on Antennas and Propagation*, vol. 68, no. 4, pp. 2675–2683, 2020.

List of Publications

- [1] **Q. Yang**, S. Gao, Q. Luo, L. Wen, Y. Ban, X. Ren, J. Wu, X. Yang, and Y. Liu, "Millimetre-wave dual-polarized differentially-fed 2D multibeam patch antenna array," *IEEE Transactions on Antennas and Propagation*, vol. 68, no. 10, pp. 7007-7016, Oct. 2020.
- [2] **Q. Yang**, S. Gao, Q. Luo, L. Wen, Y. Ban, X. Yang, X. Ren, and J. Wu, "Cavity-backed slot-coupled patch antenna array with dual slant polarization for millimetre-wave base station applications," *IEEE Transactions on Antennas and Propagation*, accepted in Jul. 2020.
- [3] **Q. Yang**, S. Gao, Q. Luo, L. Wen, X. Ren, J. Wu, Y. Ban, and X. Yang, "A low complexity dual-polarized planar antenna array differentially-fed by orthomode transducer," *IEEE Transactions on Antennas and Propagation*, accepted in Aug. 2020.
- [4] **Q. Yang**, S. Gao, Q. Luo, L. Wen, Y. Ban, X. Yang, X. Ren and J. Wu, "Dual-polarized crossed slot array antenna designed on a single laminate for millimetre-wave applications," *IEEE Transactions on Antennas and Propagation*, vol. 68, no. 5, pp. 4120-4125, May 2020.
- [5] **Q. Yang**, S. Gao, Q. Luo, L. Wen, X. Ren, J. Wu, Y. Ban, and X. Yang, "A low complexity 16×16 Butler Matrix design using eight-port hybrids," *IEEE Access*, vol. 7, pp. 177864-177873, 2019.
- [6] **Q. Yang**, S. Gao, L. Wen, X. Ren, D. Kong, and W. Liu, " $\pm 45^\circ$ linearly polarized slot-coupled patch antenna for mmWave applications," *9th Asia-Pacific Conference on Antennas and Propagation*, Aug. 2020. **(Best Student Paper Award)**
- [7] **Q. Yang**, S. Gao, H. Li, Q. Luo, L. Wen, X. Ren, D. Kong, W. Liu, and J. Wu, "Differentially-fed dual-polarized 2D multibeam antenna array for mmWave applications," *International Conference on Microwave and Millimetre Wave Technology*, Sept. 2020. **(shortlisted for the Best Student Paper Award)**

- [8] **Q. Yang**, S. Gao, L. Wen, and Q. Luo, "Antenna array driven by broadband integrated multibeam network with flat amplitudes and phases," *The Loughborough Antennas & Propagation Conference*, Nov. 2018.
- [9] **Q. Yang**, S. Gao, L. Wen, and Q. Luo, "A compact broadband 16×16 Butler Matrix for multibeam antenna array applications," *International Symposium on Antennas and Propagation*, Oct. 2019.
- [10] **Q. Yang**, S. Gao, L. Wen, Q. Luo, X. Ren, J. Wu, and Y. Ban, "Millimetre-wave dual-polarized slot array antenna using a TE_{210} and TE_{120} mode cavity," *14th European Conference on Antennas and Propagation*, Mar. 2020.
- [11] **Q. Yang**, S. Gao, X. Ren, D. Kong, W. Liu, L. Wen, Q. Luo, and J. Wu, "Millimetre-wave dual-polarized patch antenna designed for integrating with chip package," *IEEE MTT-S International Wireless Symposium*, Sept. 2020.
- [12] L. Wen, S. Gao, Q. Luo, **Q. Yang**, W. Hu and Y. Yin, "A low-cost differentially driven dual-polarized patch antenna by using open-loop resonators," *IEEE Transactions on Antennas and Propagation*, vol. 67, no. 4, pp. 2745-2750, Apr. 2019.
- [13] J. Lian, Y. Ban, **Q. Yang**, B. Fu, Z. Yu and L. Sun, "Planar millimetre-wave 2-D beam-scanning multibeam array antenna fed by compact SIW beam-forming network," *IEEE Transactions on Antennas and Propagation*, vol. 66, no. 3, pp. 1299-1310, Mar. 2018.
- [14] L. Wen, S. Gao, Q. Luo, W. Hu, **Q. Yang**, Y. Yin, X. Ren, J. Wu, "A wideband differentially driven dual-polarized antenna by using integrated six-port power divider," *IEEE Transactions on Antennas and Propagation*, vol. 67, no. 12, pp. 7252-7260, Dec. 2019.
- [15] L. Wen, S. Gao, Q. Luo, **Q. Yang**, W. Hu, Y. Yin, X. Ren, J. Wu, "A wideband differentially fed dual-polarized antenna with wideband harmonic suppression," *IEEE Transactions on Antennas and Propagation*, vol. 67, no. 9, pp. 6176-6181, Sept. 2019.
- [16] L. Wen, S. Gao, Q. Luo, **Q. Yang**, W. Hu, Y. Yin, X. Ren, J. Wu, "A compact wideband dual-polarized antenna with enhanced upper out-of-band suppression," *IEEE Transactions on Antennas and Propagation*, vol. 67, no. 8, pp. 5194-5202, Aug. 2019.
- [17] L. Wen, S. Gao, Q. Luo, **Q. Yang**, W. Hu, Y. Yin, X. Ren, J. Wu, "A wideband series-fed circularly polarized differential antenna by using crossed open slot-pairs," *IEEE Transactions on Antennas and Propagation*, vol. 68, no. 4, pp. 2565-2574, Apr. 2020.

-
- [18] L. Wen, S. Gao, **Q. Yang**, Q. Luo, X. Ren and J. Wu, "A compact dual-polarized patch antenna loaded with metamaterial unit cell for broadband wireless communication," *2019 IEEE MTT-S International Wireless Symposium (IWS)*, Guangzhou, China, 2019, pp. 1-3.